



**University Library**

Author/Filing Title ..... PERERA, M.S. ....

Class Mark ..... T .....

Please note that fines are charged on ALL  
overdue items.

**FOR REFERENCE ONLY**

0403481600



**Multi-Physics for Integrated Analysis of  
Flexible Body Dynamics with Tribological  
Conjunction in IC Engines**

*By*

**M.S.Malika Perera B.Sc (Hons.)**

**Thesis submitted in partial fulfilment of the  
requirements for the Degree of Doctor of  
Philosophy**

**Loughborough University**

**Wolfson School of Mechanical & Manufacturing  
Engineering**

**December 2006**





Loughborough  
University  
Pilkington Library

Date

6/2008

Class

T

Acc  
No.

0403481600

---

## ABSTRACT

Since the inception of internal combustion engine, there has been a continual strive to improve its efficiency and refinement. Until very recently, the developments in this regard have been largely based on an experiential basis, or backed by analytical investigations, confined to particular features of the engines. This has been due to lack of computational power, and analysis tools of an integrative nature. In recent years enhanced computing power has meant that complex models, chiefly based on multi-body dynamics could be developed, and further enhanced by the inclusion of component flexibility in the form of structural modes, obtained through finite element analysis. This approach has enabled study of dynamics/vibration response of engines in a more quantitative manner than hitherto possible. Structural integrity issues, as well as noise and vibration (refinement) can then be studied in an integrated manner. However, earlier models still lack sufficient detail to include, within the same analysis, issues related to efficiency, chiefly prediction of parasitic losses due to mechanical imbalance and friction.

It is clear that a more integrative approach, comprising inertial dynamics, component flexibility and frictional behaviour of load bearing and transmitting conjunctions is required. Although specific and detailed analysis of such conjunctions has been carried out, their integrated inclusion in an overall efficient model has been lacking. The main aim of this thesis is to introduce and apply such an integrative model, dealing with small-scale dynamics/tribology of such conjunctions, together with flexible-multi-body dynamics of IC engines, within a single analysis. This approach is, therefore, termed multi-scale multi-physics approach, which forms the main overall contribution of this thesis to knowledge.

Additionally, the inclusion of the 4-stroke combustion cycle within the analysis provides the variation of all the included physical phenomena during representative engine cycles, which has not been reported hitherto, even in detailed analysis of very confined sub-systems, such as engine bearings or piston systems. Inclusion of thermal effects in some of the conjunctions in an efficient analytical manner makes the model predictions more representative of the actual prevailing fired conditions, than many reported research carried out mainly under isothermal conditions.

The measured flywheel rotational as well as nodding motions are closely correlated with numerically predicted values both in magnitude and frequency spectrum. The main bearing, piston-to-cylinder wall and piston ring-to-cylinder wall lubricated contacts are represented by analytical solutions of the Reynolds equation. Temperature rise at the piston ring-to-cylinder wall contact is sought by the energy equation. Experimentally verified modal properties of connecting rod, crankshaft and flywheel are included in the analytical model. Analytically predicted frictional variations and dynamic behaviour of contact conjunctions are closely correlated with each other. Such that the main findings of the thesis are chiefly in line with measured, observed or surmised behaviour of IC engines, and verified analytically for the case of inertial dynamics, as well as through experimental measurements.

**Keywords :** Multi-scale multi-physics modelling, multi-body dynamics, structural vibration, piston skirt and ring-pack to cylinder friction/lubrication, tribo-dynamics of engine bearings

---

## ACKNOWLEDGEMENTS

Firstly I would like to express profound gratitude to my supervisors, Dr. Stephanos Theodossiades and Professor Homer Rahnejat for their invaluable support, advice, supervision, and encouragement throughout the course of my research.

I would also acknowledge Wolfson School of Mechanical and Manufacturing Engineering in Loughborough University for funding me with a departmental studentship and supporting my work with all available resources.

I would also acknowledge Department of Mechanical Engineering, University of Moratuwa, Sri Lanka for its support both in administrative and financial aspects throughout my research. I really appreciate the kindness and advice by its staff and colleagues during my research.

I wish to express my gratitude to all my friends and colleagues who made the whole PhD experience much more interesting and rewarding.

I am as ever, especially indebted to my parents, Mr. John and Mrs, Evelyn Perera for their love and support throughout my life including my years in school. I also wish to thank my brother and my sister for their support and understanding during my study.

---

## TABLE OF CONTENTS

Abstract.....	ii
Acknowledgements.....	iii
Table of Contents.....	iv
Glossary Of Terms.....	viii
List Of Figures.....	ix
List Of Table.....	xiii
Nomenclature.....	xiv
1 Introduction.....	1
1.1 Basic Engine Types.....	1
1.2 Historical Evolution of Engines.....	3
1.3 Noise, Vibration and Harshness.....	4
1.4 Sources of vibration in an Engine.....	5
1.5 Crankshaft Vibrations.....	9
1.6 Engine performance.....	10
1.7 Aims and Objectives.....	11
1.8 Structure of the Thesis.....	14
2 Literature Review.....	16
2.1 Introduction.....	16
2.2 Lubrication Analysis.....	18
2.2.1 Principle of Lubrication.....	20
2.2.2 Lubrication of Crankshaft Support Journal Bearings.....	22
2.2.3 Piston Secondary Motion.....	28
2.2.4 Piston Ring Analysis.....	32
2.3 Dynamic behaviour of the Crankshaft.....	37
2.3.1 Torsional Vibrations.....	39
2.3.2 Engine Noise Emission.....	41
2.4 Vibration Analysis with FEM.....	43
2.5 Crankshaft Offset.....	44
3 Multi-Physics Modelling.....	46
3.1 Introduction to Multi-Physics Modelling.....	46
3.2 Mathematical Model For Multi-Body Dynamic System.....	50
3.2.1 Multi-Degree of Freedom System.....	50

---

---

3.2.2	Lagrange's equation for multi body dynamics system .....	51
3.2.3	Generalized Forces.....	54
3.2.4	Constraining Reaction Forces .....	56
3.2.5	Kinematic System Development.....	56
3.2.6	Equations of Motion .....	57
3.3	Component Flexibility .....	58
3.3.1	Finite Element Analysis.....	60
3.3.2	Boundary Conditions .....	61
3.3.3	Modal Transformation .....	62
3.3.4	Component Mode Synthesis .....	62
3.3.5	Creation of Flexible Bodies .....	64
3.4	Method of Formulation and Solution.....	66
3.4.1	LU Decomposition (Cholesky Factorisation).....	67
3.5	Engine Dynamics.....	70
3.5.1	Translational Inertial Imbalance .....	71
3.5.2	Power Torque Fluctuations.....	73
3.5.3	Rotational Imbalance .....	74
4	Tribological contacts.....	76
4.1	Introduction.....	76
4.2	Lubrication Regimes.....	77
4.2.1	Boundary Lubrication .....	78
4.2.2	Mixed Lubrication .....	78
4.2.3	Hydrodynamic and Elastohydrodynamic Lubrication.....	78
4.3	Reynolds Equation – General Development.....	79
4.3.1	Short Bearing Approximation.....	81
4.3.2	Stiffness of Journal Bearing.....	87
4.3.3	One dimensional solution for piston skirt and ring contacts.....	89
4.4	Analysis of Friction.....	95
4.4.1	Boundary Friction Force.....	96
4.4.2	Viscous Friction Force.....	99
4.5	Temperature Effects in Lubricated Contacts .....	100
5	Numerical Model Development.....	106
5.1	Introduction.....	106

---

---

5.2	Rigid Single Cylinder Model.....	107
5.2.1	The ADAMS Multi-body System Software .....	107
5.2.2	Modelling Procedure in ADAMS .....	108
5.3	Basic Components in the Engine .....	110
5.3.1	Flywheel.....	111
5.3.2	Crankshaft.....	111
5.3.3	Connecting Rod .....	112
5.3.4	Piston.....	112
5.4	Flexible Engine Components in ADAMS .....	113
5.4.1	Modelling Procedure.....	114
5.5	Applied Forces .....	120
5.5.1	Combustion Gas Force.....	120
5.5.2	Engine Load Torque .....	122
5.5.3	Main Bearing Reaction Force .....	124
5.5.4	Main Bearing Friction Torque .....	125
5.5.5	Piston Skirt Interaction with Cylinder Wall.....	127
5.5.6	Friction Between the Piston Skirt and the Cylinder Wall.....	134
5.5.7	Friction Between The Ring and The Cylinder Wall .....	135
6	Experimentatal investigation .....	142
6.1	Introduction.....	142
6.2	Engine Testing .....	144
6.2.1	Description of Test Rig.....	144
6.3	Measurement Hardware .....	146
6.3.1	Controlled Impact Excitation.....	148
6.3.2	Acceleration Response Measurement.....	150
6.3.3	Velocity Measurement at Flywheel End.....	151
6.3.4	Combustion Gas Pressure Measurement .....	154
6.4	Signal Processing and Data Acquisition .....	155
6.4.1	Brief background in Digital Signal Processing.....	155
6.4.2	Signal Analysis .....	156
6.5	Testing Procedure .....	161
7	Results and Discussion .....	167
7.1	Single cylinder engine dynamics .....	167

---

---

7.2	The single cylinder engine model .....	172
7.2.1	Experimental verification.....	172
7.2.2	Piston secondary motion .....	185
7.2.3	Piston ring analysis .....	189
7.3	Effect of offsetting the crankshaft.....	200
8	Conclusions and Suggestions for Future work .....	205
8.1	Overall Conclusions.....	205
8.2	Contributions to Knowledge .....	207
8.3	Critical Assessment of the approach.....	207
8.4	Suggestions for Future Work .....	208
9	References.....	210

---

## GLOSSARY OF TERMS

<i>ADAMS</i>	:	Automatic Dynamic Analysis of Mechanical Systems
<i>BDC</i>	:	Bottom Dead Centre
<i>BDF</i>	:	Backward Differential Methods
<i>BEM</i>	:	Boundary Element Method
<i>CAE</i>	:	Computer Aided Engineering
<i>CMS</i>	:	Component Mode Synthesis
<i>CRDI</i>	:	Common Rail Direct Injection
<i>DOF</i>	:	Degrees Of Freedom
<i>EHD</i>	:	Elastohydrodynamic Lubrication
<i>FE</i>	:	Finite Element
<i>FEA</i>	:	Finite Element Analysis
<i>FEM</i>	:	Finite Element Method
<i>FFT</i>	:	Fast Fourier Transformation
<i>FRF</i>	:	Frequency Response Function
<i>GUI</i>	:	Graphical User Interface
<i>LDV</i>	:	Laser Doppler Vibrometer
<i>MBS</i>	:	Multi-body Dynamic System
<i>MNF</i>	:	Modal Neutral File
<i>MOFT</i>	:	Minimum Oil Film Thickness
<i>NVH</i>	:	Noise, Vibration and Harshness
<i>OFT</i>	:	Oil Film Thickness
<i>PVD</i>	:	Physical Vapour Deposition
<i>RBE</i>	:	Rigid Body Element
<i>RIM</i>	:	Reduced Impedance Method
<i>TDC</i>	:	Top Dead Centre
<i>TMM</i>	:	Transfer Matrix Method

---

## LIST OF FIGURES

Figure 1.1 Otto-Langen atmosphere engine after (Cummins 2000).....	1
Figure 1.2 Pressure(P) – Volume(V) diagram for ideal Otto cycle .....	2
Figure 1.3 Forces acting on the piston during the power stroke.....	5
Figure 1.4 whirl of journal bearings .....	7
Figure 1.5 Piston crankshaft assembly.....	9
Figure 1.6 Energy consumption in an internal combustion engine after (Anderson 1991).....	11
Figure 1.7: Model development flow diagram .....	13
Figure 2.1 Percentage noise emission from various noise sources in an engine, after (Spessert and Ponsa 1990) .....	17
Figure 2.2 Sensitivity of the engine component friction to various lubricants after (Taylor 2002).....	19
Figure 2.3 Journal instability motion .....	24
Figure 2.4 Shaft centre movement.....	24
Figure 2.5 Formation of cavitation under EHL conditions after (Aoyama <i>et al</i> , 2003) .....	25
Figure 2.6 Full Sommerfeld pressure variation in a journal.....	26
Figure 2.7 Pressure variation with Reynolds boundary conditions .....	27
Figure 2.8 Comparison of finite length and short bearing solutions after (Mourelatos 2001b) .....	28
Figure 2.9 Conventional and Articulated piston configuration .....	29
Figure 2.10 Gudgeon pin offset .....	31
Figure 2.11 Forces acting on piston ring .....	33
Figure 3.1 Euler Beam .....	47
Figure 3.2 A cantilever beam under Static(a) and Dynamic(b) loading.....	47
Figure 3.3 Multi Body system of Piston Crankshaft assembly.....	49
Figure 3.4 Two Degree Of Freedom system.....	50
Figure 3.5 Generalized forces acting on a rigid body.....	55
Figure 3.6 Deformable body coordinates.....	59
Figure 3.7 Super-element Crankshaft – Mode shape for the frequency of 2704Hz (created using MSC/Nastran) .....	65
Figure 3.8 FFT of Crank Angular Velocity for Rigid Engine Model.....	68
Figure 3.9 FFT of Crank Angular Velocity for Flexible Engine Model.....	69
Figure 3.10 Round-off and Truncation error (after (Rao 2002)) .....	70

---

---

Figure 3.11 Geometrical configuration of a single cylinder engine .....	72
Figure 4.1 Stribeck curve .....	79
Figure 4.2 Physical representation of Reynolds equation.....	80
Figure 4.3 Pressure distribution in a journal bearing.....	85
Figure 4.4 Variation of Sommerfeld number with minimum film thickness ( $L/D = 0.5$ ).....	88
Figure 4.5 Shaft whirling stability map .....	89
Figure 4.6 Ring Lubrication.....	90
Figure 4.7 Pressure distributions with Sommerfeld condition.....	94
Figure 4.8 Lubricated contact .....	97
Figure 4.9 Temperature variation along the contact.....	101
Figure 4.10 Heat flow within a lubricated contact.....	102
Figure 5.1 Rigid body Engine Model .....	109
Figure 5.2 Single cylinder engine crankshaft .....	112
Figure 5.3 Connecting rod and Piston.....	113
Figure 5.4 Enlarged view of the journal bearing in the crankshaft.....	115
Figure 5.5 Meshed crankshaft with boundary conditions.....	116
Figure 5.6 Flexible engine model in ADAMS.....	119
Figure 5.7 A cycle of combustion gas force .....	121
Figure 5.8 Combustion gas force variation for 74 engine cycles .....	122
Figure 5.9 Engine load torque and crank speed variation.....	123
Figure 5.10 Spline fitted engine load torque variation with angular velocity .....	123
Figure 5.11 Bearing and journal centre configuration.....	125
Figure 5.12 General force vector at main bearing .....	125
Figure 5.13 Main bearing friction torque.....	127
Figure 5.14 Possible piston modes inside the cylinder.....	128
Figure 5.15 Minimum film thickness variation at piston edge .....	128
Figure 5.16 Forces acting on the piston skirt.....	129
Figure 5.17 Pressure variation along the contact at piston edge.....	130
Figure 5.18 Piston kinematical and geometrical parameters for minimum film thickness calculation.....	131
Figure 5.19 Spline fitted temperature variation along the cylinder wall (Heywood 1988) ...	131
Figure 5.20 Piston friction force during one combustion cycle.....	132
Figure 5.21 Flow chart for friction force calculation.....	133

---

---

Figure 5.22 Forces acting on piston ring .....	136
Figure 5.23 Flow diagram for piston-ring friction calculation .....	138
Figure 5.24 Lubricant temperature variation at piston ring-cylinder wall interaction.....	139
Figure 5.25 Schematic diagram of multi-physics model .....	140
Figure 6.1 The E6 Engine Test Rig .....	145
Figure 6.2 E6 Engine front end.....	146
Figure 6.3 Schematic of hardware used in impact test .....	147
Figure 6.4 Time and frequency domain response of an impact excitation .....	149
Figure 6.5 Schematic diagram of an accelerometer.....	150
Figure 6.6 The laser torsional vibrometer optical geometry.....	152
Figure 6.7 Flywheel vibration measurements.....	153
Figure 6.8 Pressure sensor and calibration .....	154
Figure 6.9 FRF with the corresponding phase angle and coherence function.....	159
Figure 6.10 Enlarged FRF magnitude corresponding to 2nd peak of Figure 6.9 .....	160
Figure 6.11 Impact test apparatus set up for the crankshaft .....	161
Figure 6.12 Impact test positions on engine components .....	162
Figure 6.13 Bruel & Kjaer Conditioning Amplifier and DAC system .....	164
Figure 6.14 Front end of the PULSE software .....	165
Figure 6.15 CAD model and the actual model of the Connecting Rod .....	166
Figure 7.1 Fourier frequency spectrum for combustion gas force.....	168
Figure 7.2 Major modes of the crankshaft and the connecting rod .....	169
Figure 7.3 Forces acting on the connecting rod.....	170
Figure 7.4 Frequency spectrum for Flywheel rotational speed from multi physics numerical model .....	173
Figure 7.5 Frequency spectrum for experimentally measured flywheel rotational velocity .	173
Figure 7.6 Experimentally measured Flywheel nodding velocity .....	174
Figure 7.7 Numerically obtained Flywheel nodding velocity .....	174
Figure 7.8 Frequency spectrum for experimentally measured flywheel nodding motion .....	175
Figure 7.9 Frequency spectrum for numerically obtained flywheel nodding velocity.....	175
Figure 7.10 Bearing eccentricity and Sommerfeld number variation during a combustion cycle (for crankshaft front bearing).....	178
Figure 7.11 Bearing centre eccentricity ratio during a combustion cycle .....	178
Figure 7.12 Bearing load at 4 stroke combustion cycle.....	180

---

---

Figure 7.13 Bearing center velocity (in radial direction) during a 4 stroke cycle .....	181
Figure 7.14 Variation of friction coefficient at bearing during a 4 stroke cycle .....	181
Figure 7.15 Crankshaft bearing centre loci during a combustion cycle .....	183
Figure 7.16 Fourier frequency spectrum of the bearing force at front end of the crankshaft	184
Figure 7.17 Piston secondary motion.....	185
Figure 7.18 Piston thrust force variation at positions 1 and 2 .....	186
Figure 7.19 Film thickness and squeeze velocity variation at thrust side (at piston position 2) .....	187
Figure 7.20 Coefficient of friction for the piston skirt-to-cylinder wall contact .....	188
Figure 7.21 Fourier spectrum for angular acceleration of piston tilting motion.....	189
Figure 7.22 Reaction force variation at piston ring cylinder wall contact.....	190
Figure 7.23 Variation of film thickness and friction force at piston ring cylinder wall contact .....	191
Figure 7.24 Piston ring friction forces .....	192
Figure 7.25 Maximum lubricant pressure at piston ring to cylinder wall contact during a combustion cycle .....	193
Figure 7.26 Heat dissipation in the piston ring - cylinder wall contact .....	194
Figure 7.27 Variation of Peclet number in the piston ring-cylinder wall contact during a combustion cycle .....	195
Figure 7.28 Variation of viscosity in the piston ring-to-cylinder wall contact during the engine cycle .....	196
Figure 7.29 Percentage energy loss in the E6 engine model .....	197
Figure 7.30 Temperature rise at piston ring to cylinder wall contact for different ring thickness .....	198
Figure 7.31 Piston orientation and forces acting before and after TDC .....	201
Figure 7.32 Major thrust side force variation with crankshaft offset towards thrust side .....	202
Figure 7.33 Minor thrust side force variation with respect to the crankshaft offset towards the major thrust side .....	203
Figure 7.34 Variation of piston translation with respect to crankshaft offset.....	204

---

---

## LIST OF TABLE

Table 5.1 List of constraints for rigid engine model.....	108
Table 5.2 List of materials of engine components.....	110
Table 5.3 Material and nodel properties for engine components.....	116
Table 5.4 Frequencies calculated by FEA .....	117
Table 5.5 List of parts used in the model.....	120
Table 5.6 Engine main bearing details.....	124
Table 5.7 Holonomic and non-holonomic constraints.....	126
Table 5.8 List of parameters used for thrust force calculation .....	133
Table 5.9 List of parameters used for friction force calculation.....	135
Table 5.10 Parameters used for ring friction calculation.....	137
Table 6.1 E6 Ricardo engine manufacture specifications.....	145
Table 6.2 Hammer test frequency results for crankshaft .....	163
Table 6.3 Comparison between the hammer test results and FEM results .....	164

---

## NOMENCLATURE

$A_a$	-	Asperity contact area.....	[m <sup>2</sup> ]
$A_h$	-	Hertzian contact area.....	[m <sup>2</sup> ]
$B$	-	Width of the contact.....	[m]
$c$	-	Clearance.....	[m]
$C_k$	-	Constraint function.....	[-]
$C_p$	-	Specific heat at constant pressure .....	[m <sup>2</sup> / s <sup>2</sup> °C]
$c_{pb}$	-	Pressure coefficient of boundary shear strength.....	[m <sup>2</sup> ]
$C_q$	-	Constraint Jacobian matrix .....	[-]
$D$	-	Diameter of the journal bearing .....	[m]
$d_b$	-	Distance between laser beams .....	[m]
$e$	-	Eccentricity .....	[m]
$E_{1,2}$	-	Modulus of elasticity of material 1 (or 2).....	[Pa]
$f_b$	-	Bearing natural frequency.....	[Hz]
$F_b$	-	Boundary Friction force.....	[N]
$f_D$	-	Laser Doppler frequency shift .....	[Hz]
$F_{lr}$	-	Lubricant reaction on ring.....	[N]
$F_{rg}$	-	Gas pressure force on ring .....	[N]
$F_{rt}$	-	Radially outward ring tension.....	[N]
$F_v$	-	Viscous Friction Fore.....	[N]
$g$	-	Gravitational constant .....	[-]
$h$	-	Film Thickness.....	[-]
$h_a$	-	Film thickness at maximum pressure.....	[m]
$h_m$	-	Minimum film thickness .....	[m]
$k$	-	Stiffness.....	[Nm <sup>-1</sup> ]
$K$	-	Stiffness matrix .....	[-]
$k_c$	-	Thermal conductivity.....	[N/s °C]

---

---

$L$	-	Length of the bearing.....	[m]
$l$	-	Contact length.....	[m]
$M$	-	Mass Matrix.....	[-]
$N$	-	Journal rotational speed.....	[rev s <sup>-1</sup> ]
$N_d$	-	Rotational speed of the dics.....	[rev/s]
$n_e$	-	Number of elements in a body.....	[-]
$n_m$	-	Number of mode shapes.....	[-]
$p$	-	Local pressure at contact point.....	[Pa]
$p^*$	-	Non dimensional pressure.....	[-]
$P_a$	-	Pressure at asperities.....	[Pa]
$Q$	-	Generalized force.....	[N]
$q$	-	Generalized displacement.....	[m]
$q'_\alpha$	-	Volume flow rate in circumferential direction per unit length ....	[m <sup>2</sup> s <sup>-1</sup> ]
$q_c$	-	Constraint modes.....	[-]
$q_n$	-	Fixed boundary normal modes.....	[-]
$q'_y$	-	Volume flow rate in axial direction per unit length.....	[m <sup>2</sup> s <sup>-1</sup> ]
$r$	-	Frequency ratio.....	[-]
$r_b$	-	Radius of the bearing.....	[m]
$r_j$	-	Radius of the j <sup>th</sup> journal.....	[m]
$T$	-	Total kinetic energy.....	[J]
$u$	-	displacement.....	[m]
$u_d$	-	Dependent/boundary nodal deformation vector.....	[-]
$u_i$	-	Independent/interior nodal deformation vector.....	[-]
$u_j$	-	Tangential velocity at journal surface.....	[ms <sup>-2</sup> ]
$u_o$	-	Target velocity.....	[ms <sup>-1</sup> ]
$u_s$	-	Sliding velocity.....	[ms <sup>-1</sup> ]
$V$	-	Potential energy.....	[J]
$v_x$	-	Surface velocity in x-direction.....	[ms <sup>-1</sup> ]

---

---

$v_y$	-	Surface velocity in y-direction.....	$[\text{ms}^{-1}]$
$w$	-	Velocity in z-direction .....	$[\text{ms}^{-1}]$
$W$	-	Total load .....	$[\text{N}]$
$w_s$	-	Squeeze velocity .....	$[\text{ms}^{-1}]$
$w_s^*$	-	Non dimensional squeeze velocity.....	$[-]$
$W_x$	-	Load along the line of centres in bearing.....	$[\text{N}]$
$W_y$	-	Load perpendicular to the line of centres in bearing.....	$[\text{N}]$
$y$	-	Distance along the length of the bearing.....	$[\text{m}]$
$\alpha$	-	Included angle .....	$[\text{rad}]$
$\gamma$	-	Surface density of asperity peaks.....	$[-]$
$\gamma_s$	-	Slope of the oil limiting shear stress-pressure relation .....	$[-]$
$\varepsilon$	-	Eccentricity ratio .....	$[-]$
$\eta$	-	Dynamic viscosity.....	$[\text{Pa}\cdot\text{s}]$
$\eta_0$	-	Atmospheric dynamic viscosity.....	$[\text{Pa}\cdot\text{s}]$
$\theta$	-	Temperature .....	$[\text{°C}]$
$\lambda$	-	Lagrange multiplier.....	$[-]$
$\lambda_b$	-	Laser beam wavelength.....	$[\text{m}]$
$\Lambda$	-	Dimensionless film parameter .....	$[-]$
$\nu_{1,2}$	-	Poissons' ratio of material 1 (or 2) .....	$[-]$
$\nu_e$	-	Coefficient of thermal expansion.....	$[\text{°C}^{-1}]$
$\xi$	-	Damping ratio .....	$[-]$
$\rho$	-	Lubricant density .....	$[\text{kg}/\text{m}^3]$
$\sigma_{1,2}$	-	Average roughness of surface 1 (or 2).....	$[\text{m}]$
$\tau_e$	-	Eyring shear strength .....	$[\text{Pa}]$
$\Phi$	-	Modal matrix.....	$[-]$
$\phi$	-	Mode shape .....	$[-]$
$\omega$	-	Angular velocity.....	$[\text{rad s}^{-1}]$
$\omega_c$	-	Cutoff frequency .....	$[\text{Hz}]$

---

- 
- $\omega_b$  - Angular velocity of accelerometer base..... [rad s<sup>-1</sup>]
  - $\omega_j$  - Journal angular velocity..... [rad s<sup>-1</sup>]
  - $\omega_n$  - Natural frequency of the accelerometer..... [rad s<sup>-1</sup>]

# 1 INTRODUCTION

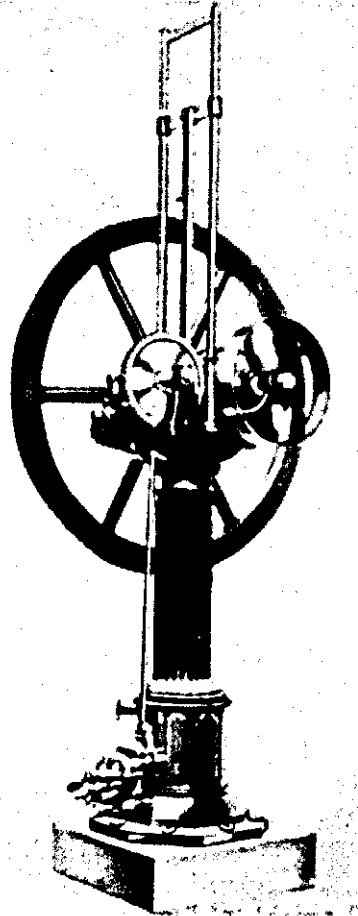


**Figure 1.1 Otto-Langen  
atmosphere engine after  
(Cummins 2000)**

## 1.1 Basic Engine Types

The internal combustion engine is a type of heat engine, which converts energy stored in fuel into kinetic energy, made available at a rotating output shaft. The chemical energy in the fuel is first converted into thermal energy by means of combustion or oxidation with air, raising the temperature and pressure of the gas inside the cylinder. The expanding volume forces the piston to travel downwards, rotating the crankshaft via a connecting rod, thus converting the translational motion into a rotary one. Even though most of the internal combustion engines

---

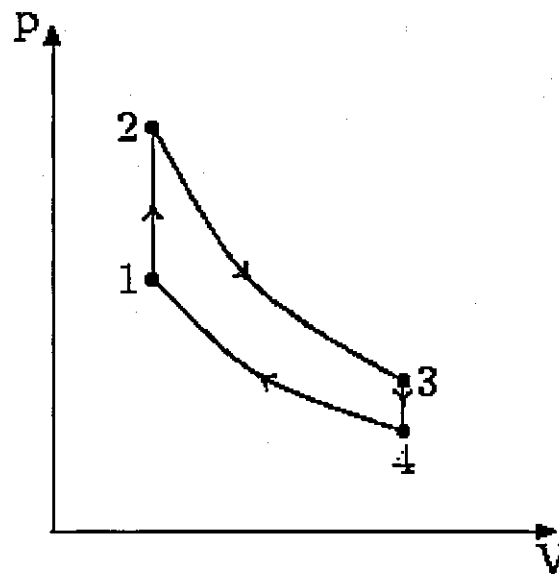


**Figure 1.2 Pressure(P) – Volume(V) diagram for ideal Otto cycle**

are reciprocating mechanisms, whereby pistons reciprocate in the cylinders, there are other types that operate differently, such as the rotary engine (sometimes called the Wankel rotary engine after the name of its original developer Dr. Felix Wankel)..

The other most important type of engine is the external combustion engine, such as the steam engines, the Stirling engine, gas turbines, and so on. The salient difference to that of the aforementioned internal combustion engines is that combustion takes place externally in a more controlled manner. As the combustion is more controlled, the efficiencies of up to 60% are theoretically possible, which is much higher than the conventional IC engines. In general, the IC engines operate in the Diesel cycle or the Otto cycle, which have theoretical efficiencies of 45% and 30% respectively. Figure 1.2 shows the pressure-volume variation of the Otto cycle. Note that the heat (energy) input takes place during the process 1-2 and work out is the area covered by the diagram.

Reciprocating engines can have only one or multi-cylinders (can be up to 20 or more, such as in catamarans). The cylinders can be arranged in many different geometric configurations. Sizes range from small airplane engines with power output of the order of 100 watts to large multi-cylinder stationary engines that produce thousands of kilowatts, which in general are used for power generation. Furthermore, there are slow speed engines with large pistons, which generate enormous amount of power, generally used in marine applications.

## **1.2 Historical Evolution of Engines**

The year 2001 marks the 125<sup>th</sup> anniversary of the modern internal combustion engine (Cummins 2000). Virtually all of the basic elements in the present reciprocating four-stroke cycle engine were present in Nicolaus Otto's creation more than a century ago. Since then minor improvements have been made to the original concept to improve efficiency and power output.

During the second half of the 19<sup>th</sup> century many different styles of internal combustion engines were built and tested. The first fairly practical engine was invented by J.J.E. Lenoir (1822-1900) and appeared on the scene about 1860, even though it was a non-compression engine with mechanical efficiency of 5%. In 1867 the Otto-Langen engine with improved efficiency of 11% was introduced. It was an important stepping-stone for the introduction of the 4-stroke cycle engine, later developed by Otto in 1876. During this time engines operating on the same basic four-stroke cycle as the modern automobile engine began to evolve as the best design (Gas Engine Magazine, Feb 1991). Although many people were working on the four-stroke cycle design, Otto was given the credit for his prototype engine in 1876.

In the 1880s the internal combustion engine first appeared in automobiles (Givens 1990). In this decade the two-stroke cycle engine became practical and was manufactured in large numbers. By 1892, Rudolf Diesel (1858-1913) had perfected his compression ignition engine into basically the same diesel engine known today. This was after years of development work, which included the use of solid fuels in his early experimental engines. Early compression ignition engines were noisy, large, slow, single-cylinder engines. They were, however, more efficient than the spark ignition engines, even though some drawbacks like high noise, harshness and dark fume existed. Modern engines use technologies like Common Rail Direct Injection (CRDI), which controls the amount of fuel into the combustion chamber precisely with accurate timing in order to maximise combustion efficiency. Whereby in the past, diesel engines were unrefined, sluggish and environmentally unfriendly, this is no longer true in modern diesel engines due to the above-mentioned advancements in combustion strategy, material and manufacturing technology. They are now powerful, smooth and very refined, so much so that they have been introduced as alternative engines in the line-up of flagship models.

---

### 1.3 Noise, Vibration and Harshness

The improved performance and compactness of modern internal combustion engines makes them a suitable power plant for automobiles. Even though, in the early stages, they were mainly used for applications like lifting elevators, water pumping and so on. Nowadays the automobile industry accounts for the main application area. There are some basic customer concerns in a modern vehicle. Outer appearance, vehicle handling, reliability and fuel efficiency are the most important among them. However, noise, vibration and harshness play an increasingly major role in the context of customer expectations.

The suspension system in most modern vehicles is sufficiently refined to counteract the effect of vibration transmitted due to the unevenness of the road surface. Imbalances of rotating parts, clearance between gear teeth, road noise from tyres and cyclic combustion force in the combustion chamber can be regarded as critical Noise, Vibration and Harshness (NVH) sources. In (Morita *et al*, 2001) combustion force is attributed to be the prominent source of noise. However, the non-uniform character of the torque generated in reciprocating engines arises due to the application of periodic combustion forces and the associated inertial forces of rotating and articulated members. Fuel injector pumps, timing gear rattle, bearing reactions, camshafts, crankshafts, etc also contribute in different ways to engine noise (Haddad and Tjan 1995).

Although most excitations from the ground are counteracted reasonably effectively through the suspension, the power plant itself is the source of noise and vibration so the dynamic analysis of the engine mechanism is required (Suh *et al*, 2000). Understanding the origins and parametric dependencies of noise and vibration is the first step in a reduction (i.e. refinement) strategy. Such concerns extend to piston-driven internal combustion engines, which may often be the major source of vehicle noise and vibration (Hoffman and Dowling 1999). The engine noise is dominant in the middle to high frequency range (0.5 to 2.5KHz). The impact of IC engine vibration on vehicle performance or customer perceived quality is typically less serious at higher frequencies, because reliable isolation strategies exist for eliminating vibration transmission from the engine to the vehicle structure.

In recent years the specific output of the engine has been increased, while the rigidity of the structure has been reduced in high-speed automobile diesel engines.

---

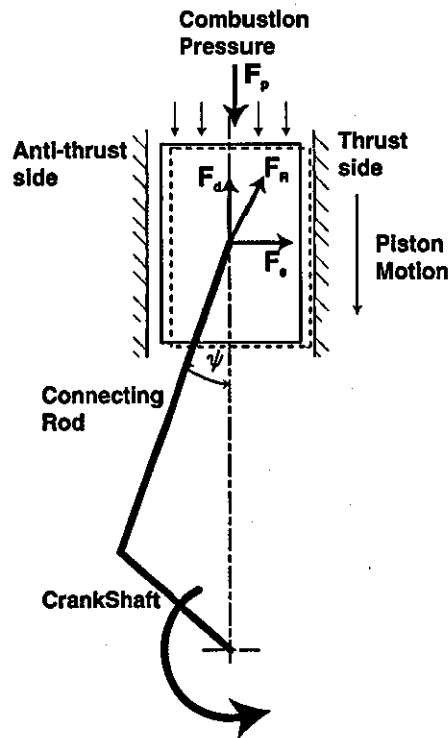


Figure 1.3 Forces acting on the piston during the power stroke

## 1.4 Sources of vibration in an Engine

In an internal combustion engine the combustion force generated in the combustion chamber induces a translational downward vertical force ( $F_p$ ) on the piston as shown in the Figure 1.3. As it is necessary to induce a rotational motion from an engine, the piston-connecting rod-crankshaft system converts this translation (or reciprocating) motion into a rotational action. This transformation produces harmonic responses as multiples of crankshaft rotational frequency, referred to as engine orders (Rahnejat 1998). In analytical calculations, higher order terms in the binomial expansion are usually neglected as is shown later, so that the frequencies related to these higher order terms cannot be observed in most theoretical studies.

Combustion process that takes place in the combustion chamber plays a major role in power generation procedure in an engine. For example, SI (Spark Ignition) system, the fuel gas mixture entered through the inlet manifold into the cylinder during intake is being pressurised during the compression cycle. The spark initiated by electrode (spark plug), at this instance, commences the combustion and the flame propagates throughout the chamber. This propagation is not spontaneous as it is intended. Thus, methods are introduced to swirl the

---

mixture and make it turbulent to enhance flame propagation. However, this non-uniform behaviour of the combustion gives rise to pressure force fluctuations, which manifests as harmonics in the combustion pressure force ( $F_p$  in Figure 1.3). The reaction force,  $F_d$ , acting on the piston from the connecting rod balances the gas pressure force  $F_p$ . As the connecting rod is at an angle  $\psi$  to the vertical, and is hinged to the piston, there is a horizontal component  $F_s$ , due to the resultant force  $F_R$ , at the connecting rod. This horizontal component forces the piston towards the right side of the cylinder wall, shown in the Figure 1.3. This side of the cylinder, where the impact often occurs is known as the *Thrust Side*. During the compression stroke, connecting rod is arranged such that the thrust force  $F_d$  reverses its direction. This action pushes the piston against the other side of the cylinder, which is known as the *anti-thrust Side*. This side force reversals during the engine cycle moves the piston horizontally and this is known as *Piston Slap motion* or *Piston Secondary motion*. At the TDC (Top Dead Centre) and BDC (Bottom Dead Centre) these force reversals are most significant.

It is known that the combustion (power stroke) pressure is much higher than the compression pressure inside the chamber. Thus, the thrust force created during the combustion cycle is much higher than the thrust force during the compression cycle. During the combustion cycle the side force component on the left side of the cylinder is very small. It is very close to zero, unless otherwise there exists a force component due to lubricant pressure. This side is also known as the *anti-thrust side* (see Figure 1.3). Throughout the piston transverse motion there is a thrust force on the piston and it changes its value depending on the film thickness and piston velocity. This force variation causes directional changes to the piston lateral velocity which causes multiple reversals in the piston tilt motion. This lateral motion, also known as the secondary motion, can generate considerable amount of noise in an engine during its operation. The frequency of these multiple reversals in the tilting motion affects the frequency of the noise generated due to slap motion.

In the context of engine vibration, the role of journal bearing cannot be under-stated. For example, it is reported that the noise with higher frequencies than 5 kHz intermittently occurs from the main bearing of a diesel engine (Aoyama *et al*, 2003). In order to cater for the higher loads in the combustion chamber the crankshaft is connected to the engine block via journal bearings, which produce higher resisting torques due to the viscous action of the lubricant.

---

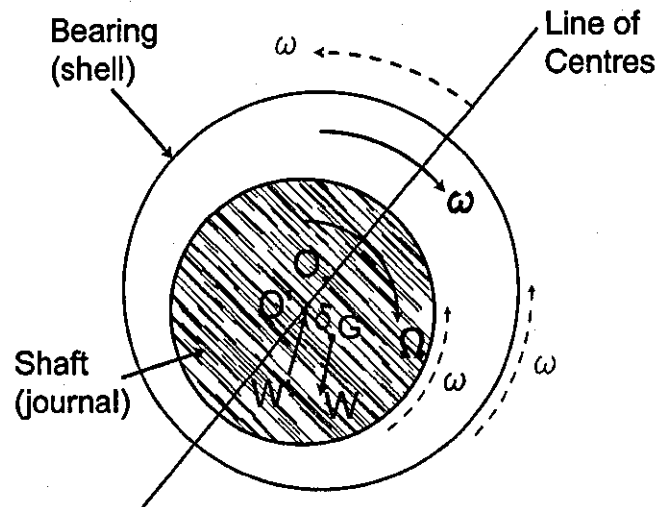


**Figure 1.4 whirl of journal bearings**

Non-concentric motion of the crankpin (journal) around the bearing shell generates pressure distribution in the lubricant, which is non-uniform (Aoyama *et al*, 2003).

When the shaft of the journal bearing, shown in Figure 1.4, is rotating at an angular speed of  $\Omega$ , the centre of gravity  $G$  which is an offset of  $\delta$  from the geometric centre of the shaft  $O'$  rotates around the shell centre  $O$ , which is equal to  $\omega$ . This creates a centrifugal force  $W$  at its centre of gravity  $G$ , which is balanced by the lubricant reaction force  $W'$ . Also, the geometric centre of the shaft  $O'$  rotates about the bearing shell centre  $O$  with an angular velocity of  $\omega$  (Note that the line passing through points  $O$  and  $O'$  is called the line of centres). This eccentric motion is called the whirling motion. Under this condition the shaft rotational speed with respect to bearing (shell) can be found by freezing the line of centres by introducing an angular velocity of  $\omega$  in the opposite direction to the whole system as shown in the figure. Thus, the relative angular velocity of the shaft becomes  $\Omega - 2\omega$ . When the whirling frequency ( $\omega$ ) is half of the shaft rotational frequency ( $\Omega$ ), there is no relative angular velocity between the shaft and bearing, therefore leading to no entrainment of the lubricant into the contact. This phenomenon is referred to as whirling or whipping motion of the journal, and is an unstable rotational event. Under these conditions, the lubricant film can travel backward (i.e. entrain in the opposite direction to the rotational direction of the journal).

The situation is rather unfortunate in 4-stroke IC engines, where half speed of crankshaft (or journal) happens to coincide with the fundamental frequency of the 4-stroke combustion process, which is also at half the rotational speed of the journal, and, can lead to resonance

conditions. This is a non-linear event, known as the jump phenomenon, where at a given speed of rotation the journal motion can jump from a seemingly stable orbit to another orbit with different amplitude instantaneously. To investigate such conditions and guard against their occurrence, it is necessary to carry out an analysis that includes inertial dynamics, flexural motion of elastic components and reaction forces from the lubricant pressure.

In compression ignition engines, the noise induced from the injector pump is an equally important source, as described earlier. For each combustion cycle, the fuel is pumped at the appropriate instant of time to the combustion chamber via the injector pump. It creates a pressure wave, which travels from the pump to the combustion chamber through a steel tube. This excitation is half the engine order in a four-stroke internal combustion engine (Spessert and Ponsa 1990) also it is more of a problem now as the injector pressures are significantly higher (around 400-450 bar)

Basically the engine imbalance occurs due to translational masses and rotating eccentric masses. There exists primary and secondary out of balance excitation from these translational masses as it is explained in section 3.5.1. These primary excitations can be balanced by adding masses where as secondary excitations can be minimised by proper phasing of adjacent crank-throws. Thus, the inertial imbalance due to the reciprocating mass of the piston and articulated connecting rod is minimised in multi-cylinder engines. Axial, torsional and lateral vibrations, which induce stresses occur simultaneously in the crankshaft of a multi-cylinder engine (Wakabayashi *et al*, 1995). The crankshaft of the multi-cylinder engine has a phase difference between the adjacent crank-throw planes, so, the four kinds of vibrations are all coupled in the crankshaft rotation.

All these noise sources, which were discussed in this section and not described fully, such as timing gear rattle, valve train excitation etc., can induce air born noise in an automobile. All cyclic excitations generated by aforementioned causes deform the body, which is adjacent to it. This will cause vibrations of structural elements. In this case, the structure deforms according to a specific mode shape or a combination of mode shapes, depending on the excitation frequency. Then, the physical boundary of the body (structure) excites the adjacent environment, which is air and creates structure-borne noise. This is the main form of energy transfer from the source of excitation to the environment. Therefore, reduction in system level vibration translates to reduction of noise emitted from the system, thereby reducing the loss

---

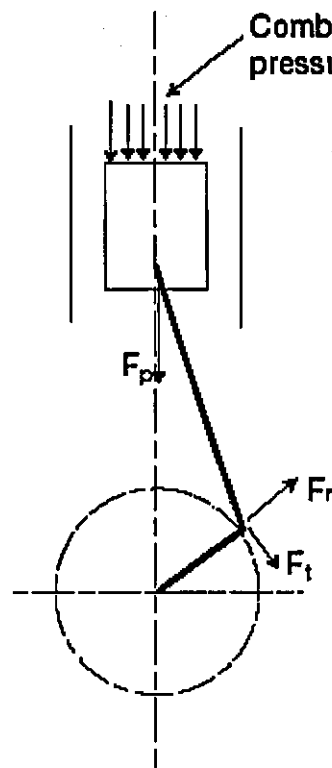


Figure 1.5 Piston crankshaft assembly

of energy. This means reduction in vibration can be regarded as an attempt to increase the efficiency of a system.

## 1.5 Crankshaft Vibrations

As discussed in earlier sections, there are various sources of vibration in an engine, some of which are well understood. However, it is difficult to usually take all these factors into account in a single model. Therefore, in this study, the piston-connecting rod-crankshaft subsystem is investigated.

At any instant of time, the radial component ( $F_r$  in Figure 1.5) of the piston force is transmitted along the connecting rod and is applied to the crankpin. This force tends to pull the crankpin away and induces instantaneous bearing support load. The tangential component ( $F_t$ ) of the gas force, on the other hand, is utilised in the rotation of the crankshaft. With every power stroke, the transmitted piston gas force is initially increased in magnitude and subsequently reduced at the end of the stroke. Both the combustion force and the orientation of the connecting rod change according to the crank angle. Therefore, the force, which creates

torque vary with the crank angle. This action imparts a “twist-untwist” action of the crankshaft (known as crankshaft wind-up or wind-down), causing torsional vibrations to occur.

The tangential force component of the piston acting on the crankshaft also induces a bending moment on the crankshaft other than the torsional moment, known as the coupled torsional-bending moment. As the force, which causes this bending moment, is indeed fluctuates due to aforementioned reasons, this will create bending vibrations, which could excite the bending modes of the crankshaft.

In a four-stroke single cylinder internal combustion engine, the fundamental frequency of the applied torque coincides with half speed of the crankshaft, and its harmonics, are, whole or half orders of the instantaneous engine speed. Therefore, there is almost an infinite number of critical speeds, and in principle, high vibratory torques may be induced at each one of these frequencies. The generated vibration amplitudes can be high enough in extreme cases to cause crankshaft or other engine component failure. However, only a few critical speeds induce seriously high vibratory torque amplitudes (Boysal and Rahnejat 1997).

Despite this, the excitations induced by the bearing cannot be neglected as discussed earlier. Due to the off-centre motion of the crankshaft on the bearing bushing, high vibration excitations can occur. This can be exaggerated by the excitations produced by piston lateral motion. Even though there is a relationship between engine speed and the excitation frequency of the combustion force, it is difficult to figure out a relationship between the crankshaft rotational speed and the slap excitation frequency (Cho *et al*, 2002).

## 1.6 Engine performance

Thermal and frictional losses are the most important aspects that would affect the engine performance. As identified by (Anderson 1991), thermal losses account for 60-65% of all losses in an engine. From the remaining 35-40%, about 15% of the energy is dissipated as mechanical and frictional losses by the articulating inertial members and conjunctions within the internal combustion engine such as piston assembly, small-end and big-end bearing, valve-train, cam-tappet, etc. (see Figure 1.6). Thus, only 13% of engine power is available to perform the useful task of propelling the vehicle.

---

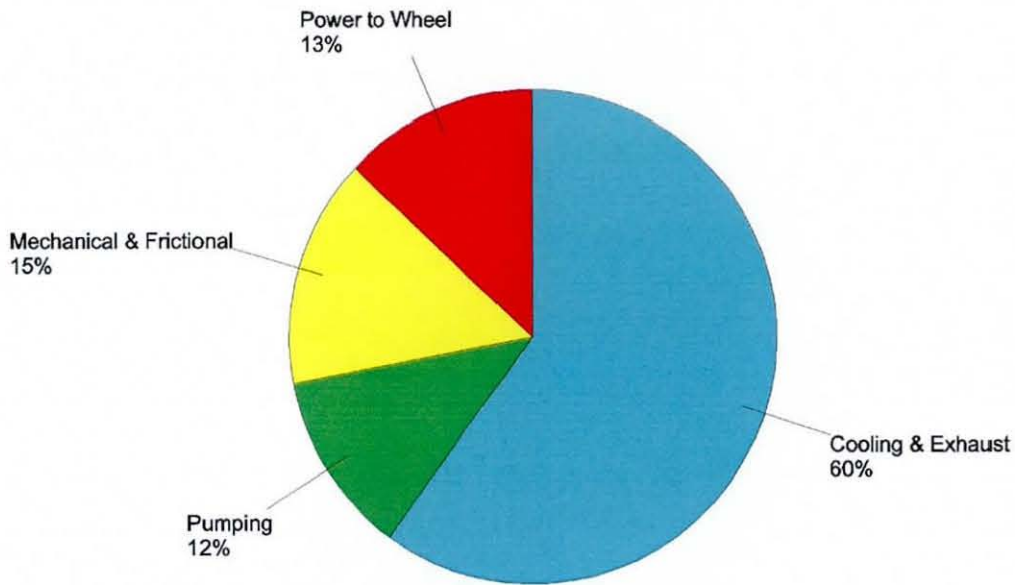


**Figure 1.6 Energy consumption in an internal combustion engine after (Anderson 1991)**

Most of the mechanical losses occur at contact conjunctions as frictional losses. The amount of energy dissipated at some of the contact conjunctions are quantified in Figure 2.2. From this figure it can be seen that most of the losses occur in the piston assembly. Bearings and valve-train assemblies contribute more or less by the same amount as each other. As can be seen from the figure various factors can influence the amount of energy lost in these sub-systems. Even though it is not possible to completely eliminate the frictional losses, they can be minimised, using various techniques. These include lubricant rheology, material properties, surface topology, geometry and operational conditions such as contact geometry or crankshaft configuration and assembly issues. However, as these changes affect sub-systems quite differently from each other, an overall improvement of frictional losses cannot be achieved just considering one sub-system in isolation. Therefore a use of system approach is requested to accommodate many sub-systems within the same.

## 1.7 Aims and Objectives.

As stated earlier, the modern trend in the automotive industry is to reduce frictional and mechanical losses, as well as noise level through reducing vibration levels. Considerable amount of effort has been expended in order to reduce vibration induced by inertial dynamics (by reducing mass as well as any imbalance in the system) in the rotating and reciprocating components of the engine. Widespread use of light-weight components intended to reduce

inertial imbalances (thus mechanical losses and inefficiency), unfortunately has to a large extent led to increased structural vibration. Therefore, an optimum balance between inertial dynamics and structural vibration has to be struck. The main design question becomes one of flexibility and weight versus noise and vibration.

It has been found that finite element solutions show differences between test results with dynamically loaded structures that undergo large rigid body motions. Solution through the use of non-linear Finite Element Analysis (FEA) has improved the accuracy of results, yet fails to provide a complete description of complex mechanical systems, including hydrodynamics and large rigid body motions (Du 1999).

A rigid body model is not sufficient to provide a realistic assessment of the system, as the reduced flexibility, gives unexpected amplitudes in some operating conditions. Therefore, a model should, have component flexibility. As a response to the highlighted short-comings, commercial multi-body dynamics software (ADAMS - Automatic Dynamic Analysis of Mechanical Systems) is used in this report to model the inertial properties of the system and the component flexibility is incorporated into the model, using an FEA software.

The hydrodynamic forces acting on the bearings, piston slap (secondary motion) motion, including the skirt lubrication and elastic properties, ring lubrication including thermal analysis and the combustion force acting on the piston top surface are also to be included in the model, as given analytical functions or splines fitted to measured data. Most of these forcing functions have been validated using an E6 test engine. Particularly, the variations in the combustion gas force and crankshaft angular velocity been measured with an acceptable degree of accuracy.

The main aim of this report is to present a detailed engine modelling method, referred to as a multi-physics approach, in which, combined rigid body inertial dynamics, structural modal characteristics of elastic components and tribological behaviour of load bearing surfaces have been included into a single model. When such a model is made, the validity of model predictions must be ascertained against experimental findings to enhance confidence in the use of this methodology. Figure 1.7 shows the basic flow chart for the entire process of model development and validation.

In order to achieve the above objectives the following steps are undertaken in this thesis:

---

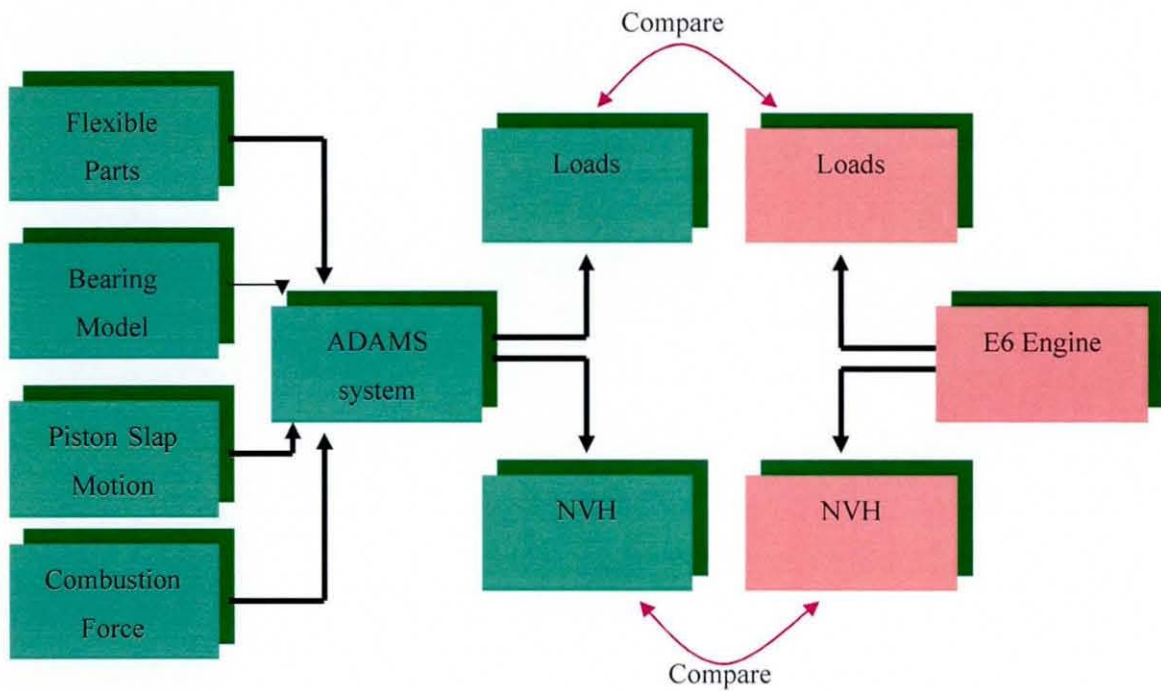


**Figure 1.7: Model development flow diagram**

- A flexible multi-body dynamics single cylinder engine model similar to the E6 experimental engine will be developed in a commercially available multi-body dynamics software. The model should be parameterized such that various configurations, if needed, can be investigated.
- The reaction forces generated by tribological conjunctions such as main bearings, piston skirt-cylinder wall and piston ring-cylinder wall will be developed, based on Reynolds lubrication in a separate subroutine that can be accessed by the main dynamics code for each of its time step.
- The model should be verified, using experimentally measured results obtained from the E6 engine.
- Validated model should be used as an analysis tool such that the effect of various configuration changes such as crankshaft offset and the piston ring thickness on engine performance can be investigated.

## **1.8 Structure of the Thesis**

Throughout this chapter the general trend and concerns of automotive industry in relation to vibrations of IC engines, and frictional and mechanical losses were discussed. Its current developments and interests were also highlighted, thereby providing necessary motivation for undertaking this research. The thesis is divided into eight chapters including the current chapter.

Chapter 2 reviews the research work carried out in this field starting from the basic historical developments and theoretical findings, to the latest experimental and research work relevant to engine vibrations. Particular attention has been paid to the use of multi-body dynamics and tribological aspects of engine components.

In Chapter 3 a comprehensive multi-body dynamic analysis is presented for single cylinder engines, including kinematic and dynamics of rigid and deformable bodies. Analytical techniques for deriving the system differential and algebraic equations of motion of a multi – body system are discussed with relation to Lagrangian dynamics. Sub-structure coupling technique is used to couple rigid body motions with elastic deformation.

In Chapter 4 hydrodynamic lubrication analysis related to certain contact conjunctions in single cylinder engine is presented. Analytical equations for lubricated conjunctions are obtained, using classical analytical approaches. Temperature variations are also obtained for these contact conjunctions, which affect the rheological characteristics of the lubricant, using the energy equation. Considering these reaction forces from the lubricated contacts, the single cylinder engine model is developed in a commercially available dynamics code, ADAMS. The construction of this numerical model with the integrated tribological subroutines is described in Chapter 5. The basic methodology used to obtain the component mode shapes, using commercially available FE package, Nastran, is also presented in the same chapter.

Chapter 6 is basically devoted to description of experimental measurements, as well as techniques used to validate the developed numerical model. The use of measuring transducers such as accelerometers, vibrometers and impact hammers are detailed and their measurements are quantified within the chapter. Comparisons are made between the measured and numerical data, presented in Chapter 7. Critical assessment of numerical results with respect to the developed multi-physics environment and its inter-disciplinary

---

characteristics is made. Also the benefits of such a holistic multi-disciplinary approach in engine design process and its usefulness in refining engine performance criteria are discussed. Finally, chapter 8 highlights the main conclusions of the research and proposes suggestions for future work to be carried out to extend the research and development findings contained in this thesis.

## 2 LITERATURE REVIEW

### 2.1 Introduction

With improved ride and handling performance of a vehicle, power train noise and vibration characteristics have become progressively more important. In the modern society, the lifestyle of many people involves the use of motor vehicles, and a significant proportion of drivers' time is spent under idling conditions or in slow moving traffics in congestion. As a result, all road users are subjected to noise sources, particularly contributed by the power train system. In contrast, noises induced from road-tyre interactions and by aerodynamics are dominant at high speeds. However, recent surveys show that drivers are more annoyed by structure-borne noise and vibration than airborne noise, the former being at a lower frequency and almost entirely induced by the power train system as reported in (Gupta 2002).

Internal combustion engine can be broadly categorised into several sub-systems concerning noise and vibration such as fuel pump system, timing belt gears, cam-tappet (valve train) system and crankshaft piston assembly. Excitations from fuel pump system are dominant particularly in CI (Compression Ignition) engines as it incorporates high injection pressures. Although the combustion pressure excitation is more dominant in naturally aspirated engines, it is greatly reduced in turbo-charged engines as reported in (Spessert and Ponsa 1990). However, noise contribution from piston assembly is retained, demonstrating its significance as an engine noise concern. Percentage noise contributions from various sources in an engine are shown in Figure 2.1.

Piston crankshaft assembly is inherently unbalanced, because the translational inertial imbalance of the reciprocating elements, such as the piston and connecting rod cannot be represented by a rotating element with a constant rotating inertia as shown in (Rahnejat 1998), using a lumped mass model. Due to this translational imbalance there exists a vibration spectrum that contains all the multiples of engine order vibration. However, it is possible to reduce or eliminate the horizontal lateral inertial force by employing counterbalanced masses along the crankshaft, whereas its vertical component can only be attenuated by proper angular positioning of the crank or introducing a proper firing order between the cylinders. However, all multiple frequency orders always exist in single cylinder

---

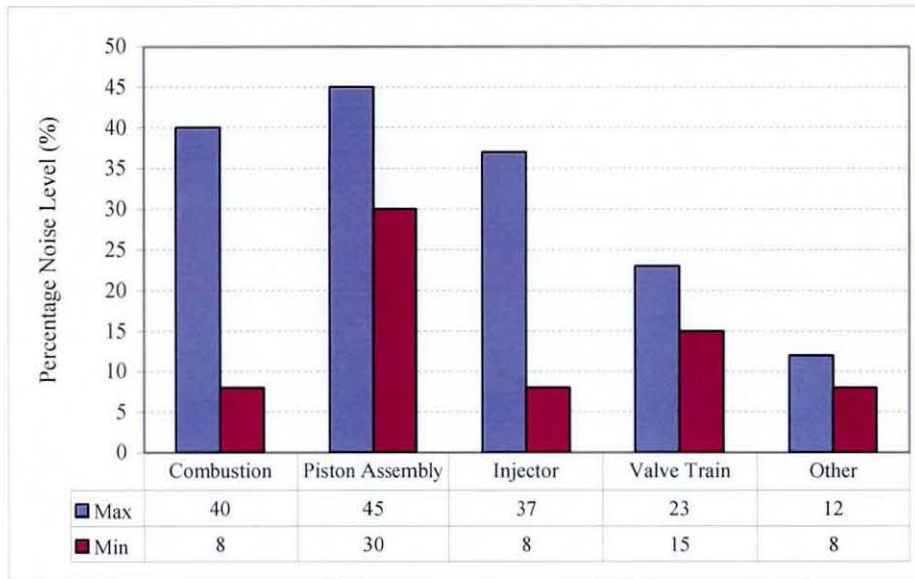


**Figure 2.1 Percentage noise emission from various noise sources in an engine, after (Spessert and Ponsa 1990)**

engines. These vertical inertial imbalances lead to torsional vibration of the crankshaft, usually in second and higher engine orders for the most commonly used 4-cylinder 4-stroke engines. This is also known as secondary inertia and can lead to coupled bending and torsional vibrations (Hesterman and Stone 1992; Hesterman and Stone 1995).

The combustion process acts as an initiation source for the spectrum of noise and vibration of an internal combustion engine. For a single cylinder 4-stroke engine, the power torque produces engine order responses, which accentuate the effect of induced inertial torque, having the same spectral content and the half engine order response as its fundamental and all its higher harmonics. This spectrum of vibration (containing half-engine orders) is known as engine roughness, which is also discussed later.

With the modern trend in high performance, low weight engines the component flexural rigidity is reduced, leading to coupled bending, torsional and translational vibrations. The experimental study carried out by (Wakabayashi *et al*, 1995) shows that bending stresses in the crankshaft are coupled with torsional vibrations and just a single degree of freedom model is not sufficient to predict system vibration behaviour. Cyclic variation of the crankshaft rotational speed reflects the non-uniform nature of the torque produced. In his statistical approach, Taraza (Taraza 2001) obtained a correlation between amplitudes and phases of the same harmonic components of the power torque and the crankshaft speed. Several approaches

that have been employed such as introducing a balancing shaft that balances the secondary inertial imbalances (Suh *et al*, 2000), using a damper pulley that reduces high frequency rotational vibrations (Morita *et al*, 2001), etc reflecting the growing need to overcome these problems.

There have been many studies of engine dynamics in literature, implementing numerical models for engines, based on Lagrangian dynamics, and integrating necessary practical features as mentioned earlier. (Boysal and Rahnejat 1997) presented a multi body dynamic model for a single cylinder engine to predict torsional vibrations by incorporating simultaneous solution of large displacement dynamics of engine components such as piston, crankshaft, connecting rod and flywheel with infinitesimal vibrations of support bearings and the trapped air fuel cylinder transient pressures. However, other main contributory factors for the dynamic behaviour such as flexibility of the components, tribological behaviour between the piston and skirt, piston ring interaction, gudgeon pin behaviour were not considered with adequate detail. In (Ma and Perkins 2003) another approach can be seen, including the engine block, engine mounts and flexibility of the crankshaft. A similar approach can be seen in (Mourelatos 2001a) with several drawbacks, such as rigid connecting rods, lack of piston lubrication information, etc. Even the methodologies used in industry for development of engines are sometimes in very abstracted form. The model developed in (Mizuho Inagaki 2002) uses a lumped mass model for the connecting rod, which is not a very good approximation as indicated in (Shiao and Moskwa 1993).

All the above mentioned factors point to a need for an integrated numerical prediction tool to incorporate all the different physical phenomena, such as inertial dynamics and tribology, with capability of dealing with the problem at various physical scales (tribological contacts through to large displacement inertial dynamics). Such a tool can be described as multi-physics multi-scale.

## **2.2 Lubrication Analysis**

Since the dawn of civilisation, man has recognised the importance of overcoming friction. Use of wheels where animal fat was used to lubricate the axle by the Babylonians as far back as 3500 BC is one such example. The Egyptians in constructing pyramids also used fat and water to move large stones carried on rolling logs with documented evidence.

---

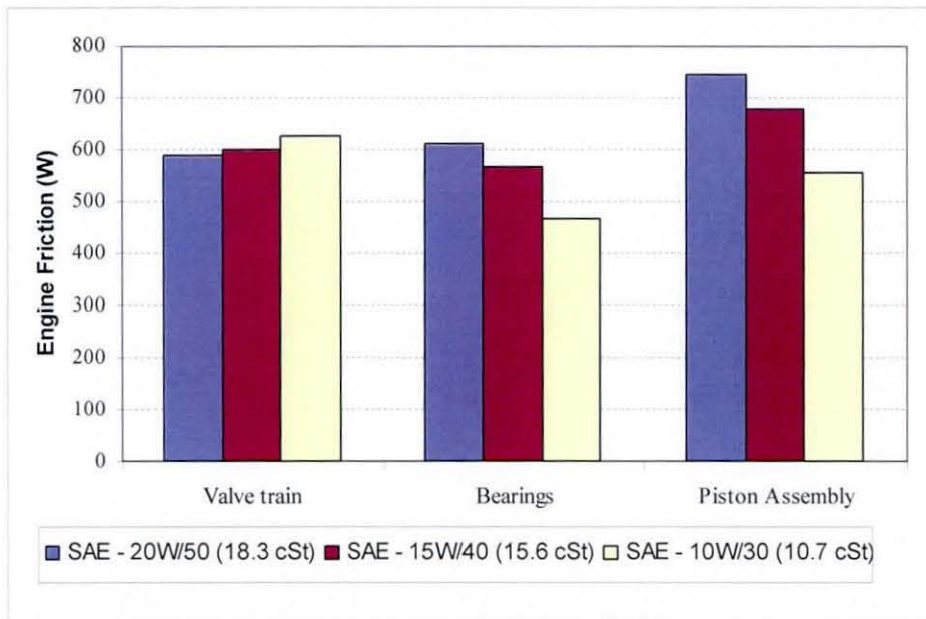


**Figure 2.2 Sensitivity of the engine component friction to various lubricants after (Taylor 2002)**

*Kinematic Viscosity @ 100°C is given for all lubricants*

In mechanical systems, interactions between two loaded mating parts that undergo relative motion with respect to one another creates tremendous amount of resistance to motion, caused by friction. This can cause catastrophic failure or damage to the machine components, such as wear, scuffing or other failure mechanisms. The introduction of a lubricant between these mating surfaces simply aims to ensure that the two solid bodies are not in direct contact, separated by a fluid film, which can be sheared with relatively low shearing force. This also aims to ensure that there is no damage to the mating surfaces, as well as reducing heat generated in the contact. Therefore, a major aspect of science of lubrication is to ensure an ever lasting lubricant film between mating load bearing surfaces under various physical conditions, thereby minimising the undesired effects of friction and wear.

When it comes to a complicated machine, such as IC engines, which consist of several sub-systems, operating under varying conditions (load and speed), the situation is rather complex. Different sub-systems respond differently for various physical properties of the lubricant such as temperature, shear rate and pressure (Taylor 2002). Figure 2.2 shows the breakdown of friction in a European type 2.0L engine for its various sub-systems and with different lubricants. It can be seen that the frictional losses in the bearing and piston assembly

decrease, while the viscosity is increased, whereas the friction increases in the valve train assembly. This is the case for piston as the proportion of viscous to boundary contribution becomes more significant with increased viscosity, at least as one effect. Already some research on the total engine frictional losses have been carried out, but more details have to be made clearer. Furthermore, the effects of lubricant viscosity on friction and wear of an engine with specific lubricated contacts have not been clearly understood. Thus, it is very complex to determine an optimised viscosity value. In fact reducing oil viscosity not only deteriorates the reliability of engine parts, but also can increase friction in some other conjunctions. Therefore, it is necessary to understand quantitatively the effects of different lubricant properties on different lubricated conjunctions under real varying operating conditions.

### 2.2.1 Principle of Lubrication

When one surface moves relative to a counter-face, the lubricant is dragged into the contact conjunction (Cameron 1966). As the passage converges and the lubricant volume entering into the contact remains constant, the almost incompressible fluid generates pressure to make its path through the conjunction. This pressure force moves the two surfaces apart, preventing a solid-to-solid contact. Even though many attempts reported in the literature about the use of animal fat as an agent of reducing friction force, a proper study about lubrication from an engineering science standpoint commenced in the 1850's with the studies carried out by Von Pauli in 1849 and Hirn in 1854 as reported in (Rahnejat 1984). They studied lubricated shafts and bearings operating under fully hydrodynamic conditions. (Petroff 1883) analysed Hirn's work in some detail in 1883. Petroff was studying the variation of frictional characteristics in a journal bearing with different types of oil, assuming that the lubricant was sheared between the shaft and the bearing. Tower (Tower 1883) showed that there were considerable pressures generated in rolling element bearings under fully hydrodynamic contact conditions. During this period (Reynolds 1886) showed, using an analytical model, that a converging wedge-shaped film generated an oil pressure distribution based on the Newton's model for slow viscous action and the well known Navier's – Stokes equation. All the subsequent lubrication investigations by many authors are founded on the fundamental work of Reynolds.

In recent years it has been recognized that the lubricated contacts with low geometrical conformity such as gears, cams, rolling element bearings behave rather differently to the

---

---

classical hydrodynamic lubrication (Dowson and Higginson 1977). High pressures generated within this type of contact affect the viscosity of the lubricant dramatically as shown by Barus and Roelands (Gohar 1988) and the lubricant becomes semi-amorphous. Furthermore, the application of high contact loads and the change in viscosity can lead to substantial local deformation of elastic solids. In contrast this local deformation changes the shape of the fluid film and concurrently the pressure distribution in the contact. Ultimately, the metal to metal contact is prevented. The formation of lubrication film due to such action is known as elasto-hydrodynamic lubrication (EHL).

Only in the past 3 decades a complete theoretical solution for an isothermal EHL of point contacts has successfully been analyzed, using simultaneous solution of the elasticity and Reynolds equation. In (Hamrock and Dowson 1976) the conjunction is divided into equal rectangular areas with a uniform pressure element over each area and pressure at each grid point is calculated using Reynolds' equation. Again (Hamrock and Dowson 1977a) presented a similar approach for a point contact under fully flooded condition. A fully flooded condition is said to exist, when the inlet distance of the conjunction ceases to influence in any significant way the minimum film thickness. The inlet distance of the conjunction is defined as the distance from the centre of the contact to the edge of the computing area. In (Hamrock and Jacobson 1983) a procedure for the numerical solution of the complete isothermal EHL for a line contact is presented, assuming that there is no side leakage. This analysis may thus be used as the foundation for more complicated analysis, incorporating surface roughness, non-Newtonian effects, and temperature effects (Balakrishnan and Rahnejat 2005; Dursunkaya *et al*, 1994; Keribar and Dursunkaya 1992; Mihailidis *et al*, 1999; Priest *et al*, 2000). Furthermore, Hamrock has formulated a relationship between minimum film thickness and physical properties such as contact load, sliding speed and material parameters. Such relationships are obtained by regression of numerical predictions over a range of these parameters or by experimentation under similar conditions. These relationships are referred to as extrapolated oil film thickness formulae. It is found that the sliding velocity is the most influential parameter on the minimum film thickness.

It was not until the late 1960s and early 1970s that the influence of lubricant starvation upon elasto-hydrodynamic behaviour received serious consideration (Chevalier *et al*, 1996; Messe and Lubrecht 2000), which can influence the minimum film thickness by deviating from fully flooded condition. Prior to this time it was assumed that the inlets were fully flooded.

---

However, in due course it was recognized that some machine elements suffered from lubricant starvation. (Hamrock and Dowson 1977b) presents a simple expression for the dimensionless inlet boundary distance. This inlet boundary distance defines whether a fully flooded or a starved condition exists in the contact. Especially in a multi-ring pack piston an oil scraper ring prevents the inflow of excess oil, thus can cause starvation. In fact, it has been shown that most multi-ring packs are operating under oil starvation (Han and Lee 1998).

### 2.2.2 Lubrication of Crankshaft Support Journal Bearings

An optimum engine design requires a system approach since the performance of each component can be strongly dependent on the other components. The crankshaft is coupled with the crankcase by hydrodynamic journal bearings (Hamai *et al*, 1990). Combustion gas pressure applied to the piston crown area is transmitted through the connecting rod and cause elastic deformation of the crankshaft. The load is transferred to the crankcase through these journal bearings. With the trend in manufacturing compact and lightweight engines, the deformation of the crankshafts has become more significant.

Due to a high degree of contact conformity, lower pressures are generated in the support bearings and, thus, hydrodynamic regime of lubrication is more likely, particularly with engines employing thick wall bushings, made of materials of high elastic modulus, such as the E6 engine. As Reynolds illustrated there is a converging wedge-shaped film generated in between shaft (the journal) and the bearing bushing. The rotating crankshaft (the journal) entrains the engine oil into this converging gap. The generated hydrodynamic pressures, supplied at typical inlet pressures of just 0.5 MPa to the contact, increase in magnitude up to 35 MPa or even higher to 150 MPa such as in the connecting rod bearing (Mihara and Someya 2002). This results in maintaining a fluid film in between two mating surfaces in relative motion. The maximum pressure in the journal can be seen at about 60° after TDC in a four stroke engine (Mihara *et al*, 1995). The oil film thickness is severely affected by the operating condition of the engine. In terms of bearing lubrication, at maximum speed with no load or when deceleration the most severe operating conditions can occur. Under this severest loading scenarios the maximum stress point can be seen in the base of the crankpin and the web or else in the base of the main journal, depending on the force acting on the crankshaft (centrifugal force or centripetal force).(Hamai *et al*, 1990).

---

---

A key issue in the analysis of engine bearings is the coupled complex elastodynamics of the crankshaft system and the hydrodynamics of the journal bearing supports under transient conditions, occurring due to variation in combustion gas force. Also, particular attention has to be paid to the elastic deformation of the bearing housing under its conforming contact with the journal, if thin shell bearings made of materials of low elastic modulus are employed (Gupta 2002). Very high pressures generated can cause fatigue spalling in thin shell bearings due to inelastic sub-surface deformation, leading to forming globular grits (due to pitting of contact surfaces). Wear can also take place due to diminution of the gap (Kineshita *et al*, 1989). Furthermore, the dynamic nature of the transmitted force on the bearing support can cause eccentric orbit of the journal, a condition referred to as whirl, which can result in the conical motion of the flywheel. This problem is more pronounced with the journal bearing situated nearest to the position of the flywheel (Kineshita *et al*, 1989) (Boysal and Rahnejat 1997). Theoretical investigations have shown that there exist different points within the eccentricity circle of a journal that can produce the same force, but with different eccentricities (Kryniski 1991). Thus, external force carried by the bearing such as the weight of the crank, combustion force, etc can be balanced in two different positions under same speed conditions. Due to this reason, vibrating shaft jumps from one stable position to another, creating high amplitude oscillations known as the jump phenomenon. This effect has been observed, much earlier and explained through numerical analysis for dynamically loaded journal bearings. (Newkirk 1924) reported the first instance of bearing instability. He demonstrated that under certain combinations of speed and load, the journal centre did not remain fixed as predicted by steady state Reynolds equation, but precessed or orbited about the equilibrium position at a speed approximately half its rotational speed. (Pinkus and Sternlicht 1961) who provided a full Sommerfeld solution for hydrodynamic journal bearings explained the journal instability in terms of the angle of inclination of the resultant force vector to the line of centres of the journal and the bearing bushing. The movement of the shaft centre under the influence of the resultant force vector  $F_R$  is not towards the centre of the bearing  $O_b$ , due to the influence of the angle  $\phi$  as shown in Figure 2.3. Instead the shaft centre is forced to move in an orbit around the bearing centre, which causes the whirl of the journal centre about the centre of the bearing. The whirl frequency of the journal is established by the speed that the shaft can pump lubricant into the bearing clearance considering laminar flow conditions for the lubricant. Since the bearing sleeve (i.e. bushing)

---

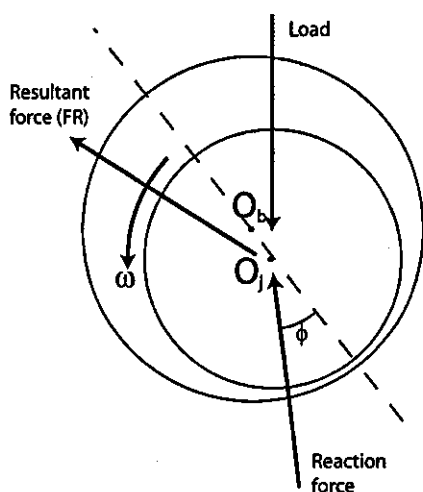


Figure 2.3 Journal instability motion

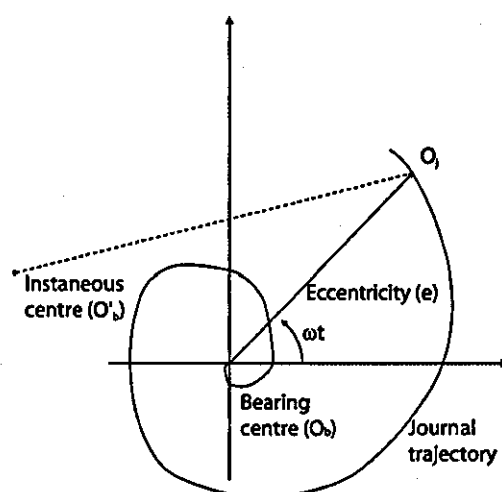
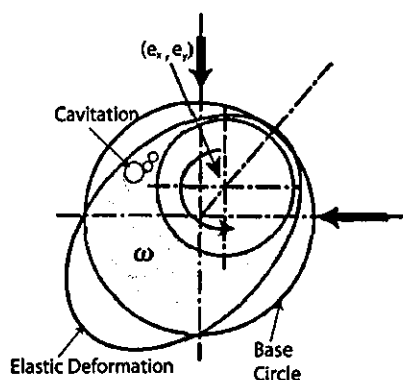


Figure 2.4 Shaft centre movement

is stationary and the flow is laminar. The lubricant is entrained into the converging gap at half the surface speed of the journal as it is explained in section 1.4. Therefore, an adverse excitation frequency for a journal bearing is half the speed of the shaft it supports. While the existence of this frequency is not a major obstacle for rotor-dynamic problems, its existence in a four stroke IC engine has a significant influence as this frequency is coincident with the half engine order, being the fundamental firing frequency, initiated due to the combustion process. This effect may lead to instability during such jumps.

Under the imposed physical conditions, the journal would run at some eccentricity. The region above the line of centres is subjected to diverging space, while the region below the line of centres is subjected to a converging gap (see Figure 2.5). The lubricant builds high pressures, when pumped into the converging wedge, whereas it is subjected to low pressures, when it comes into the divergent gap. Squeeze effect which takes place due to pure normal motion (convergence of contacting surfaces) of the journal also contributes to the generation of pressures. It creates negative pressures in the case of separation of solids. When the pressure falls below the saturation pressure of the lubricant solution, the dissolved air starts to come out from the solution, forming cavitations. Generally, mineral oils contain 8 to 12% of dissolved air (Hamrock *et al*, 2004). Under EHL conditions, the mass conservation of the fluid flow in the flooded area and the cavitated area can be used to predict the presence of cavitation in a main bearing (Elrod 1980). During the operation of the journal in the engine, circumstances can rapidly change, causing cavitations to intermittently occur. The occurrence



**Figure 2.5 Formation of cavitation under EHL conditions after (Aoyama *et al*, 2003)**

of this and the collapse of cavitation may lead to a noise with high frequency over 5 kHz, from main bearings under certain operating conditions (Aoyama *et al*, 2003).

Bearing hydrodynamics is greatly affected by both deformation of the crankshaft and the engine block (Garnier *et al*, 1999). Therefore, a structural model of the crankshaft, a structural model of the engine block and a lubrication model of a support bearing should be coupled together in a good mathematical model of the engine bearing system. It is common in studies of crankshafts to represent the oil film hydrodynamics either by the mobility method (Choi *et al*, 1992; Katano *et al*, 1991b) or by their simple combination (Morita and Okamura 1990; Okamura *et al*, 1990), even though these methods neglect the important effects of journal bearing misalignment (Ichikawa *et al*, 1995) or the effects of oil holes or oil grooves. Various simplified approaches have been used to solve the Reynolds equation, such as the *long bearing approximation*, which assumes that the pressure variation along the bearing length is negligible, and the *short bearing approximation*, which assumes that the pressure variation along the circumferential direction is negligible (Hamrock *et al*, 2004). Both these methods are widely used to arrive at simplified analytical solutions (Mourelatos 2001b; Pinkus and Sternlicht 1961) (Childs *et al*, 1977; Kirk and Gunter 1975).

Though Reynolds equation can be used to find pressure distribution in a lubricated conjunction, there were some mathematical difficulties. In 1904 Sommerfeld neatly overcame these integration difficulties by using a new mathematical substitution method known as the *Sommerfeld substitution* (Hamrock *et al*, 2004). However, the pressure distribution obtained using the Sommerfeld's approach is skew symmetric about the minimum film thickness as

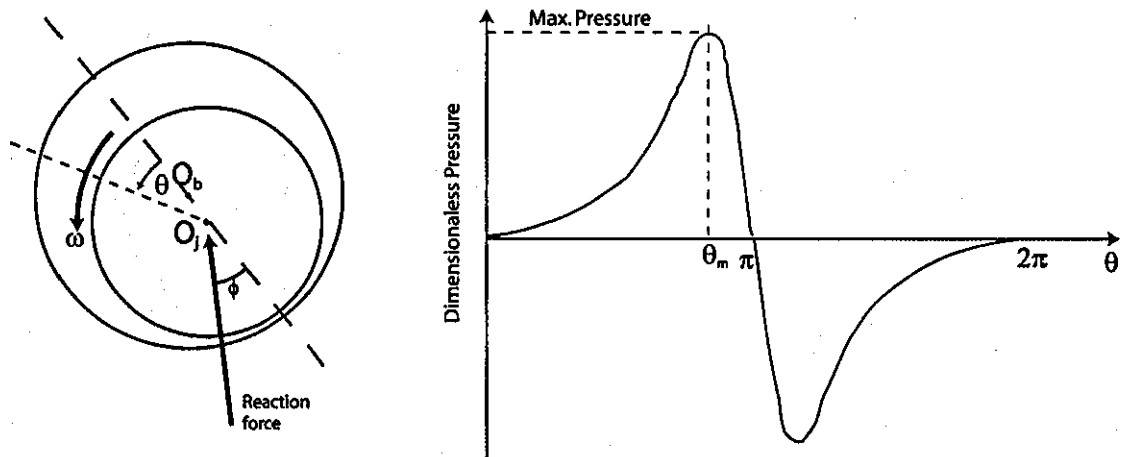


**Figure 2.6 Full Sommerfeld pressure variation in a journal**

shown in Figure 2.6. This may lead to the fact that the resultant load carrying capacity along the line of centres is predicted to be zero and the resultant lubricant reaction force acts at right angles to the line of centres. This implies that, as load is applied to the bearing, the journal centre moves away from the bearing at right angles to the load vector, which is not a rational conclusion. Also, under the Sommerfeld condition the pressures in the divergent film are all lower than the ambient pressure. As mineral oils contain dissolved air, they commence to come out of the solution, whenever the pressure falls below the saturation pressure. In many situations the saturation pressure is very close to the ambient pressure, and whenever the pressure falls below ambient, these dissolved gasses are liberated from the lubricant. Thus, mostly ambient pressures are maintained in the divergent clearance.

This difficulty of predicting sub-ambient pressures by the normal Sommerfeld (referred to as the full Sommerfeld) analysis has led to the suggestion that the sub-ambient pressures predicted by the analysis should be ignored. This approach which limits the analysis to the convergent film is known as the *half-Sommerfeld solution*. This approximation in fact leads to more realistic predictions of some bearing characteristics, but also leads to a violation of mass flow continuity due to its non-continuous nature of pressure variation at the minimum film thickness position. Boundary conditions should be applied to solve the Reynolds equation. One such boundary condition is the outlet boundary condition at which the film ruptures and when the pressure is considered to become ambient. Thus, with incorrect boundary conditions deviations occur from exact pressure distribution. There are many cavitation boundary conditions used in the literature. The simplest is the half-Sommerfeld condition as discussed above, which assumes zero load carrying capacity within the cavitated

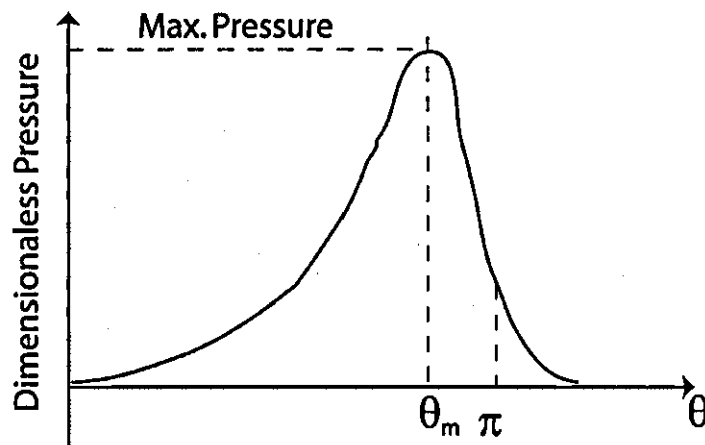


Figure 2.7 Pressure variation with Reynolds boundary conditions

area (Pinkus and Sternlicht 1961). Yet another cavitation condition is the Gumbel condition in which the Reynolds equation is first solved subjected to specific boundary pressures at oil hole and the two bearing ends. Then, the cavitation region is determined by disallowing the existence of sub-ambient pressures. A more accurate cavitation condition is that of Reynolds or Swift-Stieber condition, which requires the pressure gradient to be zero and the pressure to be equal to the cavitation pressure at the cavitation boundary (Paranjpe and Goenka 1990) (see Figure 2.7). However, Mourelatos claims that the most accurate cavitation condition is the Jakobsson-Floberg and Olsson (JFO) condition, which conserves mass flow rate, both at the film rupture point and at the reformation boundaries (Mourelatos 2001b). This will increase the computational cost substantially by about 50% in analysis of bearing lubrication with Reynolds boundary conditions (Mourelatos 2001b).

The most used and generally accepted boundary conditions, suggested in literature, is the Reynolds cavitation conditions that leads to a finite length solution. To have a better understanding of both finite length bearing solution and short bearing approximation, which is the most widely used simplified approximation, the solutions have been compared in (Kirk and Gunter 1975) as shown in Figure 2.8. Solid lines represent the finite length solution reported to have come from digital computer solutions carried out by (Pinkus and Sternlicht 1961). In addition, the corresponding Sommerfeld number, which is proportional to the reaction load, obtained from the short bearing solution is plotted for the same bearing length to diameter ( $L/D$ ) ratios. It is easy to see that the assumption is very good for  $L/D$  ratios of

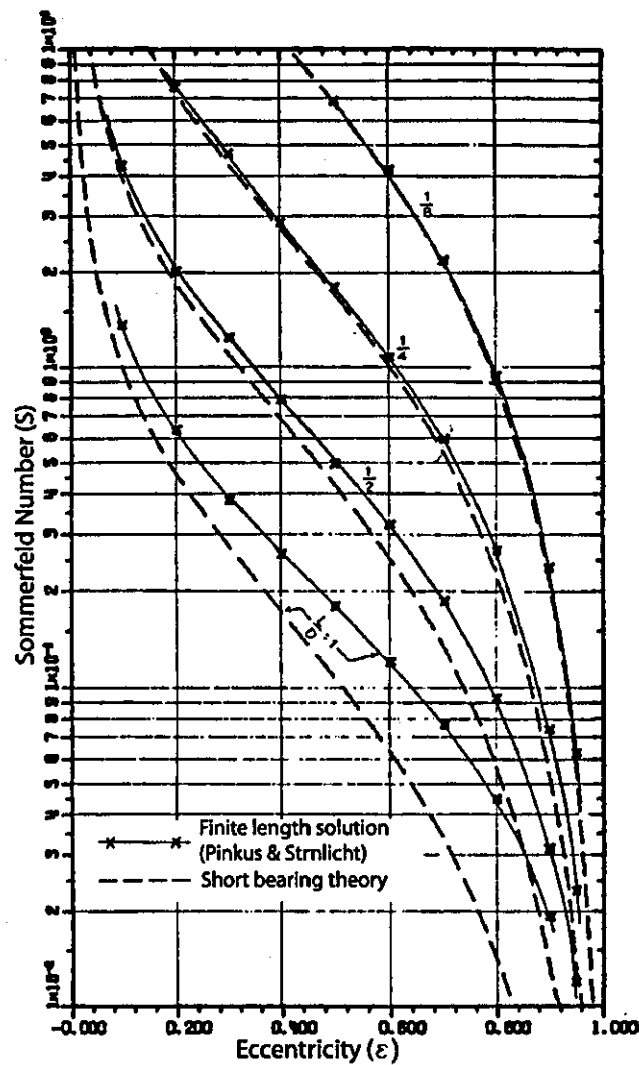
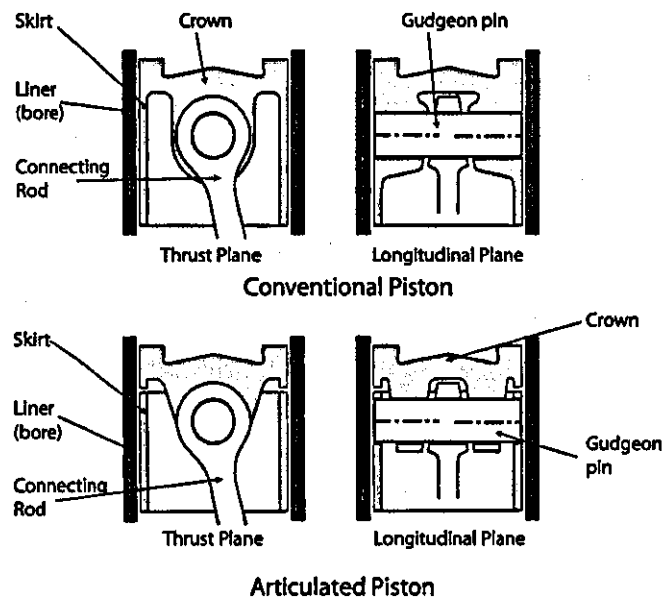


Figure 2.8 Comparison of finite length and short bearing solutions after (Mourelatos 2001b)

0.5 or less. However, it is also noticeable that the difference is progressively reduced for less eccentricity ratios for any  $L/D$  ratio.

### 2.2.3 Piston Secondary Motion

In an IC engine, the piston is the reciprocating agent, which undergoes various kinds of transition forces such as combustion force, piston skirt to cylinder wall or liner interaction forces and pin bore reaction. Depending on the application, several piston skirt designs are used. Full skirt pistons, half skirt pistons and articulated piston configurations show noticeable performance variations. Full skirt pistons are widely used in normal cars and



**Figure 2.9 Conventional and Articulated piston configuration**

motorbikes, whereas half skirt pistons are mostly used in high performance engines such as in the motor sport. Articulated pistons are widely used in heavy diesel engines such as for tractors, caterpillars etc. Articulated pistons split the functions of axial and side load support between two separate components named as crown and skirt, which are free to move relative to each other as shown in Figure 2.9. The crown carries the axial loads such as the combustion and inertial forces, while the skirt supports the side force on the piston assembly needed to balance the moment of these loads about the crank pin. Requirement in performance and durability of a piston greatly depends on the application of the piston. For an example, engine of a F1 motor race engine is expected to survive only for 450 km, whereas for normal car engines one would expect more than 200,000 km (of course at considerably less unfavourable conditions).

The primary motion of the piston is well described by the kinematics of the slider crank mechanism, which is essentially the reciprocating motion in the process of converting linear motion into the rotary motion of the crankshaft. However, the clearance between the skirt and the liner, which is essentially present to accommodate for the different thermal expansion coefficients for the two sliding bodies and for the purpose of lubrication deviates the piston motion from its primary motion alone. These additional motions; laterally and through tilting are known as piston *secondary motions*. Though this clearance is very small, it is large enough to produce piston secondary motion and finally to create unwanted noise and

vibration, when side forces can cause impact and noise propagation, a phenomenon referred to as *piston slap*. Piston secondary motions have long been recognized and linked to the issues of friction, piston slap noise, liner vibrations and cavitation, skirt scuffing, cylinder wear and oil consumption. In recent years piston secondary motions have been analytically and experimentally investigated in order to gain insights regarding these issues and used for the proper design of pistons. The early models like (Bishop and Leavitt 1975; Haddad and Howard 1980) have generally excluded any representation of tribology of mating surfaces in the piston assembly, even though these models are aimed for calculation of noise and vibration.

Some engines are fitted with pistons, with an offset gudgeon pin, which can be used to reduce the thrust side force on the piston. In IC engines the offset is to the thrust side of the piston as shown in Figure 2.10. The primary reason for the gudgeon pin offset together with enhanced fluid film presence is to reduce piston slap impact by viscous dissipation on the thrust side of the cylinder bore soon after the piston passes the top dead centre during the power stroke (Balakrishnan 2002). Number of attempts can be seen in literature in the investigation of piston slap noise. (Haddad 1995; Haddad and Tjan 1995) has investigated piston slap noise using energy approach, in which he has considered the piston as a rigid body and possible piston orientations within the cylinder were identified. Momentum balance was used to predict the successive orientations and the kinetic energy loss was obtained during each change of orientation, which was supposed to be the dissipated energy as slap noise. It has been revealed that offsetting the crankshaft or the gudgeon pin towards the piston thrust side reduces this energy loss, whereas the piston centre of gravity does not respond to this loss of energy.

Another attempt by (Cho *et al*, 2002), utilizing a measured point mobility method to represent lubricant reaction and a rigid piston revealed that the maximum impact force under slap condition was around  $70N$ . However, impact force induced from piston slap is greatly affected by the clearance between the piston skirt and the cylinder liner, bearing friction and the crank speed (Farahanchi and Shaw 1994). Slap noise is prominent at about  $5^\circ$  degrees of crank angle after the TDC during the power stroke which generates block vibrations up to a frequency of 2 KHz (Teraguchi *et al*, 2001).

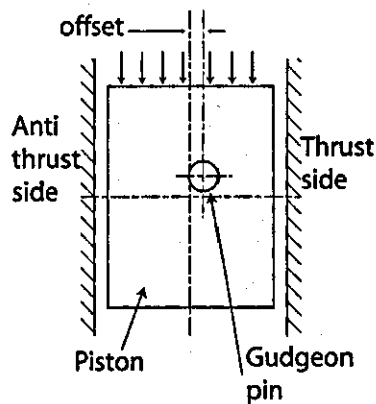


**Figure 2.10 Gudgeon pin offset**

The friction force generated between the piston bore and the piston skirt is strongly affected by piston slap motion. Due to the impact nature of the slap motion the side force generated is high and so is the friction force. This friction force is then transmitted to the other components of the engine, which may lead to unwanted noise and vibration other than the obvious frictional power loss. However, the issues of piston friction, slap noise, liner vibrations and cavitation, skirt scuffing, and oil consumption are strongly related to each other and cannot be addressed in isolation. Thus, hydrodynamic lubrication in piston skirt-to-cylinder bore, boundary lubrication due to asperity contacts at TDC or BDC, deformation of liner leading to EHL conditions, thermal effects on both lubricant and structural member (thermal deformations that causes the change in clearance between the piston and cylinder liner due to different thermal expansion coefficients), availability and transport of lubricant (oil starvation) must all be ideally considered together with piston secondary motions in order to obtain a good insight into the piston behaviour. Nevertheless, combining all these effects into a holistic model in great detail would lead to unacceptable computation times, but it is possible with the acceptable approximate mathematical techniques, which form the basis of the research reported in this thesis.

Whilst early investigators ignored hydrodynamics of the skirt bore interface, various subsequent investigators have studied the skirt lubrication problem in greater details. (Knoll and Peeken 1982) have considered the skirt lubrication problem in isolation, without regard to full inertial dynamics or overall component flexibility. Using finite element solutions for Reynolds equation, they have calculated maps of dimensionless side load capacity and tilting moment as a function of the Sommerfeld number, based on axial lateral and tilt velocities and

tilt angles, for a perfectly cylindrical skirt. The need to account for possible oil starvation at the dead centres of the cylinder was also highlighted. (Keribar and Dursunkaya 1992) have investigated the skirt lubrication problem by considering motions of the piston, pin, rod and skirt (for articulated pistons) calculated separately and subsequently solving Reynolds equation to obtain the contact pressure and film thickness distribution in the skirt-bore and wrist-pin interfaces. This amounts to a quasi-steady approach. Dynamics was treated in a generalized fashion to find the axial, lateral and tilting motions of the piston, wrist-pin and the position of the connecting rod. Perturbation technique was used to find the parameters needed to solve the Reynolds equation. Their work was subsequently extended, incorporating skirt elastic deformations in (Dursunkaya *et al*, 1994). Skirt deformations were calculated using a skirt compliance matrix derived from a finite element model of the piston. In (Yang *et al*, 2001) authors have used the same type of methodology, but here the effects of asperity contact friction in the skirt bore were also included into the model, using a statistical approach, which was presented by (Greenwood and Tripp 1970). A more detailed investigation has been carried out by (Balakrishnan and Rahnejat 2005), including inertial dynamics, secondary motions of the piston and the effect of rigid body approach and separation of the contiguous load bearing surfaces. Elastic deformation of the skirt and bore were taken into consideration under isothermal conditions, dividing the skirt into a dense computational mesh of 180 x 80 for an actual skirt profile.

Lubricant supplied to the skirt-bore interface considerably affects piston slap and friction. By supplying an adequate amount of lubricant into the skirt, a relatively thick oil film can be formed in the conjunction. Piston slap motion can be reduced by the fluid film as it increases the impact time, thus reducing the force at the impact. This paves the way, not only to reduce slap noise, but also to reduce piston friction considerably as shown by (Teraguchi *et al*, 2001) from their experimental work.

#### 2.2.4 Piston Ring Analysis

The process of power generation in an IC engine starts from the translational motion of the piston inside the cylinder bore that takes place due to pressure difference between the combustion chamber and crankcase pressure. A diametral clearance of about 60–100 $\mu\text{m}$  is present between the piston skirt and the cylinder liner in order to compensate for different thermal expansions between them. On the other hand, such a clearance is mandatory to

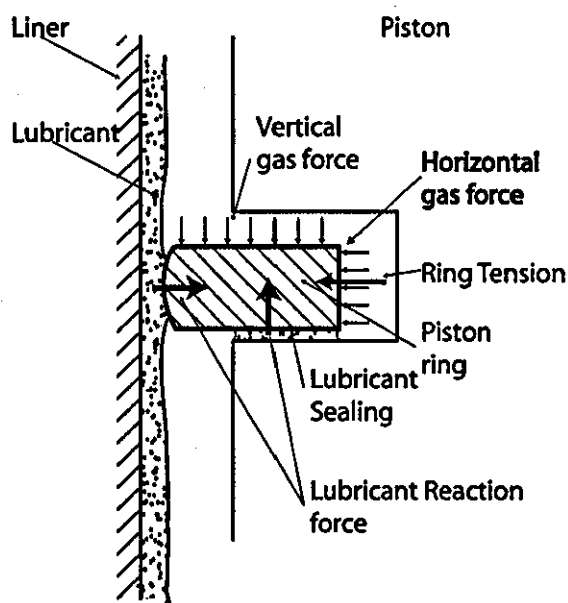


**Figure 2.11 Forces acting on piston ring**

maintain a proper lubricant film, reducing friction and wear between the piston skirt and the cylinder liner. Isolation of high pressure combustion chamber, preventing any gas leakage into the cylinder block obviously enhances the power output of the engine significantly. The task of isolation is supposed to be achieved by the piston ring pack, while ideally maintaining a minimum friction force. Tribological and sealing qualities of piston rings have long been recognized as important influential parameters for power loss, fuel consumption, oil-consumption, blow-by and harmful exhaust emissions. Due to the complexity of the features of the piston ring- cylinder wall contact, a comprehensive analysis of piston rings has somewhat lagged behind other engine components.

Piston ring is subjected to various forces as shown in Figure 2.11. Combustion gas force acting in the vertical direction pushes the ring onto the bottom face of the piston ring groove. Lubricant film is formed underneath the ring and the piston and prevents any gas leakage through the gap. Generally the ring radius is larger than the radius of the cylinder bore. Therefore the ring is squeezed in radial direction when it is inserted into the cylinder bore such that it sits firmly while having a radially outward tension force on the cylinder bore, which is called the ring tension force. Both horizontal gas force acting on the ring and the ring tension tend to push the ring against the cylinder bore and are balanced by the lubricant reaction acting on the cylinder bore. While maintaining a sufficient reaction force to

compensate for ring tension and gas force, the lubricant film between the cylinder liner and the ring prevents any gas leakage through the gap. However higher ring forces against the cylinder wall causes smaller film thickness that will increase the piston friction force. Generally the piston ring friction accounts for 20% of total piston-liner frictional forces as can be seen from the Figure 7.29. Therefore excessive ring tension must be avoided. Furthermore, the piston and gudgeon pin inertial forces, as well as body forces make the system more complex (Priest *et al*, 2000).

Under the influence of such forces, the piston ring pack exhibits a complex dynamic behaviour, which includes the dynamics of the rings and related gas flow and oil flow, twisting of the piston ring and its influence on ring-liner and ring-groove lubrication and unsteady oil supply to the upper piston rings and its effects on ring-liner lubrication. Due to mutual interconnection between ring lubrication and dynamics one cannot study one aspect alone, while neglecting the other.

Even though prevention of gas leakage is the intended task of the piston ring, it cannot totally be eliminated owing to many reasons. Due to dynamic nature of its forces ring may lose its stability in the axial and radial directions, which is known as ring flutter (Tian 2002a), and introduce new paths for gas leakage in addition to the ring gap. The rate of gas leakage due to ring flutter is much greater compared to the leakage through the ring gap (Tian *et al*, 1996). Furthermore, ring flutter has a profound influence on the oil flow in the piston, which directly affects oil transport and oil consumption. Additionally, the net dynamic force on the ring may augment ring twist within an engine cycle, thus causing additional effects to the piston tilt (Kurbet and Kumar 2004). These may change the clearance gap between the ring running surface and the cylinder liner. Minimum film thickness has two important effects on ring-liner lubrication. Firstly, the location of the minimum film thickness determines the width of the convergent part of the ring running surface, and thus the radial load carrying capacity of the ring. Secondly, radial loading varies with the minimum film thickness if there exists a gas pressure difference between the regions separated by the ring. This influences friction and asperity contacts between the liner and the ring (Tian 2002a; Tian 2002b).

Furthermore, prevailing lubrication conditions between a single ring and the liner should not be considered as isolated from the entire system. Instead, the lubrication condition of a ring largely depends on its oil supply, which is determined by the lubrication between the ring

---

preceding it (leading its sliding motion) or the lubrication of itself during the previous stroke (Han and Lee 1998). In the liner region, where the oil control ring can reach, the upper piston rings are lubricated by the oil left by the lower rings (i.e. its inlet meniscus is determined by the preceding ring's outlet lubricant flow). In the upper dry region, where the oil control ring cannot reach, the top two rings need to entrain the oil from the lower liner region in order to lubricate themselves. As a result of these dependencies between different rings and the liner locations, the lubrication condition of the ring exhibits frequent shifts between hydrodynamic lubrication, mixed lubrication and pure boundary lubrication (Cho *et al*, 2000). Additionally, the regime of lubrication largely depends on the sliding speed of the ring. Theoretical and experimental studies have confirmed that piston rings enjoy hydrodynamic lubrication throughout most of the engine cycle, but that a transition to mixed or boundary lubrication can be expected near the dead centres with special regards to TDC (Dowson *et al*, 1983).

In a lubricated contact one body can be moved relative to the other in tangential direction or in normal direction. Tangential motion is known as sliding and normal motion is known as squeeze action or the squeeze film action. The velocity that the two contacting bodies are approaching or departing normal to each other is called the squeeze velocity, which contributes a lubricant pressure to be built up at the contacting point. The squeeze effect is more pronounced in pressure building at places where the sliding velocity is nearly zero or completely stopped momentarily such as TDC. Even though the adverse conditions at the ring-liner contact occurs at the TDC position, as might be expected from simple considerations of the cyclic variations of the entraining velocity, the thinnest film occurs shortly after the TDC owing to the beneficial effect of squeeze-film action there. The movement of the ring towards and away from the cylinder liner causes the squeeze action. The motion towards the liner causes a negative squeeze velocity producing higher pressures in the contact so as the load bearing capacity. Under hydrodynamic conditions the predicted minimum oil film thickness shortly after TDC are often as small as  $0.1\mu\text{m}$  and sometimes even smaller (Dowson *et al*, 1983). With the composite surface roughness of nearly  $0.4\mu\text{m}$  (based on average roughness values ( $R_a$ )) in most conventional engines, boundary or mixed regimes of lubrication become prevalent. Therefore, Dowson explored the role of Elastohydrodynamic (EHL) lubrication at such adverse conditions in the contact. During EHL conditions high contact pressures of around hundreds  $\text{MPa}$  were predicted such that the iso-viscous assumption does not hold true as it does under hydrodynamic conditions. Such an

increase of pressure at the contact converts the lubricant into a semi – amorphous state, and thus piezo-viscous conditions are necessary to be considered. In their study of ring-liner EHL interaction (Dowson *et al*, 1983) used the Barus equation (4.68) to represent the pressure effect on viscosity. Viscosity ratio of 2 was considered to be the limiting factor for EHL conditions to occur which gives  $50\text{MPa}$  at a temperature of  $150^{\circ}\text{C}$ .

Most of the numerical studies carried out on ring-liner interactions are based on one-dimensional (1-D) models which assume no flow in the circumferential direction of the ring also known as line contact approximation (Hamrock and Jacobson 1983). Moreover, the piston ring and cylinder liner were assumed to be perfectly circular, and the film thickness was taken to be uniform in the circumferential direction. None of these assumptions are particularly true in practice, particularly due to flexibility of ring and the cylinder liner. Studies have shown that there is a considerable difference between one-dimensional and two-dimensional (2-D) solution for a rigid piston ring (Liu *et al*, 1998). 2-D solutions always show a lesser film thickness compared to 1-D solutions due to circumferential flow, which in turn decreases the hydrodynamic pressure to support the load and lead to a smaller film thickness (Yang and Keith 1996a). On the other hand, lubrication aspects in ring-liner are also affected by ring flexibility due the non-uniform stiffness of the piston ring, resulting in its deformation into a non-circular shape under dynamic loads. Under these conditions the gap between ring ends as well as the gap between piston ring-to-cylinder liner are changed, thus enhancing blow-by (Yang and Keith 1996b). Also due to dynamic excitations modes of the flexible ring can be excited. The predicted in-plane ring deformation, using simple beam theory shows significant radial deformations of about  $2\text{mm}$  for a normal piston ring of  $82\text{mm}$  diameter and  $2\text{mm}$  face-width (Okamoto and Sakal 2001).

Mathematical models of piston ring dynamics and lubrication are predominantly sensitive to correct description of boundary conditions, used to solve the Reynolds' equation and properly prescribe cavitation conditions occurring in the diverging outlet region of the lubricant film between the piston ring and the cylinder wall. The formation of gas cavities in the diverging region of the lubricant film influences the shape of the hydrodynamic pressure profile as discussed by (Cameron 1966). This consequently has an effect on load carrying capacity of the interface. Sommerfeld approximation as it is discussed in the previous section is the simplest, even though the standard assumption is Reynolds' criterion, considering lubricant pressure at trailing ends are equal to the gas pressure as formulated by (Dowson *et al*, 1979).

Recently very different set of boundary conditions, based on the assumption flow separation rather than gaseous cavitation has been presented by (Priest *et al*, 2000).

Prediction of temperature rise in lubricated contacts between machine elements is an important issue as this affects lubricant viscosity as well as, at significantly high temperatures, the structural integrity of the mating solids. The laws expressing the conservation of energy can be used to relate heat generation through compressive and viscous heating to convection and conduction cooling (Gohar 1988). Generally, convection cooling is not significant in EHL contacts, since the lubricant film is quite thin. (Cameron 1966) justifies its omission with an order of magnitude analysis for hydrodynamic bearings. The maximum temperature difference in a typical EHL contact would be about  $30^{\circ}C$  according to (Mihailidis *et al*, 1999), and this is more than enough to change lubricant rheological properties within the contact. The higher thrust force applied in relatively smaller area and higher cylinder wall temperatures due to the combustion process makes the situation rather complicated in piston ring-cylinder liner conjunction.

### 2.3 Dynamic behaviour of the Crankshaft

Non-uniform character of the torque produced in a reciprocating I.C. engine results in a cyclic variation in the crankshaft's speed. When various noise sources have been ranked according to their importance, the combustion excitation is identified as the critical source (Haddad and Tjan 1995). Because the crankshaft is an elastic structure, its response to the different harmonic components of the applied torque is different and changes with engine speed. Engine crankshaft can cause vibrations of the engine and power plant structures. Early in the design stage a precise prediction of the three dimensional vibration behaviour of the total crankshaft under running conditions and the behaviour of the engine structure due to crankshaft excitation are essential.

In recent years engineers have sometimes designed the dimensions of the crankshaft by considering the noise level as well as the induced stresses. This reflects the growing importance attached to noise and vibration issues (Katano *et al*, 1991a). The following processes are supposed to be the causes for the structure born rumbling noise:

---

1. The inertial force by the reciprocating mass of the piston and the connecting rod system pushes and pulls the crank pin, resulting in torsional vibrations of the crankshaft.
2. In this state, the combustion gas pressure in the combustion chamber causes the piston and connecting rod to induce inertial torque variations in the crankpin attached to each cylinder.
3. Both combustion gas force and the connecting rod forces on the piston create a side thrust force that pushes the piston against the cylinder wall, creating an impact force.
4. The crankshaft, accelerated by the exciting force, rotates and gives rise to varying journals' reactions.
5. The shock, thus generated, vibrates the cylinder block through the main bearings as well as the cylinder wall, and causes noise to be radiated from the cylinder block surface. Vibration is subsequently propagated to the cabin through the engine mounts.
6. The cabin panels vibrate in response to the rumbling noise.
7. The cabin air cavity resonates under the engine excitation.

Since this process involves a large chain reaction, it is not sensible to analyse given sub-systems in isolation. Thus, several system approaches have been made to study the dynamic behaviour of the crankshaft system.

In (Katano *et al*, 1991a) the crankshaft behaviour and the source of the rumbling noise was simulated in order to clarify the effect of crankshaft vibration on its support bearings after it is accelerated by the induced inertial imbalance. This study was based on the non-linearity of the oil film, dynamic characteristics of the crankshaft and the flexibility of the cylinder block. The mobility method was used to relate the rate of change of eccentricity to the loading and the current state of the bearings. Components' mass, inertial properties, stiffness and damping matrices were partitioned to distinguish between the degrees of freedom under several loading conditions.

(Boysal and Rahnejat 1997) presented a multi-body numerical non-linear dynamic model of a single cylinder internal combustion engine. The model comprises all rigid body inertial members, support bearings, joints, couplers and connections between various engine components, as well as means of vibration damping, such as the crankshaft torsional damper. The detailed model is parameterised, thus enabling virtual prototype testing of various engine

---

designs, as well as allowing the engine designer to carry out a comprehensive noise, vibration and harshness investigation of engine performance. This new approach was basically concentrated on engine design. It incorporated large displacement dynamics of engine components, combustion pressure and infinitesimal vibrations of support bearings.

Combination of multi-body dynamics with flexible bodies is an advantage for geometric non-linear FEA and rigid body dynamics. (Du 1999) investigated a V6 engine, which had been modelled with multi-body dynamics and flexible bodies. Impedance method and a full FE method to model the oil film bearing were used to represent hydrodynamic bearings as two alternative approaches. Model synthesis technique was used to reduce the size and number of resulting equations, representing the stiffness and mass of the crankshaft and the engine block. It was concluded that the vibration behaviour was largely different with a flexible engine block, when compared to a rigid block.

(Piraner *et al*, 2002) used a simplified approach, developed in the industry. It first combines a "quasi-static" crankshaft model and a rigid hydrodynamic bearing model to address crankshaft fillet bending stress and bearing performance characteristics. Then, the crankshaft bending loads are combined with the torsional loads to simulate stress at any location in a crankshaft FE model. ADAMS and ANSYS were the main software tools used.

### 2.3.1 Torsional Vibrations

At any instant of time the radial component of the piston force is transmitted along the connecting rod and is applied to the crank pin. This force tends to pull the crankpin away and induces an instantaneous bearing support load. The tangential component of the piston force is utilised for crankshaft rotation. During piston motion inside the cylinder the inertial piston imbalance increases in magnitude and subsequently reduces at the end of the stroke. This action results in an imparted twist-untwist action on the crankshaft, inducing torsional vibrations. Owing to the combustion cycle, the gas pressure inside the combustion chamber varies with a maximum pressure force at the power stroke, a few degrees after the TDC. In a four stroke internal combustion engine the applied torque's fundamental frequency coincides with half the crankshaft speed and its harmonics are at whole or half orders of the same speed (Rahnejat 1998). Half order harmonics of the engine torque are only contributed by the gas pressure and integer harmonics orders up to sixth order are mainly contributed by the

---

reciprocating inertia (Taraza 2001). Due to small, but inherent variations in cylinder operation, the pressure varies from cycle to cycle and cylinder to cylinder, causing fluctuations of the mean value of the cylinder torque (Taraza 2001). Therefore, there are an infinite number of critical frequencies, and in principle high vibratory torques can be expected at each of these frequencies, which are referred to as unexpected rotational frequencies. This phenomenon was first observed by Draminsky (see (Draminsky 1965)). (Hesterman and Stone 1992) pointed out that this is due to variations in inertia of large reciprocating mass and, thus a constant inertial assumption is not particularly valid for reciprocating masses. It has been known for some time that the torsional vibration of reciprocating engines and pumps cannot be modelled accurately by representing the reciprocating mechanism by a constant inertia. It further varies with the angular position. The major component of this variation is a twice per revolution cyclic effect and hence termed as *secondary inertia*. The consequences of this secondary inertia effect can be serious for torsional vibrations, causing secondary resonance and even instability.

(Goldsbrough and Baker 1926) used the linearized Floquet model (a non-homogeneous differential equation with periodic coefficients) for low speed multi-cylinder engines with certain assumptions such as, no relative twist between neighbouring crank assemblies, the flexible connecting rods are massless, connecting rod is infinitely long and higher order terms in the resulting equations were considered as not significant. He made an experimental rig and consequent correlations between the predicted and measured results were deemed as being very good, although deviations were noticed as the piston weight was increased. Based on his experimental work, Goldsbrough concluded that the flexible shaft was subjected to vibrations at all speeds, and within a certain defined range these vibrations were unstable (Hesterman and Stone 1995). However, revealed induced cyclic stresses at the service speeds were found to be well in excess of those predicted. In order to explain these unusually high stresses, Draminsky developed a theory based on non-linear analysis (Draminsky 1965).

Balancing of reciprocating inertia has become a severe problem for three cylinder engines of  $180^\circ$  phase difference configuration as only 50% of the unbalanced primary reciprocating moments are eliminated by adding counterweights to the crankshaft system. This enhances primary pitching moment on the engine. (Suh *et al*, 2000) investigated the effects of balance shaft on this pitching moment with the aid of DADS and MSC/Nastran, taking into account dynamic and inertia properties respectively. It has been observed that the rigid body motions

of the engine with the primary balance shaft are largely reduced due to the transformation of 50% of the unbalanced pitching moment into the yaw moment in a three cylinder configuration. In engines with large reciprocating masses the effect of inertia variation is significantly more pronounced

The variation of torsional inertia with time, which results in a secondary resonance, affects crankshaft failures. The induced inertial torque may have components at any integer multiples of engine speed. If any of these contributions coincide with component frequency an unexpected resonance may occur. If the oscillation occurs at resonance condition (multiples ( $n$ ) of the engine speed coincident with undamped natural frequency), then there is a consequential oscillation at  $n-2$  and  $n+2$  as well (Hesterman and Stone 1992). Until recent times, one-degree of freedom analysis was predominant in the process of crankshaft vibration analysis. which is not able to capture the coupled bending and torsional vibrations. However, the later use of Transfer Matrix Method (TMM) has allowed investigation of coupled vibrations in crankshafts (Wakabayashi *et al*, 1995).

### 2.3.2 Engine Noise Emission

The main energy source for the engine as the power plant is the combustion process from which a certain amount is utilized for coupled axial, bending and torsional vibrations of the crankshaft. Some of the energy is dissipated from the crankshaft itself due to its internal damping and in the form of acoustic energy. However, another significant amount of vibration energy is transferred to the engine block through the main crankshaft support journal bearings. The piston secondary motion also creates significant amount of excitations on the engine block (Spessert and Ponsa 1990). These excitations with various frequencies are absorbed by the engine block and dissipated through them to the environment as acoustic (air born) energy (or noise), and to lesser extent as heat It is known that the engine noise is dominant in the middle to high frequency range (0.5 to 2.5 KHz) (Athavale and P.R. 1999). It has been determined that this noise is mainly caused by the fundamental natural vibrations of the cylinder block.

Parallel to the development of light weight, high output power engines, made of materials with significant elasticity and thermal expansion the attention towards noise emission has become significant as a perceived quality issue. Thus, the need for more detailed analysis has

---

become paramount. Other than balancing and phasing of crankshaft some other approaches such as counter-balanced shafts (Suh *et al*, 2000) and torsional dampers (Morita and Okamura 1990) have been used to reduce crankshaft vibrations. (Okamura *et al*, 1990) used a method, referred to as the *dynamic stiffness matrix method* to study the effect of crankshaft three dimensional vibrational behaviour with a torsional damper. In their analysis main bearings were represented as spring - damper combinations. They found that engine block vibrations reduced with the increased mass and moment of inertia of the front pulley. The same was concluded in a more detailed analysis carried out by (Athavale and P.R. 1999), using FEM and BEM to examine the effects of coupled torsional and lateral bending vibrations of the cylinder block and the crankshaft on engine noise.

Even though the dynamic damper pulleys are used to reduce both crankshaft vibrations and engine noise, it is observed that sometimes engine noise level is not reduced as would be expected (Morita *et al*, 2001). Since the crankshaft pulley is attached to the front end of the crankshaft, its vibration can induce engine front noise. Indeed it is reported that a crankshaft pulley, could become a noise source at the engine front. The axial vibrations of the dynamic damper pulleys have been measured together with radiated noise in front of the engine under operating conditions. It has been found that the damper can be quite significant in noise radiation (Morita *et al*, 2001). In the low frequency range ( $< \sqrt{2} \times$  pulley natural frequency), axial vibration of the damper mass can exert a significant influence on the engine front noise, whereas in the higher frequency range the influence of the axial vibration of the damper mass on engine noise is small.

Torsional dampers have been attached to engine crankshafts only for the control of the crankshaft torsional vibrations. However, the torsional damper is a mass-spring system of three-dimensions, so the torsional damper can exert some influence on the three-dimensional vibration behaviour of the crankshaft system. Since, the inertia ring of the torsional damper rotates with the crankshaft, gyroscopic vibrations can also be generated. The gyroscopic couple of the front pulley also affects the vibration behaviour of the crankshaft, and thus the noise emission. In large engines there are two types of bending vibrations found unexpectedly: one is due to the coupling with torsional vibrations and the other is due to gyroscopic vibrations by the front and rear pulleys (Kimura *et al*, 1997).

---

(Okamura and Yamashita 1997) investigated the influence of the mass and moment of inertia and the accessory gears on three-dimensional vibrations of the crankshaft system. Three-dimensional vibrations of the crankshaft system were measured by hammer and shaker tests. Torsional vibrations were investigated initially using Holzer's method and the three-dimensional vibrations calculated by dynamic stiffness method. The change in the natural frequency, when the gear train is attached near the flywheel, is negligible (essentially small). This happens as nodal points, where zero displacement points in normalized mode shapes of the crankshaft, stand closer to the attachment point of the gears. In the lowest frequency mode shapes nodal points can be seen closer to the front as well as rear end of the crankshaft. However, nodal point at rear end is more accessible than that of the front end nodal point. Therefore, it is concluded that the gear train should be engaged to the crankshaft system at the crankshaft rear end as close as possible to the nodal point of the crankshaft. This will significantly reduce the vibration transmission to the attached gear train.

## 2.4 Vibration Analysis with FEM

Even though conventional stress analysis for a crankshaft can be used earlier in the design stage due to their reduced cost and time requirement, a detailed analysis cannot be performed without FEM, which is quite time consuming and expensive. Accuracy of the FEM increases with an increase in the number of elements used in a solid model. This in turn increases the processing time, as well as the memory requirements for a detailed model. Therefore, even for a relatively simple crankshaft, tedious modelling and expensive computation costs are inevitable. Thus, a number of reducing techniques are used to alleviate the computational costs of large FEM undertakings.

To overcome these difficulties of FEM analysis (Nagamatsu and Nakao 1983) developed the Reduced Impedance Method (RIM), in which the crank journal and crankpin are approximated as round bars. The resulting derived impedance matrix is in a closed-form, using TMM. Thus, FEM analysis is only needed for the crank arm and the counter weights. By further enhancing this methodology (Okamura *et al*, 1995), simplified the crankshaft three dimensional analysis by approximating these crank arm and counter weights as simple rectangular beam blocks.

(Knoll *et al*, 1997) developed a software package to simulate the dynamics of a flexible crankshaft and a flexible engine block, coupled by non-linear, distributed, elasto-hydrodynamic fluid film bearing reaction forces. The main idea for this was to change the base of the solution domain from a large set of locally-defined finite element base functions to a small set of globally-defined base functions, which would satisfy the relevant dynamic behaviour. Using this software model, 69885 DOFs in an engine block was reduced to 72 master DOFs and 50 additional model DOFs.

(Hu *et al*, 2003) presented a finite element based formulation for modelling the dynamic behaviour of a rotating flexible shaft supported by a flexible structure. The coupling effect between the rigid-body rotation and the flexible deformation of the shaft was considered and represented by non-linear coupling terms in the mass matrix and forcing vectors in the global system of equations. A specialized coupling algorithm was developed between a flexible and rigid-body dynamic formulation of a rotating shaft with the flexible body dynamic equations of the support structures. In the new coupling algorithm the flexible DOF for both the shaft and the support structure were represented as a condensed set of internal and retained DOF in a Craig-Bampton formulation.

(Mourelatos 2000) presented a structural analysis, using dynamic sub-structuring with Ritz vectors for predicting the dynamic response of an engine crankshaft based on the finite element method. The model couples the crankshaft structural dynamics, the main bearing hydrodynamic lubrication and engine block stiffness. A two level dynamic sub-structuring technique was used, based on finite element method.

## 2.5 Crankshaft Offset

Offsetting the crankshaft axis with respect to the cylinder axis has been thought to be a method to reduce piston side force, by closely adhering to the thrust side and limiting lateral secondary motions. Hence, piston friction is expected to be reduced, by reducing the chance of high impact forces. (Nakayama *et al*, 2000) modified a single cylinder engine to have a crankshaft offset and piston frictional force was measured in real time, using a floating liner method. In addition, Laser Induced Fluorescence (LIF) technique was employed to measure oil film thickness on the piston skirt area, and gap sensors were used to measure piston motion. In accordance with the measurement results, crankshaft offset changed piston slap

---

---

motion. Hence, the conditions of piston skirt contact and oil film development changed, in addition to changes in piston side force. These affected the piston friction characteristics. Crankshaft offset decreased piston friction during the expansion stroke, while in the compression stroke it was same, but increased the piston side force only slightly. Additionally, piston skirt tilt angle at TDC was reduced with respect to the cylinder wall by the crankshaft offset. Thus, a wider area of upper piston skirt contacted the cylinder wall and helped develop a coherent oil film and reduce friction.

(Cho *et al*, 2003) presented an analytical method to investigate the effects of crankshaft offset over the engine friction. In their study mathematical models were used for evaluating the friction level for all engine parts. The model was tested by off-setting the crankshaft axis towards the thrust side. The magnitude of piston acceleration and external forces acting on it and on the crank pin were affected by the offsetting. Thus, such changes directly affected the dynamics and the tribological characteristics of engine moving parts. In their mathematical model the journal motion within the engine bearing was described by a non-linear equilibrium equation. However, the crankshaft system was supported by the main engine bearings, which are statically indeterminate. It was, therefore, difficult to determine an accurate bearing load. The steady-state form of Reynolds equation was used as the governing equation for lubrication analysis, assuming that the engine bearing was operating in the fully hydrodynamic regime of lubrication. Long bearing approximation was used for piston ring – skirt interactions, while two-dimensional mixed lubrication was considered for the piston skirt – cylinder wall interactions.

Cho *et al* also observed an increase in the piston side force at the anti-thrust side during the compression stroke, while it decreased during the expansion stroke at the thrust side with the crankshaft offset. There was a crank offset to minimize the mean side force, but its value was found to be very much dependent on the engine speed. As the engine speed was increased, the amount of offset to minimize the mean side force was decreased, and it was noted that the crank offset had a good effect on the side force reduction at low engine speeds.

## 3 MULTI-PHYSICS MODELLING

### 3.1 Introduction to Multi-Physics Modelling

The engine system defined in this thesis consists of piston, connecting rod, crankshaft and flywheel, which are subjected to various excitation forces dominated by the combustion gas force, and the transmitted resisting torque. Modern engine development is dominated by certain requirements. The most important of these is improved efficiency, which is mainly sought by reduction of mechanical and frictional losses. There are also significant thermal losses, which are not subject of investigation within this thesis, but thermal contributions to frictional behaviour in contacts has been taken into account. Mechanical losses are induced mainly by the inertial imbalance of components that are subjected to large rigid body motions. Fluctuating rotational velocities and eccentric motion of components lead to dynamic loadings in structural components. All the components in the engine are somewhat flexible and their deformations take place, which lead to vibration; another source of mechanical losses.

It is clear that a fundamental and interactive methodology must be developed to deal with the multi-physics nature of aforementioned phenomena. Clearly, Lagrangian dynamics is the appropriate methodology to deal with multi-body rigid-body dynamics of an assembly of parts, which are constrained together to ensure functional assurance. This approach forms the fundamental work reported in this thesis. The rigid-body approximation is good enough to calculate static forces acting on either slow moving or stationary bodies. However, when it comes to complicated and fast moving structures like engine assembly, which undergo large variation of forces within very small period of time, the behaviour of the system is more complex. A dynamic load differs from a static load, especially in two different respects. First, its magnitude, direction or point of application varies with time, whilst the resultant time varying deflection and stresses constitute the dynamic response. Of greater importance, the second aspect concerns the role played by the acceleration of components in structural dynamics problems. Figure 3.2(a) shows a cantilever beam under static loading. The deflection and internal stresses depend directly on load  $P$ . On the other hand, Figure 3.2(b) shows a similar cantilever subjected to time varying load  $P(t)$ . The acceleration of the beam

---

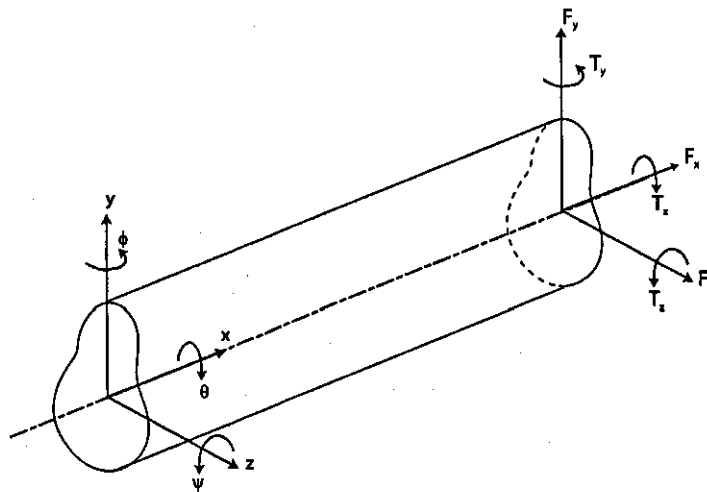


Figure 3.1 Euler Beam

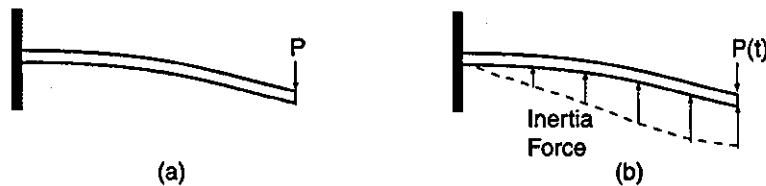


Figure 3.2 A cantilever beam under Static(a) and Dynamic(b) loading

gives rise to a distributed inertial force. If the inertial force contributes significantly to the deflection and internal stresses in the structure, then investigation of dynamic behaviour (i.e. transient response) is required.

Thus, the inclusion of elastic behaviour of certain system components in the dynamics analysis is critical to investigate the resulting vibration and noise phenomena. This can be achieved in a number of ways: the simplest form being the use of Euler beams to represent elastic behaviour of the system components, as the first approximation (see Figure 3.1). In this case the mass and the inertial properties are discretised as lumped parts, interconnected by Eulerian beams. This approach is known as the Transfer Matrix Method (TMM), and its accuracy improves with progressive discretisation. The beam elements are represented by stiffness matrices, providing a relationship between the relative displacements of the end of the beam in all six degrees of freedom motion with the applied forces and moments (Rahnejat 1998). Determination of damping is quite difficult, but it is usually (for convenience) introduced as a percentage of the stiffness and mass matrix coefficients. Following the experimentally obtained value of 0.7% for the damping ratio as given in equation (6.8) the

---

damping ratio of 1% is used for convenience, for all flexible components in the model as it makes little difference to the calculated outcome. Another approach can be by analytical determination of the component flexibility, taking into consideration the various modal behaviours, such as in axial, bending and torsional deformations. The resulting stiffness matrix can then be obtained by combination of various contributing modal responses. This approach has been highlighted by (Okamura *et al*, 1990) as Dynamic Stiffness Matrix Method (DSMM) and successfully applied to engine dynamics problems (Okamura and Morita 1999). Whichever the method of elemental discretisation, it is very important to progressively capture higher number of modes of vibration with increasing input energy into the system. Therefore, the most suited approach would be to employ finite element analysis with Lagrangian dynamics, which, in combination, may be referred to as elastodynamics and Figure 3.3 shows the elastodynamics engine model.

With the growing trend in reducing losses due to inertial imbalance, the modern engines are manufactured with light weight and compact components. The trend in reducing the mass and improving stiffness augments the range of effective natural frequencies of interest. A large number of elements would normally be required in order to capture high frequency structural modal responses of the system components. This increases the size of the stiffness and mass matrix in the FEA that render the necessary time-marching analysis computationally impossible or extremely time and memory intensive. Thus, the suitable approach is to undertake finite element modal analysis by inclusion of sufficient number of elements of suitable type with experimental verification and select the modal responses at frequencies of interest to include in the multi-body analysis. This approach is known as the Craig-Bampton Component Mode Synthesis (CMS), which will be discussed in greater detail later.

Once the desired modal responses are included in the form of the suitably reduced mass and stiffness matrices into the Lagrangian dynamics analysis, the elastodynamics behaviour of the system can be simulated under given excitations such as the application of variable combustion gas force. This approach provides both the rigid body dynamics and structural dynamics responses of the system. All the above methodology and their fundamental basis, as well as their development is outlined in this chapter.

The mathematical model discussed here includes the kinematic relations, which describe the motion of system linkages. In this model these variations are in the range of metres or radians

---

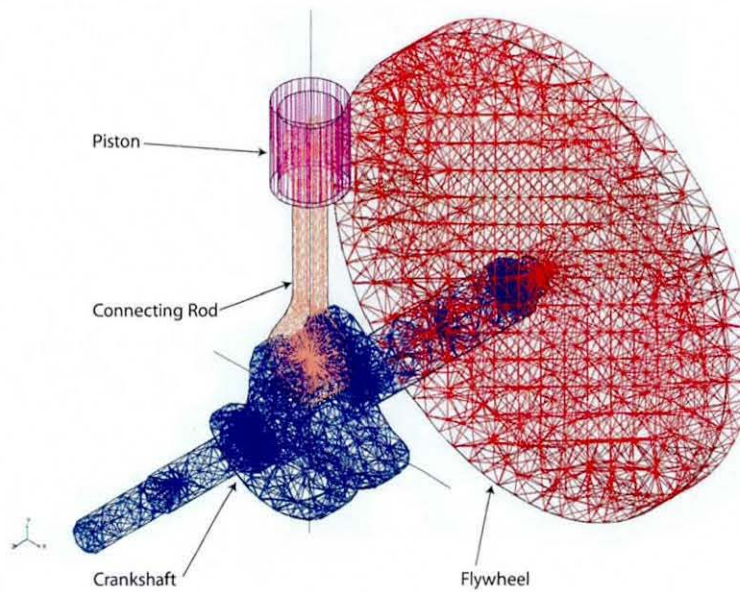


**Figure 3.3 Multi Body system of Piston Crankshaft assembly**

of rotation. On the other hand, the model also handles flexible bodies with deformations in the range of fractions of a millimetre. Of course the variation within the lubricated contacts (both in terms of localised deformation of mating parts and small movements in oil film thickness) is in the micrometer range. Thus, model analysis is on a multi-scale basis.

Perhaps the most demanding step in any dynamic analysis is the creation of a representative and realistic mathematical model of the system. Analytical models fall into two basic categories; *continuous models* and *discrete parameter models*. The number of displacement quantities, which must be considered in order to represent the effects of all significant inertial forces is called the *number of degrees of freedom* (DOF) of the system. Thus, a continuous system represents infinite DOFs. The discrete parameter models shown here are called the *lumped mass models*, because the mass of the system is assumed to be represented by a small number of point masses or particles. Complex systems are converted into lumped mass models (or discrete parameter models), which makes the calculations easier and more efficient.

Multi-body systems consist of parts held together by joints, couplers, gears, bearings and generally elements, which introduce constraints against the various motions of parts attached to them. Therefore, numerical modelling of multi-body systems requires the formulation of mathematical models for the whole set of different constraints. Joints such as spherical,

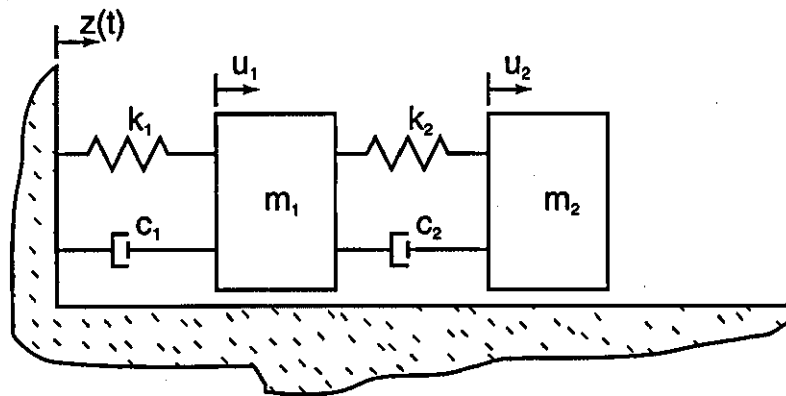


Figure 3.4 Two Degree Of Freedom system

universal, revolute and translational can be categorised in terms of lower level of constraint primitives. These constraint primitives in turn introduce the reactive forces and moments that are responsible for the enforcement of the constraining functions.

Once these numerical constraints are developed, it is possible to apply physical laws like the Newton's law, stress-strain relationships, etc to obtain the differential equations of motion which describe the analytical model, in mathematical language. A continuous model leads to a partial differential equation, while a discrete parameter model leads to ordinary differential equations. These mathematical models can be obtained using Newton's laws or the Lagrange's equation. The methods highlighted in this thesis are devoted to the use of constrained Lagrangian dynamics, which forms the basis of the multi-body approach.

## 3.2 Mathematical Model For Multi-Body Dynamic System

### 3.2.1 Multi-Degree of Freedom System

Although SDOF models may adequately describe the dynamical behaviour of some systems, in most cases it is necessary to employ more advanced models like MDOF models. For example, the dynamic behaviour of the continuous model shown in Figure 3.2 (b) is adequately described by a SDOF model, if the forcing function  $P(t)$  is a slowly varying function of time. The dynamic analysis of most real structures is based on MDOF systems. The equation of motion for the configuration shown in Figure 3.4 can be written in matrix form as follows, where:  $w = u - z$ , Either Newton's law or energy methods can be used to obtain this equation.

$$\begin{pmatrix} m_1 & 0 \\ 0 & m_2 \end{pmatrix} \begin{Bmatrix} \ddot{w}_1 \\ \ddot{w}_2 \end{Bmatrix} + \begin{pmatrix} (c_1 + c_2) & -c_2 \\ -c_2 & c_2 \end{pmatrix} \begin{Bmatrix} \dot{w}_1 \\ \dot{w}_2 \end{Bmatrix} + \begin{pmatrix} (k_1 + k_2) & -k_2 \\ -k_2 & k_2 \end{pmatrix} \begin{Bmatrix} w_1 \\ w_2 \end{Bmatrix} = \begin{Bmatrix} -m_1 \ddot{z} \\ -m_2 \ddot{z} \end{Bmatrix} \quad (3.1)$$

In mathematical language this can be written as,

$$m\ddot{w} + c\dot{w} + kw = p_{eff} \quad (3.2)$$

Where  $P_{eff}$  is the external force.

The use of Newton's law to derive such an equation is rather a difficult task, if a mechanism has a large number of kinematic relations, because all the independent variables should relate to each other by kinematic relations. Therefore, the task of deriving equations of motion for MDOF systems is greatly simplified by the Lagrange's approach.

### 3.2.2 Lagrange's equation for multi body dynamics system

The main difficulty in the use of Newton-Euler method in deriving equations of motion for connected bodies is the need to determine all the kinematic relations together with separate freebody diagrams for each inertial component. However, the principle of virtual displacements eliminates the necessity of using forces of interaction directly. Although the principle of virtual displacements can be extended to permit the derivation of equations of motion of MDOF systems, it is far easier to use the Lagrange's equations for this purpose. Lagrange's equation can be derived either from the principle of virtual displacements or from Hamilton's principle, which is given as (Craig 1981):

$$\delta \int_{t_1}^{t_2} (T - V) dt + \int_{t_1}^{t_2} \delta W_{nc} dt = 0 \quad (3.3)$$

The motions of bodies are generally constrained to move in a predetermined manner. Thus, the coordinates of such bodies have to be connected with kinematic constraints in order to determine the coordinates in terms of the generalized equations. The kinematic equations used for this purpose are called *equations of constraint*, which are usually algebraic functions. Each one of these general coordinates should be able to vary while keeping all other generalized coordinates constant. For an N-DOF system, the *generalized coordinates* are

defined as any set of  $N$  independent quantities, which are sufficient to completely specify the position of every point within the system.

The multi-body engine model is a constrained non-linear dynamics model, incorporating the elastic behaviour of the engine components such as connecting rod, crank, etc. As previously mentioned, this model is created in ADAMS, a multi-body dynamics code developed by MSC Software. The code is based on automatic generation of the equations of motion, for each part of the engine assembly, based on constrained Lagrangian dynamics (Lagrange 1788), and using generalized Eulerian body 3-1-3 frame of reference. If the generalized coordinates are denoted by,  $\{q_j\}_{j=1 \rightarrow 6} = \{x, y, z, \psi, \theta, \phi\}^T$ , then:

$$\frac{d}{dt} \left( \frac{\partial T}{\partial \dot{q}} \right) - \frac{\partial T}{\partial q} + \frac{\partial V}{\partial q} + \sum_{n=1}^m \lambda_n \frac{\partial C_n}{\partial q} = Q_{nc} \quad (3.4)$$

For most mechanical and structural systems the kinetic energy can be expressed in terms of generalized coordinates and their first time derivatives as shown in equation (3.5).

$$T = T(q_1, q_2, \dots, q_n, \dot{q}_1, \dot{q}_2, \dots, \dot{q}_n, t) \quad (3.5)$$

The term  $\frac{\partial T}{\partial \dot{q}}$  is the conjugate momentum in the co-ordinate direction  $q$ , for instance consider the translational motion in  $x$ , then the kinetic energy  $T = \frac{1}{2} m \dot{x}^2$  and  $\dot{q} = \dot{x}$ , then the momentum can be given as  $M_x = \frac{\partial T}{\partial \dot{x}} = m \dot{x}$ . This is also true for all other translational degrees of freedom, where  $q = y$  or  $z$ . For rotational degrees of freedom, given by the Euler angles  $\psi, \theta, \phi$  which are: first rotation about z-axis, second rotation about the new x-axis, final rotation about the new z-axis respectively, the kinetic energy  $T = \frac{1}{2} I \dot{\psi}^2$  and momentum  $M_\psi = I \dot{\psi}$ . The rate of change of momentum (translational or rotational) provides the inertial force. Therefore:

$$\frac{d}{dt} \left( \frac{\partial T}{\partial \dot{q}} \right) = \frac{d}{dt} (m \dot{q}) = m \ddot{q} \quad (3.6)$$

for  $q = x, y$  or  $z$  and,

$$\frac{d}{dt} \left( \frac{\partial T}{\partial \dot{q}} \right) = \frac{d}{dt} (I\dot{q}) = I\ddot{q} \quad (3.7)$$

For  $q = \psi, \theta$  or  $\phi$

Thus, the first term on the LHS of the Lagrange's equation (3.4) is the inertial force. When the coordinates have been chosen properly in-line with the directions of motion, then  $\frac{\partial T}{\partial q} = 0$ , since the kinetic energy is not a function of displacement. The kinetic energy for a rigid body system can be represented using vector notation as follows:

$$T = \frac{1}{2} \begin{bmatrix} \dot{q}_t^T & \dot{q}_r^T \end{bmatrix} \begin{bmatrix} m_{tt} & m_{tr} \\ m_{rt} & m_{rr} \end{bmatrix} \begin{bmatrix} \dot{q}_t \\ \dot{q}_r \end{bmatrix} \quad (3.8)$$

Where subscripts  $t$  represents translational displacements and  $r$  represents rotational displacements. Middle term of the RHS of the equation represents the mass matrix.  $m_{tt}$  is the translation mass,  $m_{tr}$  is the coupled translational and rotational mass and  $m_{rr}$  is the rotational mass. However, a greater simplification of the mass matrix of equation (3.8) can be achieved if the origin of the body reference is attached to the mass centre of the body (see (Shabana 1998)) such that the  $m_{tr}$  term becomes zero. Therefore, for simplicity and to eliminate the inertia coupling between the translation and rotation of the body reference, the origin of the rigid body reference is often attached to the centre of mass of the body.

$$V = V(q_1, q_2, \dots, q_n, t) \quad (3.9)$$

The potential energy, which includes both strain energy and the potential energy of any conservative external forces, can be expressed in terms of the generalized coordinates alone as shown in equation (3.9). The term  $\frac{\partial V}{\partial q}$  is the rate of change of potential energy with respect to displacement. For rigid inertial parts,  $V$  is the potential energy, whilst for flexible members this represents the stored strain energy. In any case, Euler has shown that:

$$F_q = \frac{-\partial mgz}{\partial z} = -mg$$

And the negative sign indicates the direction of gravity. In case of a flexible member such as a spring the stored strain energy is  $\frac{1}{2}kx^2$ , then :

$$F_q = -\frac{\partial\left(\frac{1}{2}kx^2\right)}{\partial x} = -kx$$

Which is the restoring force.

### 3.2.3 Generalized Forces

The virtual work of generalized forces,  $Q_1, Q_2, \dots, Q_n$  as they act through virtual displacements caused by arbitrary variations in the generalized coordinates, can be expressed as a linear function of those variations as shown in (3.10).

$$\delta W = Q_1 \delta q_1 + Q_2 \delta q_2 + \dots + Q_n \delta q_n \quad (3.10)$$

The forces acting on a system are twofold: the elastic restoring forces and other external forces. Elastic forces can be restored by reversing the motion and thus they are considered as conservative forces. External forces are non-conservative. Therefore, the total work done on a system can be represented as:

$$\delta W = \delta W_c + \delta W_{nc} \quad (3.11)$$

It is important to mention that these conservative forces give rise to potential energy and if the potential energy is taken into consideration for Lagrange's equation, then the virtual work component due to conservative forces is neglected in the calculation of the generalized forces. Even though the development of virtual work is essential for particles, it can easily be extended to the case of rigid bodies. Thus, these elastic restoring forces and other applied forces can be transformed to the Euler's generalized coordinates by the application of the *principle of virtual work* that can be written as:

$$\delta W = F^T \delta r_p \quad (3.12)$$

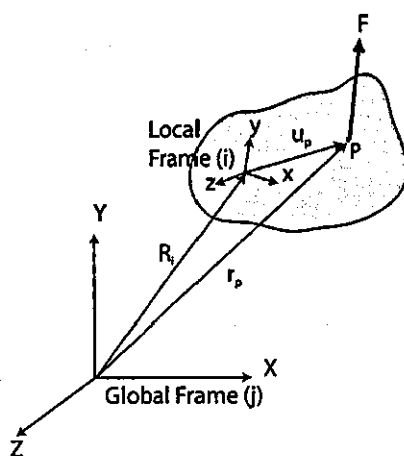


**Figure 3.5 Generalized forces acting on a rigid body**

Where  $F$  is the forcing function applied on the body and  $r_p$  is the position vector to the point of application of the force  $F$  as shown in Figure 3.5. Then, the virtual work due to the application of force can be given in more explicit form (Shabana 1998),

$$\delta W = F^T \begin{bmatrix} I & A_j u_p \end{bmatrix} \begin{bmatrix} \delta q_t \\ \delta q_r \end{bmatrix} = \begin{bmatrix} F^T & F^T A_j u_p \end{bmatrix} \begin{bmatrix} \delta q_t \\ \delta q_r \end{bmatrix} \quad (3.13)$$

Where  $I$  is an identity matrix and  $A_j$  is the transformation matrix from the local frame of reference ( $i$ ) to the global frame of reference ( $j$ ) given by:

$$[A_j] = \begin{bmatrix} \cos \psi \cos \phi - \sin \psi \cos \theta \sin \phi & -\cos \psi \sin \phi - \sin \psi \cos \theta \cos \phi & \sin \psi \sin \theta \\ \sin \psi \cos \phi + \cos \psi \cos \theta \sin \phi & -\sin \psi \sin \phi + \cos \psi \cos \theta \cos \phi & -\cos \psi \sin \theta \\ \sin \theta \sin \phi & \sin \theta \cos \phi & \cos \theta \end{bmatrix} \quad (3.14)$$

Where  $\psi, \phi$  and  $\theta$  are the Euler angles and  $u_p$  is the position vector of point  $P$  in the local frame of reference. Then, the equation (3.13) can be written in a more simplified form as:

$$\delta W = \begin{bmatrix} Q_t^T & Q_r^T \end{bmatrix} \begin{bmatrix} \delta q_t \\ \delta q_r \end{bmatrix} \quad (3.15)$$

Where  $Q_t$  and  $Q_r$  are the generalized forces associated with the generalized translational and rotational coordinates, respectively. This implies that a force acting on an arbitrary point  $P$  is

equivalent to a force that has the same magnitude acting at the origin of the body frame of reference and a moment acting on the same body.

### 3.2.4 Constraining Reaction Forces

The first three terms on the LHS of the equation (3.4) deal with inertial, body and restoring or restraining forces, respectively. The last term gives the reaction forces caused by the constraining elements. The RHS of the equation represents all the non-conservative forces. The  $n$  constraint functions for the different joints in the engine model are represented by holonomic and non-holonomic functions. Holonomic functions are displacement dependent constraints, such as the restriction of motion in a given direction; a revolute joint, which is time independent or a coupling joint of the crankshaft and camshaft according to a set ratio. These functions can be used to eliminate dependent coordinates of the system. Non-holonomic constraints restrict the kinematically possible values of velocities of the bodies of the system such as constant velocity motion. In a non-holonomic system, some coordinates may be independent, but their variations are dependent. These constraint functions can be represented in matrix form as follows (Rahnejat 1998):

$$\begin{bmatrix} C_k \\ \dot{q}_j \frac{\partial C_k}{\partial q_j} \end{bmatrix} = 0, \quad j=1 \rightarrow 6, \quad k=1 \rightarrow n \quad (3.16)$$

For instance, for a revolute joint there are 5 constraining functions (such that  $C_n$  in equation (3.4) gives 5 equations,  $n=5$ ). The term  $\frac{\partial C_n}{\partial q}$  provides the effect of the constraint in direction  $q$ . The reaction force in the direction  $q$  is given by  $\lambda_n \frac{\partial C_n}{\partial q}$ , where  $\lambda_n$  is the Lagrange multiplier. However, there may be many contributing reactions in a given direction, thus the summation mark in Lagrange's equation.

### 3.2.5 Kinematic System Development

In multi-body systems, kinematic constraint equations may exist because of mechanical joints or specified motion trajectories. The constraint equations of the multi-body system for a virtual displacement can be written as:

$$C_q \delta q = 0 \quad (3.17)$$

Where  $C_q$  represents the constraint Jacobian matrix. For holonomic systems, all system coordinates can be divided into a set of dependent coordinate  $q_d$  and a set of independent coordinates  $q_i$ . For instance, for the engine system shown above either  $\theta^2$  or  $R_x^4$  can be considered as the independent coordinates and the rest of coordinates can be considered as the dependent coordinates. Thus, the vector  $q$  of generalized coordinates can be partitioned and constraint equation can be written as:

$$C_{q_d} \delta q_d + C_{q_i} \delta q_i = 0 \quad (3.18)$$

Where  $C_{q_d}$  and  $C_{q_i}$  are the constraint Jacobian matrices associated with the dependent and independent coordinates respectively. If the constraints of equation (3.17) are linearly independent and  $C_{q_d}$  is non-singular, (where its inverse exists), the dependent coordinates can be written as:

$$\delta q_d = -C_{q_d}^{-1} C_{q_i} \delta q_i \quad (3.19)$$

The whole set of generalized coordinates can then be written in terms of independent coordinates as follows:

$$\delta q = \begin{bmatrix} \delta q_i \\ \delta q_d \end{bmatrix} = \begin{bmatrix} I \\ -C_{q_d}^{-1} C_{q_i} \end{bmatrix} \delta q_i = B q_i \quad (3.20)$$

Thus, the configuration or the state of a multi-body system, consisting of interconnected rigid bodies, for a given virtual displacement of independent variables can be obtained using equation (3.20).

### 3.2.6 Equations of Motion

The formulated kinetic energy for each body using equation (3.8) provides the inertial forces of the system. The virtual work formulated in equation (3.15) provides all conservative and non-conservative (body forces and external forces) generalized forces including damping forces in the system. The vector of non-linear algebraic constraints, describing mechanical

joints in the system as well as specified motion trajectories, provides the reaction forces in relevant locations. All these generalized forces, inertial forces and constraint reactions can be implemented in Lagrange's equation (3.4). Thus, the differential-algebraic set can be represented as follows (Orlandea *et al*, 1976; Rahnejat 1998):

$$\begin{bmatrix} \frac{d}{dt} \left( \frac{\partial T}{\partial \dot{q}} \right) - \frac{\partial T}{\partial q} & \left[ \frac{\partial C}{\partial q} \right]^T \\ \left[ \frac{\partial C}{\partial q} \right] & 0 \end{bmatrix} \begin{bmatrix} \dot{q}^T \\ \lambda^T \end{bmatrix} = [Q] \quad (3.21)$$

Where  $Q$  is the vector of generalized forces. The matrix in the above equation provides the coefficient of the unknown vector  $[\dot{q}^T \ \lambda^T]^T$  and is known as the Jacobian matrix  $[J]$ . In the engine model there are 109 constraints, thus there are 109 unknown Lagrange multipliers to be evaluated in each time step. There are also 16 rigid bodies including ground, which gives a total of 90 rigid body motions in the engine model, such that a total of 199 generalized coordinates ( $q$ ) to be calculated in each time step. Thus, there are 199 differential-algebraic equations to be solved simultaneously in each time step excluding the flexibility of parts. The use of Gruebler-Kutzbach equation (5.1) to calculate the total number of degrees of freedom is given in page 141.

The advantage of using constrained Lagrangian dynamics is that these equations are automatically generated by a code such as ADAMS. The disadvantage of the method of automatic generation of equations is that many equations are set, where the given direction is already constrained, resulting in a very large Jacobian matrix, which is further filled with zero entries to form a square Jacobian matrix. The advantage of the method, however far outweighs this disadvantage, because otherwise the equations of motion must be derived analytically through the Newton-Euler method, by breaking the system into a number of free-body diagrams and specifying all reactions accurately, a procedure which is prone to possible errors, when a very complex system such as the current model is considered.

### 3.3 Component Flexibility

For multi-body systems consisting of interconnected rigid bodies, kinetic equations can be used to develop general formulations for the dynamic differential equations of motion. In

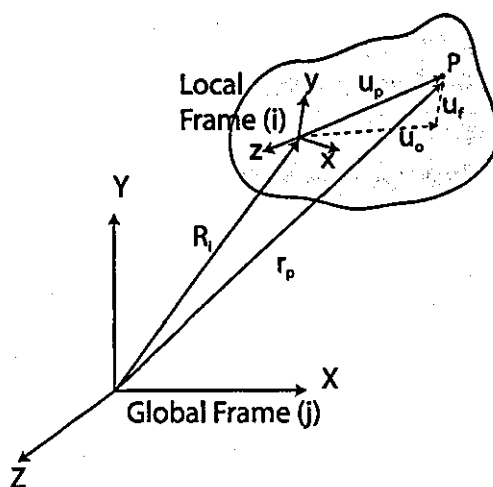


Figure 3.6 Deformable body coordinates

rigid bodies it is considered that the distance between two arbitrary points on the body remains unchanged during any form of applied force. Thus, the force can be considered as producing a linear acceleration for the whole body together with an angular acceleration about its centre of mass as shown in section 3.2.3. In elastic bodies, while the body is moving with respect to the global frame of reference according to the kinematic relations, the particles inside the body move with respect to its inertial frame of reference according to its elastic compliance. Therefore, the dynamic equations of motion for a rigid multi-body dynamics system can be defined in terms of the mass of the body, the inertial tensor and the generalized forces acting on the body in terms of reference coordinates, as discussed in the above sections. However, in a deformable body there is an elastic deformation other than the body (reference) motion. Thus, the configuration of each deformable body in a flexible multi-body system is identified by using two sets of coordinates, *reference* and *elastic*. Reference coordinates define the location and orientation of a selected body reference, while the elastic coordinates describe the elastic deformation with respect to the body reference. Thus, the position vector of any point within a body can be given as follows for a rigid body (see Figure 3.6):

$$r_p = R_j + A(u_0 + u_f) \quad (3.22)$$

Where  $u_f$  is the displacement due to elastic deformation, which can be given as a combination of shape functions in consistent mass formulation or shape vectors that can be obtained either experimentally or mathematically (i.e. mode shapes).

### 3.3.1 Finite Element Analysis

In Finite element analysis a continuous flexible body is represented by a collection of interconnected beams or elemental regions, with specified constitutive relations. A 3-dimensional Bernoulli-Euler beam element in the body can be subjected to transverse, bending and torsional motions, according to the forces applied on the body. The stiffness and mass matrices for the beam element can be obtained using the beam theory considering assumed shape functions as described in (Craig 1981). This mass matrix is called the *consistent mass matrix*, as the same shape functions are used to obtain both the mass and stiffness matrices. This leads to a coupling between translational coordinates and rotational coordinates in the mass matrix, which creates difficulties in solving the mesh for mode shapes. This problem can be eliminated by using the lumped mass model, which simply assumes that the mass of the beam element is purely concentrated on its two end points, which are nodal points of the mesh and these mesh points are connected by a spring, which has a spring constant depending on the material parameters. These nodal displacements can be transformed from the local coordinate system to the global coordinate system using the transformation matrix  $T$ . Then, the forces associated with nodes can easily be transformed into the global system using the virtual work approach, thus:

$$F_g = T^T F_l \quad (3.23)$$

Where  $F_g, F_l$  represent forces in the global and the local coordinate systems respectively. In a similar manner using the potential energy, the stiffness matrix in global coordinates can be obtained as:

$$k_g = T^T k_l T \quad (3.24)$$

where: subscripts  $g$  and  $l$  represent the global and local systems. Transformation for the mass matrix can be obtained using the kinetic energy as:

$$m_g = T^T m_l T \quad (3.25)$$

These matrices can be assembled in such a way that system force, stiffness and mass matrices can be formed. Then, the component stiffness and mass matrix becomes:

$$K = \sum_{i=1}^{n_e} L_i^T k_{gi} L_i \quad (3.26)$$

And:

$$M = \sum_{i=1}^{n_e} L_i^T m_{gi} L_i \quad (3.27)$$

Where  $n_e$  and  $L_i$  are the number of elements in the component and locator matrix as described in (Craig 1981), respectively.

### 3.3.2 Boundary Conditions

Dynamic analysis requires boundary conditions to be stated, so that components can be connected to each other applying an appropriate synthesis technique. When a flexible body is constrained certain displacements are inhibited, the most straight-forward procedure for enforcing such a condition is to partition the system into independent or active degrees-of-freedom ( $u_i$ ) and dependent or constrained degrees-of-freedom ( $u_d$ ), as shown below;

$$\begin{bmatrix} m_{ii} & m_{id} \\ m_{di} & m_{dd} \end{bmatrix} \begin{Bmatrix} \ddot{u}_i \\ \ddot{u}_d \end{Bmatrix} + \begin{bmatrix} k_{ii} & k_{id} \\ k_{di} & k_{dd} \end{bmatrix} \begin{Bmatrix} u_i \\ u_d \end{Bmatrix} = \begin{Bmatrix} f_i \\ f_d \end{Bmatrix} \quad (3.28)$$

These can be obtained by partitioning component stiffness matrix (3.26) and mass matrix (3.27) and the force vector (3.23). For instance, if  $u_d = 0$  due to imposed constraint conditions, then the equation (3.28) can be written as:

$$m_{ii} \ddot{u}_i + k_{ii} u_i = f_i \quad (3.29)$$

Then, this equation can be solved for the eigenvalues and the corresponding eigenvectors, giving the natural frequencies and mode shapes of the component (flexible body) under the specified boundary conditions. Free-free normal modes can be obtained by equation (3.28), simply putting the external force vector as zero, where no coordinates are constrained to the body.

### 3.3.3 Modal Transformation

The discretisation of a component into a finite element (FE) model represents an infinite number of degrees of freedom with a finite, but very large number of finite element degrees of freedom. The most important aspect of the FE analysis in dynamics problem, as outlined in section 3.3.1, is that it can take into consideration small linear elastic deformations of the flexible body relative to the local frame of reference. These elastic deformations or shape vectors are the eigen-vectors of the body obtained, using equation (3.28). So that the linear elastic deformations of the nodes can be given as a linear combination of shape vectors as:

$$u_f = \sum_{i=1}^{n_m} \phi_i q_{mi} = \Phi q_m \quad (3.30)$$

Where  $n_m$  is the number of mode shapes, and the scalar factors of amplitudes  $q_m$  are the modal coordinates and modes  $\phi_i$  are included in the columns of the modal matrix,  $\Phi$ . A reduced order model can be achieved by solving only for  $n_m$  mode shapes, where  $n_m < n_e$ . This concept is called *modal superposition* which means that the behaviour of a component with a very large number of nodal DOFs can be captured with a much smaller number of modal DOFs. The  $n_m$  mode shapes should be selected such that a good approximation of a pre-determined frequency area of mode shapes is included.

### 3.3.4 Component Mode Synthesis

The modal transformation method described above can be used to transform a larger set of physical coordinates  $u_f$  to a smaller set of modal coordinates  $q_m$ . In large scale multi-body dynamics problems it is necessary to reduce the number of coordinates in this manner, if a solution is to be obtained within a reasonable time. The Component Mode Synthesis is used to couple all the sub-structures in the multi-body system in order to obtain a dynamic response. The determination of the modal mass matrix  $M$  can be achieved according to the Craig-Bampton (Craig and Bampton 1968) reduction method, which is one of the most general methods for *Component Mode Synthesis* technique.

In this technique the component is basically divided into two sets of DOFs. First, there are the boundary DOFs ( $u_d$ ), which are not subjected to modal superposition. These are the nodes

which are used to connect one body to another in structural coupling. Thus, these are dependent on the other member of the assembled system. Second set of DOFs are the interior DOFs ( $u_i$ ) which are subjected to modal superposition. These are the independent DOFs.

Additionally, two sets of mode shapes are defined as follows:

1. The **Constrained Modes** ( $q_c$ ) are static shapes that are obtained by giving each of the boundary degrees of freedom a unit displacement, while holding all other boundary degrees of freedom fixed. There is a one-to-one correspondence between the modal coordinates of the constrained modes and the displacement in the corresponding boundary degrees of freedom,  $q_c = u_d$ . These modes can be obtained by setting  $f_i$  to zero and  $u_d$  as an identity matrix of an order equivalent to the number of boundary DOFs in equation (3.28).
2. The **Fixed Boundary Normal Modes** ( $q_n$ ), which are obtained by fixing the boundary degrees of freedom and computing a solution for the eigen-value problem. These modes can be obtained by setting  $f_i$  to zero and  $u_d$  to a zero matrix, as all the boundary DOFs are fixed in equation (3.28). These modes define the modal expansion of the interior degrees of freedom.

The relationship between the physical degrees of freedom, the Craig Brampton modes and their modal coordinates is expressed as:

$$u = \begin{bmatrix} u_d \\ u_i \end{bmatrix} = \begin{bmatrix} I & 0 \\ \phi_{ic} & \phi_{in} \end{bmatrix} \begin{bmatrix} q_c \\ q_n \end{bmatrix} = \psi q \quad (3.31)$$

where:  $\phi_{ic}$  are the physical displacements of the interior degrees of freedom in the constrained modes, and  $\phi_{in}$  are the physical displacements of the interior degrees of freedom in the normal modes. The first column of the matrix  $\psi$  represents the constrained modes and the second column represents the fixed normal modes. The modal superposition, as described in section 3.3.3, can be used in matrix  $\phi_{in}$  to reduce the number of modal coordinates accordingly.

The component generalized stiffness ( $k_{cg}$ ) and mass ( $m_{cg}$ ) matrices are obtained through the following transformations:

$$k_{cg}^l = \psi^{lT} k^l \psi^l = \begin{bmatrix} I & \phi_{ic} \\ 0 & \phi_{in} \end{bmatrix}^l \begin{bmatrix} k_{dd} & k_{di} \\ k_{id} & k_{ii} \end{bmatrix}^l \begin{bmatrix} I & 0 \\ \phi_{ic} & \phi_{in} \end{bmatrix}^l \quad (3.32)$$

$$m_{cg}^l = \psi^{lT} m^l \psi^l = \begin{bmatrix} I & \phi_{ic} \\ 0 & \phi_{in} \end{bmatrix}^l \begin{bmatrix} m_{dd} & m_{di} \\ m_{id} & m_{ii} \end{bmatrix}^l \begin{bmatrix} I & 0 \\ \phi_{ic} & \phi_{in} \end{bmatrix}^l \quad (3.33)$$

where the superscript  $l$  represents the component number. It is shown that the use of constrained modes leads to an uncoupled stiffness matrix  $k_{cg}^l$  in the component generalized coordinates (Craig 1981). Constraint compatibility as discussed in section 3.2.5 in equation (3.20) for a rigid multi-body system is used to synthesize the system stiffness matrix ( $K$ ) and the mass matrix ( $M$ ), which are used in the Lagrange's equation of motion such as:

$$K = B^T k_{cg} B \quad (3.34)$$

Where:  $k_{cg}$  is the component generalized stiffness for all components in the system, and:

$$M = B^T m_{cg} B \quad (3.35)$$

Where:  $m_{cg}$  is the component generalized mass for all the components in the system and  $B$  is the transformation matrix (see (Craig 1981)).

### 3.3.5 Creation of Flexible Bodies

In the engine model the crankshaft, connecting rod and flywheel are modelled as flexible bodies. As it is explained in section 5.4.1, the experimental results show that the first natural frequency of the piston is 9000Hz. However significant engine order excitations are starting from 15Hz which is the half engine order and goes up to about 500Hz. Therefore with such low excitation frequencies it is difficult to excite modes of natural frequencies of 9000Hz and thus components with higher first natural frequencies such as piston are included into the model as rigid bodies. Four noded, three-dimensional tetrahedral elements have been used in the super-element creation. The number of elements and their size has been kept large enough



**Figure 3.7 Super-element Crankshaft – Mode shape for the frequency of 2704Hz (created using MSC/Nastran)**

so that the modes with complicated shapes can be captured efficiently. This has been verified by hammer testing (see section 6.3.1) of these components and comparing the obtained spectral content with those calculated. Boundary conditions for the meshed component have been applied according to the required functionality within the engine assembly. This has been achieved by placing a master node at each of the connecting points of the component with its neighbouring components, and rigidly connecting the master node with the slave nodes in the proximity area, which is referred to as RBE2 (Rigid Body Element) element in the MSC-Patran/Nastran. Since the master node's DOFs are independent, this node can be promoted as an attachment point and can be used as the connecting node to the neighbouring bodies.

The interested frequency area for this analysis is around 1000 Hz, as the prominent lowest excitation frequency remains around 20 Hz. A sufficient number of natural modes have been selected for the super-element creation, in order to obtain accurate results in the specified frequency area. There is no exact rule regarding the number of modes that one should keep in the super-element model. Although a general rule of thumb is that the number of modes

should cover at least twice the desired frequency area that should be kept. Consequently, each component includes a variety of modes, starting from low frequency bending behaviour and leading onto complicated shapes that are combination of bending, axial and torsional modes. As an example, a mode shape corresponding to the natural frequency of 2704Hz is shown in Figure 3.7.

### 3.4 Method of Formulation and Solution

Preceding sections discuss the use of energy method to formulate the equations of motion for a multi-body dynamics model, using Lagrange's equation for both rigid and flexible components. In the engine model developed there are rigid, as well as flexible components interconnected by constraints. As it is described in section 3.2.6 this differential-algebraic set of equations for the multi-body system model can be represented in the form given by equation (3.21), even for a system including flexible components. Thus, the general form of Lagrange's equation, which can deal with the aforementioned components can be stated as:

$$\frac{d}{dt} \left( \frac{\partial T}{\partial \dot{q}_j} \right) - \frac{\partial T}{\partial q_j} + \sum_{k=1}^n \lambda_k \frac{\partial C_k}{\partial q_j} = Q_{q_j} \quad (3.36)$$

Where  $Q_{q_j}$  represents applied forces on the system, including the conservative forces, and

$\{q_j\}_{j=1 \rightarrow 6} = \{x, y, z, \psi, \theta, \phi\}^T$  denotes the rigid body degrees of freedom, and

$\{q_j\}_{j=6 \rightarrow 6+n_m} = \{x, y, z, \psi, \theta, \phi, q_m\}^T$  denotes the flexible body degrees of freedom ( $q_m$  are the modal coordinates and  $n_m$  is the total number of  $q_m$  s)

Then, the Jacobian matrix can be formulated as given in equation (3.21) and this is a sparse matrix, where most of elements are zero (Rahnejat 1998). It also contains linear and non-linear algebraic equations and partial differential equations. Thus, the method of solution must be able to handle all the above simultaneously. The commercially available multi-body dynamics simulation code ADAMS is based on automatic generation of the equations of motion, using constrained Lagrangian dynamics, formulated in the generalized Eulerian 3-1-3

frame of reference. The compliance of flexible members is given by stiffness and damping matrices obtained during the super-element modal analysis outlined in section 3.3.4.

### 3.4.1 LU Decomposition (Cholesky Factorisation)

For a set of linear equations which has to be repeatedly solved with different homogenous terms, the LU decomposition is recommended (Orlandea *et al*, 1976; Rahnejat 1998). The LU decomposition represents the replacement of the Jacobian matrix given in equation (3.21) by a product of two triangular matrices, known as the lower and upper triangular matrices. In the lower triangular matrix all the non-zero elements occupy the diagonal elements or below it, whilst in the upper triangular matrix all such terms reside on or above the diagonal. Then:

$$[L].[U]=[J] \quad (3.37)$$

Where  $[J]$  is the Jacobian matrix. Thus, equation (3.21) can be written as:

$$[J].\{q \ \lambda\}^T = \{Q\} \quad (3.38)$$

The LU decomposition can be used to solve equation (3.38) as follows:

$$[J].\{q \ \lambda\}^T = ([L][U]).\{q \ \lambda\}^T = [L].([U].\{q \ \lambda\}^T) = \{Q\} \quad (3.39)$$

The above equation can be represented by a pair of equations. The first step is to solve for vector  $\{V\}$ , which can be found by:

$$[L].\{V\} = \{Q\} \quad (3.40)$$

Then, the second step is to solve:

$$[U]\{q, \lambda\}^T = \{V\} \quad (3.41)$$

These matrices are sufficient for the solution of a linear system. However, the set of equations in the multi-body system presented here have non-linear equations as well. These non-linear equations are solved using the Newton-Raphson method with Backward Differencing Method (BDF).

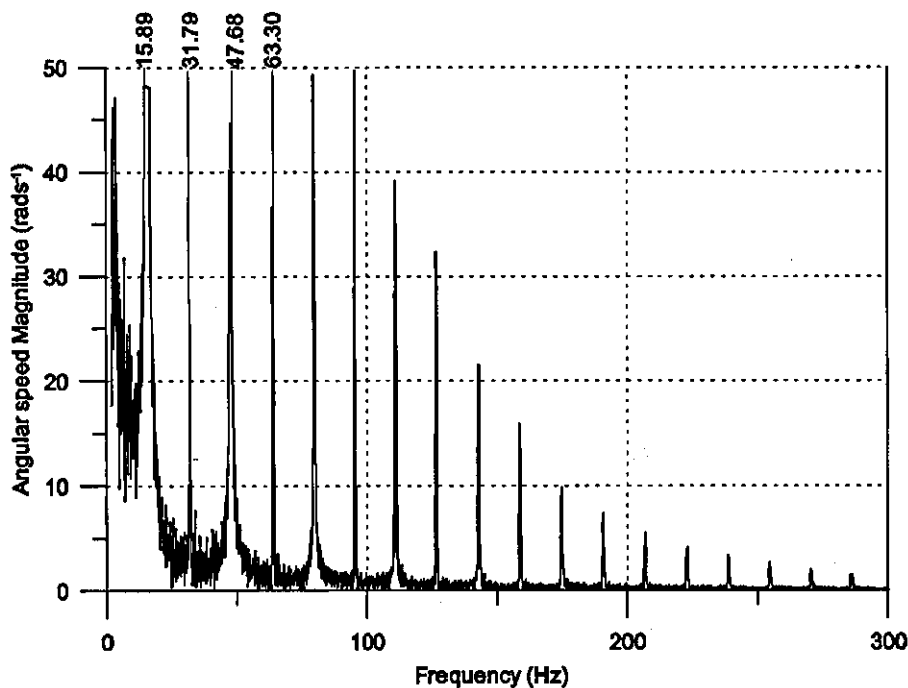


**Figure 3.8 FFT of Crank Angular Velocity for Rigid Engine Model**

As mentioned earlier, the Jacobian matrix contains differential equations of motion other than linear and non-linear algebraic equations. The non-linear differential equations can only be solved by numerical multi-step integration methods. The multi-body system of equations of motion is referred to as a stiff system, as it contains a system of equations, which provide slowly changing actual solution with another solution nearby rapidly changing. A certain class of integrators operate well on “stiff” equations. Gear (Gear 1971) has proposed a multi-step stiff integrator, which is used in ADAMS solver named “Gstiff” to solve a mix of linear, non-linear and differential equations, simultaneously. The procedure can be extended to a system including any number of components, unless limitations are imposed by computational power. MSC/Nastran is used for the super-element creation as described in previous sections. These components are then connected by the sub-structure coupling technique called Component Mode Synthesis, while imposing necessary joints such that the system behaves according to the required kinematic relations. Thus, this system can undergo non-linear constrained rigid body motions, while also undergoing displacements due to component flexibility.

Figure 3.8 and Figure 3.9 compare two models, one with rigid bodies only and the other including component flexibility. Fast Fourier Transformation (FFT) analysis of the crankshaft angular velocity variation for the rigid engine model is given in Figure 3.8. As the engine

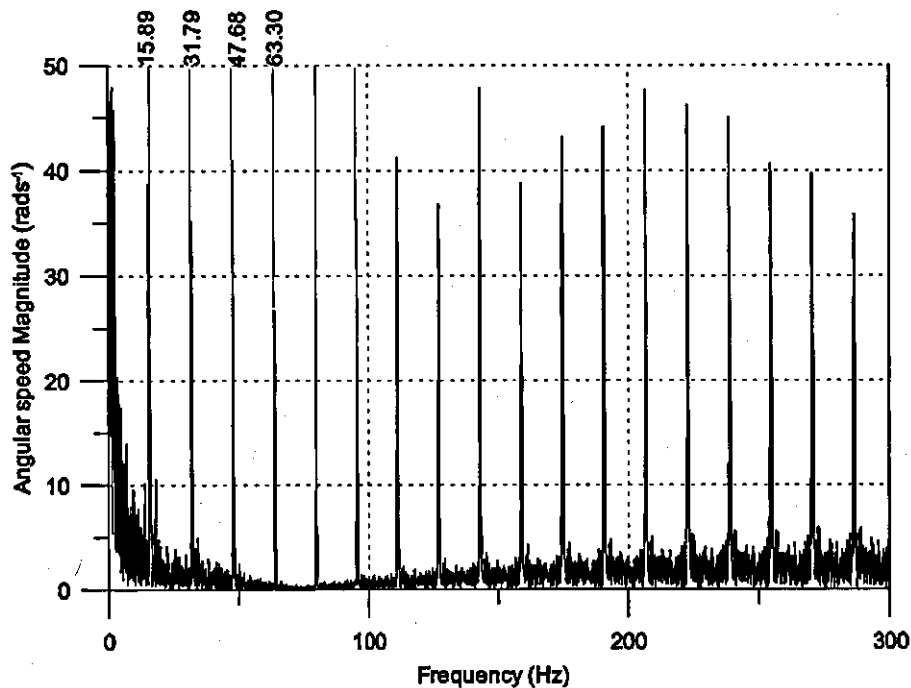


**Figure 3.9 FFT of Crank Angular Velocity for Flexible Engine Model**

speed is 1900 rpm, the first engine order excitations can be seen at 31.79 Hz. Also, the engine half-order excitations due to combustion gas force variation can be seen at 15.89 Hz. In the rigid model the engine excitations are progressively diminishing whilst harmonic orders are increased, where as in flexible model higher magnitudes can be seen even at higher frequency harmonics (see Figure 3.9).

The procedure outlined so far uses well developed and established methods to assemble the equations of motion and constrained functions into a mathematically understandable and solvable form. The solution greatly depends on the reliability of the numerical technique that has been used to solve the differential-algebraic set of equations. Basically, there are two types of errors involved in the numerical solutions of ordinary differential equations; the round-off errors and the truncation errors. The round-off error is caused by the limited number of significant digits used in the computation. The truncation error is caused by the approximate procedure used in computed function values, for instance in Euler's method. The truncation error is caused by the truncation of higher order derivative terms in the Taylor's series expansion. Again the truncation error can be divided into two categories; the local truncation error caused by the application of the method in one step, and the propagated

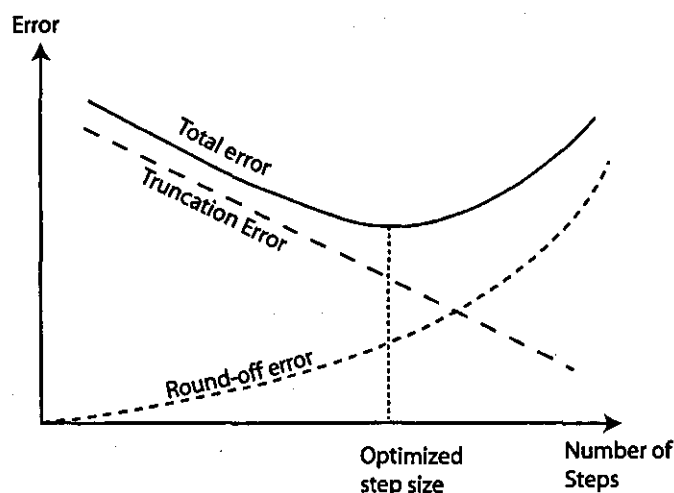


**Figure 3.10 Round-off and Truncation error  
(after (Rao 2002))**

truncation error caused by the accumulation of errors of the previous steps. The sum of these two gives the total truncation error (ref (Rao 2002)).

The truncation error in Euler's method can be reduced by using smaller step sizes. As the step size is reduced the number of steps to be used increases, thereby increasing the round-off error. Thus, the round-off error increases as the truncation error is reduced as shown in Figure 3.10. Although this figure shows that there is an optimum step size to minimise the total error, usually its value is not known before hand. Hence, in practice, for a given differential equation, a series of solutions, each with a smaller step size, can be generated until two successive step sizes give essentially the same solution.

Another important consideration in the numerical solution of differential equations is the numerical stability of the method used. In general, a numerical method is considered to be unstable if it gives an unbounded solution (errors grow at an exponential rate) for a problem for which the exact solution is bounded. The numerical instability occurs whenever the error propagates without bounds.

### 3.5 Engine Dynamics

The main objective of the thesis is to develop and demonstrate the multi-physics, multi-scale approach in dynamic analysis of multi-body systems. For the purpose of demonstration engine dynamics has been chosen. In particular, a single cylinder engine is used as example

for the investigations. Single cylinder engines are often used for developments and proof of concepts, such as the introduction of new technologies and analysis techniques, therefore the same approach is employed here. In dynamic analysis one objective is to understand the NVH characteristics of the engine, and the other is its efficiency with regard to minimization of the frictional and mechanical losses. Validation of any modelling method used in respect of NVH characteristics can be carried by comparing the results with closed form analytical solutions, as highlighted by (Rahnejat 1998). This approach is undertaken, and complemented later with experimental studies (see chapter 6).

### 3.5.1 Translational Inertial Imbalance

Among most of the engine parts the piston-connecting rod-crank sub-system can be regarded as the most important system in terms of dynamics. The basic function of this sub-system is to convert the reciprocating applied gas force into a rotational moment (torque) applied to the crankshaft. This system can be considered as one, having two degrees of freedom: rotation of the crankshaft and the reciprocating motion of the piston. The rotation of the crank is pre-determined by geometric constraints, thus is kinematic. Figure 3.11 shows a simple model of a single cylinder engine.

In order to yield a realistic solution from this simplified model the articulating mass of the connecting rod must be divided into two concentrated masses, one at the piston, which is purely translating, and the other at the crankshaft, which is purely rotating. Thus, the translating mass of the connected rod and the piston is given by  $m_1$  and the rotating mass of the connecting rod and crankshaft pin is given by  $m_2$  as shown in Figure 3.11.

The combustion force represented by  $F_c$ , induces a torque on the crankshaft equivalent to:

$$T_p = \frac{F_c d}{\cos\phi} \quad (3.42)$$

$d$  can be replaced by  $l_c$  and  $r_c$ , which are engine design parameters, and:

$$d = (l_c + r_c) \sin\phi_c \quad (3.43)$$

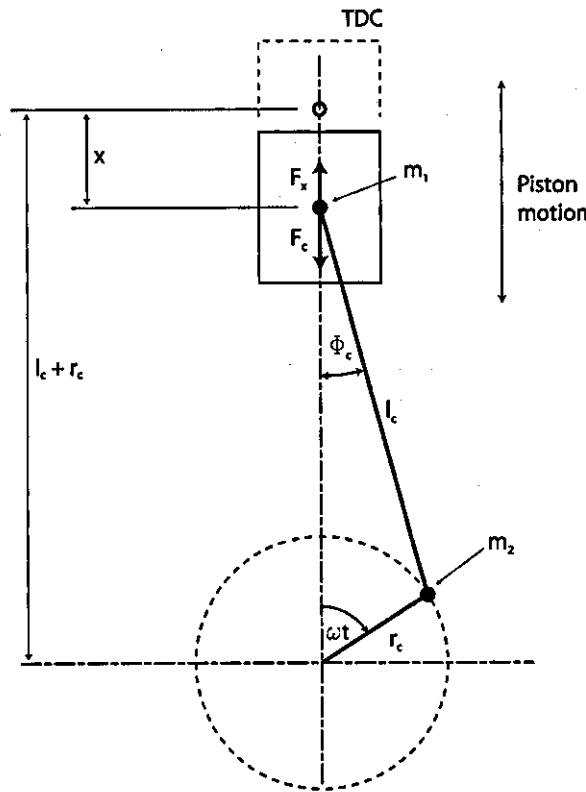


**Figure 3.11 Geometrical configuration of a single cylinder engine**

Therefore, the torque can be represented by:

$$T_p = (l_c + r_c) \tan \phi_c \times F_c \tag{3.44}$$

The acceleration of the translational imbalance mass  $m_1$ , gives rise to an inertial force  $F_x$ , in the direction of piston travel as shown in Figure 3.11. In turn the inertial force  $F_x$ , induces a torque,  $T_i$ , about the crankshaft. This torque, together with the power torque,  $T_p$ , is responsible for the twist-untwist motion of the crankshaft.

Referring to Figure 3.11, the simplified displacement of piston,  $x$  can be obtained using binomial expansion, and eliminating the higher order terms as shown in (Rahnejat 1998),

$$x = r_c (1 - \cos \omega t) + \frac{r_c^2}{2l_c} \sin^2 \omega t \tag{3.45}$$

The velocity and acceleration of the piston can then be obtained by successive differentiations of the above expression. Then, the inertial translational imbalance force can be given as:

$$F_x = m_1 r_c \omega^2 \left( \cos \omega t + \frac{r_c}{l_c} \cos 2\omega t \right) \quad (3.46)$$

Substituting the moment arm  $d$  (equation (3.43)) in terms of vertical distance between the instantaneous piston position and the crank centre, and assuming that  $\phi_c$  is small, and ignoring higher order terms, the induced inertial torque can be represented as:

$$T_i = \frac{1}{2} m_1 r_c^2 \omega^2 \left( \frac{r_c}{2l_c} \sin \omega t - \sin 2\omega t - \frac{3r_c}{l_c} \sin 3\omega t \right) \quad (3.47)$$

The practical implications of the above simplified analysis is that due to the translational imbalance introduced by the piston acceleration and the connecting rod articulation, there exists a vibration spectrum that contains all the multiples of engine orders ( $\omega, 2\omega, 3\omega, \dots$ ). The fact that the higher order terms do not appear in the final results here is due to the limited binomial expansion in the derivation process. These frequencies can easily be seen in the FFT of crank angular speeds shown in Figure 3.8 and Figure 3.9. However, it is clear that the influence from higher order terms is quite small compared with the effects from the first few engine order harmonics for a rigid body system. However, one should not ignore the higher order terms when considering flexible bodies, as a small excitation can be significant at resonant conditions.

### 3.5.2 Power Torque Fluctuations

The power torque fluctuations can be expressed as a Fourier series, based upon a complete engine cycle, which corresponds to a  $720^\circ$  degree crank angle rotation for a four-stroke engine. Therefore, the power torque  $T_p$  in equation (3.44) can be represented in the form of the  $k^{\text{th}}$  harmonic of the engine cycle frequency as in (Rahnejat 1998), thus:

$$T_{jk} = F_c^{jk} e^{ik(\omega t - \psi)/2} \quad (3.48)$$

Where  $j$  denotes the cylinder identity number. When the equation is simplified for a single cylinder engine by letting  $j=1$  and  $\psi=0$  (the phase shift), it can be written as:

$$T_k = p e^{ik\omega t/2} \quad (3.49)$$

It can be observed that the power torque for a single cylinder engine is a function of the varying combustion force power series, with contributions at all multiples of  $\omega$ . Clearly odd values of  $k$  give rise to half-order contributions, whilst the even values of  $k$  yield whole multiples of engine order. Thus, the effect of the engine whole order multiples clearly coincides with the inertial imbalance. The half-engine order responses are quite clear in Figure 3.8 and Figure 3.9, especially in the lower engine orders. As frequency increases, the effect is attenuated.

### 3.5.3 Rotational Imbalance

Rotational imbalance is caused by mass  $m_2$ , with the mass of the crankpin rotating at a distance to the centre of rotation of the crankshaft. This rotational imbalance induces a horizontal inertial force in the y-direction as:

$$F_y = -m_2 r \omega^2 \sin \alpha t \quad (3.50)$$

It is possible to reduce or eliminate this horizontal inertial force by employing counterbalancing masses along the crankshaft. The vertical imbalance component will always remain in a single cylinder engine, although it can be reduced in multi-cylinder engines by properly adjusted phase angles.

The simple analysis highlighted above is particularly useful in the identification of the spectral contents of the both experimentally and numerically obtained frequency domain responses, as they are the most prominent excitations in a single cylinder engine. The experimentally obtained vibration spectrum is very complex, and contains not only whole and half-order multiples of engine order, but also other contributions that often appear at rather strange multiples of engine order.

It is obvious that analytical methods employ various simplifications in order to obtain a simple solution. For instance, the elimination of higher order terms in the binomial expansion is already shown to lead to omission of certain higher engine order contributions. Thus, one cannot completely rely on analytical results. Therefore a numerical model must be validated against experimental findings as far as possible, that increases the level of confidence of the model. On the other hand, there are also some limitations in experimentation as it depends on various factors such as accuracy of instrumentation, environmental effects and physical

limitations like accessibility, which are discussed later in Chapter 06. Therefore, special care must be taken when selecting experimental measurements during a model validation. Conversely, such a validated numerical model can be used to predict the system behaviour, which otherwise cannot be measured (forces at gudgeon pin) or expensive measuring techniques (cylinder liner force) has to be utilized.

In this multi-physics numerical model development, so far the emphasis is put on the development of a rigid body system, incorporating component flexibility. It is also important to note that the basic joint primitives are used for all constraint formulations, which is not exactly the physical situation in actual systems. In particular in IC engines, lubricated contacts, such as crankshaft support engine journal bearings, piston-cylinder interactions are quite complicated than simple kinematic constraints often used in traditional multi-body analyses. Proper use of tribological contacts must be made instead of merely introducing constraints. These provide frictional and contact forces, which may be regarded as forms of restraint rather than rigid constraints. The next chapter is devoted to basic physical approaches for development and use of lubricated contacts within the multi-physics analysis framework.

---

## 4 TRIBOLOGICAL CONTACTS

### 4.1 Introduction

This chapter provides the theoretical basis for lubricated contacts included in the multi-physics model of IC engines. The model comprises a number of such load bearing conjunctions. These include the sliding contact of piston skirt-to-cylinder bore, which is a partially conforming contact, with a fairly large contact area. The contact of piston compression ring against the cylinder wall is also considered, which has a much smaller contact area than that of the piston skirt, as well as a lower degree of conformity and smaller clearance. Thus, the piston ring-to-cylinder wall contact is subjected to a more severe lubrication condition. The model also includes the closely conforming contacts in the main crankshaft engine journal bearings (for three such conjunctions). In a real engine there are clearly other lubricated contacts, such as the highly loaded non-conforming cam-tappet conjunction, their higher loaded (than the support journal bearings) contacts of the big-end and small end connecting rod bearings. The model, as described in the previous chapter pertains to the piston-connecting rod-crank sub-system, thus it does not take into account the camshaft and valve train system. Furthermore, the connecting rod bearings are represented by kinematic constraints in order to reduce the model complexity. However, the integrated methodology reported here can easily be expanded to take these into account (see suggestions for future work in chapter 8).

In the engine model, the crankshaft is connected to the engine block via the main engine bearings, which in the case of the test engine used in this thesis (a Ricardo E6 single cylinder engine) can be treated as a hydrodynamic journal bearing. Main bearing has to withstand against the transmitted effect of high combustion gas forces and the reciprocating inertia of the articulated mass of the connecting rod and the piston assembly. In general, the maximum number of such main support bearings would be the number of cylinders plus one. One bearing can be placed in between each set of pistons and two at each end of the crankshaft. In low power engines the number of bearings could be less than its maximum number. Most of modern engines are fitted with journal bearings. As the surface area between the two contacts is large (i.e. a closely conforming contact) it can withstand very high loads. The frictional

---

loss in journal bearings is comparatively high and as a consequence high performance engines such as those in motorsports are fitted with roller or needle bearings, which are very expensive and less durable. A coherent lubricating film must be present to keep the two contacting surfaces apart and guard against incidence of wear. Therefore, there is a designed gap between the mating surfaces, referred to as the *clearance gap*. This clearance gap is filled with the lubricant due to a combination of entraining motion of the lubricant into the resulting wedge shape and by squeeze film retention due to load. As a result the crankshaft “floats” on this film of fluid. Journal bearings are designed to support shafts and to carry radial loads with minimum power loss and wear.

Fluid film lubrication can broadly be categorized into two regimes, namely hydrodynamics and elastohydrodynamic. Hydrodynamic regime of lubrication occurs mostly at low to medium loads and moderate to high speeds of entraining motion. Thus, the generated pressures are insufficient to cause local deformation of contacting elastic solids. Such conditions are prevalent in closely or partially conforming contacts with relatively large load bearing surface areas, such as in journal bearings. Under elastohydrodynamic regime of lubrication the contact area is usually very small, mostly as a result of non-conforming mating surfaces, and the forces acting are sufficiently high to cause local deformation in the contact zone. Frictional losses in fluid film lubrication are due to viscous shearing effect in the lubricant film under sliding conditions. Thus, the viscosity of the lubricant and the film thickness play crucial roles. If the film thickness is bridged, asperity interactions also play an important role, and a mixed regime of lubrication results.

## 4.2 Lubrication Regimes

With regard to the contacts considered in this thesis, three regimes of lubrication must be considered. These are mixed lubrication, hydrodynamic and fluid film lubrication. The fluid film lubrication can be divided into hydrodynamic and elastohydrodynamic lubrication depending on the pressures involved. In the multi-body dynamics model, hydrodynamic regime of lubrication is considered for the engine bearings. This is true for the particular engine under consideration (i.e. the Ricardo E6 engine). The bearing bushing is considered thick, and made of steel, thus not subject to deformation. In some modern engines, the bearing bushing is a shell, made of materials of low elastic modulus such as tin-based alloys.

---

This encourages localized deformation of the shell under pressure, enhancing the gap for formation of a lubricant film. Solutions for such bearings have been provided by (Gupta 2002) and (Rahnejat 2000). The regime of lubrication can alter throughout the piston cycle, both in the piston skirt-to-cylinder wall or liner conjunction, and in the contact of the piston ring. For the E6 engine the cylinder liner is 2.5mm thick, made of steel, and the combustion pressure generates side forces which are insufficient to cause any localized deflection of the bodies in contact (see results later). Thus, hydrodynamic regime of lubrication is considered, where depletion of film below a certain level points to mixed regime of lubrication, discussed later, and taken into account. Friction in such cases due to boundary contributions is also taken into account.

#### **4.2.1 Boundary Lubrication**

When the speed of entraining motion of the lubricant ceases or becomes very slow the lubricant film thickness reduces and the contact load is carried by surface asperities in the contact area. Any tribological contribution is due to the adsorbed molecules of the lubricant and/or thin oxide surface layers. These are the typical characteristics of boundary regime of lubrication. Such conditions rarely occur in load bearing surfaces in engines, but the propensity for its occurrence is most likely in piston-cylinder interactions at TDC or BDC. The most likely outcome is mixed regime of lubrication.

#### **4.2.2 Mixed Lubrication**

A hydrodynamic pressure is built up in the lubricant, when the speed increases. Characteristic for mixed lubrication is that the loading is carried by a combination of hydrodynamic pressure and the contact pressure between the asperities of both surfaces. It is the intermediate region between boundary lubrication and hydrodynamic lubrication.

#### **4.2.3 Hydrodynamic and Elastohydrodynamic Lubrication**

At high speeds the hydrodynamic pressure increases such that the surface asperities are completely separated by a lubricant film. Characteristic for hydrodynamic conditions is that the applied contact load is carried by the hydrodynamic pressures generated by the lubricant film. If the load is sufficiently high, then localized surface

---

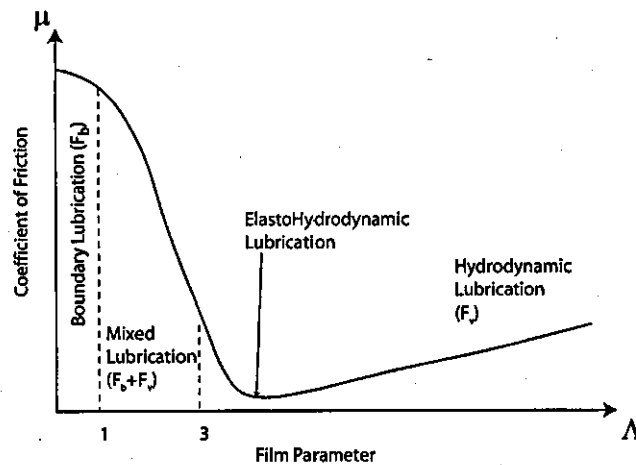


**Figure 4.1 Stribeck curve**

deformation also takes place due to higher contact pressures. This leads to elastohydrodynamic regime of lubrication, which also results in a dramatic increase in the viscosity of the lubricant in the contact.

As a representative example for journal bearings, the Stribeck diagram of Figure 4.1 is frequently used as a convenient tool to surmise the prevalent regime of lubrication. The diagram represents friction coefficient  $\mu$  with respect to a dimensionless film parameter  $\Lambda$ . At low film thickness where the film parameter becomes low, the asperity tips of two contacting bodies are in touch and leave stick-slip conditions to occur. This increases the friction force enormously. However with increasing film thickness the friction is gradually decreased until the elastohydrodynamic lubrication is taking place, since the amount of asperities in touch are progressively decreased. At elastohydrodynamic conditions the asperity tips are deformed and the surface is leveled due to elastic deformation thus decreasing friction further. In hydrodynamic lubrication the coefficient of friction is increased with increasing film thickness owing to viscous drag effect of the lubricant.

### 4.3 Reynolds Equation – General Development

Using Newton's slow viscous fluid model, Navier (in 1823) and Stokes (in 1845) derived a generalised equation for fluid flow called the *Navier-Stokes equation*. Navier-Stokes equation is derived considering the equilibrium of various forces on a representative element of the fluid, involved its motion, such as:

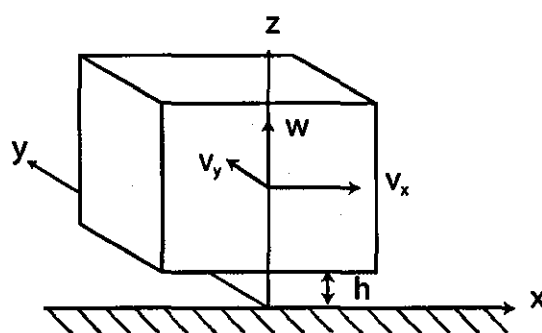


Figure 4.2 Physical representation of Reynolds equation

1. Surface forces
2. Body forces
3. Inertial forces

Navier-Stokes equation is the most general form of fluid flow equation. In 1886 Reynolds simplified this equation by making certain assumptions for the case of lubrication of contact surfaces in relative motion, separated by a thin fluid film, as follows.

1. Body forces, such as gravitational or magnetic forces, are neglected. This assumption is generally true for lubrication with non-conducting fluids.
2. Owing to slow viscous motion, inertial forces can be ignored.
3. Pressure through a section of the lubricant film in its depth can be considered to be constant, since the film thickness is very small.
4. No slip occurs between the fluid film and the adjacent solid boundaries.
5. The flow is considered to be laminar and velocity of fluid need not change in direction. In such narrow conjunctions the film is considered to be almost flat, no change of velocity is considered owing to negligible changes in curvature in small contacting regions.
6. The fluid is considered to be Newtonian

As such Reynolds simplified the Navier-stokes equation, eliminating basically the body and inertial forces (as well as surface tension) and presented the following equation (4.1) for a lubricated conjunction. In his equation he relates the pressure at a location in contact to the film thickness, lubricant viscosity and relative motion of surfaces (see Figure 4.2).

$$\frac{\partial}{\partial x} \left[ \frac{h^3}{\eta_0} \cdot \frac{\partial p}{\partial x} \right] + \frac{\partial}{\partial y} \left[ \frac{h^3}{\eta_0} \cdot \frac{\partial p}{\partial y} \right] = 12 \left[ \frac{v_x}{2} \cdot \frac{\partial h}{\partial x} + \frac{v_y}{2} \cdot \frac{\partial h}{\partial y} + w \right] \quad (4.1)$$

The right hand side of equation (4.1) contains three terms. Each of them contributes to the velocity induced flow in the bearing. The first two terms of the right hand side are described as flow due to surface velocities, and are referred to as Couette flow terms. These are net flow rates due to pressure gradient. The last term is referred to as squeeze film action, which considers the mutual convergence of contacting solids at the conjunction. This equation is equally applicable for EHL lubrication, when the film shape, given by  $h$  embodies their localized deformation under load. For hydrodynamic lubrication the fluid properties (viscosity and density, not considered in equation (4.1)) do not vary significantly with pressure throughout the bearing and thus may be considered to be constant. This condition is referred to as isoviscous. Also note that Reynolds' equation is for isothermal conditions only.

### 4.3.1 Short Bearing Approximation

It is quite difficult to obtain analytic solutions for Reynolds' equation for general cases, involving film thickness variation in both  $x$  and  $y$  directions. For these cases one has to resort to numerical discretisation techniques and solutions using finite differences and relaxation methods. However, when physically justified various simplifications are used to obtain an analytical expression for given contact conjunctions. Under hydrodynamic lubrication condition in the bearing, the motion is regarded as pure rolling along the  $x$ -direction and hence  $v_y$  is considered to be negligible (this condition is referred to as no side-leakage). The velocity in the vertical direction (along the contact normal) is called the squeeze velocity  $w$ , which can be ignored under steady-state conditions, since:  $w = \frac{\partial h}{\partial t}$  as the bearing clearance is very small. Under non-steady conditions, the squeeze velocity can be determined in a time-based analysis by first order approximation as:  $w = \frac{h_{new} - h_{old}}{\Delta t}$ , where film thickness at any location in two successive time steps, denoted by the step-size  $\Delta t$  is taken into account. Taking these assumptions into consideration the Reynolds equation (4.1) for steady state condition (ignoring the squeeze film effect) can be rewritten as:

$$\frac{\partial}{\partial x} \left[ h^3 \cdot \frac{\partial p}{\partial x} \right] + \frac{\partial}{\partial y} \left[ h^3 \cdot \frac{\partial p}{\partial y} \right] = 6v_x \eta_0 \frac{\partial h}{\partial x} \quad (4.2)$$

Here, the iso-viscous conditions are considered and density is assumed to be a constant. Side leakage, or flow in the  $y$ -direction, is associated with the second term in equation (4.1). If the pressure in the lubricant film has to be considered as a function of  $x$  and  $y$ , the solution to the Reynolds equation can rarely be achieved analytically. In many conventional lubrication problems pressure variation in one direction is considered to be negligible compared to the other direction, such as in very long bearings, or short width bearings considered in this thesis as a good approximation for the engine bearings. If  $y$  is considered to be the direction that has insignificant changes in generated pressures, then:

$$\frac{\partial}{\partial x} \left( \frac{h^3}{\eta_0} \frac{\partial p}{\partial x} \right) = 6v_x \frac{\partial h}{\partial x} \quad (4.3)$$

After integrating this equation with respect to  $x$  and making use of the boundary conditions:

$$\frac{dp}{dx} = 0, \text{ when } x = x_m, \text{ and } h = h_m$$

Where,  $h_m$  is the film thickness at the maximum pressure point and  $x_m$  is the distance to the maximum pressure point along  $x$ . Then, the Reynolds' equation for the fluid film in the journal bearing reduces to:

$$\frac{dp}{dx} = 6v_x \eta_0 \frac{h - h_m}{h^3} \quad (4.4)$$

According to the Reynolds pressure distribution there is a maximum pressure point within the contact. Under hydrodynamic conditions the lubricant pressure reaches its maximum in the converging wedge which is slightly before the minimum film thickness point along the entraining direction. In the diverging region negative lubricant pressures exists which does not support for the load carrying capacity and it is known as the cavitation region in the contact. Due to this sub ambient pressure the dissolved gasses in the lubricant releases as a form of air bubbles which may then corrodes the bearing surface. Release of dissolved air from the lubricant causes the pressure to be close to atmospheric. Thus, it assumes zero

---

pressure in the cavitated region. With contact geometry, kinematics and lubricant rheology solutions to Reynolds equation can be sought. Solutions can be obtained by direct integration of Reynolds equation analytically, if for the prevailing conditions it can be reduced to a one-dimensional problem. This means the variation along the other contact dimension can be considered as negligible. For example, if one of the contact dimensions  $x$  or  $y$  is considered to be infinitely long, its effects upon variation of generated pressure distribution is negligible, or in other words the pressure remains constant in that direction. This condition is known as *Long Bearing Approximation*. If this condition persists, then there is negligible side leakage as assumed earlier. Long bearing approximation is an applicable assumption for bearings with the diameter to length (some times referred to as width) ratio:  $(2R/L)$ , being less than 0.5 as highlighted by Sommerfeld and detailed by Cameron (Cameron 1966). Solutions for all tribological contacts pertaining to long or short bearing assumptions can be found analytically if the film shape is described geometrically. The same, of course, is true for engine journal bearings (Hamrock *et al*, 2004). Yet the expression is not particularly useful as an analytical solution, since it is difficult to obtain the load components by further integration. In 1904 Sommerfeld neatly overcome this integration problem by introducing a mathematical relationship called the “Sommerfeld substitution” as it is discussed in Chapter 2. The use of Sommerfeld substitution leads to evaluation of pressure distribution for the complete journal. However, the pressure distribution is skew symmetric, generating positive pressures in the converging film ( $0 \leq \alpha \leq \pi$ ) and negative pressures in the diverging gap ( $\pi \leq \alpha \leq 2\pi$ ), the integration of which leads to no load carrying capacity. Thus, half-Sommerfeld condition is used, where the negative pressures are ignored. Once the pressure is known the load components can be calculated. It is convenient to determine the components of the resultant load along and perpendicular to the line of centres (this is the line joining the centre of the journal to the geometric centre of the bushing).

Then, the force along the line of centres becomes zero due to the symmetry of the pressure distribution with use of full-Sommerfeld condition, which is not practical. This demonstrates that for a full-Sommerfeld solution the resultant normal load acts at right angles to the line of centres, that is the attitude angle is  $90^\circ$ . So that as the load is applied the shaft centre moves away from the bearing centre at right angles to the load vector. To overcome these difficulties the half-Sommerfeld solution, which neglects the negative pressures inside the contact

---

domain is considered. As mineral oil contains dissolved air and gases liberate in it at low pressures to maintain its saturation pressure, the above assumption is considered to be reasonable, but does not indicate the correct film rupture point and the commencement of the cavitation region.

Similarly, for cases that the length of a bearing is very short compared to its diameter the pressure gradient along its length alters more dramatically and its effect is taken into account in favour of abandoning the circumferential pressure variation in the bearing. For a fluid film bearing the circumferential flow rate ( $q'_\alpha$ ) and the axial flow rate ( $q'_y$ ) can be given as follows (Hamrock *et al*, 2004):

$$q'_\alpha = -\frac{h^3}{12\eta_0 r_b} \frac{\partial p}{\partial \alpha} + \frac{hr_b \omega_b}{2} \quad (4.5)$$

$$q'_y = -\frac{h^3}{12\eta_0} \frac{\partial p}{\partial y} \quad (4.6)$$

(DuBois and Ocvirk 1953) stated that for short-width journal bearings the term 1 in equation (4.5) is small relative to term 2. That is, for short-width journal bearings the pressure induced flow (1 in eq. (4.5)) in the circumferential direction is small compared to the Couette flow term (2 in eq. (4.5)). Therefore, they assumed that:

$$q'_\alpha = \frac{hr_b \omega_b}{2} \quad (4.7)$$

It should be emphasized that this assumption means that:  $\partial p / \partial \alpha = 0$ , and the significant pressure variation occurs along the  $y$ -direction. This condition can be employed for short-width bearings with diameter-to-width ratios in excess of 2 as indicated by (Cameron 1966) and as a first approximation for piston ring to cylinder wall contact with very short width rings. The result of this assumption is that the Reynolds' equation given in equation (4.2) reduces to:

$$\frac{\partial}{\partial y} \left( h^3 \frac{\partial p}{\partial y} \right) = 6\eta \omega_b \frac{\partial h}{\partial \alpha} \quad (4.8)$$

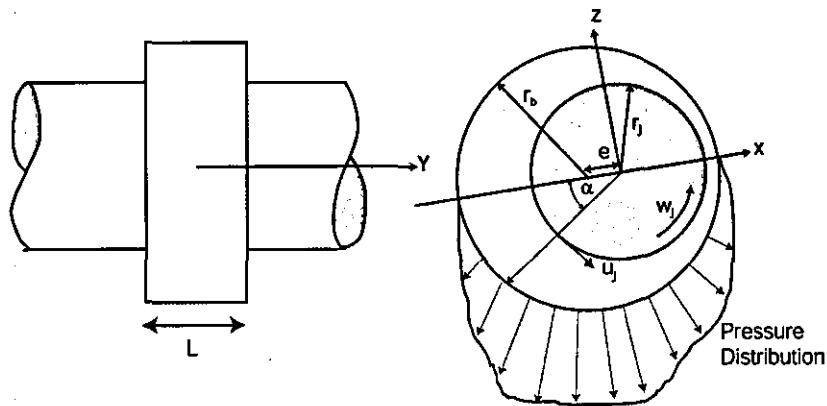


Figure 4.3 Pressure distribution in a journal bearing

The short-width-journal-bearing theory is valid as long as the diameter to width ratio is greater than or equal 2 (Kirk and Gunter 1975). Of course larger the ratio, better agreement with exact numerical solutions is found (Pinkus and Sternlicht 1961). Consider that there is no misalignment between journal and bushing, and the film thickness is a function of  $\alpha$  only. Then, considering the appropriate boundary conditions and integrating pressure distribution around the journal one can obtain (Hamrock *et al*, 2004):

$$p = \frac{3u_j \eta_0 \epsilon}{r_j c} \left( \frac{L^2}{4} - y^2 \right) \frac{\text{Sin}\alpha}{(1 + \epsilon \text{Cos}\alpha)^3} \tag{4.9}$$

Where, the eccentricity ratio is defined as:

$$\epsilon = \frac{e}{c} \tag{4.10}$$

This equation shows that the parabolic function governs the axial variation of pressure, whereas the geometric film function dictates the circumferential variation of pressure (see Figure 4.3). Sub-ambient pressures predicted by eq. (4.9) are ignored, and it is assumed that positive pressure region from  $\alpha = 0$  to  $\alpha = \pi$  carries the total load of the bearing (i.e. half-Sommerfeld assumption).

The load carrying capacity can be calculated by integrating the pressure distribution around the circumference. As such the components of the load vector along ( $W_x$ ) and perpendicular ( $W_z$ ) to the line of centres can be expressed as follows (Boysal and Rahnejat 1997; Cameron 1966; Taylor 2002):

$$W_z = \frac{u_b \eta_0 L^3}{4c^2} \frac{\pi \varepsilon}{(1 - \varepsilon^2)^{3/2}} \quad (4.11)$$

$$W_x = \frac{u_b \eta_0 L^3}{c^2} \frac{\varepsilon^2}{(1 - \varepsilon^2)^2} \quad (4.12)$$

The altitude angle  $\psi$ , which is the angle between line of centres and the resultant force can be given as,

$$\tan \psi = \frac{\pi \sqrt{1 - \varepsilon^2}}{\varepsilon} \quad (4.13)$$

The friction or the traction force in a lubricated conjunction is generated due to the relative sliding motion of the two contacting surfaces. Here  $u_j$  refers to the surface velocity of the journal, whereas  $u_b$  is the surface velocity of the bearing bushing.

$$F = \int_{-L/2}^{L/2} \int_0^b \left( \frac{h}{2} \frac{\partial p}{\partial x} + \frac{\eta (u_j - u_b)}{h} \right) dx dy \quad (4.14)$$

With the short bearing approximation,  $\frac{\partial p}{\partial x} = 0$  (as already explained above), thus after integration:

$$F = \frac{-2\pi \eta u_j r_j L}{c} \cdot \frac{1}{\sqrt{1 - \varepsilon^2}} \quad (4.15)$$

The first quotient is known as the “Petroff friction”, which would be present where the journal and the bearing shell are concentric (i.e. rotating cylinder friction). The second quotient is termed the “Petroff Multiplier”. Note also the higher the  $\varepsilon$ , the greater the friction and hence more heat is generated. The negative sign indicates opposition to the direction of entraining motion. Thus, an estimate of coefficient of friction can be obtained as:

$$\mu = \frac{8r_j c}{L\varepsilon} \cdot \frac{(1 - \varepsilon^2)^{3/2}}{(1 + 0.63\varepsilon^2)^{1/2}} \quad (4.16)$$

### 4.3.2 Stiffness of Journal Bearing

The total bearing load ( $W$ ) can be obtained as:

$$W = \sqrt{W_x^2 + W_y^2} \quad (4.17)$$

Thus:

$$W = \frac{u_j \eta L^3}{c^2} \frac{\pi \varepsilon}{(1 - \varepsilon^2)^2} \left[ \left( \frac{16}{\pi^2} - 1 \right) \varepsilon^2 + 1 \right]^{1/2} \quad (4.18)$$

Equation (4.18) provides the relationship between load and eccentricity. A more common way of expressing this relationship is in terms of the dimensionless group called the Sommerfeld number ( $S$ ) such as:

$$S = \frac{W}{NDL\eta} \frac{c^2}{r_j^2} \quad (4.19)$$

Note that  $r_j \approx r_b = D/2$  and  $N$  is in rev/s. In terms of  $S$ , equation (4.18) for a short width bearing, can be represented:

$$S = \left( \frac{L}{D} \right)^2 \frac{\pi^2 \varepsilon}{(1 - \varepsilon^2)^2} \sqrt{0.62 \varepsilon^2 + 1} \quad (4.20)$$

From this equation it is clear that  $S = f(\varepsilon, L/D)$ . It can be seen from the definition of  $S$  in equation (4.19), that  $S \propto W$ . Also by definition  $h_m = c(1 - \varepsilon)$ . Taking these relations into consideration the variation of  $S$  with the minimum film thickness  $h_m$  for a given  $L/D$  ratio can be obtained, which is effectively the load-deflection curve as shown in Figure 4.4. The figure shows that the bearing is stiffest in the vicinity of the minimum film thickness and softer at both ends.

As mentioned in (Gohar 1988) a bearing can simplify into a simple mass spring arrangement. Then, the natural frequency of the system can be given as:

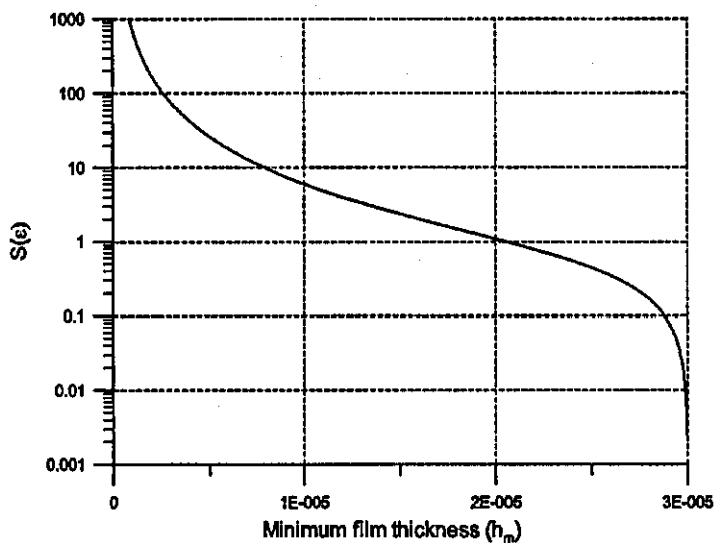


Figure 4.4 Variation of Sommerfeld number with minimum film thickness ( $L/D = 0.5$ )

$$f_b = \frac{1}{2\pi} \sqrt{\frac{gk}{W}} \quad (4.21)$$

Where  $k$  is the stiffness of the oil film such that:

$$k = \frac{\partial W}{\partial e} = \frac{1}{c} \frac{\partial W}{\partial \varepsilon}$$

Substituting this into the frequency equation and making use of Sommerfeld substitution (4.19) the bearing natural frequency can be obtained as follows: (Gohar 1988)

$$f_b = \frac{n}{2\pi} \sqrt{\frac{g}{c}} \quad (4.22)$$

Where  $n$  is an index such that  $n \approx 1.3$ , when  $\varepsilon \leq 0.65$  and it increases rapidly for  $\varepsilon > 0.65$ . This implies that oil film stiffness is quite non-linear. It is clear that oil whirl becomes severe in bearings when the shaft speed equals to twice the bearing natural frequency, such that (Kryniski 1991):

$$\omega_j = 2\omega_n = 2 \times 2\pi f_b = 2n \sqrt{\frac{g}{c}} \quad (4.23)$$

Thus:

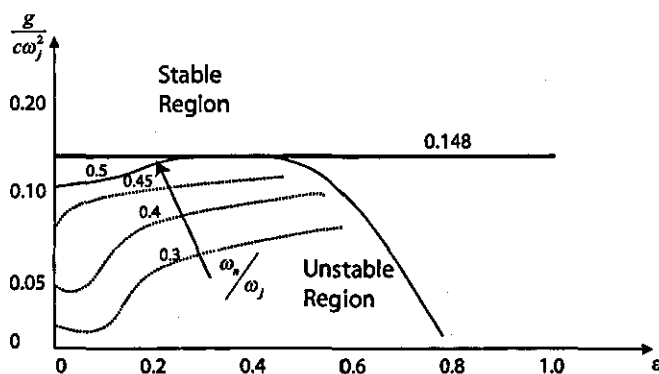


Figure 4.5 Shaft whirling stability map

$$\frac{g}{c\omega_j^2} = \frac{1}{4n^2} = \frac{1}{4(1.3)^2} = 0.148 \tag{4.24}$$

Therefore, for safe operation of a rotor supported by journal bearings, the ratio  $\frac{g}{c\omega_j^2}$  must always be greater than 0.148 for all values of  $\epsilon$ . Of course the analysis here is a simplified approach in one-dimensional analysis. By using equation (4.23) the safe operational region for a bearing can be found, considering the ratio of bearing rotational speed and its natural frequency. The stability map, in two-dimensions, using numerical solutions is given in Figure 4.5, which is used in bearing design (Cameron 1966; Gohar 1988).

### 4.3.3 One dimensional solution for piston skirt and ring contacts

Thus far the theory outlined above (for short bearings) is developed and used in the thesis for the engine journal bearings, which for the case of the E6 single cylinder engine have a diameter-to-length ratio of approximately 1.9. This is very close to the value of 2 required for its accuracy (Kirk and Gunter 1975). The alternative would have been to simultaneously solve Reynolds' and film thickness equations (Reynolds' equation in 2-dimensions) numerically. This would have added significant time to the model computations, with an inordinate corresponding rise in analysis time. Such solutions, in fact are already available (Gupta 2002; Okamura and Morita 1999; Rahnejat 2000), and should replace the current approach for diameter to length ratios between 0.5 and 2, where a finite-width bearing results. However it is noted that at higher sommerfeld numbers and low eccentricity ratios, deviation

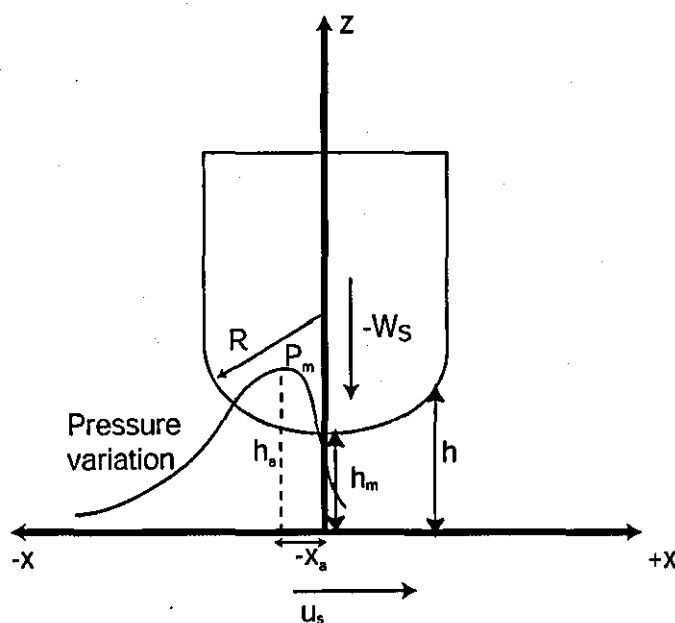


Figure 4.6 Ring Lubrication

of short bearing solution from finite width bearing solution is insignificant (Pinkus and Sternlicht 1961).

For the case of piston ring, of very short width and long perimeter, such that the ratio of its diameter to its width is typically of the order of 0.01 or less, one can assume with good justification that pressure variation along its width is far more significant than circumferentially. Thus, many investigators have used infinite line contact analysis approach such as a roller on a semi-infinite elastic half-space (a one-dimensional analysis) to obtain an analytic solution, such as (D'Agostino *et al*, 2002). This is a similar approach to the case of the long bearing analysis described previously, with the difference that the ring - cylinder wall constitutes a small contact area which is rather poorly conforming. The full Reynolds equation can be simplified using an infinitely long contact assumption where there is no side leakage, thus zero pressure gradient in the  $y$ -direction (note that the axial direction of the contact is along the ring face-width, denoted in Figure 4.6 as the  $x$  direction). Thus, using the same approach as in (Rahnejat 1984):

$$v = 0 \text{ and } \frac{\partial P}{\partial y} = 0 \quad (4.25)$$

Thus, applying these conditions into equation (4.1):

$$\frac{\partial}{\partial x} \left[ \frac{h^3}{\eta_0} \cdot \frac{\partial p}{\partial x} \right] = 12 \left[ \frac{v_x}{2} \cdot \frac{\partial h}{\partial x} + w \right] \quad (4.26)$$

Furthermore, for an iso-viscous lubricant, the viscosity  $\eta = \eta_0$ , Thus:

$$\frac{\partial}{\partial x} \left[ h^3 \cdot \frac{\partial p}{\partial x} \right] = 12\eta_0 \left[ \frac{v_x}{2} \cdot \frac{\partial h}{\partial x} + w \right] \quad (4.27)$$

Integrating equation (4.27) with respect to  $x$  to obtain the pressure gradient in the lubricant and let  $w_s = w$ :

$$h^3 \frac{dp}{dx} = 6u\eta_0 h + 12w_s \eta_0 x + C_1 \quad (4.28)$$

The constant of integration  $C_1$  can be evaluated using the boundary conditions:

$$\frac{dp}{dx} = 0 \text{ at } x = -x_a \quad (4.29)$$

Which is the point where:

$$p = P_{\max} \text{ and } h = h_a$$

Assuming a parabolic variation for the hydrodynamic film thickness in the direction of flow as:

$$h = h_m \left( 1 + \frac{x^2}{2Rh_m} \right) \quad (4.30)$$

The pressure gradient can be obtained as:

$$\frac{dp}{dx} = \frac{6\eta_0}{h_m^3 \left( 1 + \left( \frac{x^2}{2Rh_m} \right) \right)^3} \left( \frac{u_s}{2R} (x^2 - x_a^2) + 2w_s (x + x_a) \right) \quad (4.31)$$

Equation (4.31) can be solved, using the following dimensionless groups:

$$\tan \bar{x} = \frac{x}{\sqrt{2Rh_m}}$$

$$\tan \bar{x}_a = \frac{x_a}{\sqrt{2Rh_m}}$$

$$p^* = \frac{h_m^{3/2} p}{6u_s \eta_0 (2R)^{1/2}} \quad (4.32)$$

$$w_s^* = \frac{w_s}{u_s}$$

$$h_m^* = \frac{h_m}{R}$$

Thus:

$$\frac{dp^*}{d\bar{x}} = \left\{ \sin^2 \bar{x} \cos^2 \bar{x} - \tan^2 \bar{x}_a \cos^4 \bar{x} + \frac{4w_s^*}{\sqrt{2h_m^*}} (\sin \bar{x} \cos^3 \bar{x} + \tan \bar{x}_a \cos^4 \bar{x}) \right\} \quad (4.33)$$

Implementing these substitutions and integrating equation (4.31), the pressure variation can be evaluated as:

$$p^* = \frac{1}{8} \bar{x} - \frac{1}{32} \sin 4\bar{x} - \tan^2 \bar{x}_a \left( \frac{3}{8} \bar{x} + \frac{1}{4} \sin 2\bar{x} + \frac{1}{32} \sin 4\bar{x} \right) + \frac{4w_s^*}{\sqrt{2h_m^*}} \left\{ -\frac{3}{32} - \frac{1}{8} \cos 2\bar{x} - \frac{1}{32} \cos 4\bar{x} + \tan \bar{x}_a \left( \frac{3}{8} \bar{x} + \frac{1}{4} \sin 2\bar{x} + \frac{1}{32} \sin 4\bar{x} \right) \right\} + C_2 \quad (4.34)$$

The constant of integration ( $C_2$ ) can be found using the following boundary conditions for a fully flooded inlet condition:

$$p = 0 \text{ when } x = -\infty \quad (4.35)$$

Which can be represented in dimensionless form as:

$$p^* = 0 \text{ at } \bar{x} = -\frac{\pi}{2}$$

Substituting these values into equation (4.34), the pressure distribution can be obtained as:

$$\begin{aligned}
 p^* = & \frac{1}{8}\bar{x} - \frac{1}{32}\sin 4\bar{x} - \tan^2 \bar{x}_a \left( \frac{3}{8}\bar{x} + \frac{1}{4}\sin 2\bar{x} + \frac{1}{32}\sin 4\bar{x} \right) \\
 & + \frac{4w_s^*}{\sqrt{2h_m^*}} \left\{ -\frac{3}{32} - \frac{1}{8}\cos 2\bar{x} - \frac{1}{32}\cos 4\bar{x} + \tan \bar{x}_a \left( \frac{3}{8}\bar{x} + \frac{1}{4}\sin 2\bar{x} + \frac{1}{32}\sin 4\bar{x} \right) \right\} \quad (4.36) \\
 & + \frac{\pi}{16} \left( 1 - 3 \tan^2 \bar{x}_a + \frac{12w_s^*}{\sqrt{2h_m^*}} \tan \bar{x}_a \right)
 \end{aligned}$$

Pressure distribution can be obtained, if  $\bar{x}_a$  is known. The outlet boundary condition can be used to calculate this value. Assuming  $p^* = 0$  at  $\bar{x} = \pi/2$ . (Where  $x = \infty$ )

$$\tan \bar{x}_a = \frac{\left\{ -\frac{12w_s^*}{\sqrt{2h_m^*}} \pm \sqrt{\frac{72w_s^{*2}}{h_m^*} + 12} \right\}}{-6} \quad (4.37)$$

When  $w_s^* = 0$ , which is the rolling element condition, the value of  $\tan \bar{x}_a = \pm 1/\sqrt{3}$ . This describes the Sommerfeld condition. It can also be seen that when  $\frac{72w_s^{*2}}{h_m^*} \gg 12$ , then  $\tan \bar{x}_a = 0$ . At this point only the squeeze action is prominent and entraining motion is not that important for the pressure development.

Numerical results obtained for dimensionless pressure variation for given  $w_s^*$  values are illustrated in Figure 4.7. Here, the negative pressures have to be neglected, as they do not support any load. It can be observed that as  $w_s^*$  increases negatively (i.e. larger velocity of normal approach), the pressure distribution increases in magnitude and the maximum pressure approaches the position of  $\bar{x} = 0$  (this is the centre-line of the contact and the position due to pure normal approach). When  $w_s^* = 0$ , the pressure distribution is that of half Sommerfeld condition, where  $\tan \bar{x}_a = -1/\sqrt{3}$ .

As it is mentioned earlier ignoring the negative pressures in the Sommerfeld solution fails to satisfy the continuity of the mass flow in the contact. Thus, at the outlet a cavitation boundary condition must be adopted. For this purpose it is usual to employ the Reynolds or Swift-

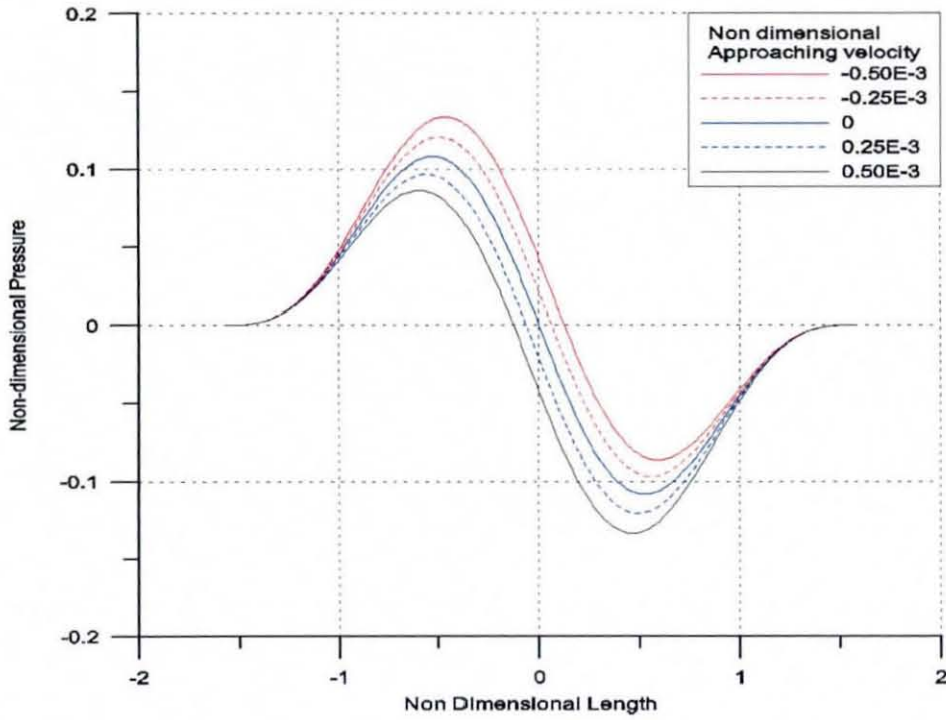


**Figure 4.7 Pressure distributions with Sommerfeld condition**

For different non-dimensional approaching velocities ( $w_s^*$ )

Steiber boundary conditions (Rahnejat 1984). In such cases both the pressure gradient and the pressure return to zero at the point of film rupture:

$$p = \frac{\partial p}{\partial x} = 0 \text{ at } \bar{x} = \bar{x}_r \tag{4.38}$$

By applying this boundary conditions into the equation (4.27) and following a similar procedure or by following the substitution procedure as shown in (Rahnejat 1984), the non-dimensional pressure distribution can be obtained as follows:

$$\begin{aligned}
 p^* = & \frac{1}{8} \bar{x} - \frac{1}{32} \sin 4\bar{x} - \tan^2 \bar{x}_r \left( \frac{3}{8} \bar{x} + \frac{1}{4} \sin 2\bar{x} + \frac{1}{32} \sin 4\bar{x} \right) \\
 & + \frac{4w_s^*}{\sqrt{2h_m^*}} \left\{ -\frac{3}{32} - \frac{1}{8} \cos 2\bar{x} - \frac{1}{32} \cos 4\bar{x} - \tan \bar{x}_r \left( \frac{3}{8} \bar{x} + \frac{1}{4} \sin 2\bar{x} + \frac{1}{32} \sin 4\bar{x} \right) \right\} \\
 & + \frac{\pi}{16} \left( 1 - 3 \tan^2 \bar{x}_r - \frac{12w_s^*}{\sqrt{2h_m^*}} \tan \bar{x}_r \right)
 \end{aligned} \tag{4.39}$$

Note that equation (4.39) can simply be obtained by just replacing  $\bar{x}_a$  in (4.36) by  $-\bar{x}_r$ . Now the pressure distribution can be found, if the film rupture point is known.  $x_r$  can be determined by utilizing the other half of the boundary conditions (4.38). Thus, equation (4.39) becomes:

$$\begin{aligned} & \frac{1}{8}\bar{x}_r - \frac{1}{32}\sin 4\bar{x}_r - \tan^2 \bar{x}_r \left( \frac{3}{8}\bar{x}_r + \frac{1}{4}\sin 2\bar{x}_r + \frac{1}{32}\sin 4\bar{x}_r \right) \\ & + \frac{4w_s^*}{\sqrt{2h_m^*}} \left\{ -\frac{3}{32} - \frac{1}{8}\cos 2\bar{x}_r - \frac{1}{32}\cos 4\bar{x}_r - \tan \bar{x}_r \left( \frac{3}{8}\bar{x}_r + \frac{1}{4}\sin 2\bar{x}_r + \frac{1}{32}\sin 4\bar{x}_r \right) \right\} \quad (4.40) \\ & + \frac{\pi}{16} \left( 1 - 3\tan^2 \bar{x}_r - \frac{12w_s^*}{\sqrt{2h_m^*}} \tan \bar{x}_r \right) = 0 \end{aligned}$$

Even in the contact between piston and bore the pressure variation along the circumferential direction can be considered negligible compared to the high pressures along the axial direction. This leads to insignificant fluid flow in the circumferential direction as it is given in equation (4.25). Moreover, higher stiffness of the piston material which leads to very high natural frequencies implies that the piston behaves more like a rigid component within the domain of excitation. Even though there are many studies available in literature considering the elastic deformations of the piston-bore lubrication (Balakrishnan and Rahnejat 2005; Dursunkaya and Keribar 1992; Dursunkaya *et al*, 1994), it is found that these elastic behaviour prevails only at the peak combustion pressure. However, even in such a location the pressures are usually insufficient to significantly alter the lubricant viscosity. Thus, as (Balakrishnan and Rahnejat 2005) have found only isoviscous elastic conditions are encountered in very small parts of the cycle. Thus, the engine operating conditions demonstrate that EHL conditions may hardly be present other than possibly at engine start-up. Taking these facts into consideration the methodology developed so far can be used reasonably to predict the lubrication characteristics of the contact between the piston and the bore.

#### 4.4 Analysis of Friction

If a machine element is adequately designed, with proper fluid film lubrication the contacting surfaces are completely separated. Conversely, when the film thickness is insufficient asperity interactions take place and this can lead to excessive wear and friction. The theory of

friction expounded initially for static case by Amontons in 1699 and extended to kinetic friction by Coulomb in the 18<sup>th</sup> century is based on the supposition that it (friction) arises from asperity interactions, thus dependent on the surface quality (topography). Of course friction also arises in lubricated contacts, even with full separation of surfaces due to shearing between layers of the fluid. This viscous action causes friction, which is not only present in relative sliding of surfaces but also under pure rolling conditions, but to a much lesser extent. Therefore, for fluid film lubrication viscous friction is the dominant source, whilst Coulomb friction acts under boundary regime of lubrication. These two phenomena contribute to the total friction in mixed regime of lubrication.

In order to identify the lubrication regime a dimensionless parameter can be defined as follows:

$$\Lambda = \frac{h_m}{\sqrt{\sigma_1^2 + \sigma_2^2}} \quad (4.41)$$

Smaller  $\Lambda$  results more frequent random contacts between asperities. Under such conditions *boundary* lubrication occurs. Larger film parameters result in more coherent lubricant films, which lead to hydrodynamic lubrication. However, great differences in geometric conformity from hydrodynamically lubricated conjunctions to elasto-hydrodynamically lubricated conjunctions make it difficult for clear distinctions to be made. Therefore, rough estimates are used to distinguish between regimes of lubrication as shown in Figure 4.1. Thus, it is reasonable to consider friction force between two surfaces to be made up of two contributions: a boundary friction  $F_b$  and a viscous friction  $F_v$ . Film parameter is used to identify the prominent friction component as shown in Figure 4.1.

$$F_f = F_b + F_v \quad (4.42)$$

#### 4.4.1 Boundary Friction Force

Boundary lubrication occurs when the asperities are in contact. The lubrication conditions can still prevail on asperity tips and in the oil film trapped between the asperities (see Figure 4.8), but friction arising from these are quite different. The distribution of peaks and valleys on a surface cannot be calculated precisely due to its random nature. Thus, a statistical approach

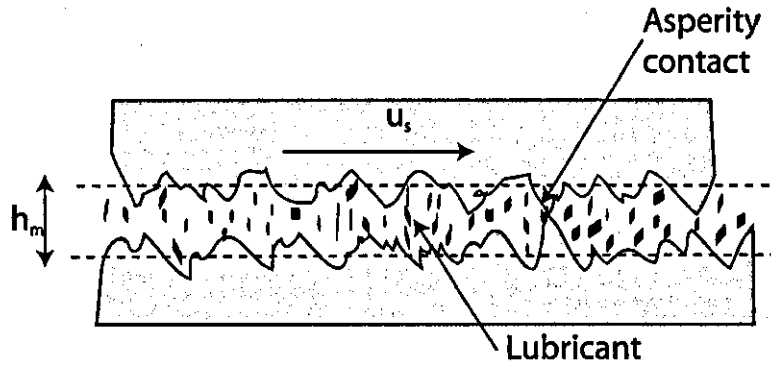


Figure 4.8 Lubricated contact

can be used to predict tribological aspects within a boundary lubrication contact. In the same manner proposed by (Greenwood and Tripp 1970) and used by (Teodorescu *et al*, 2003) for a cam tappet contact, a model considering the Gaussian distribution of asperity heights and constant radius of curvature of the asperities is used here to obtain the load carried by asperity contacts. Asperity contact area is given by (Greenwood and Tripp 1970):

$$A_a = \pi^2 (\gamma\beta\sigma) A_h F_2(\Lambda) \quad (4.43)$$

The load carried by asperities can be given by:

$$P_a = \frac{8\sqrt{2}}{15} \pi (\gamma\beta\sigma)^2 \sqrt{\frac{\sigma}{\beta}} E^* A_h F_{3/2}(\Lambda) \quad (4.44)$$

Where,  $E^*$  is composite or reduced elastic modulus given by:

$$\frac{1}{E} = \frac{1}{2} \left[ \frac{1-\nu_1^2}{E_1} + \frac{1-\nu_2^2}{E_2} \right] \quad (4.45)$$

$\sigma$  is the combined root mean square (RMS) surface roughness given by:

$$\sigma = \sqrt{\sigma_1^2 + \sigma_2^2} \quad (4.46)$$

The two statistical functions  $F_2(\Lambda)$  and  $F_{3/2}(\Lambda)$  are defined as:

$$F_n(\Lambda) = \frac{1}{\sqrt{2\pi}} \int_{\Lambda}^{\infty} (s - \Lambda)^n e^{-s^2/2} ds \quad (4.47)$$

Which has been fitted into two fifth order polynomials such as (Teodorescu *et al*, 2003):

$$F_{\frac{1}{2}}(\Lambda) = -0.0046\Lambda^5 + 0.0574\Lambda^4 - 0.295\Lambda^3 + 0.7844\Lambda^2 - 1.0776\Lambda + 0.6167 \quad (4.48)$$

$$F_2(\Lambda) = -0.0018\Lambda^5 + 0.0281\Lambda^4 - 0.1728\Lambda^3 + 0.525\Lambda^2 - 0.8043\Lambda + 0.5003 \quad (4.49)$$

According to (Greenwood and Tripp 1970; Teodorescu *et al*, 2003) the group  $\gamma\beta\sigma = 0.055$  and  $\sigma/\beta = 10^{-3}$ , has been used for the calculations. If the load acting on the contact is known, then the Hertzian contact area  $A_h$  can be found by the following equation (Kushwaha 2000):

$$A_h = \sqrt{\frac{4WRI}{\pi E}} \quad (4.50)$$

Where  $R$  is the equivalent radius of the two contact surfaces:  $\frac{1}{R} = \frac{1}{r_1} + \frac{1}{r_2}$ . Thus, the boundary friction force can be given as:

$$F_b = \tau_e A_a + c_{pb} P_a \quad (4.51)$$

Where  $\tau_e \approx 2MPa$ , which is the Eyring shear stress and  $c_{pb} \approx 0.17$  (K.L.Johnson 1985; Teodorescu *et al*, 2003). When asperity interactions take place, the lubricant film is quite thin and its behaviour (in parts, i.e. at the asperity tips) is assumed to be non-Newtonian. Thus, the Eyring shear stress defines the limiting value of shear stress, where non-Newtonian behaviour occurs (thus it identifies the asperity tip contacts). The film parameter  $\Lambda$  can be used to distinguish the regimes of lubrication within a contact. As it is shown in Figure 4.1, boundary lubrication can exist in both mixed and boundary lubrication regimes. Therefore, in the algorithm developed in this thesis and used in the multi-physics model the film parameter is used to determine whether boundary lubrication exists, and then equation (4.51) is used to calculate the boundary friction force.

#### 4.4.2 Viscous Friction Force

Viscous friction force is produced by shearing of the oil film trapped between the two contacting surfaces. Depending on the oil film thickness, the lubricant can behave as a Newtonian liquid such that the shear stress is linearly related to the shear strain or it may behave in a Non-Newtonian manner. (Eyring 1936) has proposed a model, which incorporates the non-linear viscous behaviour. According to this model the shear stress is linearly varying with shear strain until it reaches the Eyring shear strength ( $\tau_e$ ), which is about 2MPa for most lubricants. Subsequently, it starts to deviate from linearity. Taking this behaviour into consideration the shear stress can be used to identify the lubricant behaviour as previously pointed out. Thus:

$$\frac{\eta u_s}{h_m} = \tau \leq \tau_e \quad (= 2\text{MPa}) \quad (4.52)$$

Then, the Newtonian behaviour prevails within the contact and the shear stress becomes:

$$\tau = \frac{\eta u_s}{h_m} \quad (4.53)$$

However, if the inequality (4.52) is not satisfied, then the Non-Newtonian behaviour prevails and the shear stress is determined by the rheological properties of the oil such as:

$$\tau = \tau_0 + \gamma_s \left( \frac{P - P_a}{A_h} \right) \quad (4.54)$$

Where  $\gamma_s$  is the slope of oil limiting shear stress-pressure relationship and this could be approximated to a mean sliding velocity  $\left( \frac{u_s}{2} \right)$  of the contact. Thus, depending on the situation the viscous induced stress can be calculated either by (4.53) or (4.54).

During the piston motion inside the cylinder bore any of lubrication regimes can dominate. In piston mid-stroke the hydrodynamic lubrication condition is predominant due to high sliding velocities and relatively low side forces. At dead centres the velocity instantaneously becomes zero, thus producing no lubricant entrainment, especially when this happens at the TDC during the power stroke of the engine. Here the situation becomes more severe due to a

high side force. Under these conditions there is a better chance of boundary lubrication conditions to occur at top dead centre, which can be represented by the described procedure.

#### 4.5 Temperature Effects in Lubricated Contacts

Thus far all the analytical methods described are based on the assumption that isothermal solutions to tribological contacts suffice as first reasonable approximation. This also happens to be the approach by many other investigators, such as those cited in this chapter. However, in all contacts the temperature of the lubricant rises from that of the bulk oil temperature, and this reduces its viscosity, which in turn reduces the film thickness. In conjunctions with lower pressures and larger gaps, and particularly at lower shear rates the temperature rise is less pronounced, and one may ignore the temperature effect, at least as a first approximation. However, in less conforming conjunctions and at high shearing rates, such as the case of piston ring to cylinder liner contact temperature rise and its effect of viscous behaviour of the lubricant should not be neglected. Thus, Reynolds pressure variation at the contact changes whilst altering the reaction force. In fact, prediction of temperature rise in such lubricated contacts of a machine element is an important contribution to the engineering design process. The conservation of energy at a point in the lubricant film is the fundamental equation that is necessary for this prediction. Assuming that there is no other external source of heating present, the pressure along the thickness of the film is constant under steady state condition. Considering the fluid flow is only in the  $x$ -direction the 2-dimensional energy equation for a contact is given by (Gohar 1988) as:

$$\underbrace{v_e v_x \theta \left( \frac{\partial p}{\partial x} \right)}_{\text{compressive heating}} + \underbrace{\eta \left( \frac{\partial v_x}{\partial z} \right)^2}_{\text{viscous heating}} = \underbrace{\rho v_x C_p \left( \frac{\partial \theta}{\partial x} \right)}_{\text{convection cooling}} - \underbrace{k_c \left( \frac{\partial^2 \theta}{\partial z^2} \right)}_{\text{conduction cooling}} \quad (4.55)$$

Where  $\theta(x)$  is the temperature rise of the oil from the inlet,  $v_e$  is its coefficient of thermal expansion,  $C_p$  is the specific heat at constant temperature and  $k_c$  is the thermal conductivity. As it can be seen from the equation (4.55), the heat is generated due to compressive action as well as viscous action in a contact and this heat is dissipated to the environment by convection or by conduction cooling. Lubricants behave as incompressible (volume does not change with pressure) fluids in low pressures but it undergoes compression at high pressures

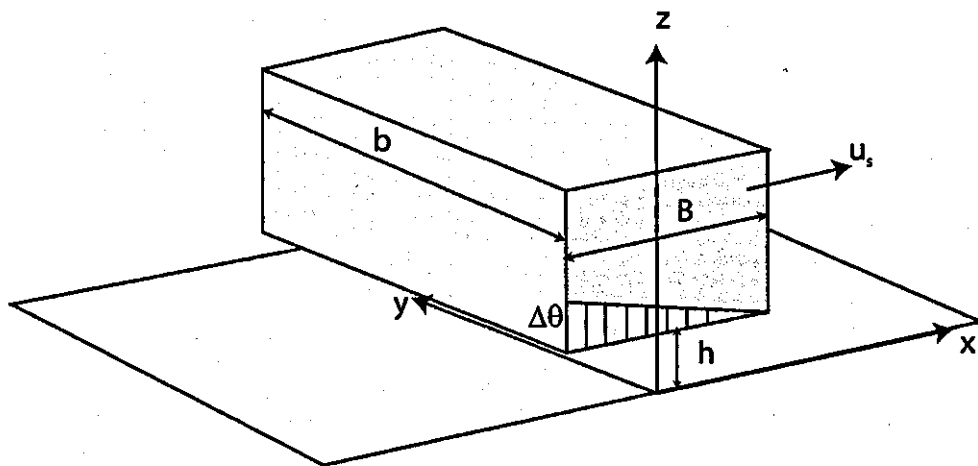


Figure 4.9 Temperature variation along the contact

such as in 100MPa's. Under such pressures the heat is generated due to compression action which is represented in the first term of the left side of the equation. On the other hand low film thickness and higher sliding velocities cause higher shear rates to happen in the lubricant, causing heat to generate at the contact. This heat is represented in the second term in the left side of the equation. Then, this heat is dissipated into the film boundary solid surfaces either by conduction cooling or by convection cooling. Depending on the situation various terms in equation (4.55) contribute quite differently and, thus it is possible to simplify it under certain conditions. For example, under hydrodynamic conditions the pressure variation is quite small compared to EHL conditions (Gohar 1988). Therefore, it is possible to neglect the effect due to compressive heating, while it is inadvisable to make such an assumption under EHL conditions. Assuming that hydrodynamic conditions are prevalent in the contact such as piston ring-to-cylinder wall, the affects due to compressive heating has been neglected from the equation. The viscous heating becomes the most prominent from the heat generation point of view and the equation (4.55) becomes:

$$\eta \left( \frac{\partial v_x}{\partial z} \right)^2 = \rho v_x C_p \left( \frac{\partial \theta}{\partial x} \right) - k_c \left( \frac{\partial^2 \theta}{\partial z^2} \right) \quad (4.56)$$

The generated heat in the contact changes the temperature in the lubricant and thus it changes the lubricant viscosity. The change in viscosity affects the Reynolds pressure distribution at the contact and new pressure variation needs to be calculated in the contact as an iteration process.

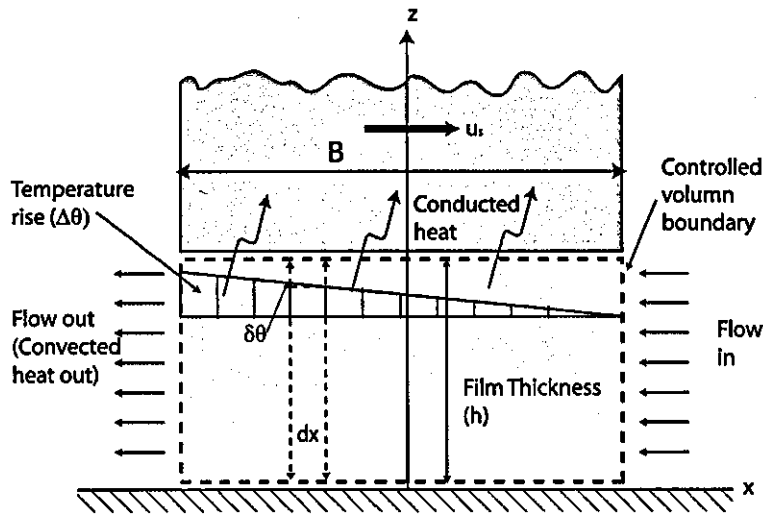


Figure 4.10 Heat flow within a lubricated contact

First, the relative significance of the terms in the right hand side of the equation must be determined in relation to the film thickness, which could be used to differentiate the mode of heat removed from the contact. This would also pave the way for a simplified analytical solution, since otherwise both terms on the right hand side of the energy equation (4.55) are retained.

Convection cooling happens when the heat is carried away along by the lubricant film as shown in Figure 4.10. Let the average fluid velocity be  $u_s/2$  and the maximum average temperature rise in the film will be  $\Delta\theta/2$ . Then, the convected heat flow across a distance  $dx$  at a position  $x$  is:

$$\rho C_p \frac{d\theta}{dx} dx \int_0^h \left(\frac{u_s z}{h}\right) dz = \rho C_p \left(\frac{d\theta}{dx}\right) \left(\frac{u_s h}{2}\right) dx \tag{4.57}$$

Taking into consideration the whole contact domain, which is  $-B/2 \leq x \leq B/2$ , and considering a linear temperature rise in the contact such that  $d\theta/dx = \Delta\theta/2B$ , then:

$$\frac{\rho C_p u_s h}{2} \left(\frac{\Delta\theta}{2B}\right) \int_{-B/2}^{B/2} dx = \frac{\rho C_p u_s h (\Delta\theta)}{4} \tag{4.58}$$

Therefore, the total convected heat through the contact can be given by equation (4.58). Heat within the film can also be removed away by conduction as shown in Figure 4.10. When the heat is carried away by conduction, then the solution assumes that the temperature gradient across the film varies linearly for each value of  $x$  rising from zero at its bottom surface to a value of  $\frac{\delta\theta}{h}$  at the top as shown in (Gohar 1988). This gives a parabolic temperature distribution across the film. Thus, the heat flow rate into the top surface through a column of width  $dx$  and height  $h$  is:

$$k_c dx \int_0^h \left( \frac{d^2\theta}{dz^2} \right) dz = k_c dx \left( \frac{\delta\theta}{h} \right) \quad (4.59)$$

Substituting:  $\delta\theta = x \frac{\Delta\theta}{B}$  as the temperature rises linear across the contact, into equation (4.59) the total conducted heat flow can be calculated as:

$$\frac{k_c \Delta\theta}{Bh} \int_0^B x dx = \frac{k_c \Delta\theta B}{2h} \quad (4.60)$$

This equation provides the heat removed by conduction. Substituting values from equations (4.58) and (4.60) into the energy equation (4.56), considering the whole contact domain:

$$\int_{-B/2}^{B/2} \int_0^h \eta \left( \frac{\partial v_x}{\partial z} \right)^2 dz dx = \frac{\rho u_s C_p h \Delta\theta}{4} + \frac{k_c (\Delta\theta) B}{2h} \quad (4.61)$$

Assuming that a linear velocity variation across the fluid film:

$$\frac{\partial v_x}{\partial z} = \frac{u_s}{h} \quad (4.62)$$

Thus, equation (4.61) becomes:

$$\frac{\eta u_s^2 B}{h} = \frac{\rho u_s C_p h \Delta\theta}{4} + \frac{k_c (\Delta\theta) B}{2h} \quad (4.63)$$

The temperature rise within the contact can be obtained from equation (4.63). However, it is known that when the film is thick such as in hydrodynamic lubrication the most dominant

heat removing mechanism is convection, where as under EHL conditions conduction is most prominent (Cameron 1966; Gohar 1988; Rahnejat and Gohar). If a condition can be imposed to distinguish the effective cooling method under prevailing circumstances, then the amount of calculations can be reduced, and an analytical solution can be established. The *Peclet* number, which is a dimensionless number, defined as the ratio of convected heat energy by the fluid to the thermal energy conducted by the adjacent solid surfaces can be used to ascertain the validity of the simplification made. By definition:

$$\text{Peclet Number } (Pe) = \frac{\text{Convected heat}}{\text{Conducted heat}} \quad (4.64)$$

Thus, from the above derivations:

$$Pe = \left( \frac{\frac{u_s h}{4} C_p \rho (\Delta\theta)}{\frac{(\Delta\theta) k_c B}{2h}} \right) = \left( \frac{\frac{u_s h^2}{2B}}{\frac{k_c}{\rho C_p}} \right) \quad (4.65)$$

The denominator of the right side of equation (4.65) is called diffusivity, which is a constant for a specific fluid. Diffusivity has the units  $m^2/s$  and for the lubricant oil of SAE 15W-40 used in the engine the diffusivity is  $7.38 \times 10^{-8} m^2/s$  at  $100^\circ C$  (Shell). Contact width ( $B$ ) for the piston ring – cylinder wall interaction is given by the ring width of  $2mm$ . Such that, the Peclet number variation during an engine combustion cycle is given in Figure 7.27. Therefore, both convection and conduction cooling are taken into consideration for the calculation of temperature rise within the contact.

Once the temperature rise ( $\Delta\theta$ ) is obtained by equation (4.63), the final temperature ( $\theta_e$ ) at contact is calculated using a relaxation method such as:

$$\theta_e = \theta_i + k_r \Delta\theta \quad (4.66)$$

Where  $\theta_i$  is the inlet temperature and  $k_r = 0.5$  (relaxation factor) for this case. Then the new viscosity corresponding to temperature  $\theta_e$  can be calculated using Vogel equation which is given by (Hamrock *et al*, 2004) as:

---

$$\ln(\eta) = -1.845 + \left( \frac{700.81}{\theta - 203} \right) \quad (4.67)$$

where  $\theta$  is the temperature in Kelvin and  $\eta$  is the viscosity in centi-poise, or by Barus equation as:

$$\eta = \eta_0 e^{\alpha p} \quad (4.68)$$

Where  $\alpha$  is the viscosity-pressure coefficient and  $p$  is the pressure. Then the minimum film thickness for the corresponding viscosity under these conditions can be found, if the total force acting on the contact is known. The detailed implementation of temperature effects at piston ring – cylinder wall interaction, using the above analysis is presented in section 5.5.7.

Even though almost all lubrication contacts are established based on Reynolds equation, it can be simplified according to the circumstances of the contact that will reduce the intensity of numerical techniques needed to solve them, as it has been discussed. This will enable modern computers to solve such an immense multi-physics numerical model within reasonable duration of time. The following Chapter is devoted to a discussion of incorporating these lubricated contacts to a commercially available multi-body dynamics software tool in an efficient and methodical manner which can be extended to any system that include kinematic relations and constraint reactions.

---

## 5 NUMERICAL MODEL DEVELOPMENT

### 5.1 Introduction

In the former chapters, theoretical basis used for multi-body dynamics, component flexibility and tribology within this thesis have been discussed, with particular reference to internal combustion engines. In this chapter these methods are combined to develop a multi-physics numerical methodology with a single cylinder engine model. Firstly, multi-body dynamics is used to develop the constrained rigid body inertial dynamics of the engine. This base model includes rigid body motions only, such as the translation of the piston, its secondary motions, angulations of the connecting rod, and rotation of the crankshaft. Then, selected rigid bodies are replaced with flexible components. These are the elements of the system that in practice are more prone to structural deformation, when subjected to the applied combustion gas force. The introduction of component flexibility lessens the stiffness of the model, while it makes it more realistic. Idealized primary joints used in the usual multi-body models such as revolute, translational, etc with well-defined motion trajectories and DOFs do not exist in real physical systems, which are subject to compliances offered by system flexibility and clearance. This also includes the reaction forces offered by the load bearing systems, which should be modelled in realistic tribological terms. Current multi-body dynamic analysis codes such as ADAMS, used in this thesis and widely in industry, do not possess these very important features, thus the analyses reported in literature using such approaches are usually devoid of practical significance, particular with regard to an in-depth scientific investigation.

Almost all contacts of an engine are ideally regarded as lubricated. The purpose, of course, is to minimize friction, wear and thus better efficient engines. One should also not underestimate the contributions made by the lubricant by removing the generated heat away from load bearing conjunctions, and thus enhance the thermal stability of engines.

Whilst the multi-physics approach expounded here includes a number of key disciplines in the same analysis, it must be noted that there are many other aspects of an IC engine that are not considered in depth during this analysis such as the behaviour of big-end bearing and the gudgeon pin interaction with piston, which also behaves in a complicated manner (Balakrishnan and Rahnejat 2005; Cho *et al*, 2003; Koizumi *et al*, 2000). Also, engine

---

housing flexibility can be quite influential in investigation of overall NVH performance in an IC engine (Garnier *et al*, 1999). This aspect is also not considered here. However, it is not possible to include all these effects into a single model with the available computational capabilities, and within sensible analysis times. Furthermore, very large and complicated models with many interactions are often not the most useful. Thus, those aspects included in the multi-physics analysis are deemed as the most influential from a combined dynamics, NVH and tribology viewpoint. The method employed also provides structural deformation data (within the elastic limit), which can be used for durability analysis (not discussed in this thesis), aside from its contributions to structural vibrations. Furthermore, within the NVH spectra, the thesis focuses on two key aspects: firstly, the engine order vibration that contribute to vehicle harshness at low frequencies, and secondly on vibrations of the piston-connecting rod-crankshaft sub-system, which are structure-borne. Thus, airborne noise is not considered, which may arise from inclusion of other attachments such as casing, covers, manifolds or other components of lighter construction. This, however, can readily be achieved by simple additions to the model.

## 5.2 Rigid Single Cylinder Model

### 5.2.1 The ADAMS Multi-body System Software

ADAMS (an acronym for Automatic Dynamic Analysis of Mechanical Systems) is a general purpose dynamic system simulation code and is a product of MSC Software. It automatically generates equations of motion of a mechanical model, based on constrained Lagrangian dynamics, described in Chapter 3. Thus, ADAMS is used to analyse a wide range of multi-body dynamic systems. It has become an industry-standard analysis code, and is used in all kind of industries such as automotive, aerospace, machinery and construction as reported by (Blundell 1991). It has an open architecture that allows users to create their own extension data set, features or subroutines (ADAMS/Solver).

In ADAMS a “marker” defines a position to which an orthogonal triad of unit vectors is attached. It identifies a location and its orientation with respect to a reference frame that can simply define geometry or a point of attachment, or centre of mass and inertial properties of a body (referred as a part in ADAMS). Orientation of any marker with respect to the global

---

frame of reference (a fixed model-based reference frame) is given by Euler Angles, whilst position of a marker is given either with respect to this global reference frame (GRF) or a local part reference frame (LPRF), depending on the manner of formulation chosen.

Input to the program consists of part geometry, mass and inertial properties, reference frame definitions, description of body types and compliances, topological and analytical constraints and the externally applied forces. The Graphical User Interface (GUI) can be used to create geometries or these can be imported from other design and analysis software.

Part translational and angular velocities, applied forces and reactions due to constraints (in terms of Lagrange's multipliers) are considered as state variables of the system. The constraint equations are predefined for each joint, when the model elements are specified. External forces and user-defined differential equations are defined as state variables and are appended to the set of equations. Description of method of formulation of equations of motion is given in Chapter 3.

### 5.2.2 Modelling Procedure in ADAMS

As the first step in the modelling procedure the reference coordinate system (GRF) and the system units (such as the SI units) are defined. Then, each part in the system model should be defined with its mass and inertial properties, the centre of mass location and part position and orientation with respect to a fixed global frame of reference (GRF). Each part possesses a certain number of markers, as previously mentioned. These markers move with the part. In every model there is a fixed part (referred to as Ground), which acts as the datum, with respect to which all motions are determined.

After defining all parts with appropriate properties, the required motions and constraints will

No	Description	Joint Type	Constraints						Total
			x	y	z	rx	ry	rz	
1	Crankshaft-ground	Revolute	*	*	*		*	*	5
2	Crankshaft-flywheel	Fixed	*	*	*	*	*	*	6
3	Crankshaft-connecting rod	Cylindrical		*	*		*	*	4
4	Piston-connecting rod	Universal	*	*	*		*		4
5	Piston-ground	Cylindrical	*		*	*		*	4
Total constraints									23

Table 5.1 List of constraints for rigid engine model

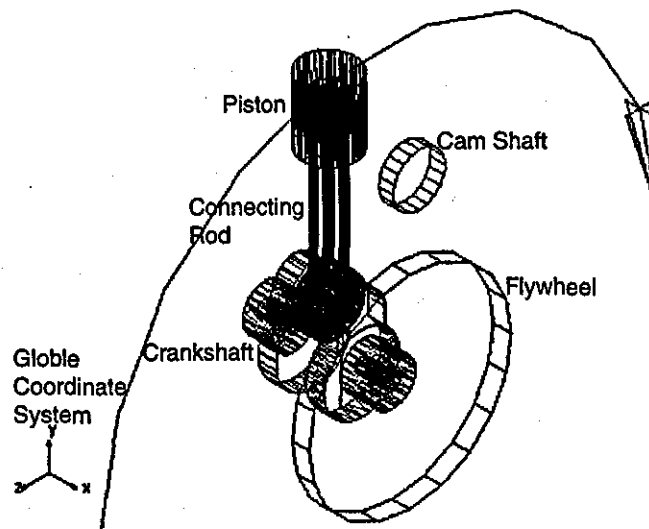


**Figure 5.1 Rigid body Engine Model**

be introduced between the parts to simulate required functional behaviour of real systems, being modelled. The standard joints in ADAMS include revolute, planar, cylindrical etc., which reduce the number of DOF of the system. Now the model is restricted to move in a way, which complies with the introduced constraints and imposed motions, according to the kinematic relations needed. In Table 5.1 a list of basic joint types used to model the rigid single cylinder engine model is given.

Having defined the constrained motions in the model, the next step is to introduce the external and internal forcing elements of the system. These forcing elements can be in the form of a force or a torque, such as the combustion gas force and the load torque. These forcing elements can be imposed as a user-defined function or a standard forcing function. Internal forces such as springs, dampers etc, are forms of reaction or restoring forces. The action force on one element essentially creates the reaction from another element within the system. The basic rigid engine multi-body system is shown in Figure 5.1.

ADAMS uses Gruebler-Kutzbach expression to calculate the degrees of freedom of the assembled model of the system:

$$DOF = 6 \times (\text{Number of parts} - 1) - \sum \text{Constraints} \quad (5.1)$$

In Table 5.1 the list of constraints are given for the single cylinder rigid-body engine model. In this model, there are 23 constraints and 5 parts, including the ground, here representing the

No	Description	Material	Mass(kg)	$I_x$ (kgmm <sup>2</sup> )	$I_y$ (kgmm <sup>2</sup> )	$I_z$ (kgmm <sup>2</sup> )
1	Flywheel	EN353 (Carbon steel)	85.23	1329590	1329590	2454628
2	Piston	LM12 (Cast Aluminum)	0.45	1950	1950	462
3	Connecting rod	EN100 (Carbon Steel)	2.01	45305	849	45745
4	Crankshaft	EN353 (Carbon Steel)	14.96	246534	236228	30071

**Table 5.2 List of materials of engine components**

engine block. If these are substituted into equation (5.1), the number of DOF becomes one, which represents a kinematic system, because the motion of the crankshaft due to the variation in combustion process is prescribed. A system having no degrees of freedom, after prescribing a motion is regarded as kinematic.

### 5.3 Basic Components in the Engine

In this analysis a single cylinder 4-stroke E6 Ricardo experimental type engine is modelled, which has a bore of 3 inches, and a stroke of 4.375 inches and produces a maximum power of 13 Bhp at speed of 3000 rpm and a maximum torque of 40 Nm at 1800 rpm. The test is carried out at the crankshaft speed of 1800rpm. Due to complexity of the problem, modelling is confined to its basic components in the dynamic analysis of piston-connecting rod-crankshaft sub-system, which is necessary for the prediction of engine torsional NVH behaviour. Thus, the parts of interest are: the flywheel, crankshaft, connecting rod and piston (see Table 5.2). The solid geometries of various components are modelled in Solid Edge and imported into ADAMS as parasolid files.

The physical engine was disassembled into its components and exact dimensions were taken. Later flexibility was introduced for the necessary parts using MSC/Nastran. The structure of the parts analysed and the global frame of reference are shown in Figure 5.1.

For all the parts shown in Figure 5.1 and listed in Table 5.2, the mass and inertial properties, geometric specifications, the location and orientation of the local part frames of reference are defined. Critical locations, such as points connecting other components through joints and points where external forces are applied are also defined by inserting markers in relevant locations. Materials for each component are carefully selected to be compatible with the

actual values. List of materials used and the mass and inertial properties are given in Table 5.2.

### 5.3.1 Flywheel

Flywheel acts as a source of potential energy in an IC engine. Its heavy weight, bolted to the crankshaft, helps to smoothen the power flow fluctuations by resisting sudden changes in the crankshaft rotational speed due to the applied varying combustion power strokes.

Some engines have dual mass flywheels, which consist of two separate parts called the primary and the secondary inertias. These two parts are usually connected by a spring-damper system with appropriately selected stiffness and damping properties (Harry 1994). When the electrical systems of automobiles evolve from 12 volts to 42 volts for the future generation of engines, the starter and the generator can be built as part of a multi-purpose flywheel (W.Pullrabek 2003). In the Ricardo E6 engine the flywheel is rigidly connected to the crankshaft by means of a threaded joint, which is represented numerically (in the model) by a rigid joint, with no relative DOF.

Normally the flywheel is connected to the gearbox through a clutch, ensuring a smooth engagement between engine and the gearbox. This thesis is mainly concerned with engine dynamics, thus the effect of the clutch is not considered. A torque element, acting opposite to the direction of rotation, is applied to the flywheel in order to represent the resisting torque on the engine, which is detailed in section 5.5.2.

### 5.3.2 Crankshaft

Crankshaft represents the transmitting torque medium through which the engine work output is supplied to the external system. The mass and inertial properties of the crankshaft are given in Table 5.2. The crankshaft rear-end is connected to the flywheel. In most engines, crankshaft front-end is connected to a pulley through a torsional damper. However, in this particular engine there is no such damper and a pulley is attached to the crankshaft at the front-end. Figure 5.2 shows the crankshaft of the E6 engine.

---

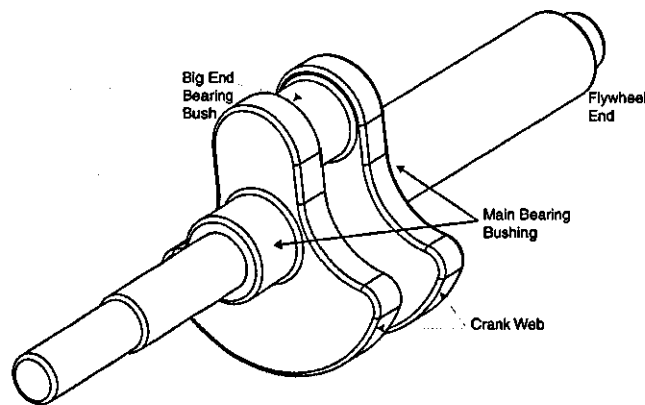


Figure 5.2 Single cylinder engine crankshaft

### 5.3.3 Connecting Rod

The connecting rod transfers the combustion gas force from the piston to the crankshaft. One end of the connecting rod is connected to the piston through a gudgeon pin and the other end is connected to the crankshaft (see Figure 5.3). The connection between the piston and the connecting rod is represented by a universal joint in the model, translating with the piston. The connection between the crankshaft and the connecting rod is represented by a cylindrical joint used in ADAMS, which rotates about the crank axis. Therefore, the connecting rod can be regarded as an articulated mass in combined translation and rotation. The universal joint at the piston end does not represent the gudgeon pin, but it ensures that the system maintains its intended function, whilst eliminating any redundant constraints.

### 5.3.4 Piston

Pistons are subjected to large temperature variations such that thermal expansions are apparent. There should be a clearance in between piston and the cylinder wall in order to compensate for this thermal expansion. This clearance may lead to lateral motions, referred to as secondary motions other than the intended transverse primary motion. These can lead to an NVH phenomenon known as piston slap (Haddad and Howard 1980). Initially, the piston is connected to the ground by a cylindrical joint allowing it to move in the vertical direction (allowing translation only) and by a universal joint connected to the connecting rod. The joints used for the piston assembly are listed in Table 5.1. Later the translational joint was replaced by the four thrust forces acting on the piston skirt in the lateral direction, which are

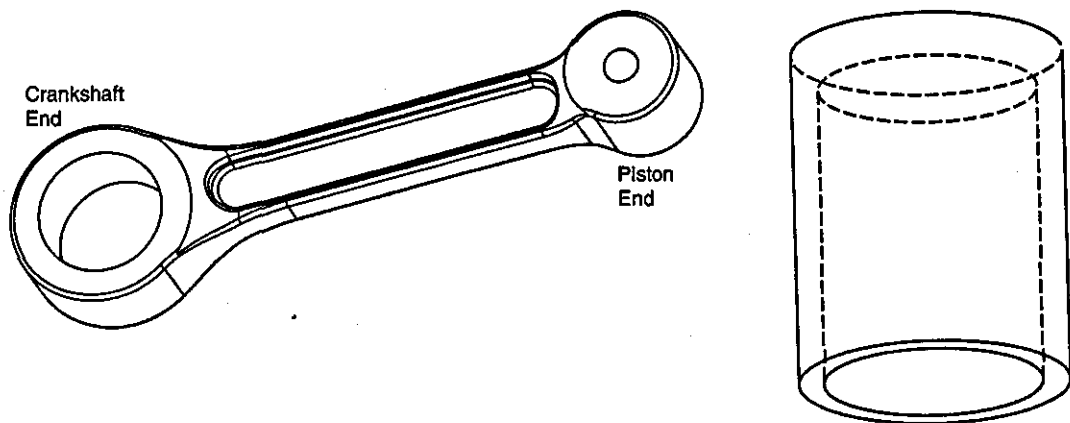


**Figure 5.3 Connecting rod and Piston**

generated due to piston skirt-to-cylinder wall interactions as discussed in section 5.5.5. A planar joint, restricting the piston to move in the  $yz$  plane is used (see Figure 5.1).

## 5.4 Flexible Engine Components in ADAMS

The kinematic relations in a mechanism provide the behaviour of its various components in the global frame of reference. Basic joints in ADAMS constrain the motions of components in specified manner. These rigid body motions are large displacements (of the order of meters or radians). However, there are micrometers to sub-millimetres range elastic deformations, which take place in the elastic components, depending on its modal behaviour under applied loads. If components in a mechanism can be represented with flexible properties, then these motions can be identified and their inclusion renders a more representative model of the physical system.

Flexibility of a component is introduced via use of FEA, converting the component into a finite number of nodes, connected by Euler beams. The discretization of a flexible component into a series of finite elements represents an infinite number of DOF with a finite, but very large number of DOFs. For a better representation of a component there should be a large number of elements in the finite model that would be sufficient to capture all the major modes that can be excited during its operation. However, a finite element model with such an accuracy needs a significant computational memory, which renders it impractical. Therefore, it is necessary to use a representation method to condense this large finite element model into an acceptable size, which can work with the available computing capability.

In this regard, ADAMS uses Component Mode Synthesis (CMS) in one of its modules, called ADAMS/Flex to introduce a new flexible inertial element called FLEX\_BODY that has been created by transforming the large number of DOFs of a component into a smaller number of modal DOFs, using the modal truncation method outlined in section 3.3.4. The most important step in this transformation is matching the properties such as mass, centre of mass location, moment of inertia and natural frequencies of the actual component with the created flexible element that could not be achieved by previous reduction methods such as the Guyan reduction (ADAMS/Solver).

Component Mode Synthesis is used to find the global elastic deformation of the engine components. However one should not be confused this with the localized elastic deformation that takes place due to high lubricant pressures at lubricated contacts known as elastohydrodynamics (EHL). Since these deformations are localized only to the contact conjunction its effect upon the system kinematics can be neglected as long as the net contact reaction force is included correctly.

#### 5.4.1 Modelling Procedure

The crankshaft, connecting rod and the flywheel are considered as flexible components of the engine during the model development process. The software tool Nastran was used for FEA representation of the flexible components in the model. The components' CAD geometries were built in Solid-Edge, which is a CAD software tool and then exported into Patran, which is the pre-processor of Nastran FEA software. Parasolid file format is used to transfer the CAD model information between the various software packages. In Patran, the geometry is discretized into a number of tetrahedral quadratic elements, using *iso-mesh* meshing technique, which maintains a constant length between the nodes, wherever possible (Figure 5.25). During this process the required elemental density is obtained by comparing the system natural frequencies through analysis with some experimental findings.

First, the component was meshed with very high element density and then the obtained natural frequencies through calculation of eigen-values were compared with that of experimental values acquired through impact hammer test data. Element density was gradually decreased, while carefully monitoring the deviation of the calculated natural frequencies from the experimental values. The minimum mesh density that still holds good

---

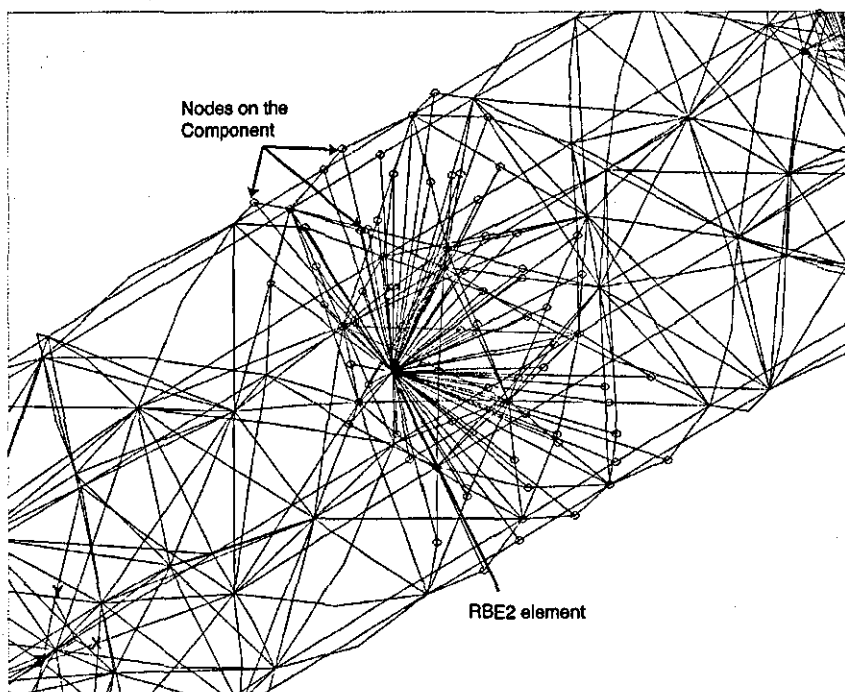


**Figure 5.4 Enlarged view of the journal bearing in the crankshaft**

for the correlation between the calculated and experimented natural frequencies was selected as the optimum mesh density. The procedures followed for the impact tests are explained in section 6.5.

Material properties for all components are given in Table 5.3. The boundary conditions are defined using an RBE2 element, which transfers the vector summation of the resulting displacement of the selected nodes into a single node, which is a rigid body element (MSC/Nastran). Therefore, the boundary conditions imposed on the crankshaft at locations of the main crankshaft support bearings, the big-end bearing and the flywheel are represented by such RBE2 elements. Figure 5.5 shows the meshed crankshaft, including the RBE2 elements at the bearings and the flywheel positions. A more clear illustration can be seen in Figure 5.4, showing linking of nearby nodes into the rigid body element (RBE2). These RBE2 elements can be used to connect a FLEX\_BODY with a neighbouring rigid body, using the ADAMS basic joints, or it can be used as a point, where an external force is applied.

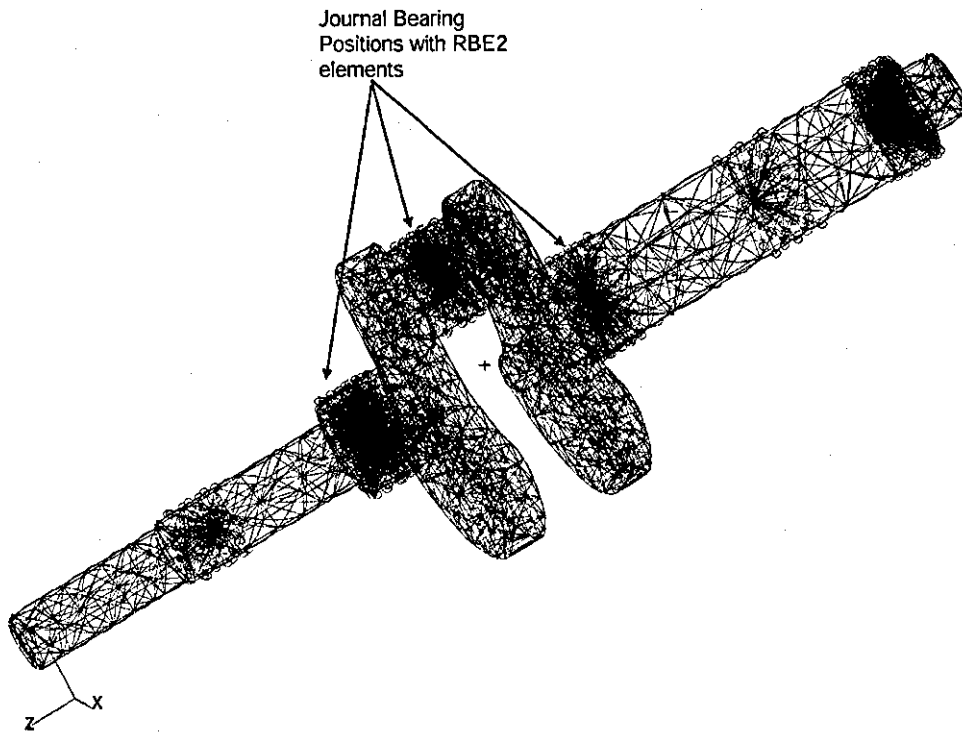


Figure 5.5 Meshed crankshaft with boundary conditions

Component	Crankshaft	Flywheel	Connecting rod
Nodes	7519	4848	6009
Elements	4322	2741	3399
Young's modulus (GPa)	205	205	205
Poisson's ratio	0.29	0.29	0.29
Density ( $kgm^{-3}$ )	7850	7850	7850
Volume (ml)	1959	10857344.2	256.2
Mass (kg)	15.38	85.23	2.011
Surface area ( $mm^2$ )	174464	452389.34	51475

Table 5.3 Material and nodel properties for engine components

(Material as well as elastic properties of the piston is not included since it is considered as a rigid body)

These rigid body nodes are used as the juncture nodes in the process of sub-structure coupling as discussed in section 3.3.2. Nastran is used to solve the eigen-value problem for the normal modes and the constrained modes. These truncated linearly independent shape vectors for each component are then transferred into ADAMS, using the ADAMS/Flex module, which is called the *Modal Neutral File* (MNF).

Frequency No	Engine Components			
	Crankshaft	Flywheel	Con Rod	Piston
1	415	1345	569	9208
2	513	1345	740	9333
3	1002	2216	1376	13736
4	1097	2808	1864	14125
5	1496	2809	3805	14909
6	1564	4431	4375	16993
7	2221	4437	4599	17136
8	2325	4589	5086	18377
9	2937	4590	6903	18892
10	3174	5201	7687	19244
11	3316	5204	7917	19346
12	3545	5759	8919	20942
13	3603	5760	9373	22297
14	3979	6550	10286	23241
15	4208	6552	11422	23374
16	4348	7061	13336	23763
17	5240	7063	14675	24525
18	5287	7467	16886	25399
19	6052	7615	17323	25841
20	6105	7617	18874	26497
21	6944	7829	19379	26882
22	7425	8628	19916	27178
23	8302	8629	20489	27663
24	8397	9070	21486	28364
25	8690	9073	21658	30078
26	8783	9441	22893	30173
27	9041	9444	22918	30823
28	9543	9887	23396	32492
29	9818	9887	23647	33007
30	10076	10726	24131	33166
31	10274	10762	25117	33176
32	10490	10782	25406	34407
33	10872	10783	26247	34777
34	12112	10837	27975	35236
35	12800	12008	29166	35369
36	13071	12011	29821	35602
37	13916	12034	30150	35981
38	13918	12034	30262	36243
39	14432	12267	30528	36465
40	14474	12268	30710	36865
41	14702	12472	32169	37681
42	15012	12475	32516	38218
43	15092	12984	32845	38456
44	15426	12992	33012	38695

**Table 5.4 Frequencies calculated by FEA**

As mentioned in section 3.5, the most prominent excitations of a single cylinder engine are its engine orders, which are induced by the combustion gas force. On the other hand, inertial imbalance also contributes to untoward motions. The experimental E6 engine was operated at

1800 rpm. Thus, the fundamental source of excitation is at half-engine order for this 4-stroke engine; i.e. at 15Hz for the crank speed of 1800 rpm. Therefore, the main excitations occur below 200Hz (about 6<sup>th</sup> engine order multiple) as can be seen in Figure 3.8. The first 66 flexible modes for the crankshaft, the first 32 modes for the connecting rod and the first 56 modes for the flywheel are considered during the MNF creation, which goes up to the natural frequencies of about 18000Hz. Table 5.4 shows the first few natural frequencies of these engine components. It can be seen from the table that the first natural frequency of the Cast Aluminium piston is around 9208Hz, which is a far higher value than the significant engine order multiples.

This leads to the conclusion that the piston behaves in a rigid manner in the system. Therefore, hereinafter it is considered as a rigid body. Table 5.3 lists the material properties and model information for the flexible components. The connecting rod, crankshaft and the flywheel have similar material properties.

As already discussed the inclusion of flexibility into the model is mostly handled by FEA, during which the component is transformed into condensed mass and stiffness matrices. Such a model can produce sufficient modal representation within the frequency range of interest with a minimum computational effort. The increase in the number of elements that the component is divided by probably would enhance the validity of the obtained mode shapes. However, concurrently, it would intensify the modal analysis procedure, which creates difficulties in solving the kinematic equations in ADAMS. As there are three flexible components in the model, reduction of number of elements even by a small percentage can save enormous computation times during a simulation, involving usually thousands of time steps.

As a convention, the rigid body element is not directly connected to a neighbouring body through a normal joint or does not apply a force to it. Instead, a dummy part, which has a very low mass (typically  $2.5 \times 10^{-5}$  kg in this model, not to unduly affect the system dynamics) is attached to the rigid body element, using a fixed joint (completely constrained). Then, the forces and the necessary joint compliances acting on the flexible body at the attachment points are applied onto these dummy parts. The dummy parts attached to the rigid elements can be seen in Figure 5.6.

---

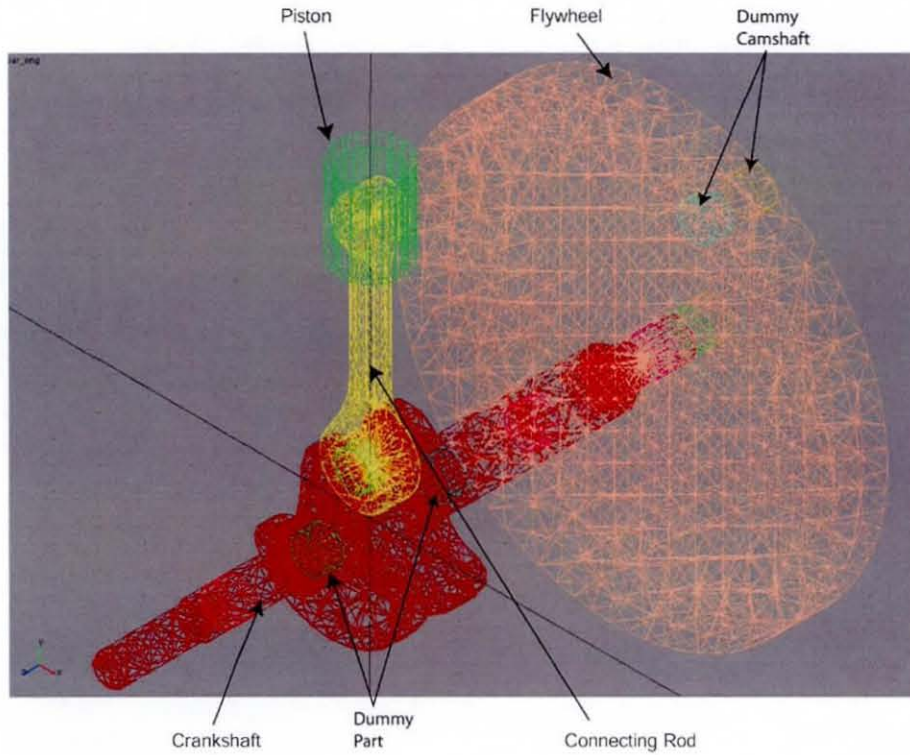


**Figure 5.6 Flexible engine model in ADAMS**

Two additional dummy parts are used other than dummy parts at rigid elements, called “*Dummy camshaft 1*” and “*Dummy camshaft 2*” as shown in Table 5.5. These are attached to the ground through revolute joints and connected to the crankshaft through a coupler, which is a joint primitive used in ADAMS to connect two revolute joints according through a set rotational ratio. The only purpose of these dummy parts is to provide proper positioning of the engine in its 4-stroke combustion cycle during its operation. Therefore, these elements act as the camshaft in the engine model, even though it is not modelled with its exact inertial properties. The “*Dummy camshaft 1*” rotates with the coupling ratio of 1:2, whereas the “*Dummy crankshaft 2*” rotates with the coupling ratio of 1:148. The former has been used to define the position in the combustion cycle for many calculations carried out during the simulation studies, whilst the latter is used to calculate the combustion gas force, coupled with the crank angle, as discussed later.

No	Part description	Mass (kg)	Moment of Inertia (kgmm <sup>2</sup> )		
			I <sub>xx</sub>	I <sub>yy</sub>	I <sub>zz</sub>
1	Crankshaft (flexible)	15.0	246534	236228	30071
2	Connecting Rod (flexible)	2.0	45305	849	45745
3	Flywheel (flexible)	85.2	1329590	1329590	2454628
4	Piston	0.5	1950	1950	462
5	Dummy camshaft 1	-	-	-	-
6	Dummy camshaft 2	-	-	-	-
7	Ground	-	-	-	-
8	Crank dummy1	-	-	-	-
9	Crank dummy2	-	-	-	-
10	Crank dummy3	-	-	-	-
11	Crank dummy4	-	-	-	-
12	Crank dummy5	-	-	-	-
13	Crank dummy6	-	-	-	-
14	Crank dummy7	-	-	-	-
15	Crank dummy8	-	-	-	-
16	Crank dummy9	-	-	-	-
17	Connecting rod dummy1	-	-	-	-
18	Connecting rod dummy 2	-	-	-	-
19	Flywheel dummy	-	-	-	-

Table 5.5 List of parts used in the model

## 5.5 Applied Forces

### 5.5.1 Combustion Gas Force

The gas pressures generated by the process of combustion are applied to the piston crown as a single component force. This force is calculated by multiplying the instantaneous combustion pressure with the crown surface area of the piston and introduced as a single component force, acting orthogonally there (along the centre axis of the piston). The gas force variation is shown in Figure 5.7. The “*Dummy camshaft 1*” is connected to the crankshaft through a coupler, which has a ratio of 1:2. This implies that for every two revolutions of the crankshaft, the *Dummy camshaft 1* rotates once, commencing from  $-180^{\circ}$  to  $180^{\circ}$  as shown in the figure. According to the cam angle, the piston gas force is calculated using an Akima spline fit.

The Akima Fit (ADAMS/Solver) is used in ADAMS to fit scattered data into a continuous function. Both the combustion gas force and the crank angle were recorded in the same time domain during the data acquisition from the test engine (see chapter 6). Then, the combustion

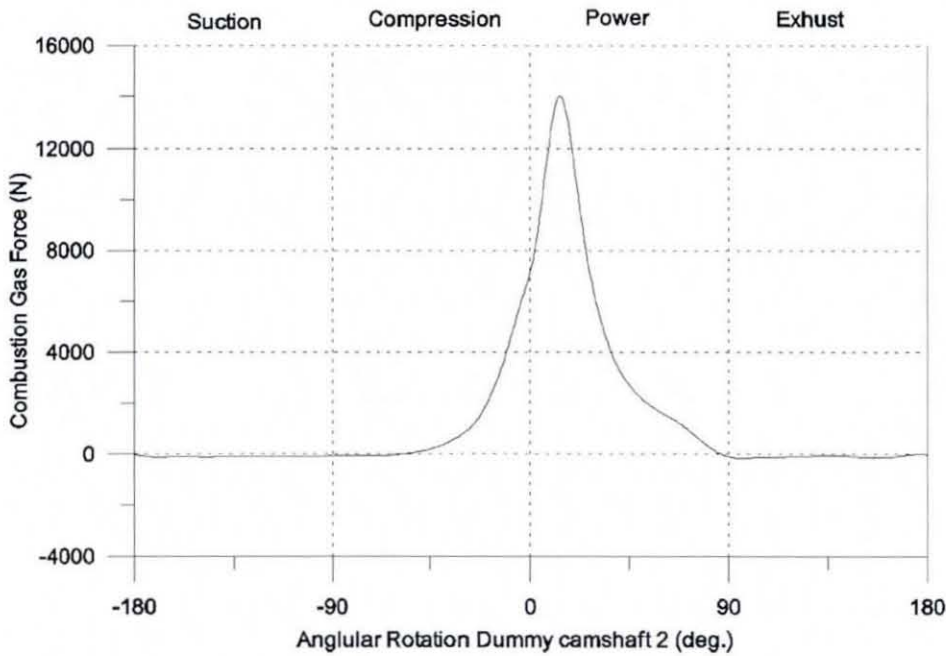


**Figure 5.7 A cycle of combustion gas force**

gas force variation is transformed into the cam angle domain as is shown in Figure 5.7. This experimental pressure data can be converted into a continuous linearly varying function of cam angle, using the following expression, which is then used in the numerical model to represent gas pressure force as a function of cam angle.

$$(AKISPL(.par\_eng.cam\_orient,0,spl\_comb, 0))$$

Where *Cam\_orient* is the cam angle and is calculated based on the camshaft rotation. *Spl\_comb* is the combustion data taken from experiments. Then, the force is obtained by multiplying the pressure by the piston crown surface area of  $4.3e-3 \text{ m}^2$ .

However, in an actual engine, there can be slight differences from one combustion cycle to another as shown in Figure 5.8, which affects the NVH characteristics of the engine, which can be captured by implementing many number of combustion cycles into the model. This cycle-to-cycle combustion variation is minimized in more modern engines, and more noticeable in older engines such as the E6. Thus, using a similar approach as described earlier, 74 measured combustion gas force cycles were inserted into the model. The “*Dummy camshaft 2*” is connected to the crankshaft through a coupler with a ratio of 1:148 such that it rotates one revolution per 148 revolutions of the crankshaft, which is used to introduce 74

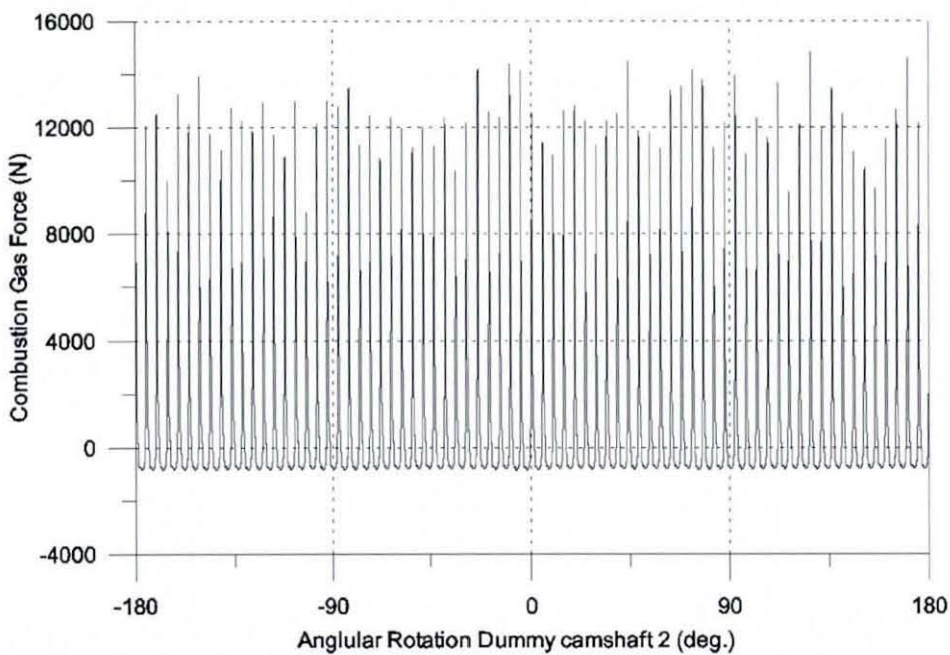


**Figure 5.8 Combustion gas force variation for 74 engine cycles**

combustion cycle data into the model. Figure 5.8 shows the combustion gas force variation for 74 combustion cycles with respect to the angular position of the “*Dummy camshaft 2*”.

The model has the flexibility to run either with repeating the same combustion gas force cycle or with repeating blocks of 74 combustion gas force cycles, including cycle-to-cycle variations. This second feature is very useful for the study of engine mis-firing, which is of course not within the scope of this investigation. Most of the analyses in the model are carried out using the earlier method which does not consider the cycle-to-cycle combustion variation.

### 5.5.2 Engine Load Torque

The resisting torque applied to the engine is considered as the load torque. In general, load torque multiplied by the angular velocity gives the power output of an engine. The engine load torque depends on many factors such as the engine speed, air-fuel ratio, throttle position, etc. Figure 5.10 shows the load torque variation for the E6 engine for an optimum air-fuel ratio and with full throttle. Again the load torque is applied to the model as a Single Component Torque in the ADAMS formulation, using an Akima Fit to represent the torque variation as a continuous function of crank angular velocity as follows:

*AKISPL(ang\_vel\_fly, 0, spl\_trq, 0)*

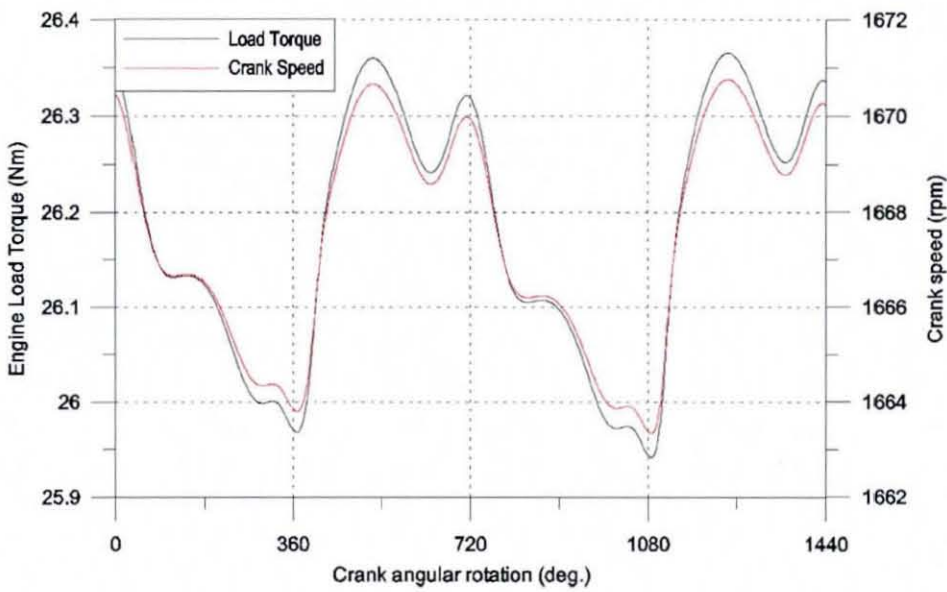


**Figure 5.9 Engine load torque and crank speed variation**

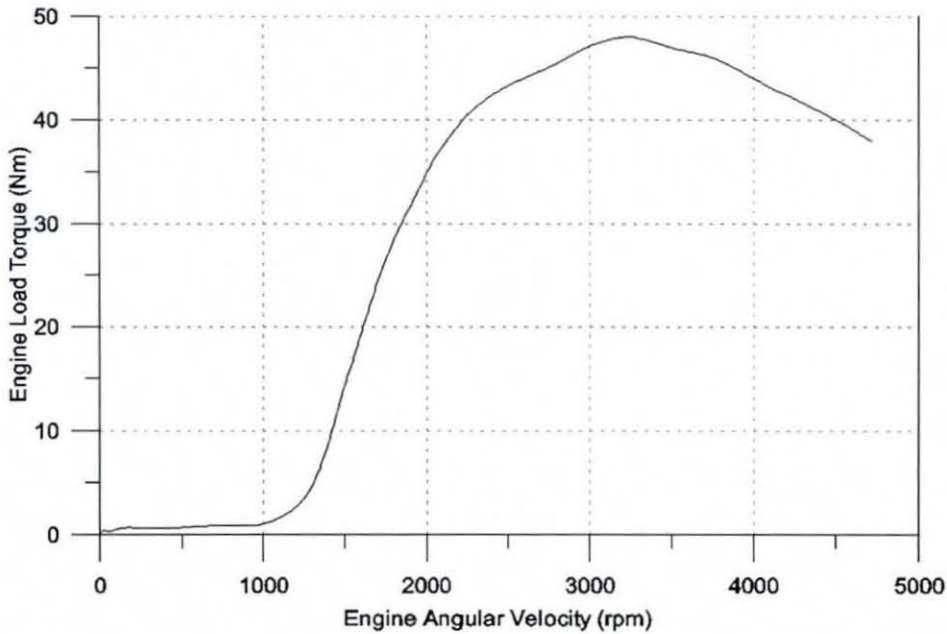


**Figure 5.10 Spline fitted engine load torque variation with angular velocity**

Where  $ang\_vel\_fly$  is the crankshaft angular velocity and  $spl\_trq$  is the torque data taken from experiments. Therefore, for every angular speed there is a corresponding load torque, which is applied to the flywheel end of the crankshaft opposite to the direction of crankshaft rotation. Figure 5.9 shows the load torque and the crank speed variation for two combustion cycles (a crank angle rotation of  $1440^\circ$ ).

No	Description	Notation	Source
1	Viscosity	$\eta$	Constant (18 Pa.s)
2	Bearing length	$L$	Cons. (40mm)
3	Bearing radius	$r_b$	Cons. (30mm)
4	Bearing clearance	$c$	Cons. (30 $\mu$ m)
5	Journal eccentricity	$dx, dy$	From ADAMS
6	Angular velocity	$\omega_b$	From ADAMS

**Table 5.6 Engine main bearing details**

### 5.5.3 Main Bearing Reaction Force

The crankshaft is connected to the engine housing by two journal bearings. With known kinematic relations, thus solution for lubricant behaviour can be sought through Reynolds equation, as discussed in section 4.3.1. The lubricant reaction forces are represented by a General Force Vector element in ADAMS, which has 3 force and 3 torque components. The bearing is assumed to be a short-width bearing, even though the diameter ( $2r_b$ ) to length (L) ratio of the bearing is actually 1.5, which is less than the typical limiting value of 2 (Hamrock *et al*, 2004). However, (Pinkus and Sternlicht 1961) has compared the finite-width solution with short-width approximation and results are plotted as shown in Figure 2.8, which shows that at low eccentricity ratios and high Sommerfeld numbers, short-width approximation deviates from the finite length solution by a negligible amount. A constant viscosity of 0.018 Pa.s and an initial clearance of 30  $\mu$ m are used for the calculation of the lubricant reaction force (other parameters used are listed in Table 5.6)

A separate Fortran subroutine is written to calculate the bearing reaction forces. ADAMS needs these reaction forces at the two main crankshaft support bearings in order to generate the Jacobian matrix for the iteration in each time step. ADAMS needs to call this subroutine twice during each iteration. Crankshaft pin (journal) displacement in the  $x$ -direction ( $dx$ ) as well as in the  $y$ -direction ( $dy$ ) and the crankshaft angular velocity ( $\omega_j$ ) are the main parameters that ADAMS passes into the subroutine at each call in relation to the bearings. Inside the subroutine the eccentricity ( $e$ ), the eccentricity ratio ( $\epsilon$ ), the angle of inclination of the line of centres to horizontal ( $\theta$ ) and journal surface velocity ( $u_j$ ) are calculated as shown below ( Figure 5.11).

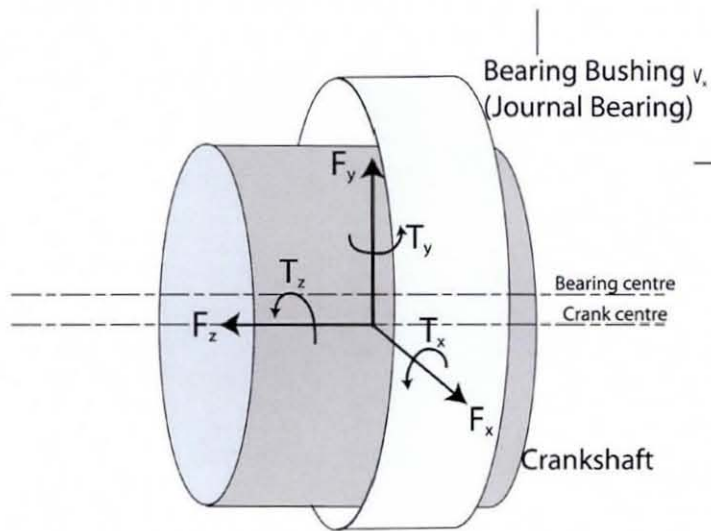


Figure 5.12 General force vector at main bearing

$$e = \sqrt{dx^2 + dy^2} \tag{5.2}$$

$$\varepsilon = \frac{e}{c} \tag{5.3}$$

$$\theta = \tan^{-1} \left( \frac{dy}{dx} \right) \tag{5.4}$$

$$u_j = r_j \omega_j \approx r_b \omega_j \tag{5.5}$$

Having calculated these values, equations (4.11) and (4.12) are used to calculate the force components acting along the line of centres ( $W_x$ ) and perpendicular to it ( $W_z$ ) (Figure 5.11), followed by the calculation of force components  $F_x$  and  $F_y$ . These are the values that are returned back into the ADAMS core inertial dynamics model as components of the General Force Vector. Figure 7.12 in chapter 7 shows the total bearing load variation in both front end bearing, as well as flywheel end bearing.

### 5.5.4 Main Bearing Friction Torque

The friction torque at the main bearing is generated due to the viscous action of the lubricant. The two contacting bodies; the journal and the bearing bushing have relative motion (in fact

No	Part I	Part J	Constraint type	Number of constraints
1	Crank dummy 1	Connecting rod dummy 2	Cylindrical	4
2	Piston	Ground	Planer	3
3	Connecting rod	Connecting rod dummy1	Fixed	6
4	Connecting Rod	Connecting rod dummy 2	Fixed	6
5	Crankshaft	Crankshaft dummy 1	Fixed	6
6	Crankshaft	Crankshaft dummy 2	Fixed	6
7	Crankshaft	Crankshaft dummy 3	Fixed	6
8	Crankshaft	Crankshaft dummy 4	Fixed	6
9	Crankshaft	Crankshaft dummy 5	Fixed	6
10	Crankshaft	Crankshaft dummy 6	Fixed	6
11	Flywheel dummy	Crankshaft dummy 6	Fixed	6
12	Flywheel	Flywheel dummy	Fixed	6
13	Flywheel dummy	Crankshaft dummy 7	Hook	4
14	Crankshaft dummy 8	Crankshaft dummy 9	Hook	4
15	Crankshaft dummy 2	Ground	Planer	3
16	Crankshaft dummy 4	Ground	Planer	3
17	Dummy camshaft 2	Ground	Revolute	5
18	Dummy camshaft 1	Ground	Revolute	5
19	Crankshaft dummy 9	Ground	Revolute	5
20	Connecting rod dummy 1	Piston	Revolute	5
21	Crankshaft dummy 7	Crankshaft dummy 8	Translational	5
22	Crankshaft	Dummy camshaft 1	Coupler	1
23	Crankshaft	Dummy camshaft 2	Coupler	1
<b>Total</b>				<b>108</b>

**Table 5.7 Holonomic and non-holonomic constraints**

the bushing is stationery). This relative sliding motion causes shearing of the lubricant, resulting in a resisting force, which is given in equation (4.14).

With the short bearing approximation, the aforementioned equation can be reduced to equation (4.15). The friction force is multiplied with the journal radius to calculate the friction torque. These calculations are performed in the same subroutine (*gfosub* see Figure 5.25), also used to calculate the bearing reaction forces. The calculated friction torque is then passed back into the ADAMS main code as the torque component about the z-axis for the *General Force Vector*, which acts opposite to the direction of crankshaft rotation.

The General Force Vector, acting on the bearing is illustrated in Figure 5.12. The forces in the x-direction ( $F_x$ ) and the y-direction ( $F_y$ ), and the friction torque about the z-direction ( $T_z$ ) are calculated by the subroutine *gfosub* and passed back into ADAMS. The crankshaft at bearing positions is constrained to move only in the xy plane by introducing planar joints

(joint numbers 15 and 16 in Table 5.7). There is no force component in  $z$ -direction in the *General Force Vector*, as this is taken by the planar joint, while restricting any motion of crankshaft in  $z$ -direction at the bearings' positions. Figure 5.13 shows the friction torque variation at the two main bearings during a combustion cycle.

### 5.5.5 Piston Skirt Interaction with Cylinder Wall

The piston in the IC engine is a component subjected to many axial and lateral forces, such as the combustion gas force, friction force between the piston and the cylinder bore or liner, as well as the side forces from the cylinder wall (on the major thrust and anti-thrust sides).

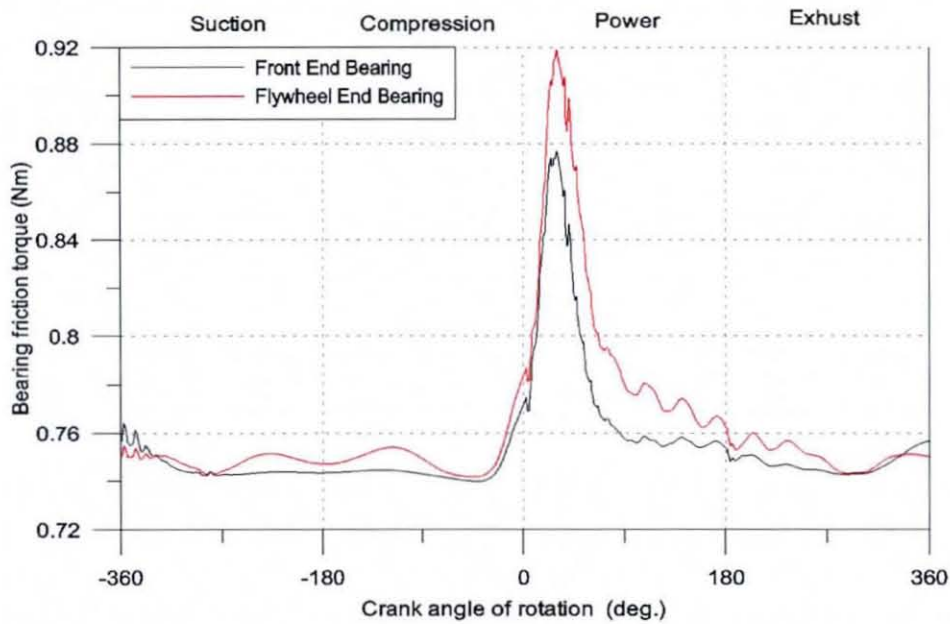


**Figure 5.13 Main bearing friction torque**

These forces also include friction force from piston ring, reaction forces from the gudgeon pin and the inertial forces due to the piston and the gudgeon pin. As mentioned earlier, it is assumed that the piston behaves in a rigid manner in the cylinder and it does not undergo large elastic deformations (due to global thermo-elastic effects). However, it can be subjected to localized elastic deformations, due to generated lubricant pressures in the various contact conjunctions.

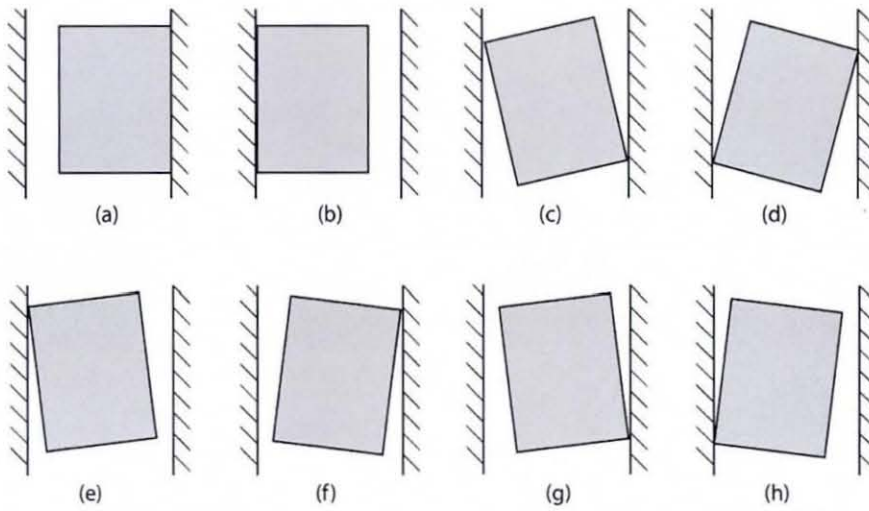


Figure 5.14 Possible piston modes inside the cylinder

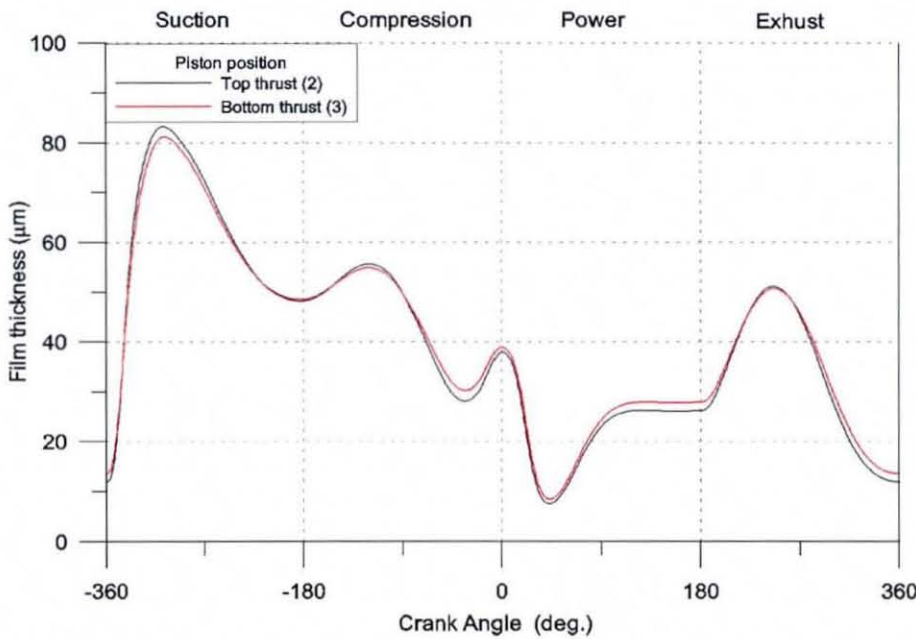
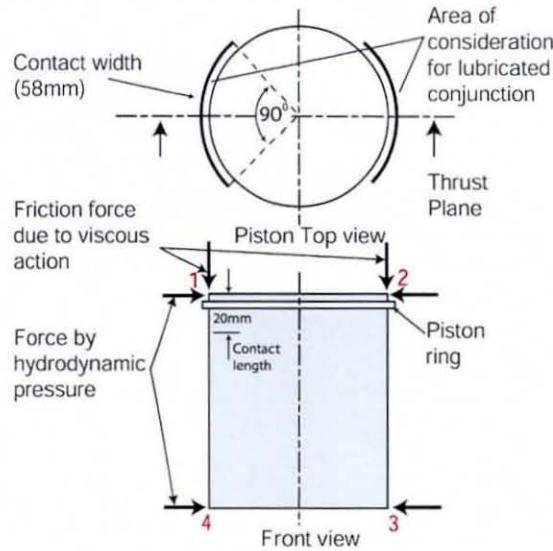


Figure 5.15 Minimum film thickness variation at piston edge

Piston skirt-cylinder wall interaction is sought by solving Reynolds equation for an iso-viscous regime of lubrication with known kinematic conditions and lubricant rheology. Assuming that the piston behaves in a rigid manner inside the cylinder, the possible modes of piston motion can be obtained as shown in Figure 5.14, depicted by (Haddad and Tjan 1995).



**Figure 5.16** Forces acting on the piston skirt

According to these configurations almost all the time piston forms a wedge effect (contact) with the cylinder wall by its edges to a varying degree of conformity, while at configurations (a) and (b), one side of the piston completely touches the cylinder wall as an exception. If kinematics of the system are known, the piston misalignment and lubricant film thickness, sliding velocity, etc can be obtained for each edge of the piston, which can then be used to calculate the thrust force at various locations within the cycle.

For this analysis, it is considered that the piston is free to move only in the  $xy$  plane, as all the forces acting on the piston are almost symmetrical about the  $xy$  plane. This is a reasonable approximation, used by many researchers (Cho *et al*, 2002; Dursunkaya and Keribar 1992; Haddad 1995), and simplifies the analysis. This condition is imposed on the piston by introducing a planar joint between the ground and the piston (see Table 5.7).

As shown in Figure 5.16, one quarter of the piston circumference, symmetrical about the thrust plane is considered for the contact as its width. This width of about 58mm and of length 20mm along the piston skirt is considered as the contact domain for the calculation of force at each edge of the piston, according to the proposed model. The length of the contact is selected by considering the contact pressure distribution under critical conditions. Figure 5.17 shows the contact pressure variation for the sliding speed of  $7500\text{mms}^{-1}$  and with various approaching velocities (varying squeeze effect due to piston secondary motions), indicating a minimum film thickness of  $4\mu\text{m}$  (see Figure 5.15), in which a maximum thrust force of

about 300N is obtained. From the figure, it is clear that the pressure starts to rise from -10mm and diminishes at 4mm. Even at these extreme conditions there is no significant pressure beyond the 10mm limit. Therefore, a skirt length of 20mm is a reasonable assumption for the length of contact.

For the contact length of 20mm there exists a width of 58mm that forms the width-to-length ratio of 2.9. This is well above the limiting factor of 2 for it to be approximated as a long bearing (Hamrock *et al*, 2004; Pinkus and Sternlicht 1961). Film thickness variation along the contact is considered to have a parabolic variation with the radius of curvature of 0.5m, as it is described in section 4.3.3, and is given by equation (4.30). Minimum film thickness ( $h_m$ ) is obtained by kinematics and geometrical relations of the piston. Knowing all the parameters as outlined in Figure 5.18, the minimum film thickness can be calculated, using the following

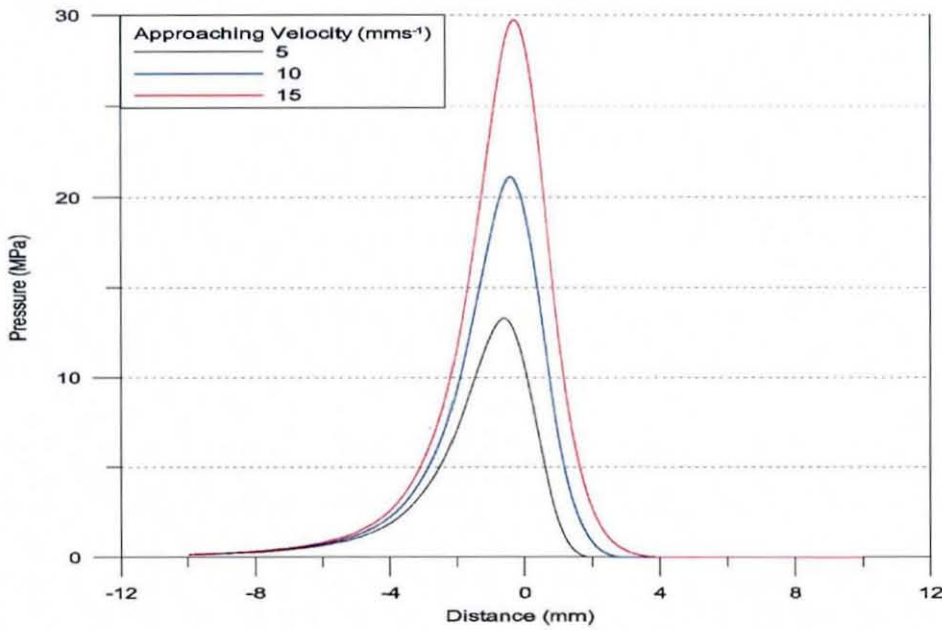


**Figure 5.17 Pressure variation along the contact at piston edge**  
 (For a sliding speed of 7500mms<sup>-1</sup> and film thickness of 4μm)

relationship:

$$h_m = x_L - a \sin \vartheta - r_{ta} \cos \vartheta \tag{5.6}$$

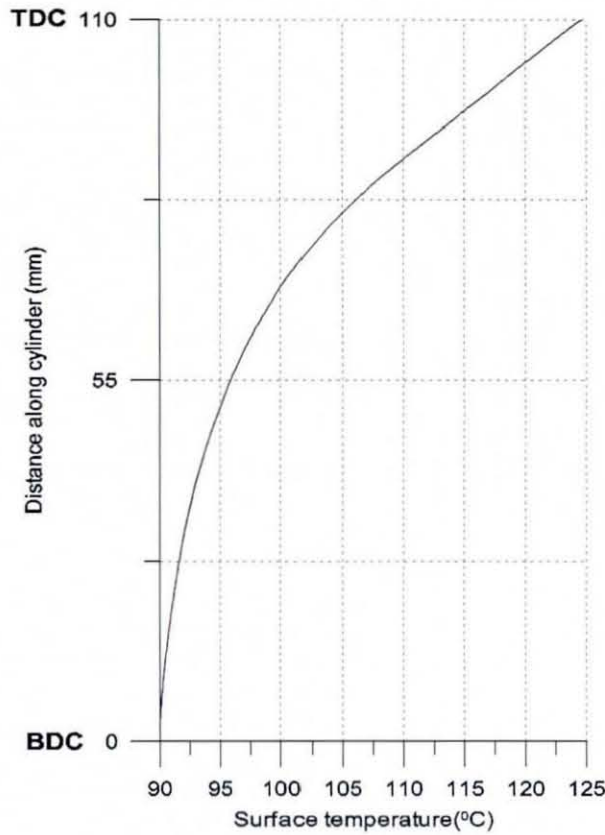


**Figure 5.19 Spline fitted temperature variation along the cylinder wall (Heywood 1988)**

The temperature along the cylinder wall does not remain constant throughout. At the TDC, the temperatures are as high as  $125^{\circ}\text{C}$  due to combustion. This reduces to about  $90^{\circ}\text{C}$  at the BDC, as significant amount of heat is absorbed by the expansion of gas. These are some approximated values taken from (Heywood 1988) for a different type of spark ignition IC engine. These values are illustrated in Figure 5.19. However, there is a significant effect on the lubricant viscosity due to the temperature variation along the cylinder. The viscosity-temperature variation for the lubricant can be sought by solving the Vogel's equation (5.7) for each temperature. Vogel's equation can be given as (Hamrock *et al*, 2004):

$$\ln(\eta) = -1.845 + \left( \frac{700.81}{\theta - 203} \right) \quad (5.7)$$

where  $\theta$  is the temperature in degrees Kelvin and  $\eta$  is the dynamic viscosity in Centi-Poise. Then, knowing the piston position along the cylinder from the inertial dynamics output,

determined by ADAMS, the effective temperature can be calculated. This temperature value is used to calculate a new temperature-adjusted value for viscosity, which is used to calculate the pressure distribution in the contact.

Pressure distribution in the contact is sought by solving the Reynolds equation, using the long bearing approximation as it is outlined in section 4.3.3. The pressure distribution is calculated in a subroutine called *SfoSub* (see Figure 5.25). Necessary kinematic parameters for each time step, such as the approaching or squeeze velocity ( $w_s$ ), sliding velocity ( $u_s$ ) and minimum film thickness ( $h_m$ ) can be obtained directly from the ADAMS output. First, the film rupture point ( $x_r$ ) for the given set of conditions is obtained by solving equation (4.40) for  $x_r$ . Then, this value is fed into equation (4.39) to obtain the non-dimensional pressure distribution. The non-dimensional pressure distribution for various squeeze-roll ratios for Reynolds fully flooded boundary conditions (D'Agostino *et al*, 2002).

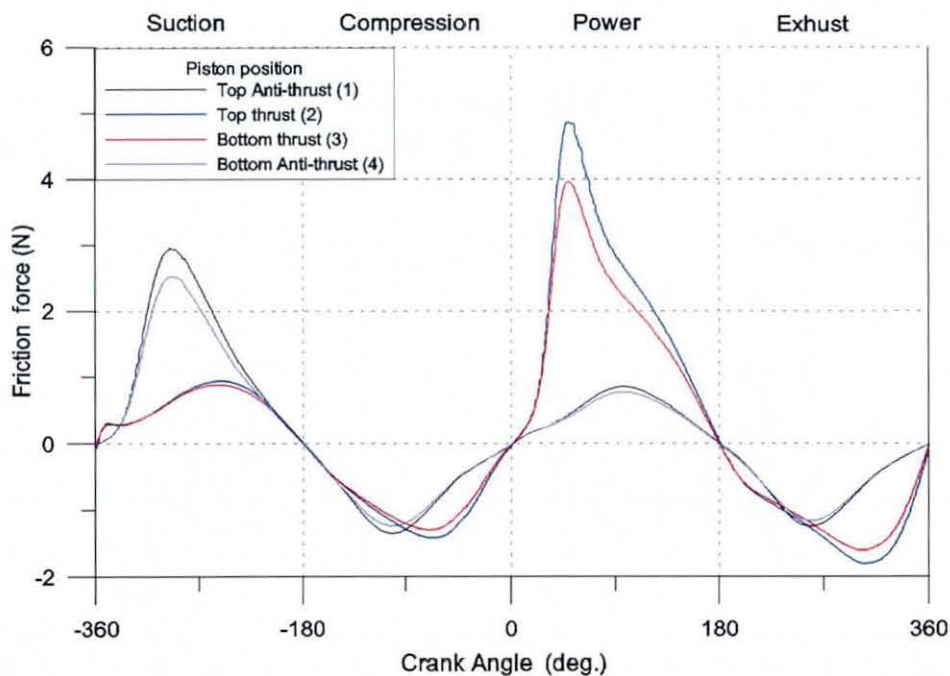


Figure 5.20 Piston friction force during one combustion cycle

No	Description	Parameter	Source
1	Contact width	-	Constant (58 mm)
2	Contact length	-	Cons. (20 mm)
3	Contact radius	$R$	Cons. (0.5 m)
4	Minimum film thickness	$h_m$	ADAMS
5	Approaching velocity	$w_s$	ADAMS
6	Sliding velocity	$u_s$	ADAMS
7	Viscosity	$\eta$	SfoSub
8	Temperature	$\theta$	ADAMS

Table 5.8 List of parameters used for thrust force calculation

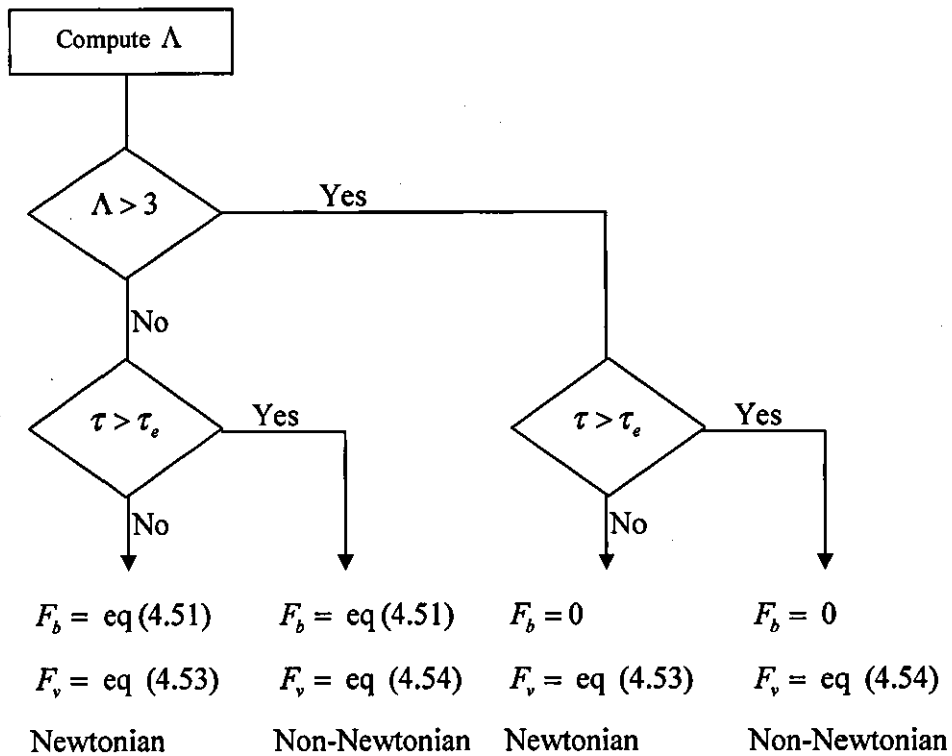


Figure 5.21 Flow chart for friction force calculation

Once the non-dimensional pressure distribution is obtained for the contact domain, it is transformed back into its physical values using the same non-dimensional groups given in equation (4.32). Then, it is doubly integrated over the contact domain to calculate the thrust force, acting on the piston skirt at a particular location of the piston. This force is then passed into the ADAMS solver as an external force on the piston at a given time step. ADAMS calls the subroutine *SfoSub* four times for each time step as there are four points considered in the

particular piston skirt location as shown in Figure 5.18. Thrust force variation at four corners of the piston during one combustion cycle is illustrated in Figure 7.18, chapter 7. The list of parameters and their values used for force calculation is given in Table 5.8.

### 5.5.6 Friction Between the Piston Skirt and the Cylinder Wall

Friction force acting at each point of consideration on the piston skirt is calculated using the boundary and viscous force contributions as outlined in section 4.4. Boundary friction is calculated using the statistical approach described in section 4.4.1. The parameters used for boundary friction calculation and their values are given in Table 5.9.

Sliding velocity ( $u_s$ ), minimum film thickness ( $h_m$ ), maximum pressure and thrust force at the contact are the main values necessary for calculation of friction. Sliding velocity and minimum film thickness can be obtained from ADAMS. Maximum pressure and the thrust load at the contact can be obtained from load calculation as described in the previous section 5.5.5. Knowing these basic values other parameters such as, the Hertzian contact area ( $A_h$ ), the non-dimensional film parameter ( $\Lambda$ ) and the shear stress ( $\tau$ ) can be calculated, using equations (4.50), (4.41) and (4.53) respectively. Then, non-dimensional film parameter is used to calculate values of statistical functions given by equations (4.48) and (4.49). Then, the asperity contact area ( $A_a$ ) and the asperity load ( $P_a$ ) are calculated, using equations (4.43) and (4.44) respectively.

Then mode of friction is obtained by examining the film parameter. If it is greater than 3, then viscous frictional conditions are regarded as prevalent and the friction force is calculated using equation (4.53). Non-Newtonian conditions may be prevalent for whatever the film thickness and this must be tested by examining the shear stress against the critical value of the Eyring stress (Cameron 1966). If it is greater than this limit, then the equation (4.54) must be used for calculation of friction. However, if the film parameter is less than 3, then both boundary friction and viscous friction may be present. Boundary friction is calculated using equation (4.51) and it is added to the viscous friction contribution, calculated using the same method as already described. Flow chart for friction force calculation is given in Figure 5.21. The friction force variation at four piston edges for a one combustion cycle is shown in Figure 5.20.

### 5.5.7 Friction Between The Ring and The Cylinder Wall

The forces acting on the piston ring section are most simply considered in terms of their axial and radial components. Axial forces such as gas pressure, inertia and ring weight in the axial direction are neglected in the analysis as these are considerably smaller, when compared to the friction force at the cylinder wall, which is also acting in the axial direction. In the radial direction ring tension, gas pressure force, lubricant reaction force and asperity contact force are considered, whilst neglecting the inertial force. Gas pressure force ( $F_{rg}$ ) and the ring tension ( $F_r$ ) act radially outwards, whilst the lubricant reaction force ( $F_{lr}$ ) and the asperity contact force ( $P_a$ ) act radially inwards on the ring as shown in Figure 5.22.

These forces are in balance during the ring operation as given by equation (5.8). Throughout most of the engine cycle the piston ring enjoys hydrodynamic lubrication even though effective film thicknesses are only of the order of micrometers. At TDC and BDC it behaves either in mixed or in boundary regimes of lubrication, and in some extreme conditions it may enter elastohydrodynamic conditions (Dowson *et al.*, 1983). However, while having comparatively a large ring thickness of 3mm, and a low operating speed of 1800 rpm, the piston ring in the experimental E6 engine is strongly expected not to be operating under EHL conditions.

No	Description	Notation	Source
1	Surface roughness	$\sigma$	Constant ( $2\mu m$ )
2	-	$\gamma\beta\sigma$	Cons. (0.055)
3	-	$\sigma/\beta$	Cons. (0.001)
4	Young's modulus (sleeve)	$E_1$	Cons. (200GPa)
5	Young's modulus (piston)	$E_2$	Cons. (70GPa)
6	Poisson's ratio (sleeve)	$\nu_1$	Cons. (0.3)
7	Poisson's ratio (piston)	$\nu_2$	Cons. (0.33)
8	Contact radius	$R$	Cons. (0.5m)
9	Contact length	-	Cons. (20mm)
10	Sliding velocity	$u_s$	ADAMS
11	Minimum film thickness	$h_m$	ADAMS
12	Viscosity	$\eta_0$	ADAMS

**Table 5.9 List of parameters used for friction force calculation**

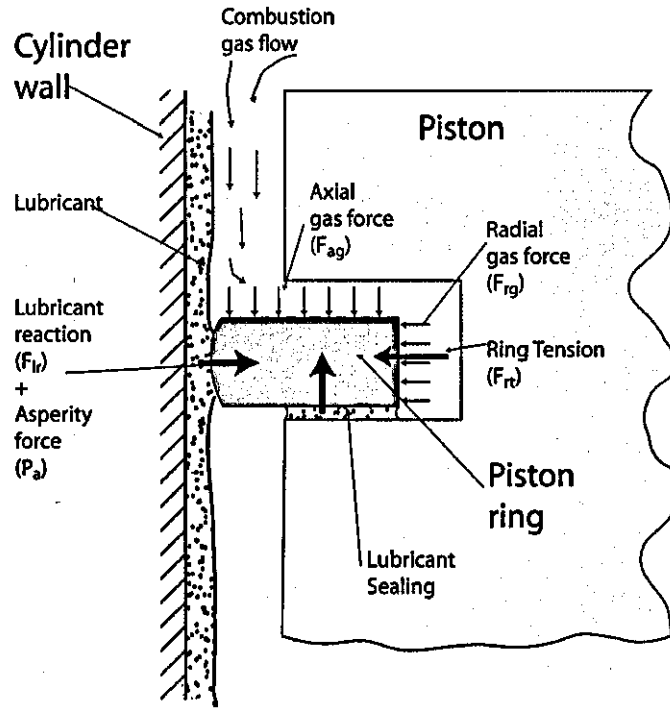


Figure 5.22 Forces acting on piston ring

$$F_{lr} + P_a - F_{rg} - F_{rt} = 0 \tag{5.8}$$

Knowing the sliding velocity, which is considered to be the same as the piston translational velocity, lubricant film thickness necessary for the radial force balance can be obtained. The gas flow from combustion chamber to the inner side of the piston ring, which creates the radial pressure force ( $F_{rg}$ ) is distributed during the downward motion of the piston as the ring resides on the top groove surface. In contrast, inner side is exposed to crankcase pressure and hence this pressure is acting on the inner ring face during the piston downward motion. However, during piston upward motion the combustion chamber pressure is applicable for the inner ring face pressures.

Normally, the undeformed ring has a diameter of 10% more than that of the cylinder bore. Changes in the ring radius during its operation inside the cylinder is almost 0.02% of its initial radius, which is very low compared to the initial deformation of the ring, such that neglecting the change in ring tension due to variation of its diameter is permissible as the film thickness between the ring and the cylinder wall varies. Thus, the radially outward ring tension force is considered to be a constant at 65N in the case of the E6 engine as mention in Table 5.10.

No	Description	Notation	Source
1	Gas pressure force	$F_{rg}$	ADAMS
2	Ring tension	$F_r$	Constant (65N)
3	Lubricant reaction	$F_{lr}$	SufSub
4	Asperity force	$P_a$	SfoSub
5	Ring face radius of curvature	$R$	Cons. (0.01m)
6	Ring height	-	Cons. (3mm)
7	Mean ring radius		Cons. (37mm)
8	Viscosity	$\eta$	SfoSub

**Table 5.10 Parameters used for ring friction calculation**

Asperities of the two contacting surfaces can interact, when the film parameter is less than 3, which means that boundary lubrication condition can contribute to friction. Under these conditions the regime of lubrication can either be mixed or entirely boundary. Under these conditions the asperities take certain amount of the applied contact force by themselves. This is given by equation (4.44). In whichever regime of lubrication, the friction force can be calculated using the method already described in section (5.5.6) for piston-cylinder wall interactions.

A parabolic ring face is considered with a radius of curvature of 0.01m for the calculation of friction force on the piston ring. As the hydrodynamic pressures generated are relatively high, with small contact area, the heat generated due to viscous action of the lubricant in this contact can cause significant effects on the rheological parameters, particularly viscosity of the lubricant. Thus, thermal effects at the contact conjunction are sought by consideration of heat balance. At certain instance of time heat can be generated in the contact conjunction, basically due to compressive (pressure loading) or viscous (shear loading) contributions. As already mentioned in section 4.5 under hydrodynamic regime of lubrication, viscous heating is dominant due to relatively low pressures compared to Elastohydrodynamics (EHD) conditions. In the mean time the heat is dissipated into the surrounding either by convection or conduction cooling. Taking these facts into consideration the heat balance is sought, using the energy equation (4.63) and the average temperature rise at the contact is obtained. As viscosity is affected by this temperature rise the new effective viscosity applicable to the contact is obtained through use of Vogel's equation (i.e. equation (5.7)). Then, the minimum film thickness, which satisfies the force balance with this new viscosity, is obtained. This

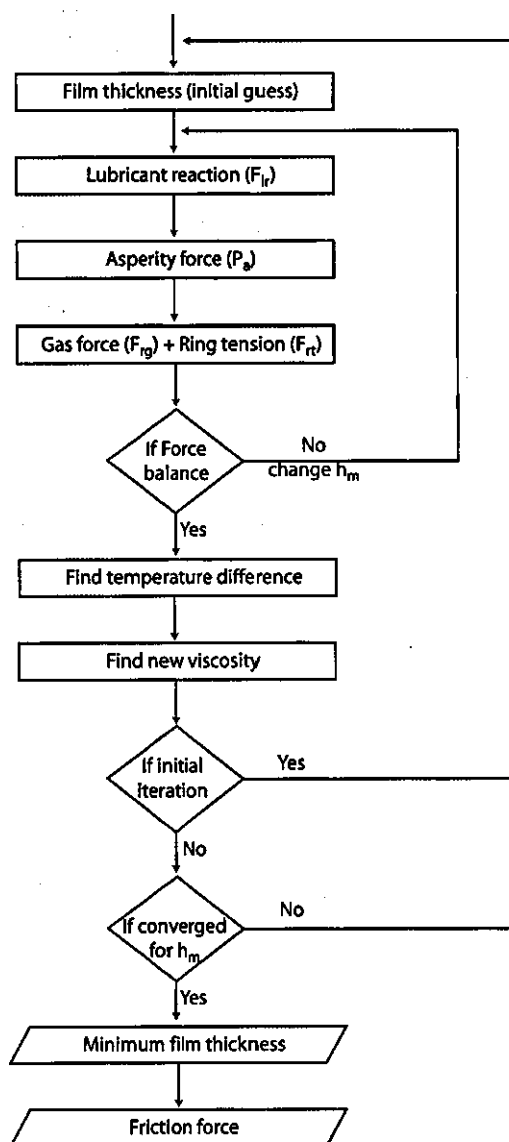


**Figure 5.23 Flow diagram for piston-ring friction calculation**

procedure is repeated until the convergence criterion is satisfied on the minimum film thickness as shown in the flow chart of Figure 5.23.

Convergence procedure commence with an initial temperature, taken according to the instantaneous position of the ring on the cylinder wall. The same temperature profile as shown in Figure 5.19 and the same method as described for the piston side force calculation in section 5.5.5 are used to obtain the initial temperature at the contact. The initial temperature and the final average temperature in the contact are shown in Figure 5.24.

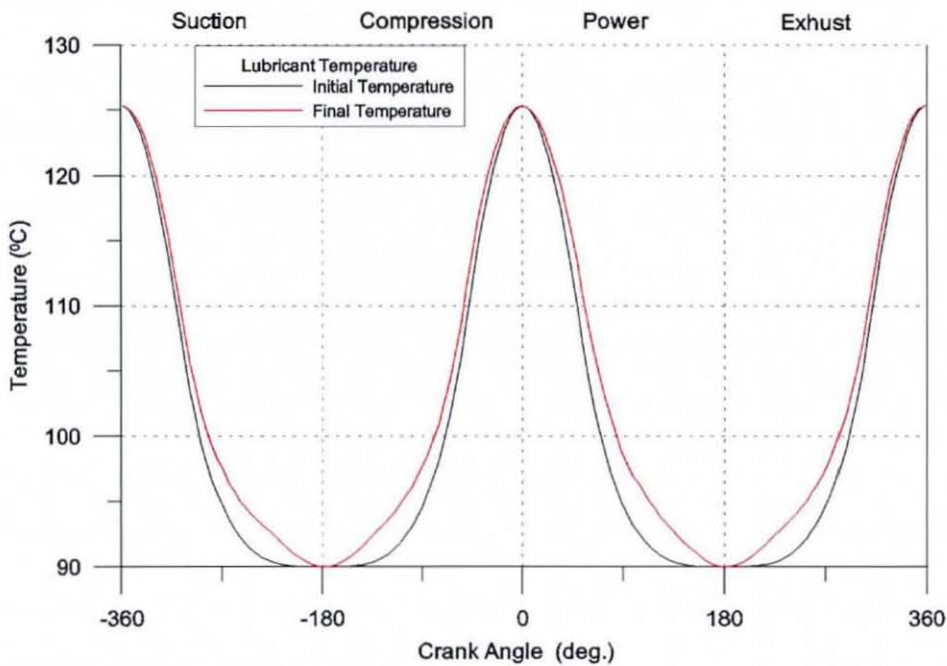


**Figure 5.24 Lubricant temperature variation at piston ring-cylinder wall interaction**

Once the film thickness is obtained, friction force on the ring is calculated, based on a new film thickness and the effective lubricant viscosity. Friction force and the minimum film thickness variation on the piston ring-cylinder wall interactions are given in Figure 7.23, chapter 7.

As the forces acting on the ring are highly time dependent, the consideration of dynamic response of the ring is highly recommended. However, with the available computing power such an in-depth analysis may take considerable amount of time, which may hinder the ability of solving the simulation in an acceptable time limit. On the other hand, for the cast iron ring of 3mm thick with operating speed of 1800rpm, this is a reasonable acceptable assumption than that for a high speed, high performance engine with relatively very small ring thickness, where modal behaviour of the ring in in-plane and out-of-plane distortions become significant.

The maximum pressure generated in the contact is greatly affected by the approaching velocity of surfaces (squeeze film effect)(Dowson *et al*, 1983). However, it is noted that this effect is not taken into consideration during the entire analysis of the ring friction force, which may create some difference, especially at dead centres where any lubricant pressure

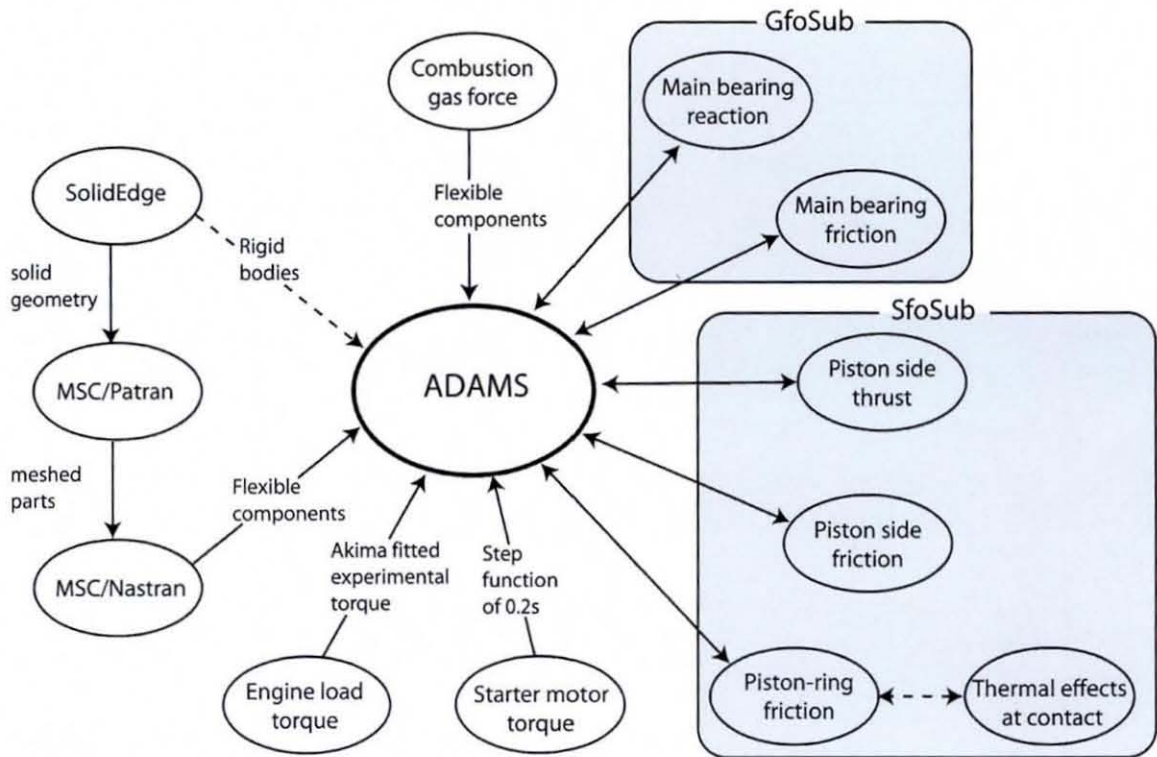


Figure 5.25 Schematic diagram of multi-physics model

building up is dominated by squeeze film action. In the current analysis, the approach of the piston towards the cylinder wall is taken into account by its secondary motions through the integrated dynamic analysis. Thus, in an indirect way the effect of rigid body approach is accounted for, but not the history of squeeze film action, which would require a transient solution of Reynolds equation in each step of time. Thus, one can regard the analysis of lubricated conjunctions here as a series of quasi-static steps. Low film thickness at dead centres can be seen in Figure 7.23, chapter 7.

Figure 5.25 illustrates the basic approach employed for the numerical model development discussed throughout this chapter. As it can be seen many software tools have been used in various detail, linked to ADAMS. Basically, the model can be divided into three major modules, namely finite element analysis handled by the MSC/Nastran, multi body dynamics handled by ADAMS and tribology handled by the developed Fortran subroutines.

A complete list of components used to develop the numerical model is given in Table 5.5. Also, a list of holonomic and non-holonomic constraints used in the model to interconnect components is given in Table 5.7. The total number of DOF of the multi body engine model,

including the elastic DOFs due to component flexibility can be obtained using the Gurebler-Kutzbach expression as:

$$\begin{aligned}\text{Number of DOF} &= \text{flexible body modes (flywheel + crank + conrod) +} \\ & 6 (\text{number of rigid parts} - 1) - \sum (\text{Constraints}) \\ &= (56 + 66 + 32) + 6 \times (16 - 1) - 108 \\ &= 154 + 90 - 108 \\ &= 136\end{aligned}$$

Thus, the model comprises 136 DOF, including 90 rigid body motions and 154 structural modes, which leads to a total of 362 algebraic and differential equations to be solved in the ADAMS solver as discussed in chapter 3.

Whatever the method used for the development of the numerical model, its validity must be ascertained as the derivations are based on certain assumptions and use of certain numerical methods. The following chapter is devoted to measurements carried out on the E6 engine in the process of validation of the multi-physics numerical model developed thus far.

## 6 EXPERIMENTAL INVESTIGATION

### 6.1 Introduction

This chapter describes the experimental measurements of vibration from the E6 Ricardo single cylinder engine. The numerical prototype described in the previous chapter is developed, based on the application of the multi-physics multi-scale modelling method to the same engine. Therefore, the main purpose of the experimental work is to obtain results, which can be used to gauge the practical use and degree of conformity of the proposed analytical approach to a real life application.

There are a number of key parameters involved in any experimental verification of a numerical method. For the current study it was important to determine parameters that can be predicted and also easily measured for the purpose of model validation. Of course many predicted parameters can also be measured. However, the task can become very arduous, if micro-scale parameters are to be measured, such as lubricant film thickness in the various modelled conjunctions. This would usually require use of optical engines, running under motorised (rather than real fired) conditions. This approach, however, is not useful for practical applications. With optical engines, it is possible to use LIF, as pointed out in the literature review to obtain a measure of film thickness in the piston-cylinder conjunction (Seki *et al*, 2000). Another approach may be the use of newly developed ultrasonic sensors attached to the outside wall of the cylinder liner, and usable under engine firing condition (Dwyer-Joyce *et al*, 2005). Alternatively, indirect measurements may be taken, for example, a measure of cylinder friction, using a floating liner (Cho *et al*, 2000). All these approaches are rather time consuming and require a fair amount of development. They are deemed as rather beyond the main scope of this research, with its focus on the development of multi-physics method and application to prediction of engine conditions. Thus, the approach undertaken in this chapter uses remote, non-contact measurements of vibration, the philosophy being that the degree of conformity of predictions with these measurements would indirectly indicate the relevance of the underlying methods used to practical applications.

Thus, the following measurements are undertaken here:

---

1. Flywheel nodding motion (being due to its conical whirl) is measured using state-of-the-art laser torsional vibrometers.
2. Engine angular velocity variation at the flywheel end

Additionally, frequency responses of engine components are also determined by impact hammer excitation. These are compared with those employed in the model.

Combined eccentric motion of crankshaft-flywheel assembly, gives rise to a conical whirling action, especially at the flywheel end due to eccentricity of the heavy mass of flywheel. This motion of the flywheel is commonly referred to as flywheel nodding action in industry. Due to this motion, points on the surface of the flywheel move in the axial direction, as well as undergoing torsional oscillations about the crankshaft axis. Some relations and details of this motion have been outlined by (Kelly 1999) with relation to an impact noise and vibration phenomenon resulting in the clutch system, referred to as whoop.

Vibration measurements are equally important in many areas such as design of structures, durability testing, machine diagnostics, etc, other than for the purpose of validation of analytical models. Natural frequencies of a machine or a structure play an extremely important role in predicting and understanding the dynamic behaviour of a system. Hence, the major reason for performing vibration test of a system is to determine its natural frequencies and mode shapes under dynamic excitations. Detailed description of such an experimental modal analysis, used with Component Mode Synthesis (CMS), which can be used to determine natural frequencies, mode shapes and damping ratios are given in this chapter.

As previously explained, engine rotational speed is affected by many factors such as, the combustion gas force, rotational and translational imbalances. Even though certain precautionary measures can be undertaken, such as balancing of parts, critically adjusting bearing clearances, employing energy reservoirs (flywheel), balance shafts, dual mass flywheels, in order to minimize angular velocity fluctuations, it is not possible to entirely eliminate these sources of excitation, which are usually inherent to system dynamics. Therefore, these excitations are embedded in engine rotational speed to a certain degree and can be captured by measuring the crankshaft angular velocity response with a required level of accuracy. Many types of sensors and transducers have been used for monitoring engine conditions. These include: eddy current gap sensors for measuring bearing loads (Moreau *et*

*al.*, 2002), strain gauges for measuring stresses at various points, including in bearings (Mihara and Someya 1995), physical vapour deposited pressure transducers (Mihara *et al.*, 1995; Mihara *et al.*, 1996; Mihara and Someya 2002) and most commonly accelerometers. Although all these measuring devices have reported to have certain degrees of success, and can be regarded as direct measurement of events, there exists a number of major problems. Firstly, those used in contact conjunctions are often subjected to wear or separation from surfaces. Secondly, those used to monitor these conjunctions as non-contact devices, such as the eddy current probes or ultrasonic sensors have insufficient resolution (sensing head being larger or of the same order as the contact dimensions), thus provide an average value at best. Finally, the response time of some of these devices are insufficient to obtain adequate data, showing variation of events. The advantage of using lasers is operation at speed of light, as well as the precise nature of measurements in a non-contact manner, thus not interfering with the process itself. The current study employs laser Doppler vibrometry (Bell and Rothberg 2000a; Bell and Rothberg 2000b), as well as piezoelectric crystal accelerometers and pressure sensors for measurement of vibrations and combustion pressure.

## 6.2 Engine Testing

### 6.2.1 Description of Test Rig

A single cylinder poppet valve 4-stroke E6 Ricardo experimental-type engine was first manufactured in 1958 by Ricardo Consulting Engineers. This engine has the flexibility to operate either with diesel fuel or gasoline at different compression ratios. Cylinder head can move relative to the cylinder, piston and crankshaft assembly, in the vertical direction, thus changing the compression ratio. Experiments were performed setting the compression ratio of 1:8 and with gasoline fuel. According to the manufacturer's specification, the engine can produce a maximum power of 13 Bhp at the speed of 3000 rpm and a maximum torque of 40 Nm at the speed of 1800rpm. The engine has a cylinder bore of 3 inches and a stroke of 4.375 inches as listed in Table 6.1. This is an undersquare or longstroke engine which has a higher stroke compared to bore of the piston. Such a configuration creates higher friction force as well as the wear rate since its higher transverse velocities. However due to higher crank radius it can create considerably higher torques compared to shortstroke engines.

Engine specifications	
Cylinder bore diameter	3 inch (76.2 mm)
Stroke length	4 3/8 inch (111.125 mm)
Engine speed range	1000-3000 rpm
Compression ratio	4.5 – 20
Spark plug size	14 mm

**Table 6.1 E6 Ricardo engine manufacture specifications**

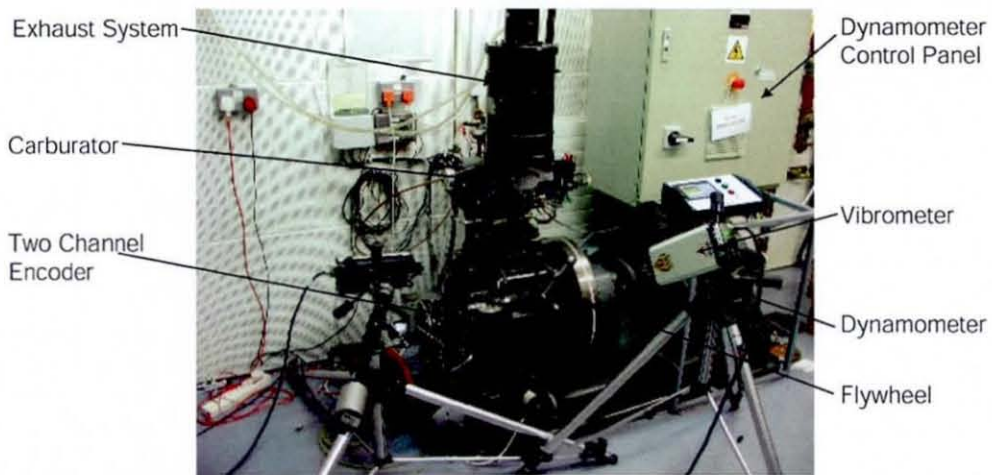


**Figure 6.1 The E6 Engine Test Rig**

The engine was fitted with a two channel pulse encoder, which can be used to obtain the crank angle position, as well as noting the position of TDC, providing 3600 pulse/rev of the crankshaft and an additional pulse, when the piston is at the TDC. Additionally, the engine can accommodate a spark-plug type Kistler pressure sensor in the combustion chamber to measure pressure variations. A number of thermocouples were fitted at various locations, including at the inlet manifold, exhaust, cooling water inlet, cooling water outlet and at the oil sump, allowing temperature measurements to be undertaken at all these locations.

The air-to-fuel ratio is optimized during the operation, using a flue-gas analyser, fitted to the engine. An integral dynamometer is coupled at the flywheel end as shown in Figure 6.1, which provides flexibility to run the engine under a pre-determined torque or speed with maximum  $\pm 5\%$  fluctuations. As the frequencies of interest of the engine is in the range of 15 – 500 Hz, and these fluctuations are taking place at very low frequency such as less than 0.5 Hz such a speed fluctuation can be accepted for the experiment. The throttle position can be adjusted, depending on application, using the attachment provided as shown in Figure 6.2.

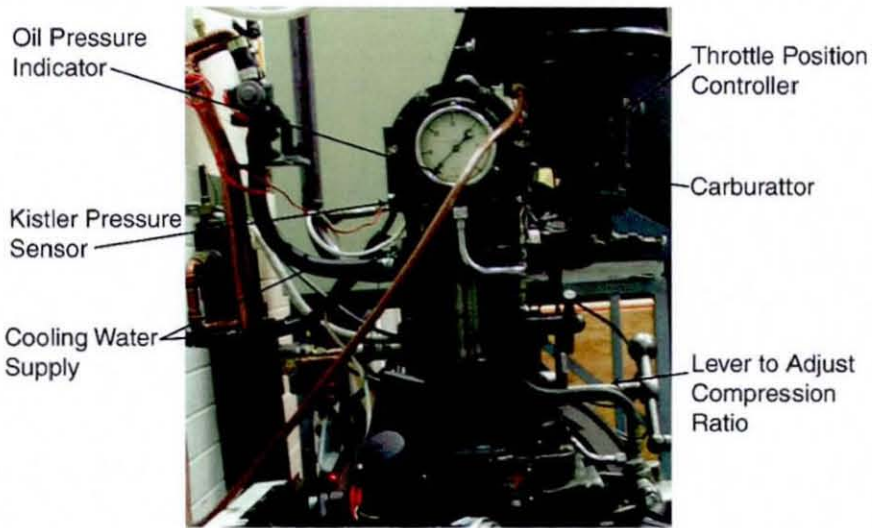


**Figure 6.2 E6 Engine front end**

During experiments the engine was run at 1800 rpm producing an average output torque of 35 Nm with full throttle, allowing the engine to produce its maximum torque. Air-to-fuel ratio of 13:1 by volume was used. Flue gas temperature of nearly  $130^{\circ}\text{C}$  at the exhaust, and a constant outlet and inlet cooling water temperature of  $70^{\circ}\text{C}$  and  $20^{\circ}\text{C}$  were marked with relevant thermocouples.

A dual beam laser vibrometer and a single beam laser vibrometer of type PolyTec OFV4000 were shun onto the flywheel surfaces as illustrated in Figure 6.7 and Figure 6.1, capturing rotational and translational vibrations respectively. A water cooled Kistler type 7061B pressure sensor was inserted into the combustion chamber as shown in Figure 6.2, measuring the combustion gas pressure variation. The TDC indicator of dual channel pulse encoder was extensively used to locate the angular position of the crankshaft with respect to the engine combustion cycle, while using laser vibrometers to obtain the rotational and translational (due to nodding action) of the flywheel. Once the setting up procedures were completed, the engine was left to run nearly half an hour in order to reach its steady state operating conditions, especially with regard to lubrication and thermal conditions, before commencing to record any measurements.

### 6.3 Measurement Hardware

Rapid advances in solid-state and computer technology have considerably changed the data acquisition and signal processing hardware in recent years (Inman 2001). Vibration

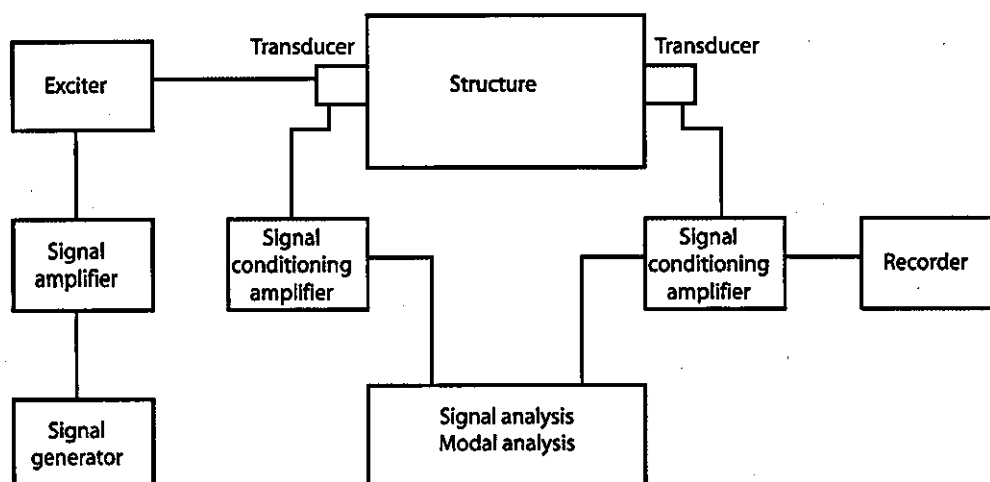


Figure 6.3 Schematic of hardware used in impact test

measurements, as well as, state measurements such as velocities, displacements, generally require several hardware components. The first basic hardware element in data acquisition is a *transducer* that converts a mechanical signal from a structure into an electrical signal. Signal conditioning amplifiers match the characteristics of the transducer to the input electronics of the digital data acquisition system. This general arrangement, including a power amplifier and a signal generator in case of an artificial signal is needed for the analysis to be carried out (such as a hammer in an impact test), and transducers to measure both the input, as well as the output signal (see Figure 6.3).

Model validation and data acquisition process of this study are based on a number of transducers. Main components in the engine model are first tested against their natural frequencies, using impact hammer tests, which recorded the acceleration response of components under controlled excitation. The impact hammer and accelerometers are the main transducers involved in this process. Subsequent testing were to measure the flywheel nodding motion and crankshaft rotational speed, using scanning laser vibrometers, which employ the Doppler frequency shift of a scattered light source caused by a moving target. Combustion chamber pressure was measured using a Quartz pressure sensor that produces an electric charge according to the applied pressure. This section discusses these transducers, their physical behaviour and the selection procedures related to the present study.

### 6.3.1 Controlled Impact Excitation

Vibration test methods are based on several assumptions. The main assumption is that lumped parameter models adequately represent the test structure and its linearity during excitations is considered to be most important. During vibration tests that mostly rely on controlled excitations imposed on the system such as impact test, shakers (electromagnetic or electrohydraulic) or impact hammers are the most widely used devices.

Shakers are capable of producing a predetermined waveform within a required frequency range, resulting easily in measurable outputs. Shakers are attached onto the test structures, while carefully selecting the size and method of attachment, minimising the mass loading effect that could lower the measured frequency. Even though the use of a stringer can minimize this effect, while controlling the direction of excitation more precisely, impact hammer has become a more popular device due to its simplicity and comparatively low cost.

Impact hammer is intended to apply an impulse excitation onto the structure that can excite system's natural frequencies. This is possible to achieve by an ideal impact excitation as it can be shown by decoupling the equation of motion of the lumped parameter model to its modal degrees of freedom (Craig 1981; Inman 2001). The peak impact load on the structure is proportional to the head mass and velocity. The load cell at the head measures the impact force.

Figure 6.4 illustrates the time history and corresponding frequency response of a hammer hit involved in a crankshaft natural frequency test. Generally, an excitation is considered to be impulsive, if its duration ( $\Delta t$ ) is small compared to the period associated with component's maximum undamped natural frequency of interest. However, the Frequency Response Function (FRF) of the particular impulse shows consistence of its frequencies up to nearly  $6000\text{Hz}$ , and it has sufficient energy to excite frequencies up to  $3200\text{Hz}$ , which is the cut-off frequency in this case.

The time history of the impulse, shown in the figure, does not represent an ideal impulse, but rather one of a finite time duration of  $230\mu\text{s}$ . Hence, the frequency response is not a flat straight line as it should ideally and theoretically be, but has a periodic form. This periodic form can be seen from the frequency response function (FRF). The duration of impulse and hence the shape of the frequency response is controlled by the mass and stiffness of both the

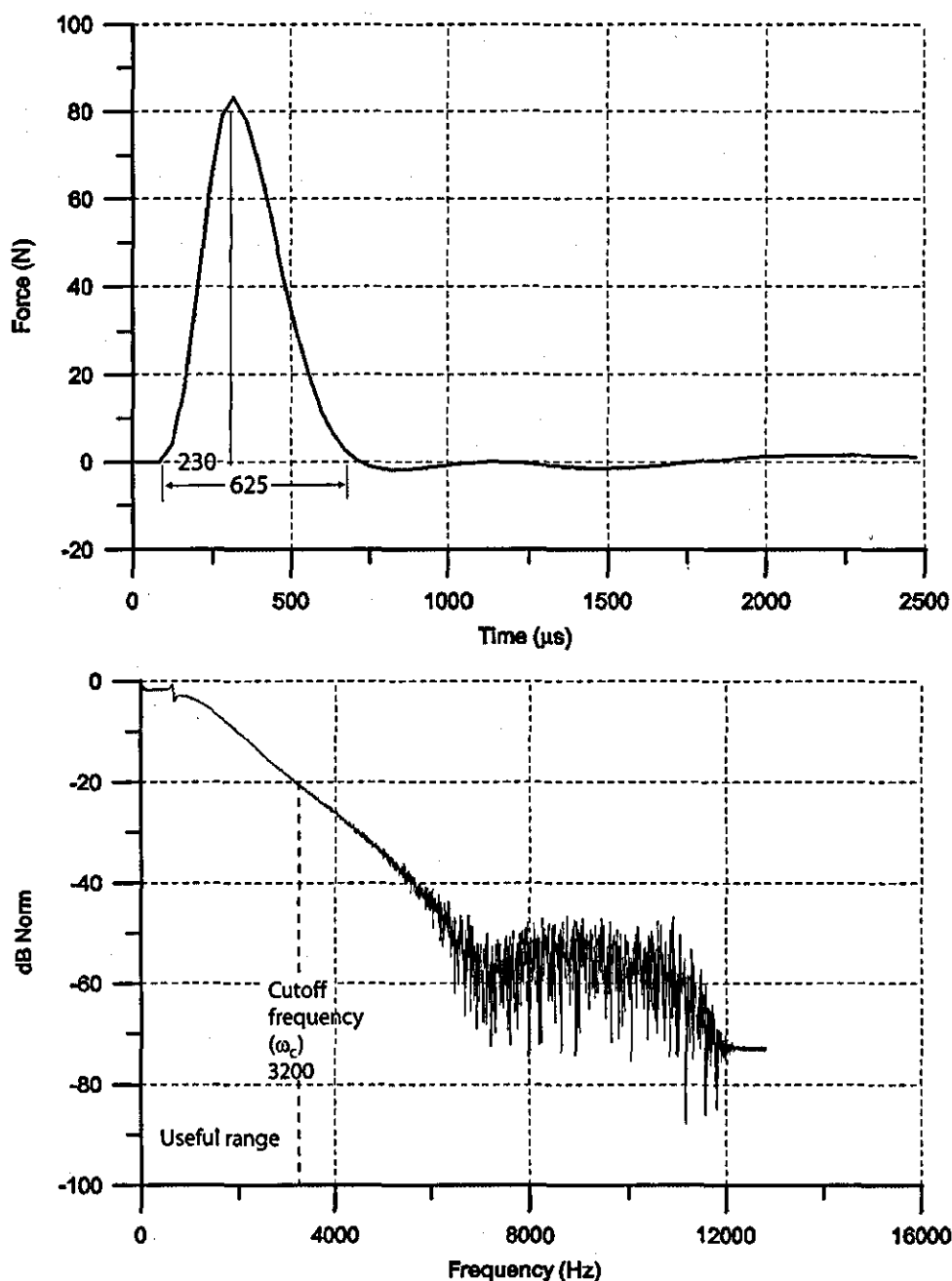


**Figure 6.4** Time and frequency domain response of an impact excitation hammer and the structure. Thus, the hammer is equipped with a number of tips that has various stiffness and mass properties. These are used to obtain an appropriate impulse excitation as far as possible.

Stiffness of hammer tip determines the *cutoff frequency* ( $\omega_c$ ), the largest value of frequency reasonably well excited by a hammer hit. As illustrated in Figure 6.4, the cutoff frequency corresponds roughly to the point, where the magnitude of the frequency response falls more

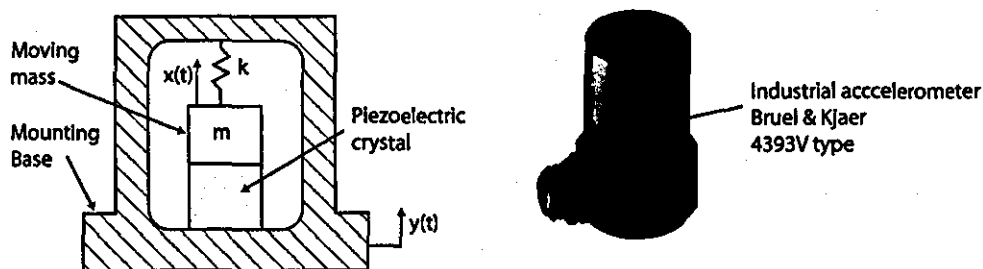


**Figure 6.5 Schematic diagram of an accelerometer**

than  $20\text{dB}$  from its maximum value, which is  $3200\text{Hz}$  in the particular case reported here. However, the test structure does not receive enough energy to excite the modes above  $\omega_c$ , which defines the useful frequency range during the excitation.

Upper frequency limit excited by the hammer is decreased by increasing the hammerhead mass and is increased with increasing stiffness of the tip of the hammer. Hammer hit is less effective in exciting modes of structure with frequencies higher than  $\omega_c$ . Although impact hammer is simple and does not create mass loading problems to the structure, it is often incapable of transferring sufficient energy to obtain adequate response signals within a larger frequency range as it can be seen from Figure 6.4. Also, excessive peak loads may potentially be damaging to the tested component. Furthermore, the direction of the applied load is difficult to control.

Experiments were carried out using a preloaded piezoelectric impact hammer of type 8200 and sensitivity of load cell  $3.75\text{pC/N}$ . It includes a hammer head mass of 40 grams and number of head tips with various stiffness values. The hammer head was selected such that the time history of the impact gives a better agreement with the ideal impulse, while eliminating multiple hits instead of one, which is quite a common problem in impact testing.

### 6.3.2 Acceleration Response Measurement

Once the system is excited in a controlled manner, the response of the system must be recorded in a reliable manner. Displacement or acceleration response of a component can be measured by a piezoelectric transducer, also known as a vibrometer that generates an electrical charge proportional to the relative displacement between its base and its moving mass as illustrated in Figure 6.5.

Piezoelectric Bruel & Kjaer type 4393V accelerometers were used during this study. These have a resonant frequency of  $55\text{kHz}$ . When the ratio between the measuring frequency over resonance frequency ( $r$ ) is small, the measured acceleration deviates only by a small amount from the actual acceleration of the measuring body. Generally, the range of frequency ratio ( $r$ ) of  $0-0.2$  is considered as the efficient range after experimental validation (Inman 2001). The accelerometers are suitable for measuring responses up to  $11\text{kHz}$ . However, according to manufacturer's specifications those chosen can reliably measure up to  $15\text{kHz}$ , even though experiments carried out needed a maximum of  $8\text{kHz}$  response only.

Mounting the accelerometer at the measuring sites is one of the most critical factors for obtaining accurate results from practical vibration measurement. Sloppy mounting results in a reduction in the mounted resonant frequency, which can severely limit the useful frequency range of the accelerometer. The ideal mounting is by a threaded stud to a flat smooth surface with a thin layer of grease between surfaces to improve the stiffness of the mounting by which a resonance frequency of  $32\text{kHz}$  can be attained (Kjaer 1982). However, as this method needs much preparation work, as well as machining on the measured component, the most commonly used alternative mounting method is a thin layer of Bees-wax sticking the accelerometer onto the component's surface. From this method a maximum resonant frequency of  $29\text{kHz}$  could be achieved with the maximum usable acceleration of  $100\text{ms}^{-2}$  as the accelerometer weight used was  $2.9\text{g}$ .

### 6.3.3 Velocity Measurement at Flywheel End

Successful measurement of vibration, using accelerometers mostly relies on firm contacts between the transducer and the measurement surface, as described above. Nevertheless, torsional, as well as translational vibration of a moving body such as the flywheel nodding motion, is not possible using an attached type transducer, especially due difficulties in rooting the connecting leads out of the crankcase. Thus, a non-contacting type vibrometer such as the scanning Laser Doppler Vibrometer (LDV) was used for this aspect. The physical principle behind LDV relies upon the detection of a Doppler frequency shift in the coherent light source scattered by a moving target. The measured frequency shift  $f_D$ , relates to object surface velocity component  $u_o$  in the direction of the incident beam as given by following equation (Halliwell 1996):

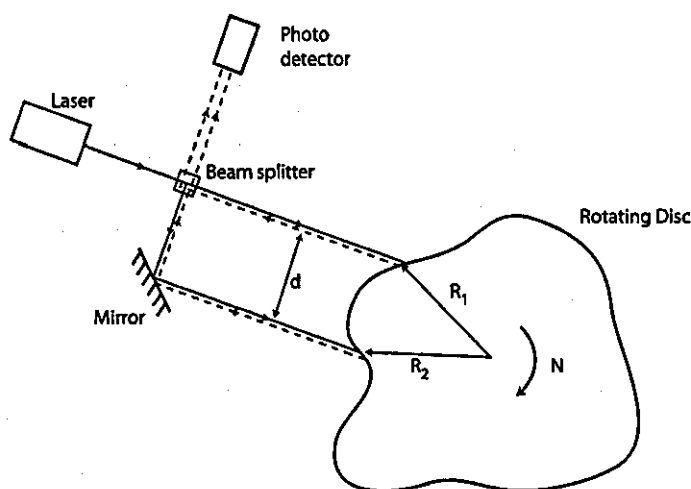


Figure 6.6 The laser torsional vibrometer optical geometry

$$f_D = \frac{2u_o}{\lambda_b} \quad (6.1)$$

Where  $\lambda_b$  is the wavelength of the incident light beam. In this way, by measuring and tracking the frequency shift  $f_D$  that is in the order of  $MHz$ , a time resolved measurement of the solid surface velocity  $u_o$  can be made.

The most important and useful form of measurement that can be made using a LDV is torsional vibrations of a rotating disc in a non-tangible manner, using a dual beam laser configuration as shown in Figure 6.6. In this case the photo-detector compares the back-scattered light of two parallel beams reflected from the rotating disc. Then, the frequency shift can be related to the distance between the beams;  $d_b$ , and the disc speed of rotation  $N_d$  by the following equation (Halliwell 1996):

$$f_D = \left( \frac{4\pi d_b}{\lambda_b} \right) N_d \quad (6.2)$$

Under nominal conditions LDV uses a low powered ( $\approx 2mW$ ) Helium-Neon beam that produces red light at a wavelength of  $\lambda_b = 6328 \times 10^{-10} m$ . The maximum frequency shift of  $1.5MHz$ , which the photo-detector is sensitive to, and the constant distance between the two beams of  $8mm$  enabled a maximum rotational speed of up to  $56000rev/min$  to be measured, which is considerably above the requirements of this investigation. Most important aspect of

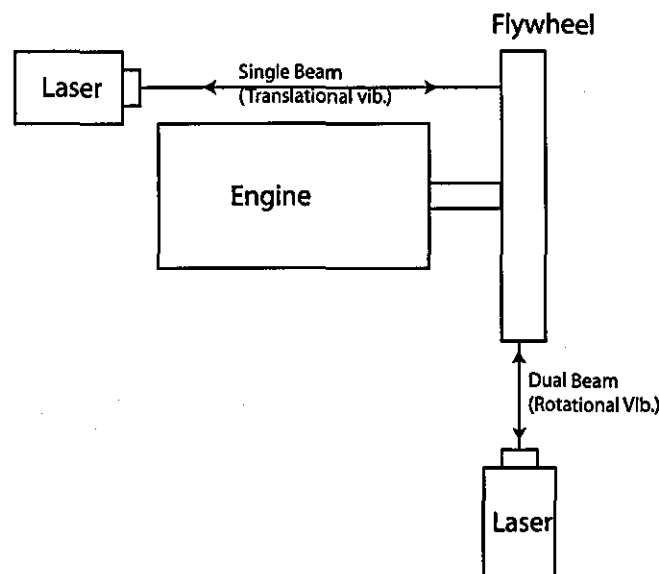


**Figure 6.7** Flywheel vibration measurements

the dual beam laser is its non-dependable nature on the topography of the flywheel rim, rigid body motion and surface irregularities in angular velocity measurement (Halliwell 1996). When the measurements are made, it is important to hold the instrument so that the incident laser beams is parallel to cross section of the flywheel as is also shown in (Bell and Rothberg 2000a). The intensity of the reflected beam from the moving object must be strong enough that photo-detector can identify. Thus, a reflected tape was adhered to the object (in this case the flywheel) and the distance between the laser head and the flywheel was optimized, ensuring a strong reflected beam to the photo-detector. The optimized distance between the laser head and the flywheel surface was found to be  $400\text{mm}$  for the LDV used in this investigation.

A pair of Polytec OFV4000 dual beam rotational laser vibrometers, capable of measuring rotational vibrations, were used during this investigation. One of these was arranged to measure translational vibrations of the flywheel, whereas the other measured the rotational vibrations as shown in Figure 6.7. Reflecting one beam directly back into the laser head with a *single point adopter lens cap* yielded a single beam configuration for the LDV, which measured the translational vibrations. The rotational and translational velocity decoder sensitivities of  $6000^\circ/\text{s}/V$  (or  $1000\text{rpm}/V$ ) and  $1000\text{mm}/\text{s}/V$  were used respectively during all the measurements. Two LDV's were placed about  $400\text{mm}$  away from the measuring point with the velocity scanning rate of  $1600\text{Hz}$ , corresponding to the time

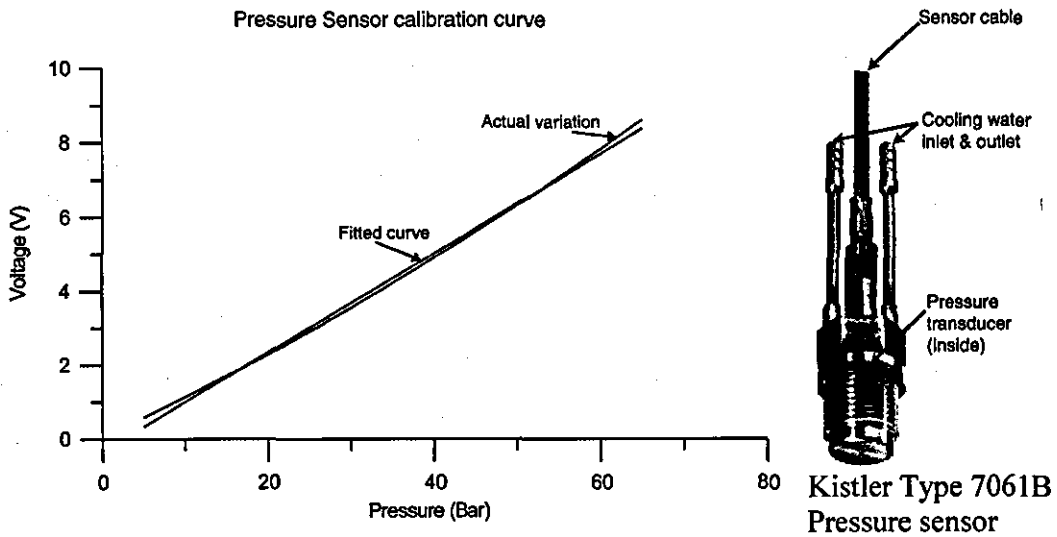


Figure 6.8 Pressure sensor and calibration

interval of  $625\mu s$ . Retro-reflected tapes were adhered to the appropriate surfaces of the flywheel in thin strips to ensure that the incident beam was reflected with minimum dispersion, providing sufficient intensity light towards the photo-detector. The LDV which measured the rotational velocity was focused as much as possible directly to the centre of the flywheel, using an intensity meter, provided with the laser head. Also the LDV used for translational velocity measurement, was aligned perpendicular to the face of the flywheel as much as possible.

### 6.3.4 Combustion Gas Pressure Measurement

Combustion gas pressure is measured by a Kistler type 7061B sensor inserted into the combustion chamber. This is a Quartz piezoelectric pressure sensor, having a measuring range of 0–250bar at a maximum temperature of  $200^{\circ}C$ . The water cooled transducer has a sensitivity of  $80pC/bar$  and is calibrated at room temperature. Voltage reading is noted, while applying a known pressure force to the pressure sensor during its calibration. Values were then plotted against pressure to obtain a calibration curve as shown in Figure 6.8. Following the relation of  $0.1341V$  per bar of pressure is obtained from the calibration curve.

$$Y = 0.1341098901 \times X - 0.3330769231 \quad (6.3)$$

During experiments the observed voltage reading from the transducer was converted back into a pressure reading. Cool water was circulated to the transducer to protect it from possible damage that may be caused due to higher temperatures.

Output impedance of most transducers is not well suited for direct input into the signal analysis equipment. Hence, *signal conditioners*, which may be charge amplifiers or voltage amplifiers are often used to amplify signals prior to their analysis, and must be properly calibrated along with the transducers in terms of both magnitude and phase over the frequency range of interest.

Once the response signal has been properly conditioned, it is routed to an analyser for signal processing. The analyser type that has become the standard is called the digital Fourier analyzer, also called Fast Fourier Transform (FFT) analyser. Basically, the analyser accepts an analogue voltage signal that represents acceleration, velocity, pressure, etc. which is then filtered and digitized for computation. The analysed signal can then be manipulated in a variety of ways to produce such information as natural frequencies, damping ratios, etc. which forms the topic for the following section.

## 6.4 Signal Processing and Data Acquisition

### 6.4.1 Brief background in Digital Signal Processing

Much of the analysis, especially in modal impact testing and engine responses is of a periodic nature and needs to perform an analysis in the frequency domain. Therefore, it is required to convert the analogue time domain signals into digital frequency domain information. The method used to perform a transformation of this nature is called the Fourier transformation from which, a periodic signal of time period  $T$  is represented by the Fourier coefficients or spectral coefficients at various frequencies.

Basically, this process is started by an Analogue-to-Digital (A/D) conversion that multiplies the signal by a square wave function, which is zero over alternate values of  $\Delta t$  and has the value of unity at each  $\Delta t$  for a small time. Here  $\Delta t$  is called the *sampling time* and special care must be taken when choosing its value as this can lead to a wrong interpretation of the analogue signal. A common error incorporating with improper sampling is called *aliasing*, which can cause high frequencies to appear as low frequencies (Inman 2001). Aliasing results

---

from Analog to Digital (A/D) conversion and refers to the misrepresentation of the analog signal by the digital record. Basically, if the sampling rate is too slow to catch the details of the analog signal, the digital representation will cause high frequencies to appear as low frequencies.

Aliasing is avoided by choosing a sampling time small enough to provide at least two samples per cycle of the highest frequency of interest. In fact, experience indicates that 2.5 samples per cycle is a better choice, which is referred to as the *sampling theorem* (Otnes and Encochson 1972). It is also possible to avoid aliasing by using an anti-aliasing low pass filter, which only allows low frequencies to pass through. Accordingly, the engine tests using LDV used a sampling time of  $625\mu s$ , which is equivalent to a frequency of  $1600Hz$ , whereas the frequencies of interest of engine excitations are up to  $500Hz$  with a cycle time of  $2000\mu s$ .

Once the digital record of signal is available, the discrete version of the Fourier transform is performed. The task of the analyser is to compute the Fourier coefficients, using Fast Fourier Transform which is developed by (Cooley and Tukey 1965). To make the digital analysis feasible, the periodic signal must be sampled over a finite time. This can give rise to another problem referred to as *leakage* (Inman 2001), which can simply occur due to not cutting the signal at any integral multiple of its period. This causes erroneous frequencies to appear in the digital representation, as a Fourier Transforms assumes that a signal is periodic within the sample record length, which is not actually the case. However, this can be minimized either by using a *window function* that forces the signal to be zero outside the sampling period or by collecting data for a longer time period that takes into consideration many number of cycles. The most commonly used window function is the *Hanning Window*.

#### 6.4.2 Signal Analysis

Most of the signals processed during the experiments were non-deterministic or random with a collection of time histories resulting from various excitations, which could have been severely affected by disturbances (noise) of various form. Such a random signal with an assembly of information of data can only be treated in a statistical manner in order to distinguish its spectral contents and separate these into spectral contributions. This process can effectively be simplified by transforming the signal from its time domain to frequency domain, employing well developed techniques as it is discussed in the previous section. Once

---

the obtained signals were transformed, clear spectra could be seen such as in the engine output response, which is dominated by engine orders and half orders that are due to translating mass and combustion force respectively. Impact testing accomplished to capture natural frequencies of components associated with its modal deformation, the situation was rather complicated as some of the frequencies resided very much closely to each other within the spectrum. In such a scenario it is important to eliminate other excitations as much as possible, which is also known as noise of the signal that would be mistaken with natural frequencies. As such, confidence in a measured quantity is increased by performing a number of identical tests and averaging the results.

If the signal is deterministic, then the Frequency Response Function (FRF), which describes the relationship between the input and the output, for the system can be derived by mathematical relations. However, when the input and output behaviour is available in the form of statistical data in time domain, a rather different approach is used to determine the FRF of the system. As such the Power Spectral Density (PSD) of autocorrelation of the excitation spectra  $S_{ff}(\omega)$  and PSD of cross correlation between the excitation and response  $S_{fx}(\omega)$  can be related to FRF  $H(j\omega)$  as follows:

$$S_{fx}(\omega) = H(j\omega)S_{ff}(\omega) \quad (6.4)$$

In the same manner PSD of autocorrelation of response spectra  $S_{xx}(\omega)$  and PSD of cross correlation between the excitation and response  $S_{xf}(\omega)$  can be related to FRF  $H(j\omega)$  as follows:

$$S_{xx}(\omega) = H(j\omega)S_{xf}(\omega) \quad (6.5)$$

Such that FRF for the same system can be calculated employing two completely different approaches as given by equations (6.4) and (6.5) that underlie the complexity of the process behind the *coherence function*, which is widely used to identify whether a signal is contaminated with noise (more rigorous derivation can be found in (Newland 1993)). Whatever the method used to calculate FRF, it must produce the same function as it is for the same system. Therefore, the *coherence function* denoted by  $\gamma^2$ , which is the ratio between

two FRF values, is used as the determining factor for the consistency of the data. Coherence can be given as follows:

$$\gamma^2 = \frac{|S_{xf}(\omega)|^2}{S_{xx}(\omega)S_{ff}(\omega)} \quad (6.6)$$

If the FRF is consistent, then both equations must produce the same result independent of the way it is calculated, and thus it should possess the value of unity. The coherence is a measurement of the noise of the signal. If it is zero the measurement is of pure noise and, if it returns the value of unity, then both excitation and response are considered not contaminated with noise.

The coherence was plotted against the frequency during each reading of the impact test as an indication of the accuracy of the data collected over the frequency range. Figure 6.9 shows the variation of FRF with the corresponding phase angle and coherence of the crankshaft, during its impact test.

Once confident of obtaining correct coherence, the data was analysed to obtain natural frequencies and mode shapes. Such a data analysis was simplified to a greater extent by using the so-called *single degree of freedom curve fit* approach. In this method the frequency response function for the compliance was sectioned off into frequency ranges bracketing each successive peak. Each peak was then analysed by assuming that it was the frequency response of a single degree of freedom system. This assumes that in the vicinity of the resonance, the frequency response function is dominated by that single mode, which is accurate for a system with such a low damping ratio.

Closely spaced natural frequencies or repeated natural frequencies of the FRF as can be seen at peaks 1 and 3 in Figure 6.9, is one of the major difficulties in modal testing of this sort. When the signal is contaminated with noise or due to leakage into side-bands, then it may be difficult to differentiate the peaks due to modal excitation. However, during resonant conditions the response signal is more prominent, and hence it is less affected by noise. As it can be seen from the figure, the peaks 1–5 occur when the value of coherence is unity.

Even though the value of coherence is below unity in between the peaks, it reaches unity at resonance. At resonance, the phase shift between excitation and the response is  $90^\circ$  as it can

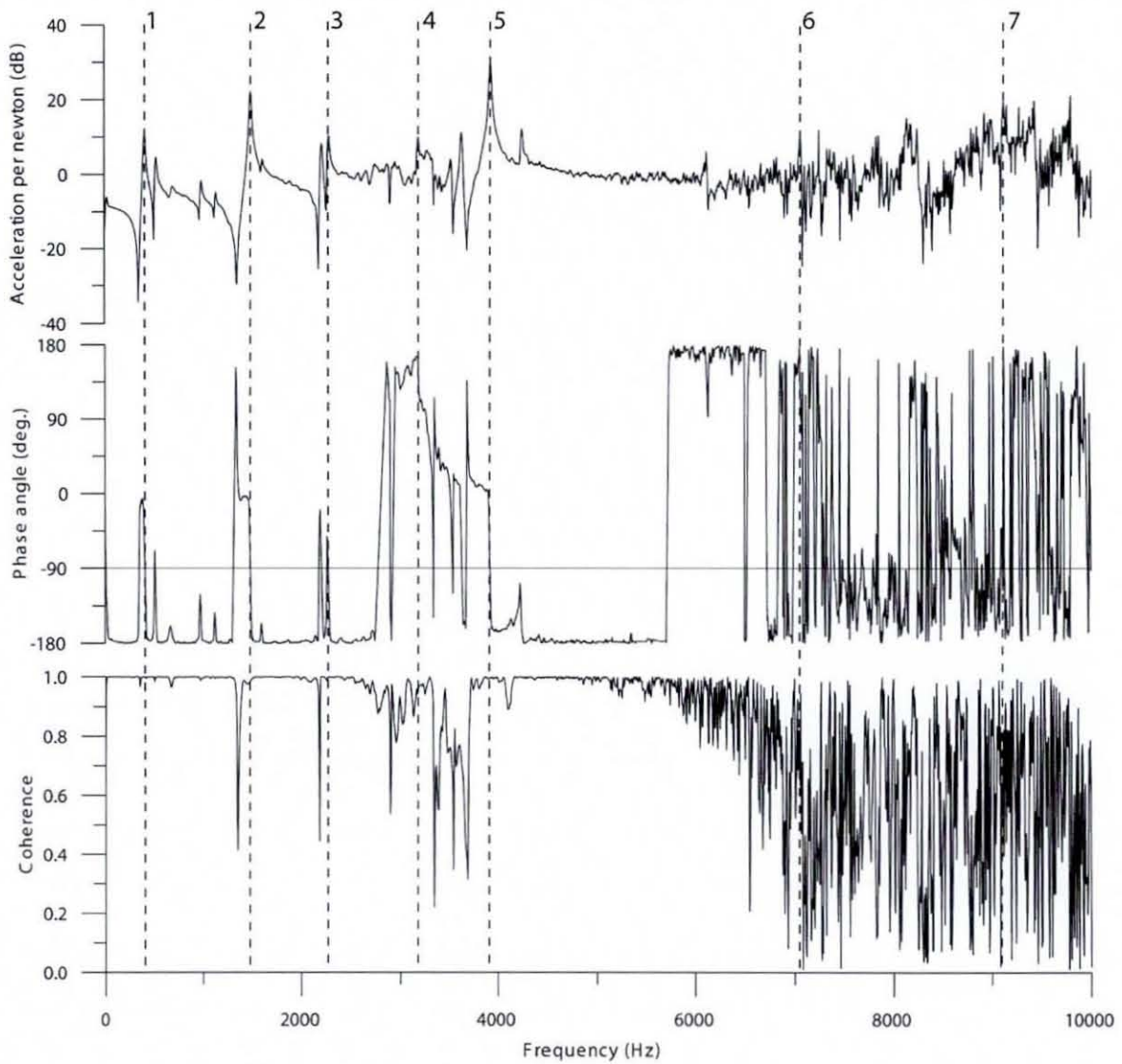


**Figure 6.9 FRF with the corresponding phase angle and coherence function**  
(Obtained during crankshaft impact testing)

be seen from a single degree of freedom system. This is also another factor that strengthens the conclusion that a peak is actually due to resonance, and which can also be seen in Figure 6.9.

When the frequencies are greater than nearly  $6000\text{Hz}$ , the coherence as well as phase shift shows inconsistency, indicating that the signal is contaminated with noise or leakage. Thus, analysis of higher frequencies is omitted. Therefore, even if FRF of the system shows a noticeable peak at this range as it is shown by peaks 6 and 7 in the figure, these values are not

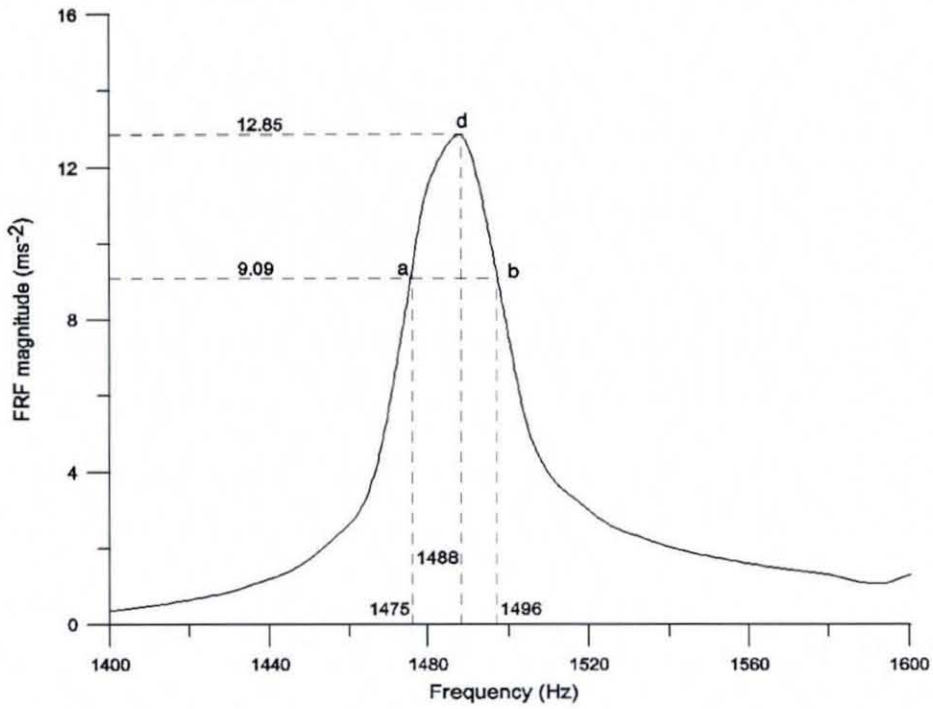


**Figure 6.10 Enlarged FRF magnitude corresponding to 2nd peak of Figure 6.9**

considered as natural frequencies of the system. It is a common practice to eliminate data with coherence less than 0.75.

Even though a single degree of freedom system is defined with a single damping ratio, this is not entirely true for a lumped parameter model that has many mode shapes. The damping ratio associated with each peak is calculated separately and it is regarded as the *modal damping ratio*. Figure 6.10 illustrates the enlarged FRF magnitude, corresponding to 2<sup>nd</sup> peak of the crankshaft FRF, given in Figure 6.9. For a system with light damping a peak of the magnitude at resonance is noticeable and the modal damping ratio  $\xi$  can be related to frequencies corresponding to two points, where the magnitude is  $1/\sqrt{2}$  times the peak magnitude, such that:

$$H(\omega_a) = H(\omega_b) = \frac{H(\omega_d)}{\sqrt{2}} \tag{6.7}$$

And:

$$\xi = \frac{\omega_b - \omega_a}{2\omega_d} = \frac{1496 - 1475}{2 \times 1488} = 0.007 \tag{6.8}$$

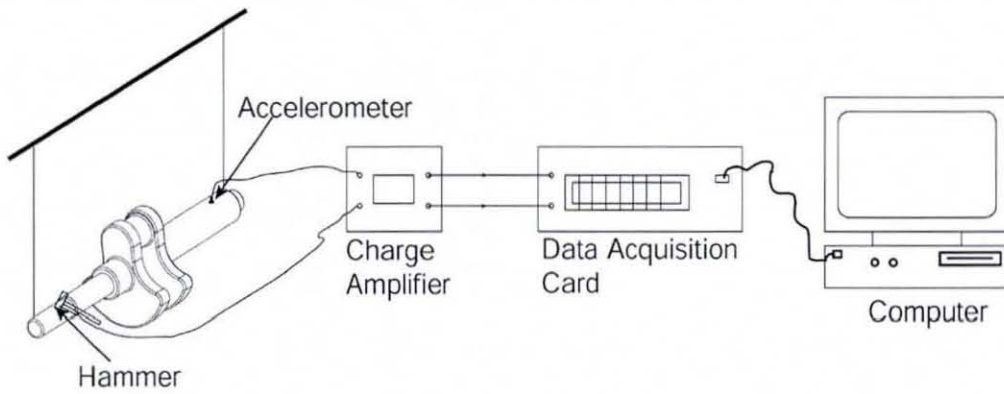


**Figure 6.11 Impact test apparatus set up for the crankshaft**

Here,  $\omega_d$  refers to the damped natural frequency and this relation is known as *3-dB down point* (Inman 2001). As it can be seen from the calculations, the damping ratio is very low: 0.007 (equation (6.8)), corresponding to the second peak. As such damped natural frequency is considered as the undamped natural frequency of the system, as there is very little difference between them.

## 6.5 Testing Procedure

This section deals with the testing procedures undertaken for the impact tests. The impact tests were performed to validate the natural frequencies that have been obtained during FEA. The engine was dismantled and components such as crankshaft, flywheel and connecting rod were tested for their natural frequencies separately.

Figure 6.11 outlines the experimental setup during impact testing on the crankshaft. The crankshaft was hung by two strings, each 1 m long. This may damp out some mode shapes as strings impose a restricted motion along their direction. The most suitable method is to have a free-free boundary condition, while the response is measured. However, such an ideal condition cannot be obtained as there must be some means to hold the test piece during the test. The strings remove only the translational degree of freedom (DOF), allowing all the other possible movements to take place.

The ultimate objective of the impact testing on components was to capture all their natural frequencies, unlike the mode shape estimation, where impact test is mostly used. In mode shape estimation, it is necessary to calculate the magnitude of the response, as well as the

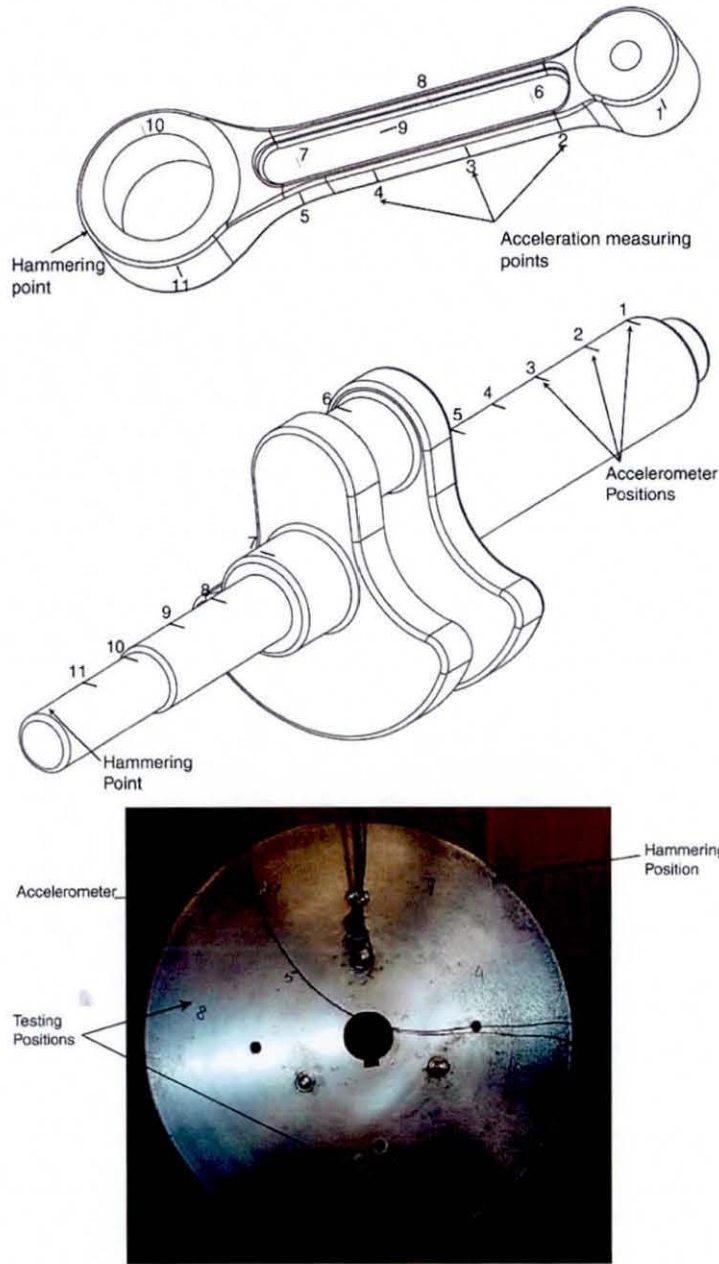


**Figure 6.12 Impact test positions on engine components**

phase difference between the response and the excitation. Phase is essential to predict the direction of motion of the response.

The component to be tested (i.e. the test piece) was excited by an impact hammer in a controlled manner and the response was recorded at various locations with mounted accelerometers. Figure 6.12 shows the locations of impact excitation and the mounted accelerometers in the cases of the flywheel, crankshaft and the connecting rod. In this

No	Accelerometer Position on Crankshaft											Average
	1	2	3	4	5	6	7	8	9	10	11	
1	413	406	406		406	406	400	406	406	406	406	406
2	525	525	525		513	513	519	519	519	519	519	519
3	988		975		975	988	981	969	975	975	975	978
4	1131		1119	1119	1119	1125	1125	1125	1125	1131	1131	1125
5	1481	1488	1481	1481	1488	1481	1481	1488	1481	1488	1481	1484
6			1600		1606	1600	1600	1606	1600	1600	1600	1602
7	2213	2206	2206	2206	2213	2213	2206		2213		2213	2210
8	2281	2288			2275		2275	2275	2275	2269	2288	2278
9			2894	2894		2900	2900	2894	2906	2906		2899
10	3044			3056								3050
11				3175		3181	3175	3181	3175	3175	3181	3178
12			3331	3338		3344	3338	3338	3338	3338	3338	3338

**Table 6.2 Hammer test frequency results for crankshaft**

manner, resonant frequencies were obtained as shown in Table 6.2 for the crankshaft (for illustration purposes the complete set of frequencies only for the crankshaft are shown). It can be noted that there are some missing frequencies at certain positions on the crankshaft. There are a number of reasons for this other than possible experimental errors, such as a node point of the relevant mode shape having coincided with the specific measurement point or there occurred no displacement in the direction of the mounted accelerometer, corresponding to a relevant mode shape at that location.

The electric charge produced by the load cell at hammer and the accelerometer were filtered and amplified by the Bruel & Kjaer conditioning amplifier and the corresponding voltage signal was fed into the PULSE type 3560C portable Data Acquisition Card (DAC). Conditioning amplifier is capable of handling 4 channels, whereas the DAC can handle 3 channels with the maximum capturing frequency of  $25kHz$ . However, only 2 channels were actually needed for these experiments as they involved use of two transducers. The signal conditioning amplifier and DAC are shown in Figure 6.13.

The data was processed by a PULSE LabShop software tool with a dual channel FFT analyzer. This is capable of calculating the FRF, cross correlation, auto correlation, etc of the excitation and response signals. Front end of the LabShop is shown in Figure 6.14, including some data on it.

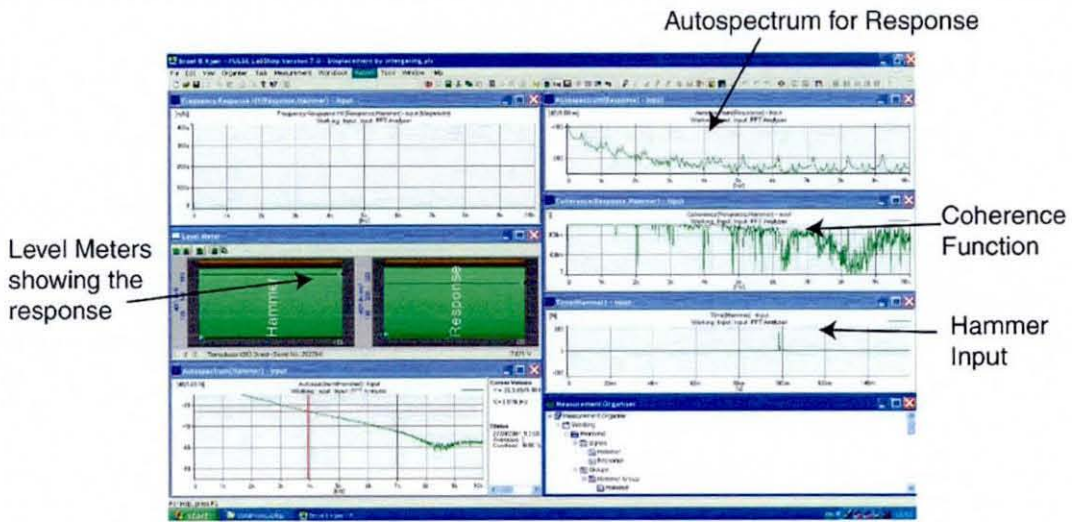


Figure 6.13 Bruel & Kjaer Conditioning Amplifier and DAC system

The FRF obtained by impact testing on the piston does not show any peak within the frequency range of 0–6000 Hz, which the data acquisition system is capable of capturing. This underpins the fact that higher natural frequencies of about 9000 Hz, which have been

Crankshaft			Connecting Rod			Flywheel		
FEM results	Hammer results	Error	FEM results	Hammer results	Error	FEM results	Hammer results	Error
415	406	-2%	569	636	-12%	1345	1330	1%
513	519	1%	740			1345		
1002	978	-3%	1376	1206	12%	2216	2138	4%
1097	1125	3%	1864	2030	-9%	2808	2938	-5%
1496	1484	-1%	3805	3291	13%	2809		
1564	1651	5%	4375			4431	4424	0%
2221	2210	-1%	4599	4600	0%	4437		
2325	2278	-2%				4589	4780	-4%
2937	2899	-1%						
3174	3178	0%						
3316	3338	1%						

Table 6.3 Comparison between the hammer test results and FEM results



**Figure 6.14** Front end of the PULSE software

observed during the analytical investigation, using the FEM approach on piston, reported in chapter 5. Therefore, as there is no reliable method to verify the modal behaviour of piston and it is obvious that its first natural frequency occurs above  $6000\text{Hz}$ , it was decided to include the piston as a rigid body in the numerical model. The solid piston geometry, mass, inertial properties, and its centre of mass location were validated against experimentally measured values.

The crankshaft, the connecting rod and the flywheel were also subjected to impact testing, and a considerable number of natural frequencies were found within the frequency range of  $0-4000\text{Hz}$ . These values show very good agreement with the natural frequencies obtained by FEA as shown in Table 6.3. Experimental and analytical frequency values obtained for the crankshaft show good agreement with error level of  $\pm 5\%$ . Frequency values obtained for the flywheel show good agreement even though there are couple of repeated frequencies present in the FEA predicted values. Error levels for the connecting rod are quite large compared with those for the other two components. As it can be seen in Figure 6.15 the actual connecting rod is an assembly of components bolted together, whereas the corresponding CAD model is a single component. This can create some differences in experimental and analytical frequencies as can be seen around 12%. However as can be seen from the Table 6.3 the first natural frequency of the connecting rod is at  $569\text{Hz}$  which is quite high compared to the frequencies of interest during this analysis. But one should not underestimate the fact that affect of resonance even with very small amplitude excitation. Therefore a CAD model of much precise connecting rod would be better. However such an accurate model increases the

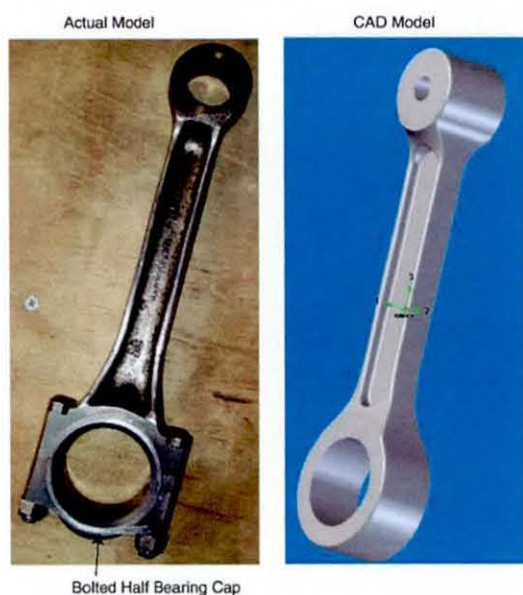


**Figure 6.15 CAD model and the actual model of the Connecting Rod**

number of element in the model quite considerably and bolted connection between lower half and upper half of the bigend bearing is only possible with fixed joint primitive in ADAMS. Such an addition increases the number of degrees of freedom considerably thus increasing thus increasing the simulation time.

## 7 RESULTS AND DISCUSSION

### 7.1 Single cylinder engine dynamics

As highlighted in Chapter 2, modern engine development is dominated by reduction of noise and frictional losses while enhancing the system efficiency. This became further challenging with the introduction of high powered low weight (high power to weight ratio) engines that use light and low stiffness material, thus reflecting the need for a detailed investigation of dynamic behaviour of an engine, with special regards to emission of noise and frictional losses. Internal combustion engine is a complicated system that includes many other sub-systems such as, fuel delivery system, cam-tappet, accessory gears, piston rings, pistons, crankshaft and main bearings that exhibit different dynamic behaviours. It is not possible to develop a numerical or an analytical model that would be capable of addressing all these sub-systems including their dynamics, elasticity, lubrication and thermodynamic behaviours with a reliable degree of accuracy. Therefore, many authors studying NVH characteristics of the engine have paid their utmost attention only to a sub-system or a part of the sub-system.

The frequency spectrum of the measured combustion gas force (see Figure 7.1) shows many excitations belonging to engine order multiples and half engine order multiples (Note that engine is running at nearly  $1800rpm$ , which gives a first engine order of  $30Hz$ ). In IC engines the gas pressure force acting on the piston is converted into a driving torque at the crankshaft end through a slider crank mechanism. During this process of conversion, many excitations are developed, which are also shown in the analytical equation (3.47). Particularly, these integer multiples of engine order excitations are due to variable inertial effect of the translating mass of the piston and the connecting rod. Even though the equation shows only up to three engine orders, there are many excitations in it, which were omitted during the binomial expansion of equation (3.45), owing to their negligible amplitude. However, it must be noted that under resonant conditions even very low amplitude excitations can cause vibrations with higher amplitudes. In fact, these excitations are responsible for the twist-untwist action of the crankshaft, which leads to torsional vibrations of the crankshaft.

---

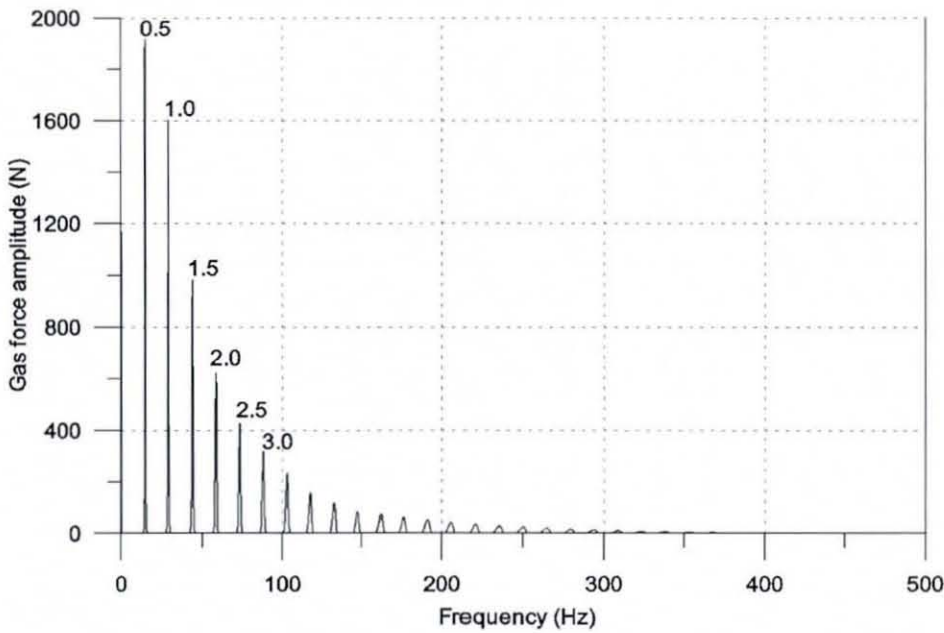


**Figure 7.1** Fourier frequency spectrum for combustion gas force

The crankshaft system can be constructed in one of two possible configurations, a planar type structure in which all the crank throws are arranged in the same plane, and a solid type structure, in which the crank throws are in different planes for different cylinders, thus enabling the combustion cycle phase balance, particularly in multi-cylinder engines. In the planar type structures, coupled vibrations occur between the bending mode in the  $y-z$  crank throw plane and the axial mode in the  $z$ -direction. Furthermore, coupling effect takes place between the bending mode that occurs in the plane orthogonal to the plane of the crank throw, which is the  $x-z$  plane and the crankshaft torsional mode about the  $z$ -direction (orientation of the crankshaft in the  $xyz$  directional coordinates is shown in Figure 5.5). The former coupling effect is referred to as the in-plane mode, because it is in the same plane as the direction of the crank throw for the planar type structures. In-plane and out-of-plane modes for the crankshaft of the E6 engine can be seen in a larger number of frequencies and some of them are shown in Figure 7.2. The responses at the first few frequencies in each case are the most significant, since they exhibit larger amplitudes and reside closer to the engine order harmonics, thus are more prone to excitation. For four cylinder in-line engines with planar structures the natural frequencies of the in-plane modes usually occur in the range  $125-1250\text{Hz}$ , and  $150-200\text{Hz}$  for the out-of-plane modes (Rahnejat 1998). However, the single cylinder crankshaft of the E6 engine used for this study contains the first bending natural frequency in  $415\text{Hz}$  and torsional natural frequency at  $513\text{Hz}$  (see Table 5.4).

Both in-plane and out-of-plane modes not only depend on the configuration of the crankshaft. The properties of the materials used, the stiffness of the supports, manufacturing methods are some other significant factors. Owing to the bulky and rigid construction of the E6 engine crankshaft, it possesses a higher first natural frequency of  $415\text{Hz}$ . However, there is no significant combustion force excitation at frequencies greater than  $300\text{Hz}$  (see Figure 7.1), such that there is no adverse effect from the crankshaft modes at this engine speed. Yet, crankshafts of most modern engines have a very low first natural frequency of around  $100\text{Hz}$  and they tend to rotate at very high speeds, producing higher engine orders, thus these effects are more significant. Low frequency excitation from the engine can cause resonance in the vehicle panels and the air cavity in the cabin, which is known as “boom” noise and occurs between  $25 - 160\text{Hz}$ . This is coupled vibration of the structure and cavity.

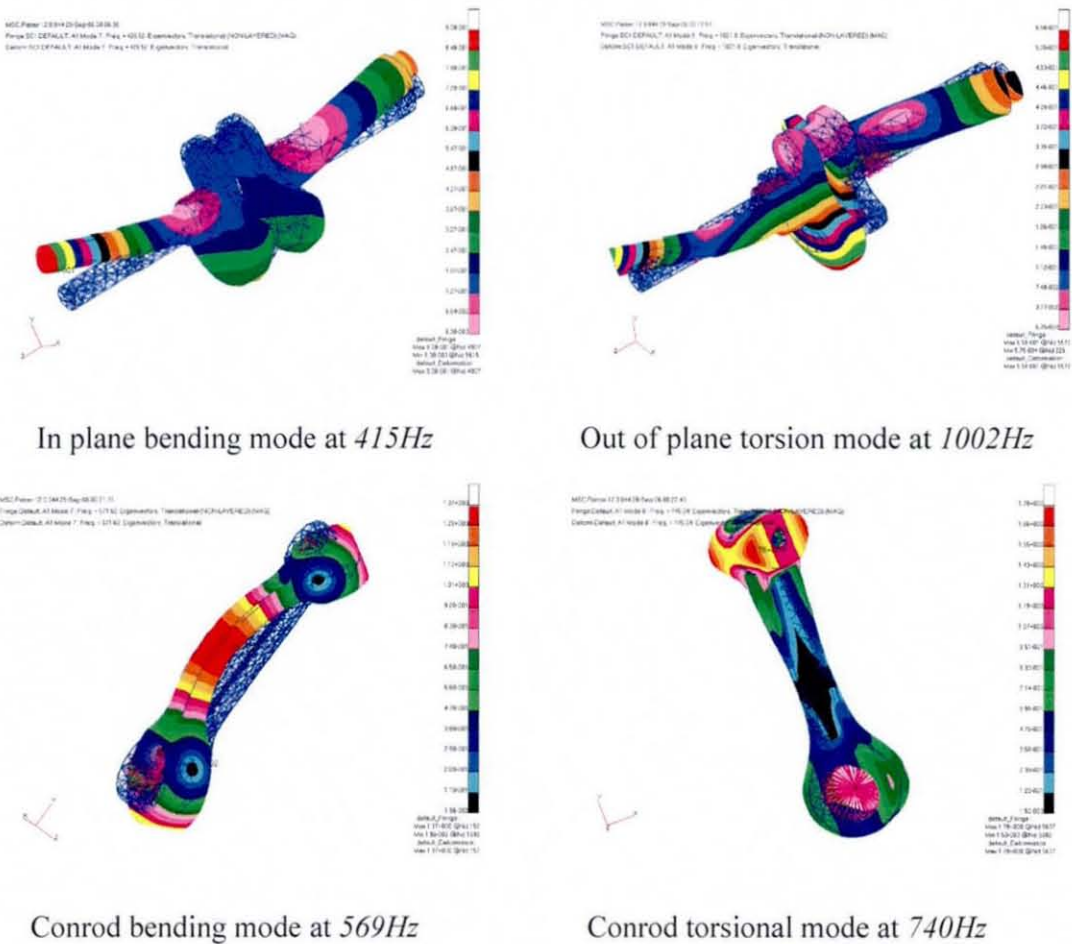
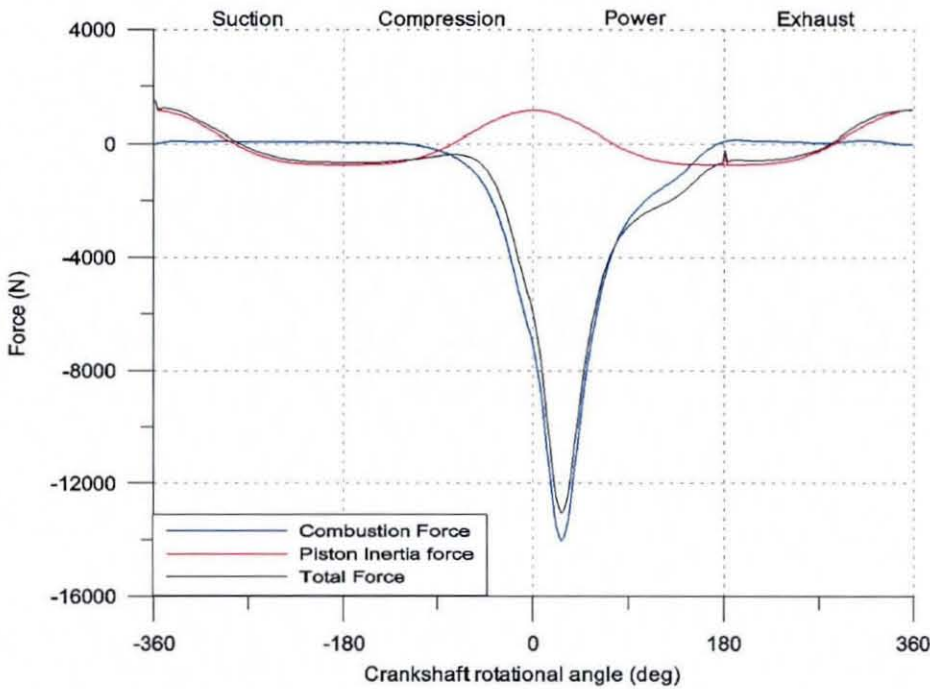


Figure 7.2 Major modes of the crankshaft and the connecting rod



**Figure 7.3** Forces acting on the connecting rod

The connecting rod is another important component in an internal combustion engine. In the process of converting translational motion into a rotary motion, the connecting rod is the one which undergoes both translational, as well as rotational motion.

The small-end of the connecting rod is connected to the piston through a gudgeon pin, which translates, while the big-end is connected to the crankshaft as the rotating end. Basically, there are two force components acting on the piston. One is the inertial force and the second is the combustion gas force. The piston and ring interactions with the cylinder wall generate friction force on the piston, which is comparatively low (in the range of  $20\text{ N}$ ). These force variations are shown in Figure 7.3. Therefore, the connecting rod is subjected to its maximum force a few degrees after the TDC, attributed to the combustion gas force. The inertial force variation on the piston contains multiples of engine order, owing to its translational motion, while the spectrum of combustion force acting on the piston comprises multiples of half engine order frequencies. This concludes the fact that the main excitation frequency of the connecting rod comprises engine orders and half engine orders. However, as already described, the combustion gas force is an assortment of many other excitation frequencies. In the E6 engine, the first natural modal frequency of the connecting rod is  $569\text{ Hz}$ , which is a bending mode (see Figure 7.2 and Table 5.4). At the maximum load, the connecting rod is subjected to a compressive force as a slender beam and this increases the prospects of

exciting the bending mode. However, as the excitation frequencies are much lower than this first natural frequency, the tendency of exciting the bending mode is quite slim. Nevertheless, this is considered to be a vital aspect during the engine design process (Fantino *et al*, 1983; Goudas and Natsiavas 2004).

Eccentric orbit of the main journal bearing can take place due to the dynamic nature of the transmitted force onto the bearing supports as described in section 2.2.2. This problem is more pronounced with the bearing at the flywheel end. Jump phenomenon, which takes place due to the existence of different equilibrium positions within the orbit for the same operating conditions, can produce excitations in many frequencies. The whirling motion that happens at twice the speed of rotation creates another excitation at second engine order as discussed in section 2.2.2. Even though primary motion of the piston is well-defined by the slider crank mechanism, there exists a secondary motion owing to clearance between the piston skirt and the cylinder liner. Though this clearance is small, it is large enough to produce secondary tilting and translational lateral motions that may create unwanted noise and vibration as discussed in section 2.2.3.

These observations highlight the complexity of the combined effects of the inertial force and torque excitations upon the formation of coupled out-of-plane and in-plane deflection modes of the flexible bodies such as the crankshaft and the connecting rod. There are many analytical approaches for solution of various engine dynamic phenomena that are useful in the understanding of complex engine dynamics spectra. A simple analysis for a single cylinder engine, including inertial forces and combustion force has been presented in section 3.5 and some other complex analysis can be found in literature (Cho *et al*, 2003; S.H *et al*, 2002). Nevertheless, many of these analytical approaches do not include the effect of other sources of non-linearity or these are included in very abstracted forms. Most prominently, these sources of non-linearity include journal bearing hydrodynamics, piston skirt - cylinder wall lubrication and friction, its secondary tilting motion and piston ring-to-cylinder wall interactions.

Furthermore, the assembly of parts in the engine model incorporates constraints, representing the attachment of parts that describe certain motions, such as translations and rotations. Analytical solutions can be obtained by linearizing these non-linear equations. However, their omission from the system dynamics equation can lead to erroneous interpretations or

---

conclusions. These shortcomings can be minimized or totally eliminated by using multi-body dynamic formulation for engine dynamics problem that can incorporate all sources of non-linearity. Many multi-body dynamics approaches related to engine dynamics can be found in literature. However, most of these concentrate basically on one aspect of an overall study as detailed in Chapter 2 rather than a system approach. (Boysal and Rahnejat 1997) have modelled a single cylinder four stroke engine, using multi-body dynamics approach, that includes hydrodynamic main journal bearings, torsional damper at the front end of the crankshaft, piston skirt – cylinder wall friction and rigid body dynamics. Current study, presented here is based on an extension to their work on single cylinder internal combustion engine.

## **7.2 The single cylinder engine model**

### **7.2.1 Experimental verification**

As discussed in previous chapters, the piston, connecting rod, the crankshaft and flywheel system of the E6 experimental engine was modelled in multi-body dynamics code, ADAMS. The model was developed starting from the basic rigid body system with constraints.

Then, the model was improved by replacing the rigid bodies with flexible bodies and some of the basic constraints with proper description of contact conjunctions, using multi physics numerical approach.

Figure 7.4 shows the spectrum of torsional vibration predicted by the multi-physics numerical model developed. The frequency composition compares well with the experimentally obtained spectrum, shown in Figure 7.5. The magnitudes also compare well, particularly for the lower frequencies. However, the experimentally obtained spectrum obtained shows higher magnitudes at higher frequencies. Unlike the numerical model, there are various other components in the actual engine such that this kind of variations could be expected.

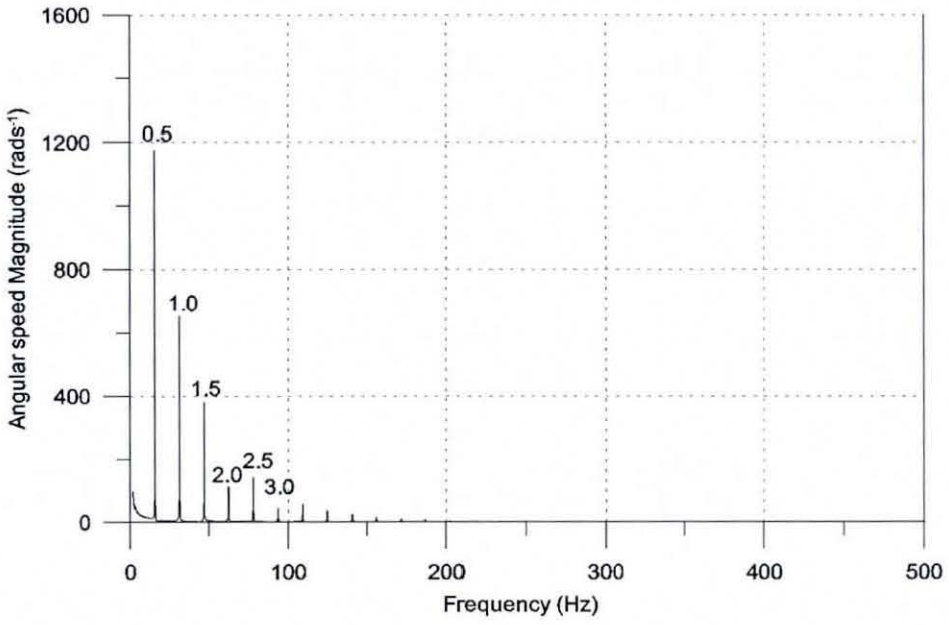


Figure 7.4 Frequency spectrum for Flywheel rotational speed from multi physics numerical model

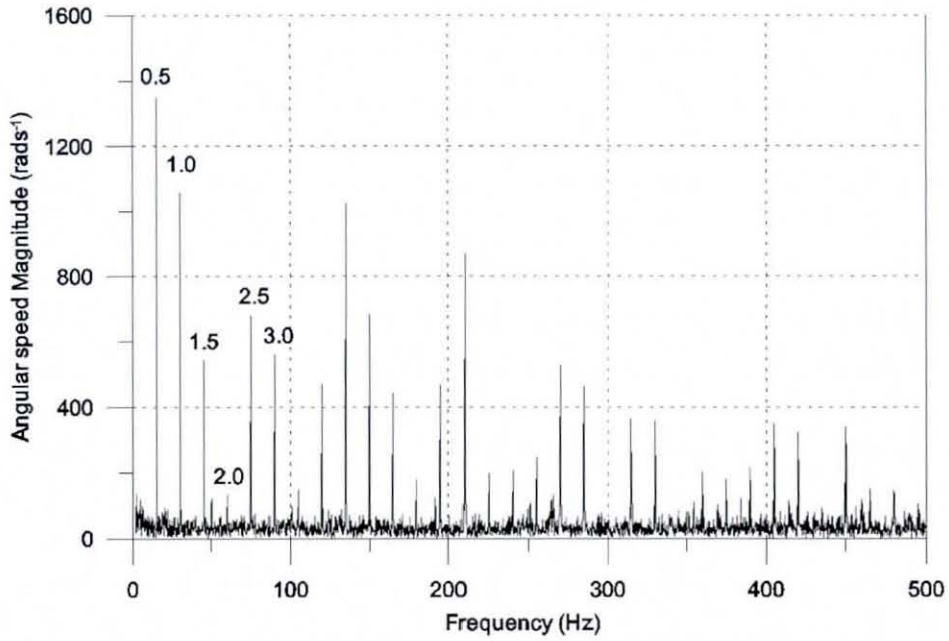


Figure 7.5 Frequency spectrum for experimentally measured flywheel rotational velocity

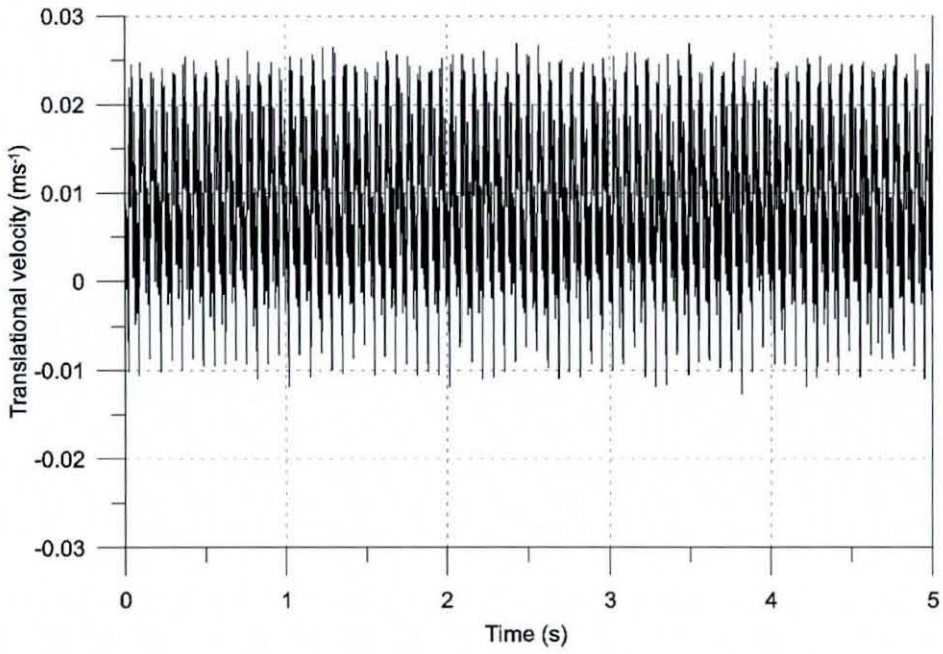


Figure 7.6 Experimentally measured Flywheel nodding velocity

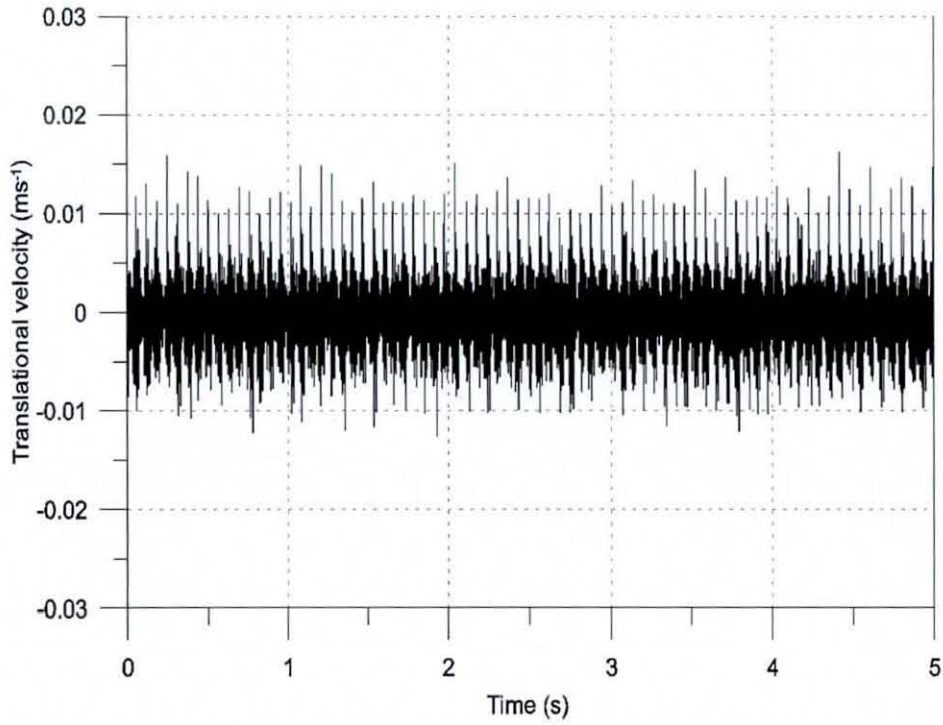


Figure 7.7 Numerically obtained Flywheel nodding velocity

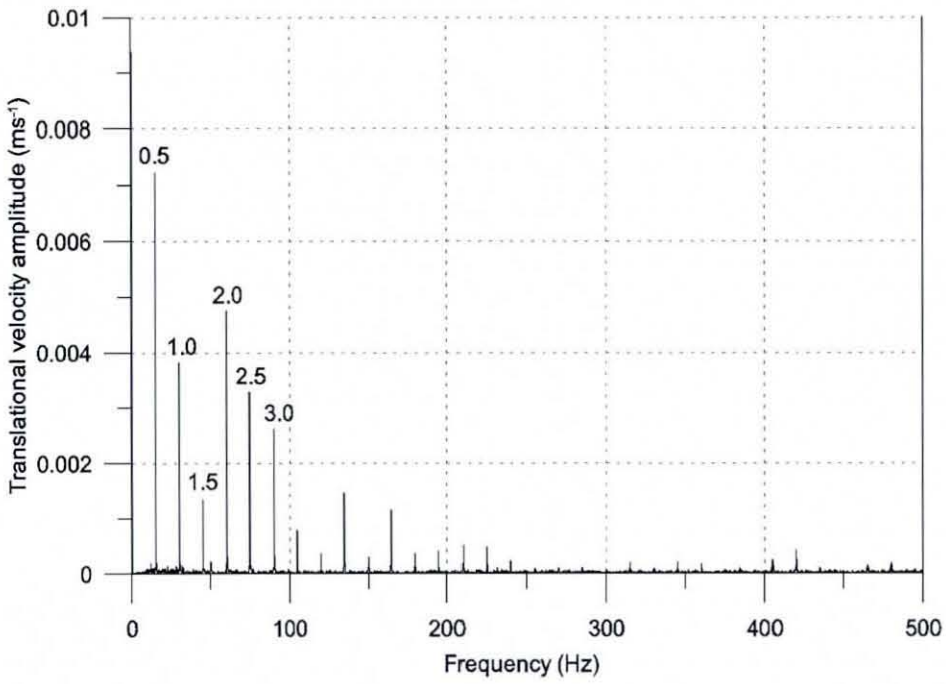


Figure 7.8 Frequency spectrum for experimentally measured flywheel nodding motion

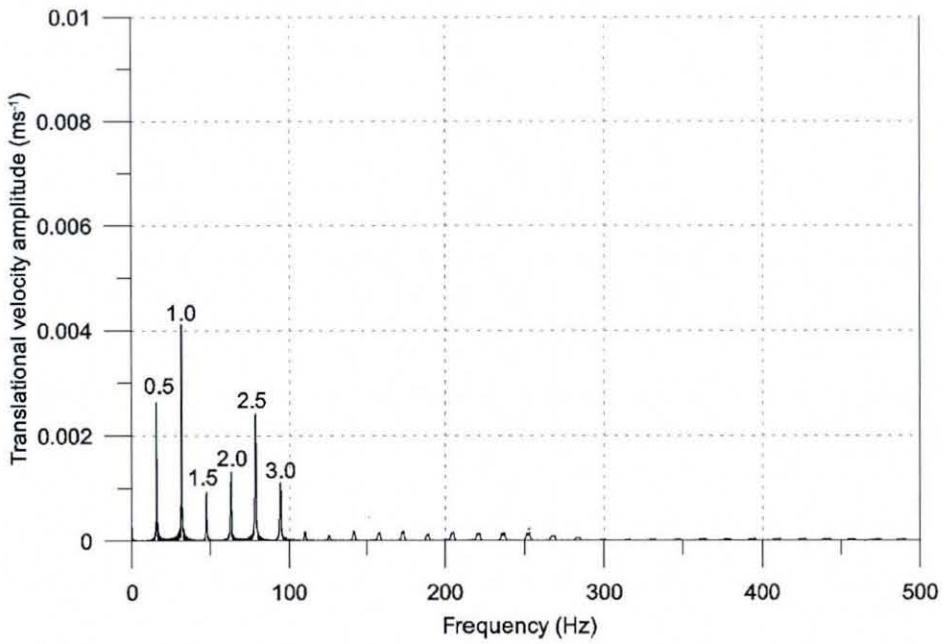


Figure 7.9 Frequency spectrum for numerically obtained flywheel nodding velocity

---

Figure 7.6 shows the experimentally measured nodding velocity of the flywheel and its frequency spectrum is given in Figure 7.8. As it can be seen the mean velocity has been shifted from zero velocity line in the Figure 7.6. The LDV which was used to measure this velocity, as explained in section 6.3.3 was originally built to measure rotational velocities. Therefore when it is used for translational velocity measurement a certain voltage reading is observed even at zero velocity thus, showing a mean velocity shift in the figure. The difference in amplitude is also possible due to stiffness of the engine block that the crankshaft and flywheel resides on. The frequency composition of the experimental data compares well with the frequency spectrum obtained from the numerical predictions, shown in Figure 7.9 (note that frequency spectrum of flywheel nodding velocities are not plotted to the same vertical scale). Also the flywheel nodding velocity is given in Figure 7.7. However, the magnitudes contributions are closely inline with experiments. It is not possible to have a rigorous comparison between these experimental and numerical spectra due to many possible reasons. In the actual engine, there are various other subsystems such as the valve train, timing gears, oil pump, etc which are not considered in the numerical model. Even in the modelled piston-connecting rod - crankshaft sub-system, complicated tribological conjunctions, such as the big-end bearing and the small-end bearing are represented by basic revolute and cylindrical joint primitives, respectively. As a result, the crankshaft bending excitations due to the combustion gas force, which are dominant at low frequencies, may not have induced bending of the crankshaft, thus under-estimating the combined torsional deflection modes (i.e. responsible for the conical whirl of the flywheel). This argument is in line with the lower spectral contributions of the numerical predictions up to 2.5 engine orders, when compared with the experimentally obtained spectral contents. The 3<sup>rd</sup> engine order compares well with the experimental results.

In both the experimental spectra a clear peak can be seen particularly at 50Hz, which is neither a half engine order nor an engine order. This is basically due to the frequency of mains electricity supply. This kind of behaviour can be seen in many experimental data acquisition, involving power supply from the mains.

It should also be noted that FFT is an averaging process, thus actual magnitudes cannot be completely relied upon. The number of time steps, the time step size and windowing method can adversely affect the amplitudes at various frequency contributions. However, when these factors are selected to coincide for the experimental and the numerical results, a different

---

level of leakage may appear due to the slight differences in the engine speeds between them. This problem can be seen in the various comparable spectra, showing slight differences in the values of engine order harmonics. The size of the time step cannot be controlled in the numerical model owing to Corrector changes based on Predicted values in the predictor-corrector approach in ADAMS solver. However, FFT is calculated on a larger time duration compared to the minimum frequency of interest, which is the half-engine order frequency, which eliminates most of these difficulties. A reasonably good comparison is obtained.

The main crankshaft journal bearings are subjected to a maximum load at an interval of every two revolutions of the crankshaft in a four stroke single cylinder engine. The induced forces due to combustion gas pressure and induced inertial forces (as shown in Figure 7.3) are balanced by the instantaneous hydrodynamic pressures generated in the main crankshaft journal bearings. Eccentricity of the journal alters and, thus, the film thickness within the designed clearance between the crank journal and bearing shell, producing necessary pressures that yield reaction forces. A typical clearance of one thousandth of the journal radius ( $30\mu\text{m}$ ) is assumed for this analysis.

The hydrodynamic pressure distribution in the journal bearing also depends on its diameter-to-width ratio, which is 0.6 for this analysis. The short-width bearing, infinitely long-width bearing and finite width bearing approximations are used, if this ratio is less than 0.5, greater than 2.0 and in between these two limits, respectively. For the current analysis the main bearings are approximated as short-width bearings.

As discussed in section 2.2.2 and illustrated in Figure 2.8, at higher Sommerfeld numbers and lower eccentricity ratios the deviation of finite-width solution from that of the short bearing solution is very small. Calculation of Sommerfeld number for a short-width bearing is given by equation (4.20). Figure 7.10 shows the variation of Sommerfeld number and journal eccentricity during a four stroke combustion cycle for the crankshaft front end journal bearing. The results verify that during a combustion cycle Sommerfeld number remains low, when the eccentricity is also low and the Sommerfeld number becomes large at higher eccentricities. Therefore, the assumption of short-width bearing is acceptable, even though it is just beyond its traditional accepted limit.

---

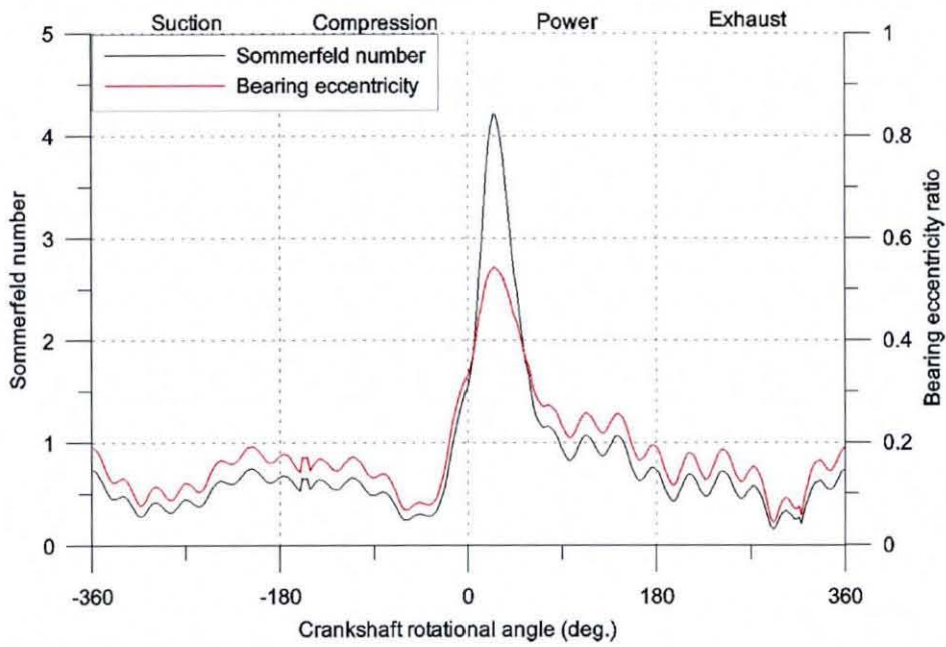


**Figure 7.10** Bearing eccentricity and Sommerfeld number variation during a combustion cycle (for crankshaft front bearing)

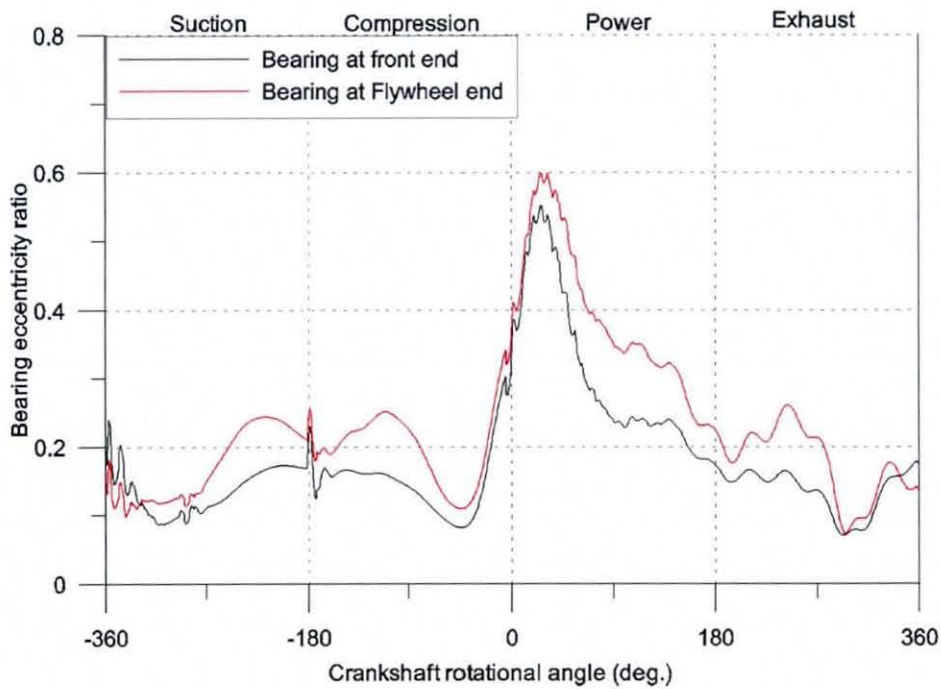


**Figure 7.11** Bearing centre eccentricity ratio during a combustion cycle

The eccentric motion of the journal generates the hydrodynamics entraining motion, as well as the rigid body squeeze effect. The approach of the journal surface towards the bearing shell is regarded as the rigid body squeeze motion. The squeeze effect is regarded as rigid,

---

when the elastic deformations are ignored during hydrodynamic analysis of journal bearings. However, modern bearings are significantly light in construction (i.e. made of materials of low elastic modulus, such as Tin-based alloys). Thus, under extreme operating conditions the bearing shell would be elastically deformed due to high pressures. In fact, this will generate sufficient lubricant film to separate the two contiguous bodies apart, a mechanism which is referred to as elastohydrodynamic lubrication. However, during these conditions viscosity of the lubricant substantially increases and pressures are as much as hundreds of  $MPa$  that are capable of deforming the adjacent elastic bodies. This is not the case for the E6 engine.

However, the solution of thin shell elastohydrodynamic problem is computationally complicated and difficult to include in the same multi-body analysis. The E6 experimental engine is fitted with a thick journal bearing bushing of  $5mm$  thickness, made of steel and subjected to low combustion pressures of nearly  $35bar$ , compared to modern engines with a shell thickness of  $1.5mm$  and combustion pressure of  $150bar$ . During a four stroke cycle, shown in Figure 7.11, the maximum eccentricity ratio is close to  $0.6$ , which means a fluid film is maintained throughout the cycle. Therefore, it is concluded that hydrodynamic lubrication exists throughout the cycle as assumed.

During the engine operation the planar-type single cylinder crankshaft is subjected to coupled bending and torsional vibrations. Therefore, this can act as a source of excitation for the crankshaft and the flywheel bending and axial float, which is known as flywheel nodding action. The bearing closest to the flywheel end is subjected to higher loads during the engine cycle. This effect is particularly pronounced during the peak combustion force. The bearing force variation is shown in Figure 7.12, which confirms this supposition. Whilst a maximum load of nearly  $6000N$  is obtained for the front end bearing, that for the flywheel-end bearing is  $7500N$ . Higher the reaction force, the eccentricity of the bearing becomes larger in order to produce the necessary hydrodynamic reaction. During a 4 stroke engine cycle most pronounced force component is the combustion gas force as can be seen from Figure 7.3, other than the inertial forces due to the various moving components. This force must be balanced by the bearing reaction force. Therefore, the bearing reaction also exhibits a similar force variation (or pattern) (see Figure 7.3 and Figure 7.12). It must be noted that other inertial forces, such as the crankshaft are not taken into consideration during this total force calculation in Figure 7.3, as it contains almost a constant inertial contribution due to its rotary motion.

---

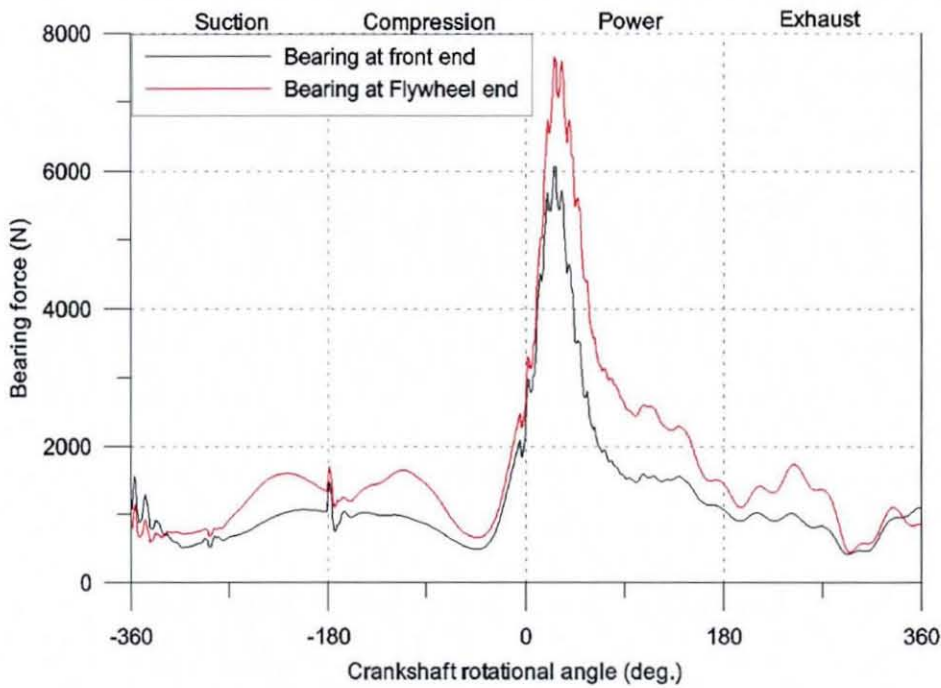


**Figure 7.12 Bearing load at 4 stroke combustion cycle**

The eccentricity ratio, given by equation (4.10) is a function of bearing reaction load. Therefore, the variation of eccentricity ratio has almost the same pattern as the bearing reaction, see Figure 7.11. The hydrodynamic reaction force in the bearing is due to combined fluid entraining motion and squeeze film effect. The approach velocity of the journal surface towards the bearing shell introduces the squeeze action upon the lubricant film. Figure 7.13 shows the bearing centre velocity variation in the radial direction. This shows that the hydrodynamic pressure is dominated by the squeeze action before its maximum value (close to the TDC in the power stroke). Once it passes over this peak reaction force the two contacting bodies are departing, decreasing at the contact reaction. It must be noted that radially outward direction from the bearing centre is considered to be positive for velocities in this plot.

This is further augmented by the variation of coefficient of friction in the bearing as shown in Figure 7.14. Under hydrodynamic conditions, the friction force in the journal bearing is dominated by the entraining motion of the lubricant. Before the bearing is subjected to its peak load the hydrodynamic pressure is dominated by the squeeze film, thus the friction coefficient decreases. However, after the peak load the two contacting bodies are departing and thus the lubricant is dragged into the contact more readily.

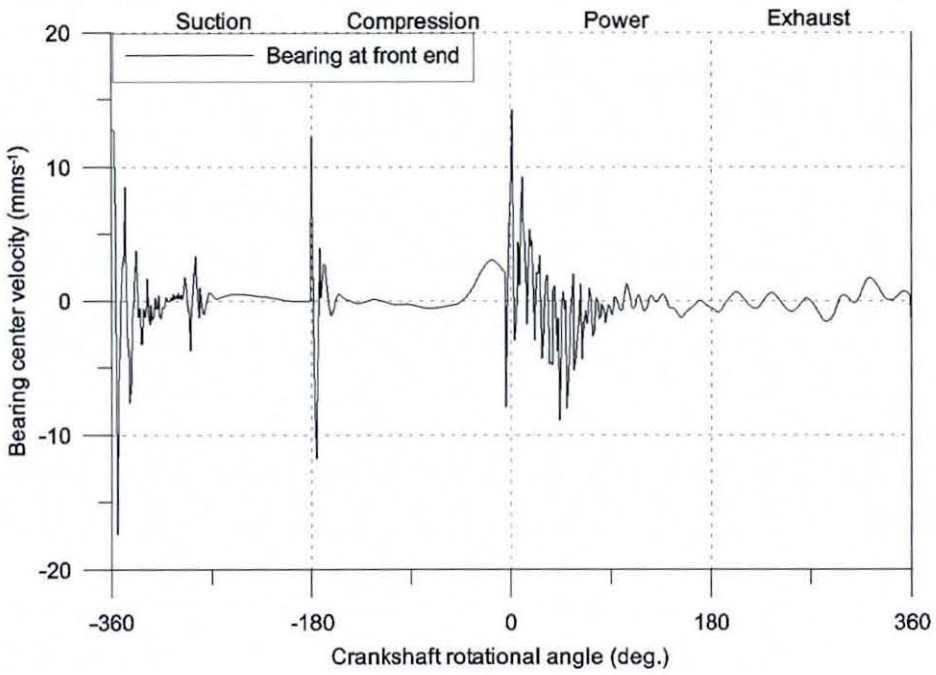


Figure 7.13 Bearing center velocity (in radial direction) during a 4 stroke cycle

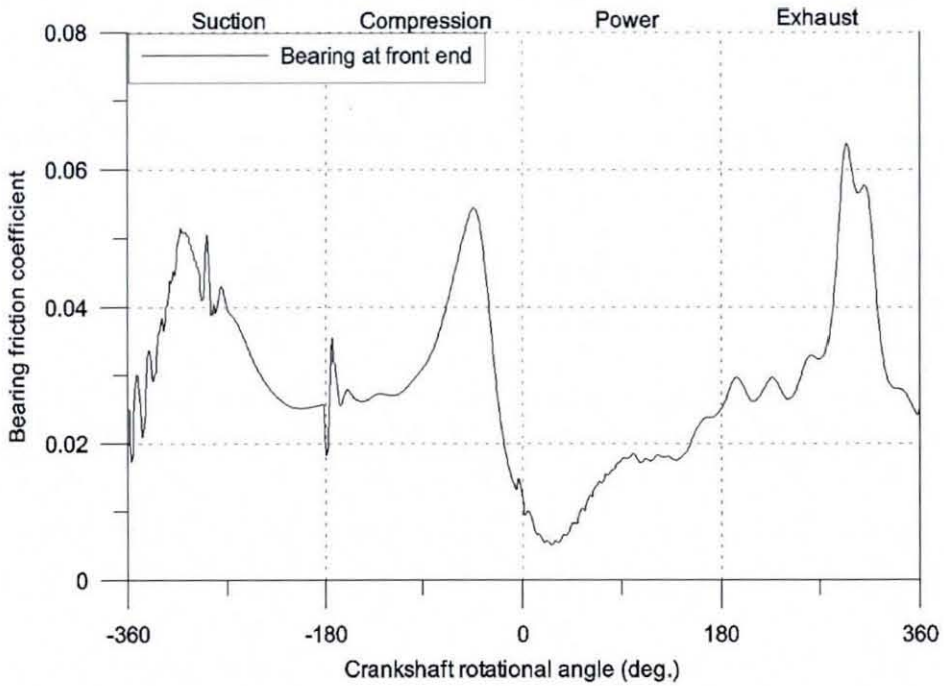


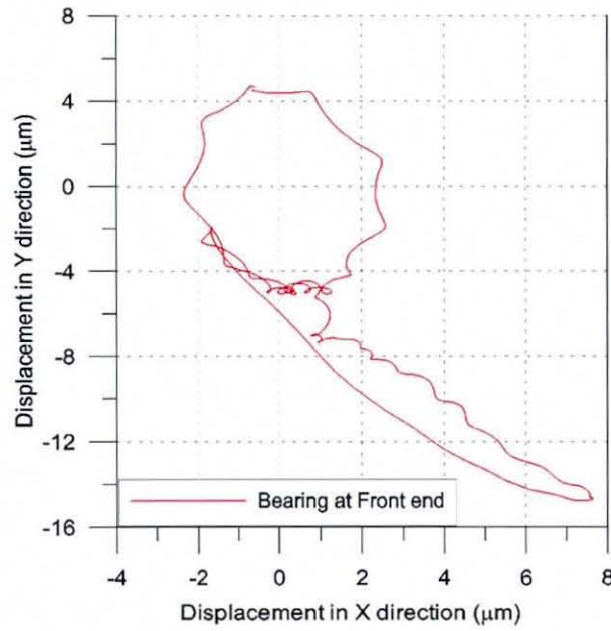
Figure 7.14 Variation of friction coefficient at bearing during a 4 stroke cycle

The same behaviour can be observed throughout the combustion cycle. Whenever the squeeze velocity becomes zero the coefficient of friction increases and it decreases when there exists a squeeze velocity. Consequently, the friction coefficient is decreased at the peak bearing loads due to squeeze action of the journal bearing and reduced effect of entraining motion (i.e. viscous friction is dominated by relative velocities of the surfaces or entraining of the fluid into the contact). Further to this, the angle between the line of centres and resultant bearing force, which is called the attitude angle (given by equation (4.13)) tends to decrease with an increase in eccentricity (which is expected as found analytically by (Cameron 1966; Pinkus and Sternlicht 1961)). Hence, the resultant force is more towards the line of centres rather than in the perpendicular direction to it. This perpendicular component is mainly responsible in the friction force (or torque) at the contact and the potential unstable bearing motion. Therefore, at higher loads, causing higher  $\varepsilon$ , stability of the journal bearing motion is enhanced while reducing the resisting torque. Consequently, with decreased  $\varepsilon$  the reaction force component in perpendicular direction to the line of centres is increased whilst increasing the friction torque. This phenomenon is also shown in the shaft whirling stability map given by Figure 4.5, which indicates bearing instability at low values of  $\varepsilon$ , as well as at higher rotational speeds.

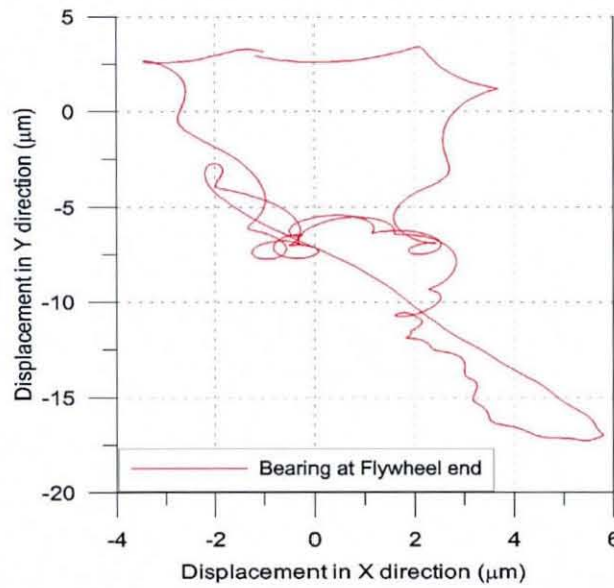
During the power stroke, the crankshaft and the connecting rod are arranged such that the radial component of the force is acting towards the  $x - (-y)$  quadrant of the crankshaft as shown in Figure 7.31. Therefore, the bearing orbit is shifted towards this direction during the peak pressure of the power stroke as shown in Figure 7.15. However, it must be noted that both the  $x$  and the  $y$  axes in the figure are not drawn to the same scale in order to provide a clear illustration, and this should not get confused with that front end bearing, which exhibits a higher eccentricity. The corresponding bearing centre orbit for the flywheel end exhibits a larger radial displacement compared to that of the front end bearing, as expected. This is because of larger distribution of inertia towards the flywheel end.

The magnitude of the combustion gas force is negligible at the BDC and increases to a maximum of  $15000N$  close to the TDC at peak combustion pressure, as shown in Figure 5.7. The vibration spectrum of the applied gas force (i.e. the signature of the 4-stroke process) is of particular interest, since its various spectral contents excite the vibration modes of the crankshaft system. Figure 7.1 shows the vibration spectrum of the combustion gas force. The

---



(a)



(b)

**Figure 7.15 Crankshaft bearing centre loci during a combustion cycle**

contribution at  $30\text{Hz}$  is due to the steady state engine speed of  $1800\text{rpm}$ . There is a significant contribution at  $15\text{Hz}$ , which is the main combustion forcing frequency of a four stroke combustion cycle as anticipated by the analytical derivations, given in section 3.5.2. The other peaks of the spectrum correspond to the multiples of this half engine order.

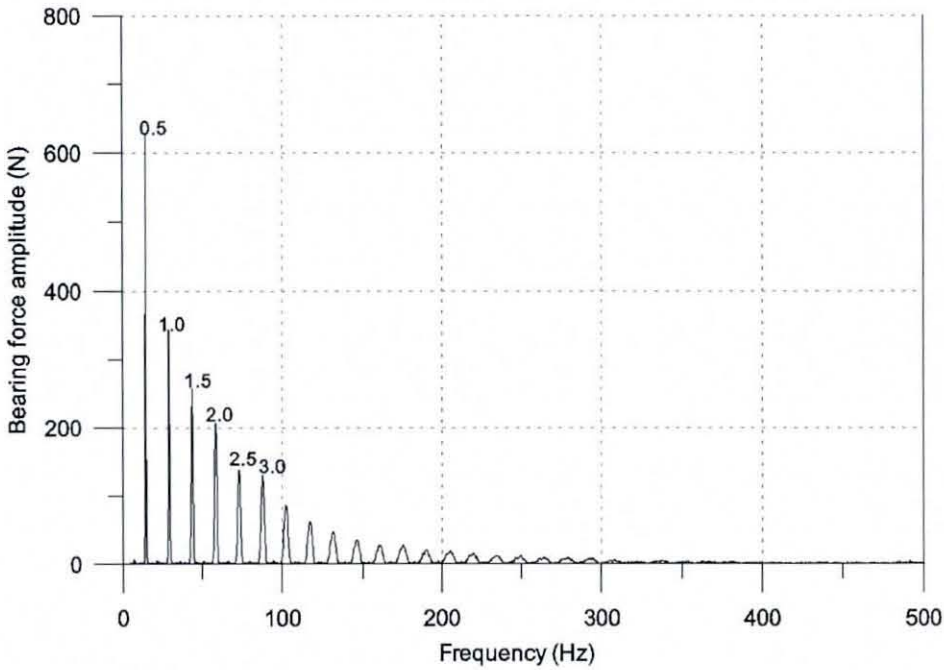


**Figure 7.16 Fourier frequency spectrum of the bearing force at front end of the crankshaft**

As combustion gas force is the main excitation in an IC engine, its effect can clearly be seen in most locations in the structure. Figure 7.16 shows the frequency spectrum of the bearing force at the front end of the crankshaft and significant spectral contents up to 300Hz can easily be seen, as it is observed in the spectrum of the combustion gas force itself. However, the half engine order content is significantly larger than the others as anticipated due to half-speed oil whirl of the journal bearings, discussed in section 1.4. Both synchronous and fraction non-synchronous whirl of the journal centre is prevalent in shaft systems supported by journal bearings and have been observed both experimentally and predicted numerically (see section 4.3.2). Figure 7.15 shows the bearing centre variation during a four stroke cycle.

An NVH concern in the internal combustions engines is piston secondary motions. This problem has been addressed by many researchers, but mainly isolating the piston and mostly under hydrodynamic conditions or sometimes using very abstracted forms such as spring damper representation of the various load bearing contacts. The complex and transient nature of forces acting on the piston, together with clearance between piston skirt and the cylinder wall encourages piston secondary motion other than the primary motion required for transmission of the useful power. This secondary motion of the piston leads to its slapping action against the cylinder bore wall that leads to wear of the piston skirt, as well as contributing the NVH spectrum of engine vibrations.

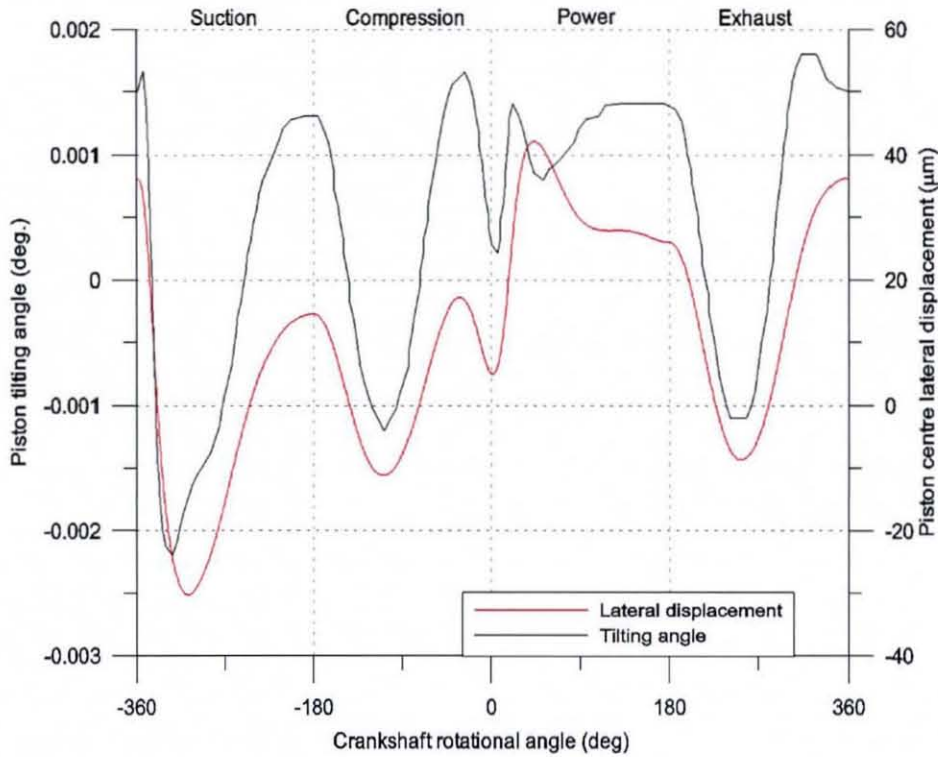
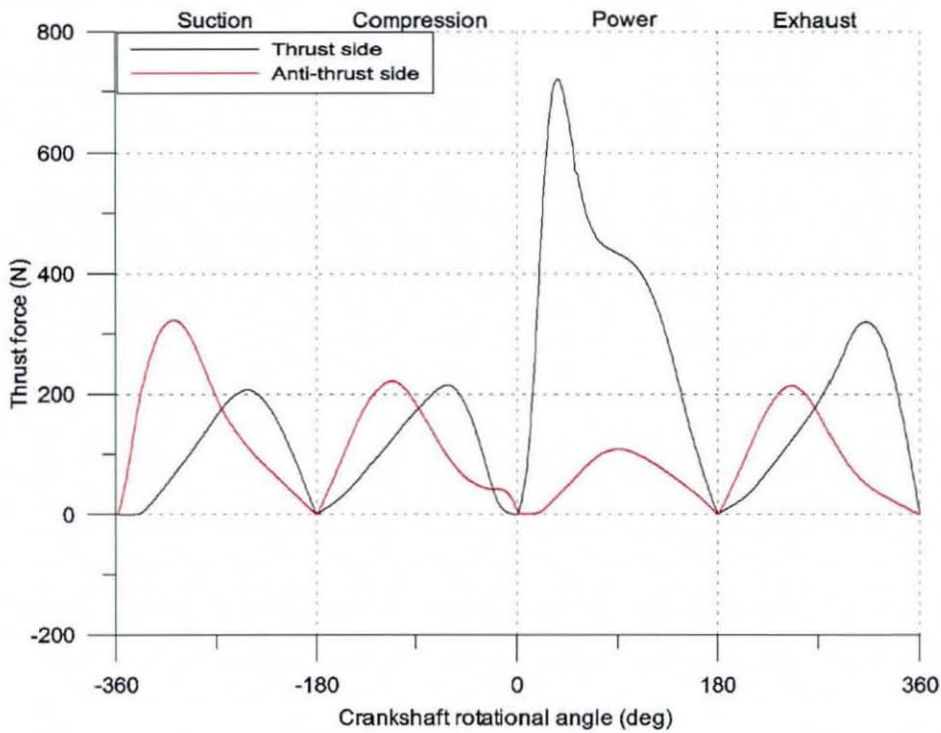


Figure 7.17 Piston secondary motion

### 7.2.2 Piston secondary motion

The secondary tilting motion of the piston can be obtained in the single cylinder multi-body model, using appropriate constraints between the cylinder bore (which is the ground/external frame) and the piston, and the latter and the connecting rod. As depicted earlier the connecting rod is constrained by a revolute joint, whilst the piston and the ground are connected by a planar joint, which is free to move on a plane orthogonal to the crankshaft axis. Piston rotation in this orthogonal plane, which leads to the slap motion is constrained by four single component forces as explained in section 5.5.5 and shown in Figure 5.16. The magnitude of these force components depend on tribological conditions in the contact conjunctions. The piston is allowed to undergo its primary translational motion along the cylinder wall, as well as the tilting motion about the z-axis (which is parallel to the crankshaft axis). The translational motion along the x-axis is also allowed (lateral motion within the confine of piston-cylinder clearance), as shown in Figure 7.17.

Piston as a rigid body is subjected to various forces within the confine of cylinder. Owing to changes in orientation of the connecting rod, the direction of reaction force alters instantaneously. Combustion gas force changes its magnitude quite rapidly during the



**Figure 7.18 Piston thrust force variation at positions 1 and 2**

combustion cycle. As a result piston executes small oscillations within the cylinder clearance, rubbing and slapping against the cylinder wall. Larger impact can then result in the major thrust side wall (see Figure 5.18). However, piston secondary motion can be decomposed into two motions. First is the tilting motion that takes place due to side-to-side oscillations of the piston and second is the translation of the piston perpendicular to the piston axis (its lateral motion). The variations of these two motions are shown in Figure 7.17. Note that piston tilt towards the thrust side is considered as positive. These two movements are greatly responsible for the piston skirt-cylinder wall lubrication as this controls the squeeze film action in the hydrodynamic lubrication.

In fact, almost all of the modern engines are fitted with the offset gudgeon pins. Particularly, gudgeon pin offset supposed to be a method of reducing frictional losses between the piston skirt and cylinder wall (Dursunkaya *et al*, 1994). However, in the current study the gudgeon pin offset is not taken into consideration as the E6 experimental engine used does not report any details for this.

From Figure 7.17, it can be seen that the tilting angles are indeed quite small. Nevertheless, these small angles lead to instances of repetitive slap of the piston against cylinder wall. Figure 7.18 shows the thrust force variation at the cylinder wall at the major thrust side and

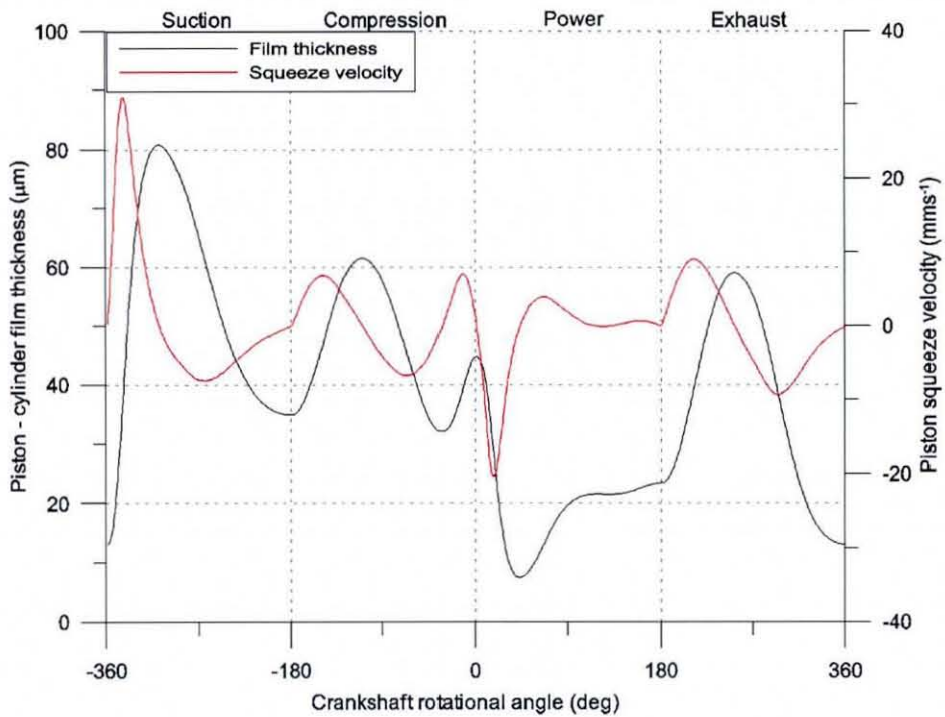


**Figure 7.19** Film thickness and squeeze velocity variation at thrust side (at piston position 2)

the anti-thrust side (piston positions 1 and 2, refer to Figure 5.18). Tilting oscillations with longer time period result in lower impact forces, while sharper oscillations result in higher impact forces.

Thrust force is at its maximum during the power stroke. Figure 7.19 shows the variation of squeeze velocity and the lubricant film thickness at piston position 2, which is the thrust side. From the figure it can be seen that soon after the piston traverses the position of the TDC during the power stroke, the squeeze velocity is sharply increased.

The variation of coefficient of friction at the piston skirt-to-cylinder wall is shown in Figure 7.20 and it varies in between 0.002 – 0.02 confirming the fact that it entertains fluid film lubrication through the combustion cycle. At the beginning of the suction stroke the force at the thrust side is very small as can be seen from the Figure 7.18 and at the same time it undergoes with small or no entraining motion. There is no squeeze velocity at this point to build a lubricant pressure. Thus, there exists a higher friction coefficient. However soon after the power stroke the friction coefficient is lowered to very small value. At this point there is a very high squeeze velocity as can be seen from the Figure 7.19. Such that the load it carried by the squeeze film pressure which does not support much for the viscous friction.

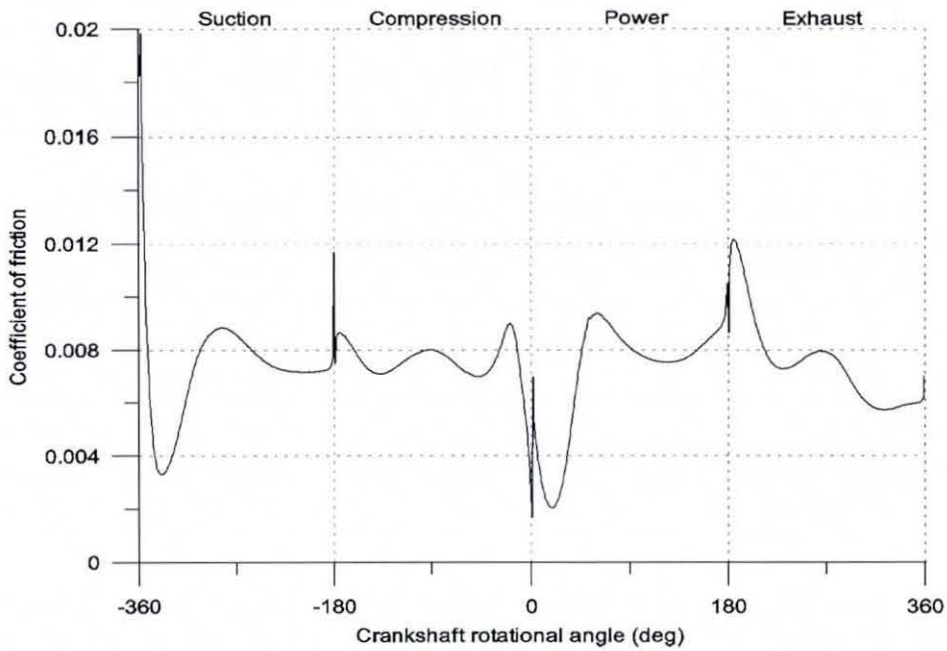


**Figure 7.20 Coefficient of friction for the piston skirt-to-cylinder wall contact**

In a real engine, normally a mixed regime of lubrication takes place particularly at the TDC and the BDC. Figure 7.19 shows that the film thickness never falls below  $9\mu\text{m}$  in this particular engine, thus there is no contribution due to boundary friction at piston-cylinder wall contact, even though entraining action of the lubricant has ceased. There is circumstantial evidence that this prediction is fair, since this engine was manufactured in late 1950's and it has been running for a considerable period of time, whilst there has been no requirement of either change of the liner or a noticeable increase in friction during its lifetime. If the engine had been running under boundary regime of lubrication for such a long period of time, this would have resulted in some failures. The large nominal clearance in this engine essentially means that it tends to avoid boundary interactions at the dead centres.

In the vicinity of the dead centres, the friction coefficient is increased. At the beginning of the suction stroke ( $-180^{\circ}$  to  $-170^{\circ}$  cam angle), the contact force at the major thrust side is almost zero as can be seen in Figure 7.18. Again the same incidence, as described above can be seen at the end of the compression stroke. At this point the thrust force is nearly zero, particularly due to rigid body separation. However, at the beginning of the compression phase, as well as the exhaust stroke, higher friction coefficients can be observed. This happens particularly due to small squeeze velocities (nearly zero) and very small film

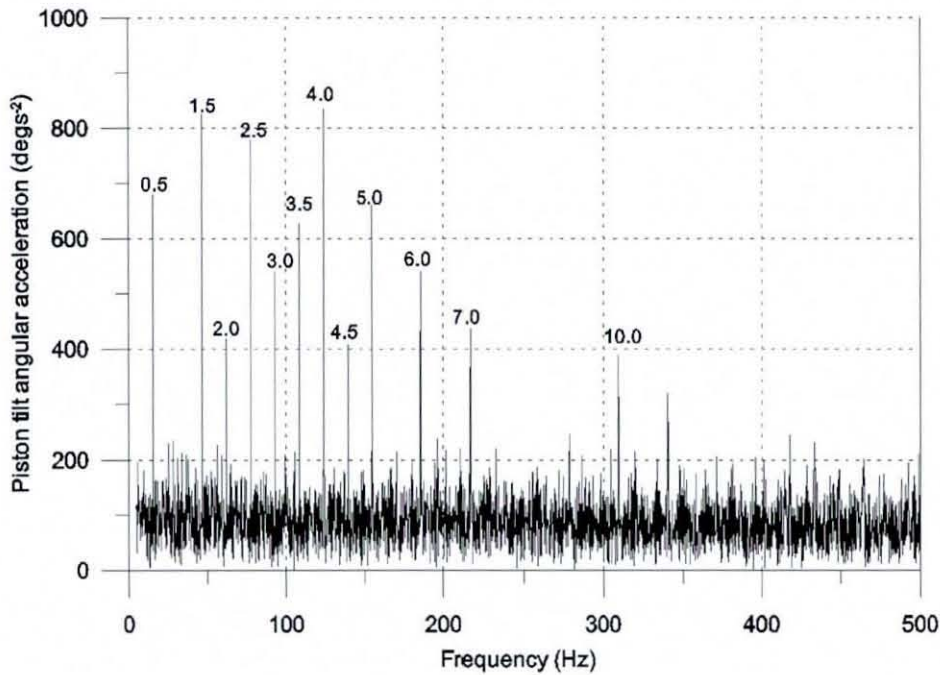


**Figure 7.21** Fourier spectrum for angular acceleration of piston tilting motion

thickness, as can be seen in Figure 7.19. It should be noted that the analysis of piston skirt-to-cylinder wall contact indicates that a hydrodynamic film is always retained, even under pure squeeze film effect. Thus, no boundary contributions occur. Hence, reducing the speed of entraining motion reduces the sliding friction, which is observed in all the predictions made. With a lower film thickness, these conditions are not observed such as in the piston ring pack.

The frequency domain representation of tilting angle is shown by the response FFT of the tilting angular acceleration given in Figure 7.21. The figure shows that main contributions occur at engine orders and half engine orders. However, most of these contributions are at engine order multiples, owing to the induced inertial torque, as anticipated. The first engine order, dominant in the piston translational motion, is absent from its tilting motion. The half engine order frequency indicates that tilting motion is coupled with combustion gas force.

### 7.2.3 Piston ring analysis

As already pointed out in the literature review (chapter 2) many researchers have directed their attention to piston ring lubrication, but mainly in isolation from system inertial dynamics and mostly under hydrodynamic conditions only. In most studies the piston secondary motions have been ignored. There is a clearance gap between the piston ring and

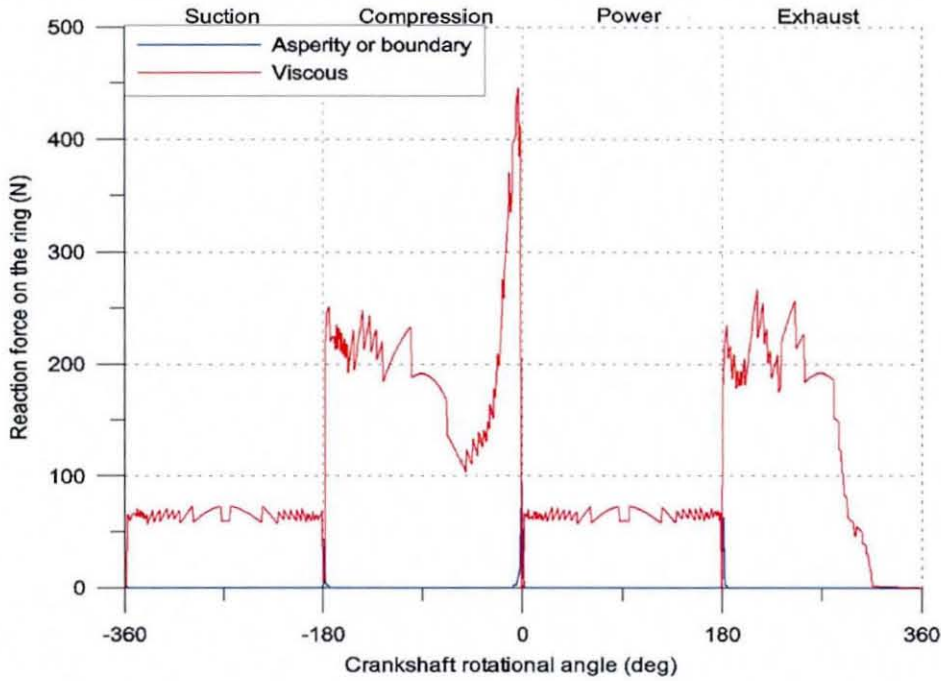


**Figure 7.22** Reaction force variation at piston ring cylinder wall contact

the groove as it is shown in Figure 5.22, thus the ring is free to move in the piston groove. Owing to this clearance the ring resides on the lower groove surface during the upward motion of the piston, whereas it resides on the upper groove surface during piston's downward motion. Therefore, when the piston is moving upwards the inner surface of the ring is subjected to the combustion chamber pressure, whilst it is subjected to the crankcase pressure during the downward motion of the piston. The force due to ring tension and inner ring pressure is balanced by the lubricant reaction force acting on the ring face-cylinder wall interface.

The total reaction force at the ring face-to-cylinder wall interface consists of two main components as mentioned in section 5.5.7, those due to hydrodynamic lubricant reaction and interaction of asperities (boundary component). Hydrodynamic force is mainly due to lubricant entrainment and vanishes with cessation of entraining motion at the dead centres. Therefore, at the dead centres the ring is totally supported by the asperity forces. Figure 7.22 shows the variation of reaction force at the piston ring face in contact with the cylinder wall. This comprises the boundary force and the hydrodynamic lubrication force. During the suction stroke and the power stroke the piston is moving in the downward direction. Therefore, the inner ring face is subjected to crank case pressure, which is almost equal to the atmospheric pressure. Therefore, the reaction force is dominated by the outward ring tension

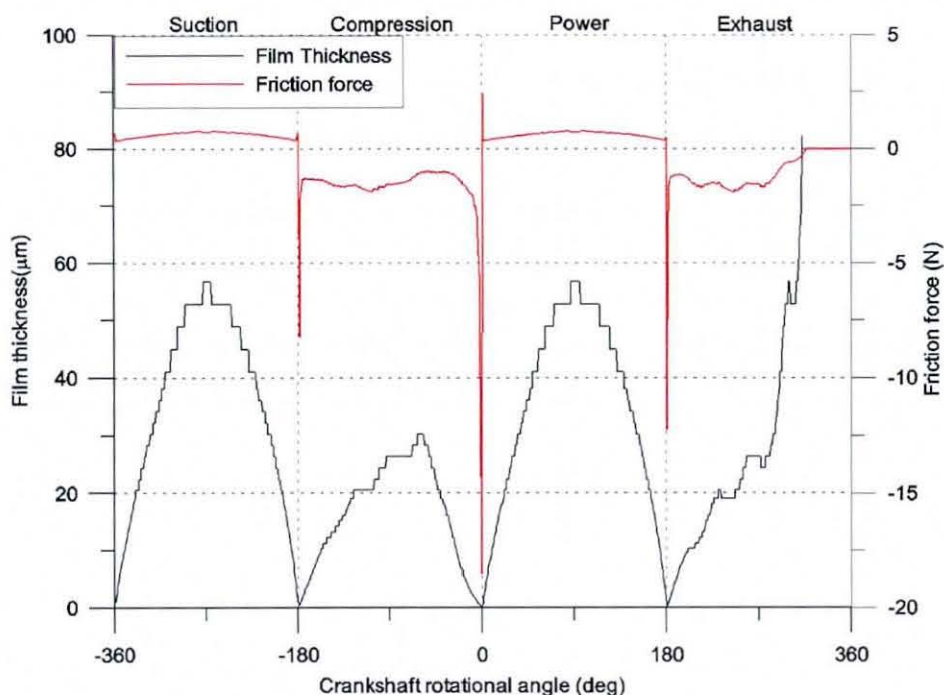


**Figure 7.23 Variation of film thickness and friction force at piston ring cylinder wall contact**

force, which is a constant force. Hence almost a constant reaction force can be seen during these two strokes. During compression and exhaust strokes the piston is moving upwards, whilst exposing the inner ring face to the combustion chamber pressure. Therefore, during these two strokes the reaction force is augmented by the gas pressure other than the ring tension and, thus, a higher ring force can be observed (see Figure 7.22).

Figure 7.23 shows the variation of minimum film thickness and the friction force at the ring face-to-cylinder wall contact for a 4 stroke combustion cycle. The film thickness is comparatively large, particularly at the suction and power strokes, where the contact loads are low. At the mid span of the stroke the peak sliding velocity occurs and, therefore, the maximum film thickness can be observed. However, the inner side of the ring is exposed to the combustion pressure during the compression and exhaust strokes. Hence, the contact load increases, whilst the minimum film thickness decreases, in order to support this higher load. The ring inner surface is subjected to the maximum gas pressure at the end of the compression stroke ( $-30^{\circ}$  to  $0^{\circ}$  crank angle). Therefore, the ring load reaches its maximum value at this point, as can be seen in Figure 7.22.

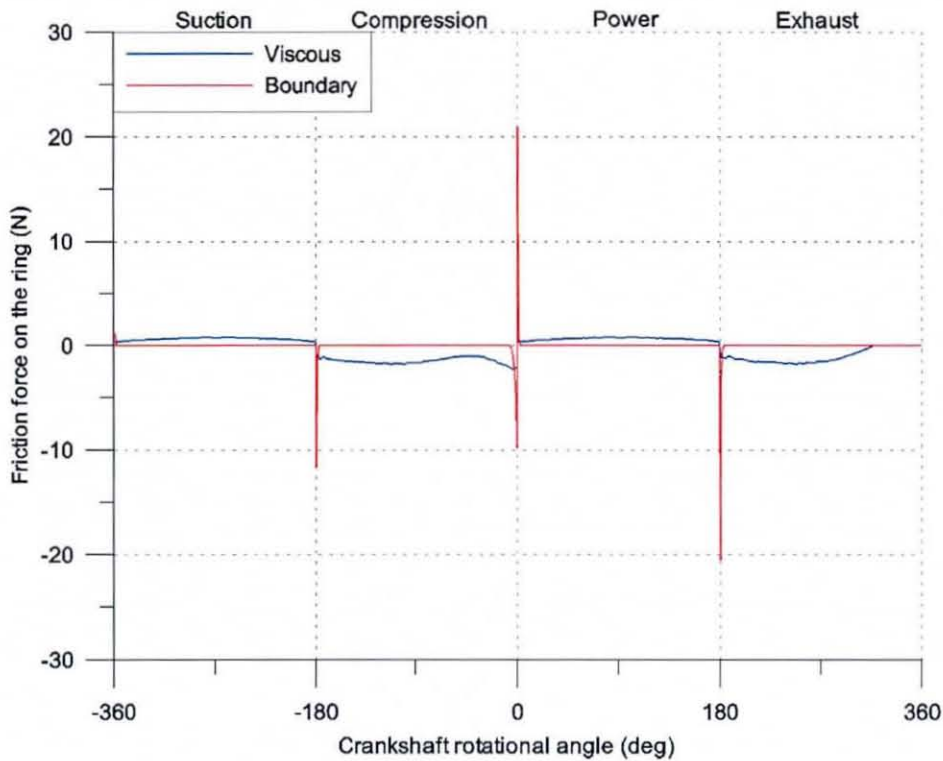


**Figure 7.24 Piston ring friction forces**

The reason for the generated friction force acting on the ring is two fold. One is due to viscous friction and the other is due boundary friction as can be seen in Figure 7.24. The maximum friction force occurs just prior to the dead centres, where the sliding velocity is zero and thus, the viscous friction component disappears. Therefore, the boundary friction is dominant at these locations, and most of the parasitic losses are due to boundary friction. Elsewhere, with the increase of sliding velocity, particularly at the mid span, the friction is increased but, by ever so small an amount, owing to the increasing viscous shearing effect. Therefore, dramatic friction force variations are due to boundary friction. Unlike friction at piston skirt-cylinder wall contact, where the minimum film thickness is quite large, here the boundary friction plays a significant contributory role to the total frictional effects with the minimum film thickness being fractions of a micrometer, predicted as low as  $0.01\mu\text{m}$ .

At the end of the exhaust stroke the combustion chamber pressure reduces and further goes into a suction pressure (see Figure 5.7). At this point the ring resides on the lower side of the piston groove as the piston is still moving in an upward direction, and hence a negative pressure force is applied on the inner ring surface. Thus, the negative pressure force (towards the centre of the ring) is counter-balanced by the ring tension force (acting radially outwards)

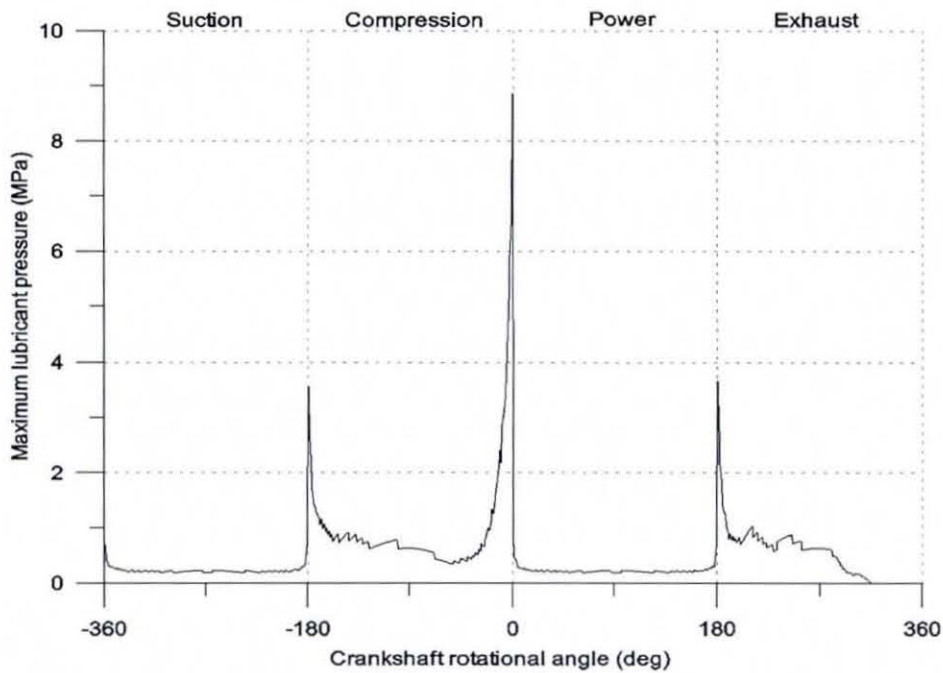


**Figure 7.25 Maximum lubricant pressure at piston ring to cylinder wall contact during a combustion cycle**

and ultimately the force between ring face and cylinder wall diminishes. There is film without a load (see Figure 7.23). Furthermore an almost zero friction force (see Figure 7.23) and a zero ring load (see Figure 7.22) are observed at the same point.

Energy lost is due to friction. The contacts dissipate mechanical energy in the form of heat and increase the contact temperature. As a part of its function the lubricant acts also as a cooling agent and takes the generated heat away from the contact. Owing to this heat generation the temperature of the lubricant increases and alters its rheological properties, particularly resulting in lowering of its viscosity (a phenomenon known as shear thinning). Unlike other contacts such as the piston skirt-to-cylinder wall and the main crankshaft support bearings, the piston ring-to-cylinder wall contact is subjected to fairly high pressures (see Figure 7.25) and a high load (see Figure 7.22). Figure 7.25 shows the maximum lubricant pressure at the piston ring-to-cylinder wall contact. The pressures are calculated based on Reynolds pressure distribution at the contact. When it comes to the dead centres the asperity contact area and the load can be calculated from equations (4.43) and (4.44), respectively. Such that with known sliding velocity, the pressure distribution at the asperity contact can be calculated.

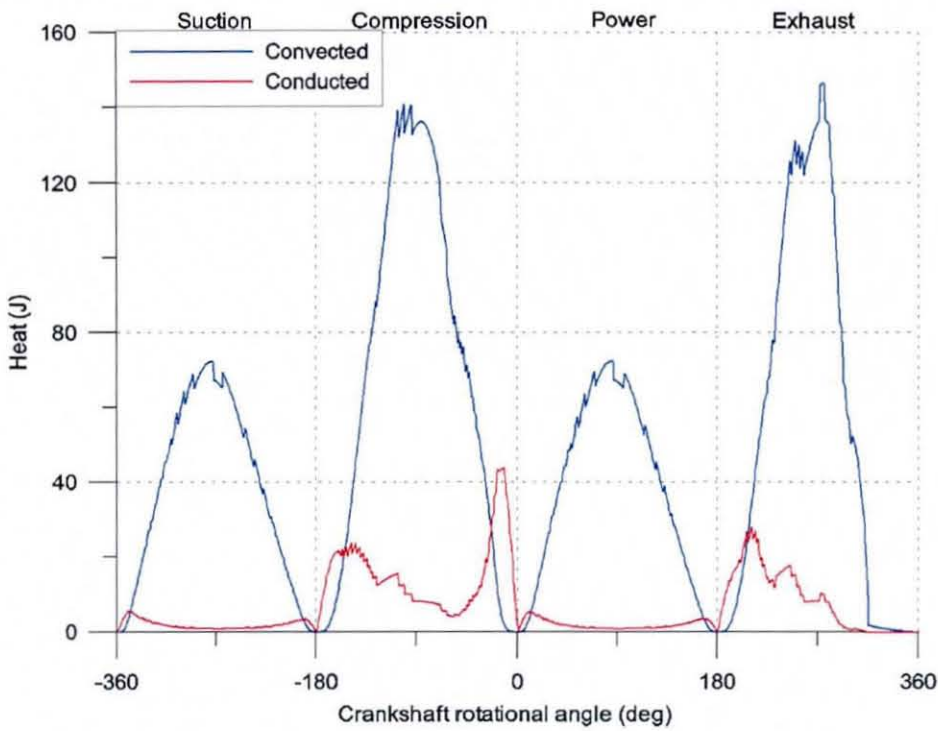


**Figure 7.26 Heat dissipation in the piston ring - cylinder wall contact**

Figure 7.25 shows the variation of maximum lubricant pressure in piston ring-to-cylinder wall contact during a 4 stroke combustion cycle. As the film thickness is lower at the dead centres higher lubricant pressures can be seen, particularly due to the influence of asperity contacts as shown by the proportion of load carried by asperity tip contacts in Figure 7.22. However, in the vicinity of the dead centres a very low sliding velocity exists, creating low entraining action. This reduces the extent of the lubricant film (as well as its thickness), thus reducing the area of the contact patch. Higher generated lubricant pressures provide the necessary reaction force. As discussed in section 4.5, the heat generated due to compressive heating and viscous heating are dissipated to the environment through convection or conduction. At very high pressures such as under EHL conditions the heating is dominated by compression of the fluid in the contact. As the maximum lubricant pressures are as low as  $9\text{MPa}$  within this contact, the effect of compression heating is ignored in the current analysis, as also mentioned in section 4.5. However, heat generation due to viscous action is dominant at low pressures and higher sliding velocities, thus it is considered as the main source of heating in this analysis.

Figure 7.26, shows the heat dissipation from various cooling terms. Wherever the film thickness is larger, convection cooling is significant as the film carries more of the heat away

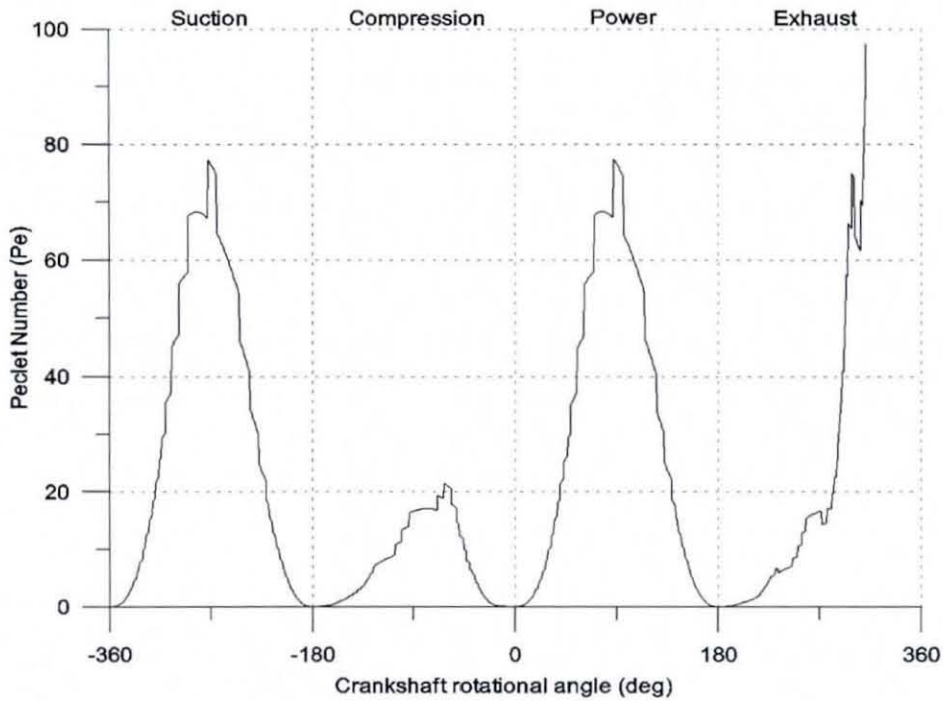


**Figure 7.27** Variation of Peclet number in the piston ring-cylinder wall contact during a combustion cycle

from the contact. Therefore, a higher contribution from the convection cooling can be seen at the mid span of each stroke, where the film thickness is relatively larger. At the dead centres, even though the regime of lubrication is not EHL, and in fact is mixed, with dominance of boundary lubrication, the film is not thick enough to carry the heat away from the contact. This is further exacerbated with smaller entraining velocities. Therefore, at the dead centres the effect of convection cooling is very low. At the vicinity of the dead centres the film thickness becomes smaller (see Figure 7.23) and the pressure is higher (see Figure 7.25). Due to these facts conduction cooling becomes more significant, particularly at the vicinity of the dead centres. The Peclet number, which is the ratio between convected heat over the conducted heat (given by equation (4.64)) also shows the same variation, see Figure 7.27. At the dead centres a low Peclet number is obtained, because of the prevalent mixed regime of lubrication, and with relatively thin films. Conduction is the dominated heat removal mechanism in these locations.

Most of the heat generated at the contact would be carried away by the solid bodies at the contact (particularly the conducted heat), which can cause thermal distortions at the solid. Although the affects of thermal distortion at the contact is not modelled in this thesis, it can be predicted by introducing thermal analysis of the solid, as the source of heat is already

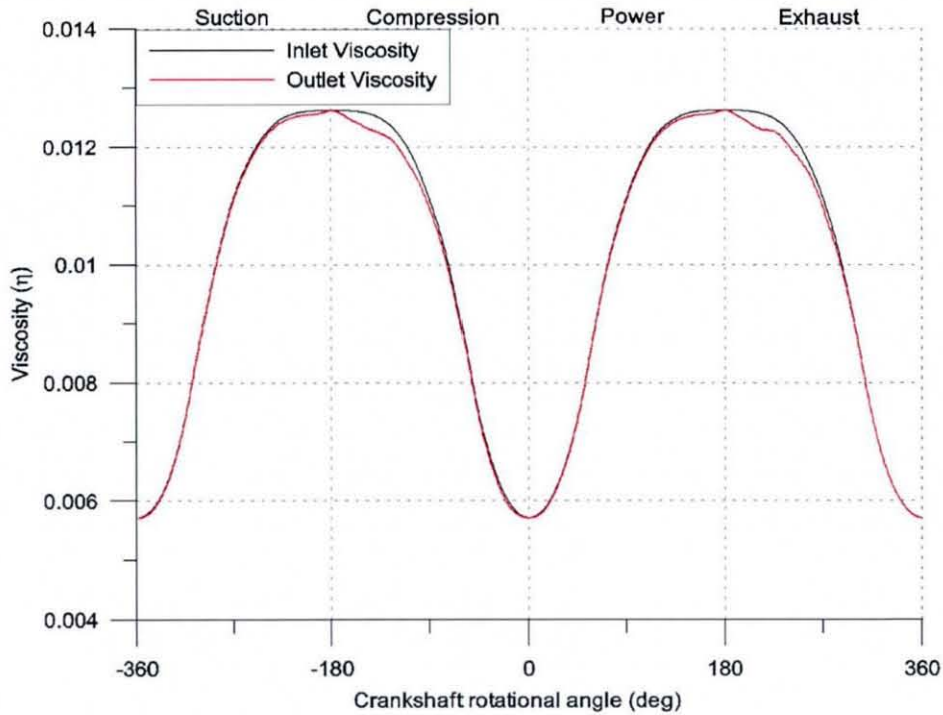


**Figure 7.28 Variation of viscosity in the piston ring-to-cylinder wall contact during the engine cycle**

analysed in the model. The lubricant temperature inside a contact does not increase linearly as it is assumed in this analysis. Inside the contact the lubricant temperature is quite high owing to transient conditions and the contact must be solved thermo-elastically in order to predict these values accurately. However in the current analysis, the contact is solved isothermally which does not take transition conditions in to account such that, the predicted inlet and outlet temperatures are very low. Remarkably higher temperature values would have been obtained, if the contact was solved in thermo-elastic conditions, which would definitely be responsible for higher thermal distortions.

Heat removal rate is directly proportional to the temperature difference in an interface. Higher heat generation in the contacts results from higher lubricant temperature difference between the film's inlet and outlet regions. The temperature rise in the piston ring-to-cylinder wall contact for different ring widths are shown in Figure 7.30. Note that in the actual engine the ring thickness is  $3\text{mm}$ . A higher temperature difference between the inlet and the outlet of the contact is prominent during mid span of the compression and exhaust stroke. As can be seen from Figure 7.26 the same positions are responsible for the higher heat dissipation. The amount of heat generation at the contact is progressively proportional to the contact lubricant pressure. Such that at about  $-80^\circ$  crank angle there is a sudden drop in temperature rise as

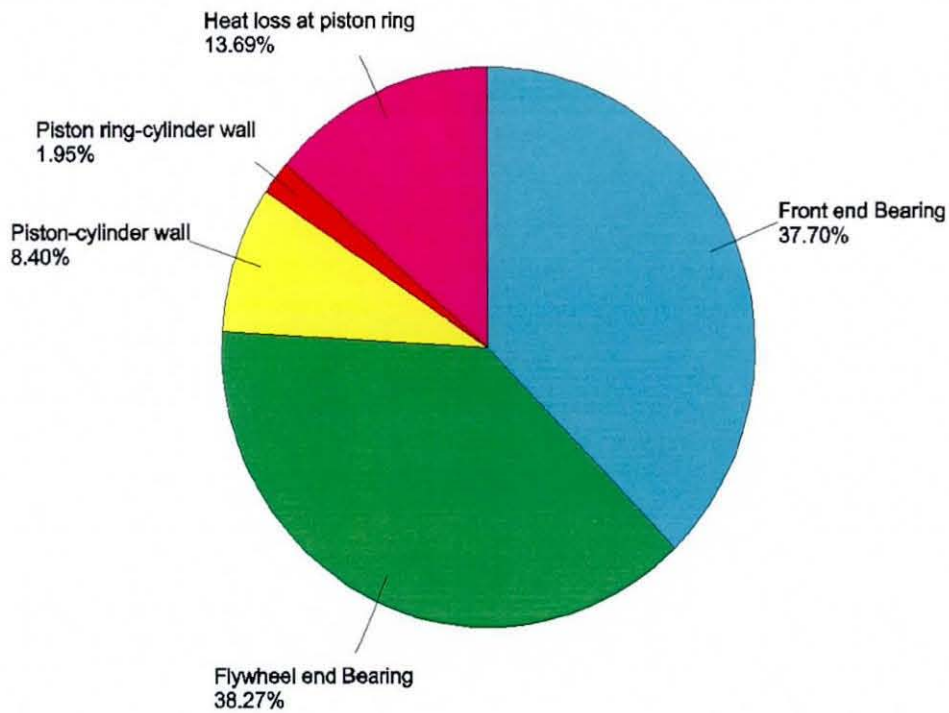


**Figure 7.29 Percentage energy loss in the E6 engine model**

can be seen in Figure 7.30, owing to a reduction in the ring face reaction force at the same point as that in Figure 7.22.

Rheological properties of the lubricant such as viscosity and density change with temperature, particularly the viscosity, which is taken into account in the current analysis. Changes of viscosity significantly affect the lubricant reaction. There are two main parameters that affect the contact temperature. Firstly, the temperature along the surface of the cylinder wall is not uniform throughout its length. As shown in Figure 5.19, the temperature varies along the cylinder wall, with a higher temperature towards the TDC due to higher combustion temperatures. Secondly, the temperature in the contact increases due to the viscous heat generation as already described, which is rather small, when compared with the change in the cylinder wall temperature (see Figure 7.30). However, both of these directly affect the lubricant viscosity in the contact. Figure 7.28 shows the variation of viscosity at the inlet and at the outlet of the contact during a combustion cycle. The change in viscosity at the inlet is due to cylinder wall temperature. The difference between the inlet and the outlet is due to viscous heat generation in the contact. As it can be seen a dramatic change in viscosity occurs due to temperature variation. However, a noticeable change in viscosity between the inlet and

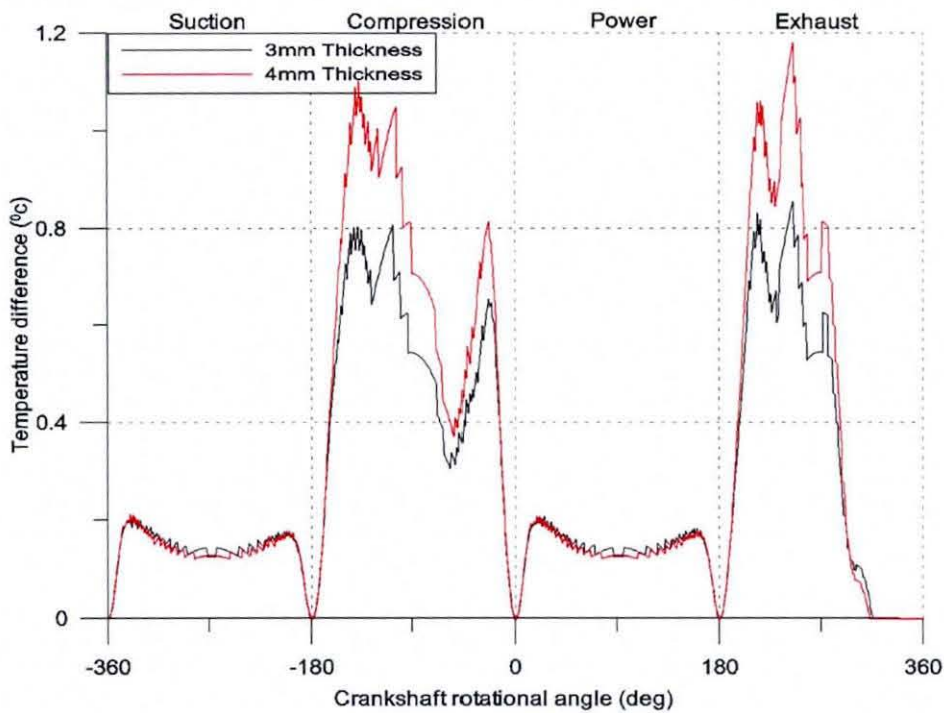


**Figure 7.30 Temperature rise at piston ring to cylinder wall contact for different ring thickness**

the outlet can be seen particularly at compression and exhaust cycles. This is mainly due to a higher contact load, causing a higher temperature difference at these locations.

Change in viscosity, kinematics and degree of conformity of the contact affect the frictional characteristics in different ways. As various contact conjunctions of the engine are modelled by introducing their characteristics, it is possible to estimate the losses in the engine that would affect the engine power output. With known frictional forces and sliding velocities energy losses at sliding contacts can be calculated. Figure 7.29 shows the percentage losses in this E6 engine's crankshaft-connecting rod-piston sub-system in terms of energy. However, it must be noted that there are many other components contributing to the engine losses, which are not considered in this model such as, cam-tappet conjunction, timing gears, oil and water pumps, etc. Even within the modelled sub-system the effect of frictional losses in big and small-end bearings are not included in the current model. Furthermore, the speed fluctuations that occur in the engine speed itself can result in mechanical losses due to imbalance and vibration.

It must be noted that unlike the E6 engine, used for the current study the operating conditions of modern engines are somewhat different. The operating speeds and combustion pressures of

modern engines are significantly higher compared to speeds and pressure considered in this study. On the other hand, in most modern engines the inner ring face is exposed into the combustion chamber through drilled holes between the ring groove and the piston top surface. This would allow high pressure combustion gasses to penetrate into the piston ring groove and increase the ring groove pressure, which is acting on inner ring face. This would increase the ring face force particularly during the power stroke, where a better sealing becomes mandatory. This paves the way for reduced initial ring tension needed to ensure better sealing at lower inner ring pressures and hence the size of the ring can be reduced. Owing to low stiffness and softer ring constructions the natural frequencies of the piston ring are reduced and enhance the chance of their coinciding with engine order multiples, particular in high performance high speed engines. In such cases the dynamic analysis of the piston ring is crucial in order to obtain a better representation of the piston ring physical behaviour.

Owing to the rather rigid (stiffer) construction of the E6 engine piston ring, when compared to the more modern engines, higher fundamental natural frequencies can be observed, which are far higher than the major engine order excitations. Also, the flexibility of the piston ring is not included in the current numerical model. In this series of quasi-static analyses, the effect of squeeze film action cannot be considered. However, for a full transient analysis, this effect must be considered, which would have to also include the modal excitation of the ring. Moreover, many papers in the literature report that in modern engines the contact between the piston ring and the cylinder wall undergoes EHL conditions, owing to its flexibility and higher contact forces acting on the small contact area.

Due to dynamic nature of the forces on the piston ring, the ring modes are easily get excited and in-plane and out-plane ring deformation takes place. This would result a higher radial clearance between the ring face and cylinder liner at some points on the ring circumference allowing high pressure gasses to pass through. When the out-plane modes are excited the clearance between the ring and the piston-ring-groove at ring top and bottom surface is affected at some points. These clearances create paths all around the piston ring allowing high pressure combustion chamber gasses to pass through to the low pressure crankcase which is known as blow-by. The effect of blow-by is further enhanced by ring wear and ring fluttering that causes ring to oscillate within the piston groove. In multi-ring pack systems, the inter-ring gas pressure is mostly dependent on the extent of blow-by. Most of these effects are not included in the current model as these are not applicable to the E6 experimental engine. In

---

modern engines with short stroke lengths and higher combustion gas force the change in viscosity due to heat generation at the contact would play a greater role than observed here.

Even though the temperature rise in the contact is quite low with the piston ring of 3mm thick, the situation can be greatly changed if some key parameters are changed, such as the ring face-width. As an example the temperature rise along with increased ring thickness (for 4mm thickness) is also shown in Figure 7.30. When the face-width is increased ring force due to gas pressure is also increased, affecting the contact temperatures. As most numerical models are based on isothermal assumption, they will not include such a variation. Therefore, isothermal analysis cannot be regarded as a valid assumption for piston ring lubrication.

The methodology developed in this study can easily be adopted for an engine with any configuration such as, a four cylinder, a six cylinder, with in-line and v-type configurations. Lubricant reaction forces, combustion forces and resisting torques can be applied, using the same approach.

### **7.3 Effect of offsetting the crankshaft**

So far, the numerical model developed for the E6 single cylinder engine is discussed in some detail, with particular reference to its tribo-dynamics. Once such a numerical model produces predictions consistent with the physical system, and thus validated, it can be used as a design tool to study various scenarios, as it is to a large extent parameterised. This is one of the main advantages of the multi-physics approach, potentially reducing the cost of physical prototyping and tests, particularly at the conceptual design stage. One particular current question of interest is offsetting of crankshafts in order to ensure adherence of the piston to the major thrust side, thus reducing the side to side motion of the piston, and the subsequent problems in loss of lubrication and also piston slapping and radiated noise. As a case study the following section is devoted to investigation of the effects of crankshaft offset, if it was to be implemented for the E6 internal combustion engine.

Crankshaft offset of an internal combustion engine is surmised to be quite effective, particularly against engine NVH, friction and slap noise (Cho *et al.*, 2003; Nakayama *et al.*, 2000). As it is mentioned earlier most modern engines are fitted with off-setted gudgeon pins in order to have a smooth force transfer at the TDC, mainly during the power stroke. The

---

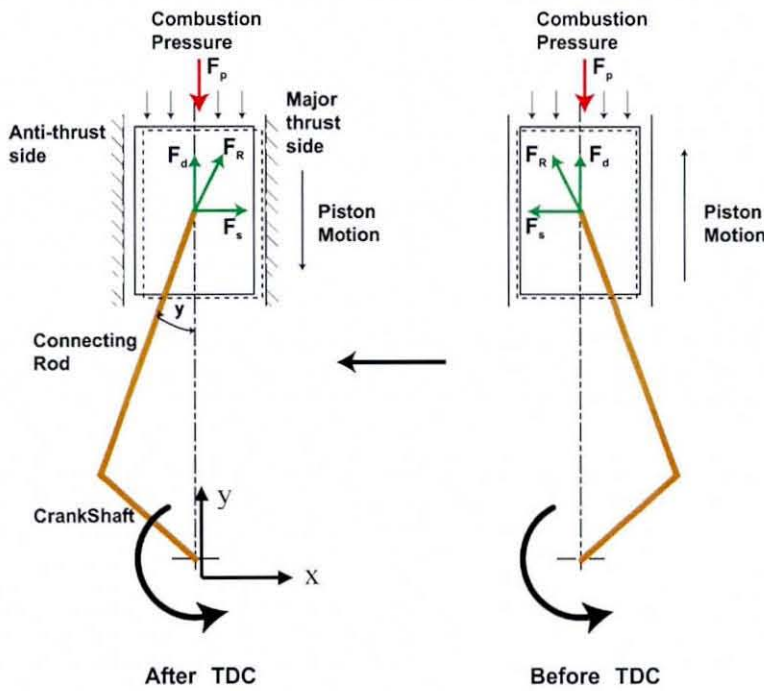


**Figure 7.31 Piston orientation and forces acting before and after TDC**

same kind of effect is expected to be achieved by offsetting the crankshaft from the piston axis. The side force acting on the piston exactly at the TDC is zero, if the crankshaft is in-line with the piston axis, as the connecting rod and the crank-throw reside on a vertical line. However, a few degrees before the TDC a net resultant force  $F_s$  acts towards the Anti-thrust side of the cylinder wall, while this reverses in direction a few degrees after the TDC, as shown in Figure 7.31. Such a sudden force variation results in the piston slap noise. The sudden rise in the side force can also lead to depletion of lubricant film, and thus undesirable conditions. Offsetting the crankshaft towards the major thrust side is expected to smoothen this force transformation.

It must be noted that change in the crankshaft position (offsetting), changes the orientation of the piston crankshaft assembly. As the multi-body numerical model developed in this study is parameterised, such a complicated change can easily be accomplished. Figure 7.32 shows the variation of major thrust side force with the crankshaft offset for a four stroke engine cycle. As can be seen an increase in the crankshaft offset progressively decreases the peak side force during suction, as well as in the power stroke, while it slightly increases the force, particularly in the exhaust cycle. Conversely, the force variation at the minor thrust side

shows a slight reduction in the peak force at the suction stroke, while an increase is noted during the compression and exhaust strokes.

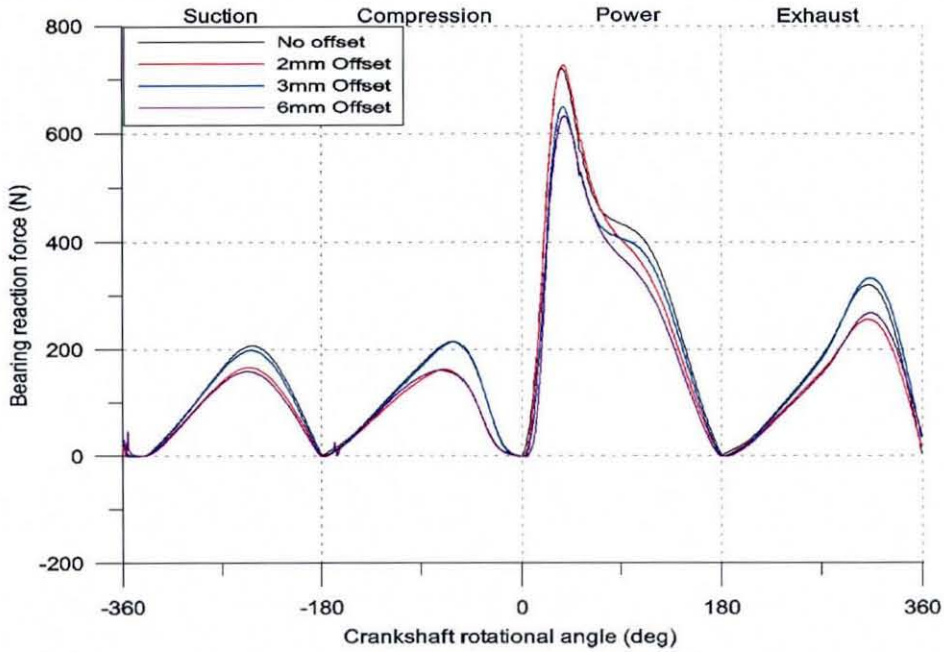


**Figure 7.32 Major thrust side force variation with crankshaft offset towards thrust side**

These two graphs only represent thrust forces acting at the top edges of the piston (piston position 1 and 2 in Figure 5.16). Almost similar variation can be seen at the lower edges as well. However, the maximum thrust force between the piston skirt and the cylinder wall exists on the major thrust side during the power stroke. With the crankshaft offset this peak thrust force is considerably reduced, while the thrust forces at some other points slightly varies as already discussed.

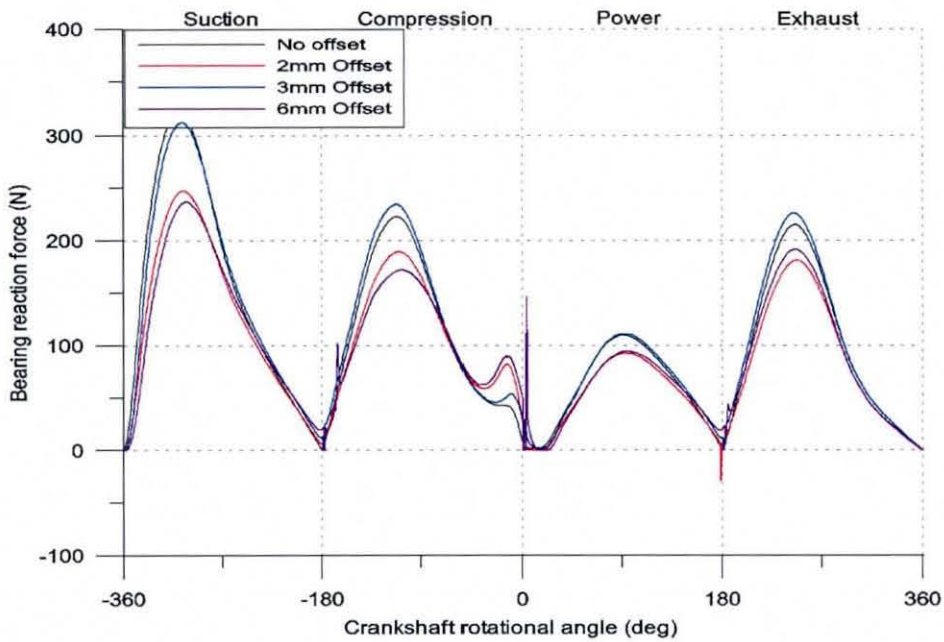


**Figure 7.33 Minor thrust side force variation with respect to the crankshaft offset towards the major thrust side**

The piston lateral motion becomes maximum in the negative  $x$ -direction during the suction stroke (at crank angle of  $-320^{\circ}$ ) and in the positive  $x$ -direction at the power stroke (at crank angle of  $40^{\circ}$ ) for a  $3\text{mm}$  offset towards major thrust side. The piston is translated within these two limits during the four stroke engine cycle as shown in Figure 7.34. Along with the crankshaft offset these maximum limits have been reduced as can be seen in the figure. On the other hand, the displacements at other places such as at compression and exhaust strokes have been increased. The crankshaft offset can be regarded as a process that smoothen the dynamic behaviour of the piston. However, excessive increase in crankshaft offset would not be supported by the numerical model and results shows a maximum of about  $4\text{mm}$  is possible with the current model. Excessive offset creates massive forces on the thrust side thus EHL would need to support such a load which is not modelled.

Crankshaft offset is also regarded as a process to change friction forces, acting on the piston skirt-to-cylinder wall. However, it is also reported that these variations are mostly dependent on the engine operating speed (Cho *et al*, 2003). Additionally, the change in viscosity of the lubricant changes the frictional force characteristics of the engine. However, the behaviour of an internal combustion engine can be changed due to various reasons.

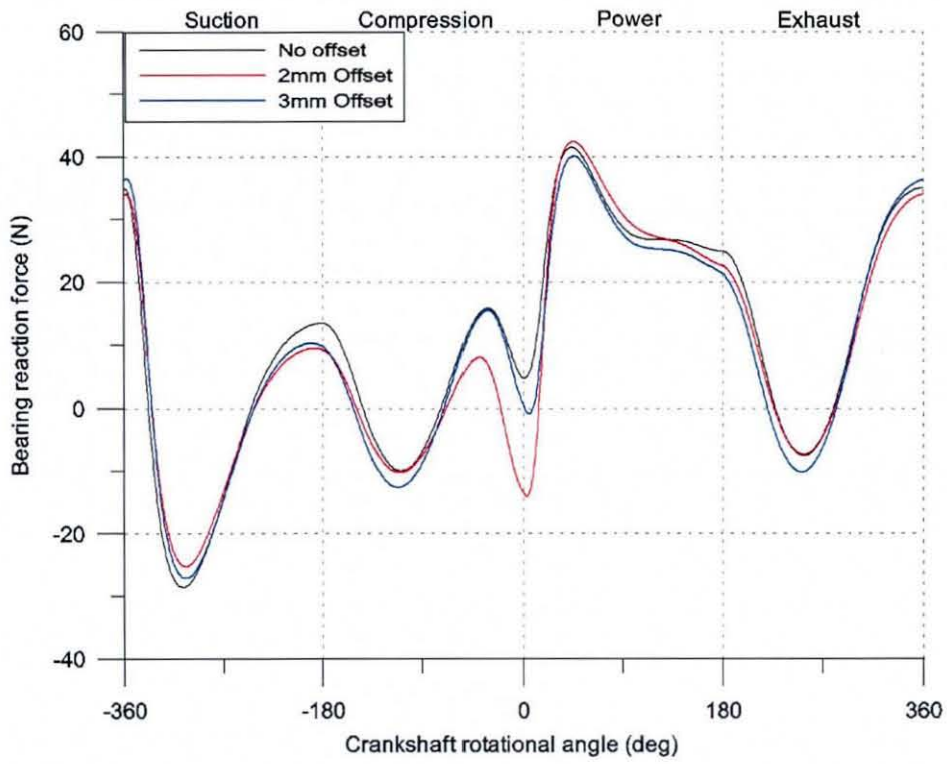


Figure 7.34 Variation of piston translation with respect to crankshaft offset

## 8 CONCLUSIONS AND SUGGESTIONS FOR FUTURE WORK

### 8.1 Overall Conclusions

The investigations in this thesis highlight the complexity of the piston, connecting rod, crankshaft and flywheel multi-body dynamics. The problem is multi-disciplinary in nature drawing the attention towards a multi-physics approach. It involves rigid inertial body motions, component flexibility, tribological contacts and their thermal considerations. Although the motion of the engine is largely prescribed, based on kinematics, induced by combustion gas force, it is greatly affected by inertial dynamics, elastic distortion of the flexible components and the complex nature of the power torque, comprising many harmonics. Furthermore, the piston is subjected to small amplitude lateral and tilting motions, which are induced by interactions between the piston and the cylinder bore, referred to as piston secondary motion. Kinetics in the contact of the mating surfaces is affected by these interactions, other than primary engine kinematics. Clearance between the piston ring and the groove allows it to move relatively freely within its confinement. Higher lubricant pressures are generated within the piston ring cylinder wall contact, which are highly transient in nature. Generated pressures and viscous friction cause a temperature rise within the contact that affects the rheological parameters of the lubricant. Therefore, the analysis includes physical disciplines, such as tribology, heat transfer, flexibility, constrained multi-body dynamics and small amplitude vibrations.

The regime of lubrication in crankshaft main bearings is considered to be hydrodynamic, even though the more modern main bearing lubrication problems with thin shells are solved based on EHL conditions. The results obtained for these bearings illustrate that the assumption is valid, with relatively large minimum film thickness existing in the case considered, giving an eccentricity ratio in the range: 0.09-0.6. The complexity of the problem is in combined solution of all the involved phenomena, all of which are non-linear in nature. The solution is obtained quasi-statically such that the contribution of both lubricant

---

entrainment and squeeze film effects can be seen. Particularly, at power stroke, the squeeze film action is significant in these bearings.

All the results obtained for piston - cylinder wall interactions point to the dominance of the hydrodynamic regime of lubrication, with relatively large minimum oil film thickness in the range:  $8-10\mu\text{m}$ , and with relatively low generated pressures in the range of few *MPa*, even at the thrust side under critical operating conditions. With the aforementioned pressure distribution and the contact conformity, iso-viscous regime of fluid film lubrication prevails. This is certainly the case in more unloaded parts of the piston cycle. When the speed of entraining motion is significant such as in the mid-stroke of piston motion a lubricant film can be retained and the coefficient of friction is quite low. At the TDC and the BDC, with diminished entraining motion, the lubricant film thickness is sufficient in the case of the E6 engine to ensure fluid film lubrication. The approaching velocities of the contiguous bodies are large enough to create necessary pressures or gaps through separation of solids, in order to keep the two bodies apart. The results of this thesis, with particular regard to film thickness have indicated that during the whole piston cycle the hydrodynamic conditions prevail in the piston to cylinder wall contact, for the particular engine under investigation, although boundary contributions have been noted at the dead centres on the case of piston ring to cylinder wall contact.

The dynamic behaviour of the engine is greatly influenced by the inclusion of flexibility of engine components. The difference in amplitude contributions at higher frequencies in the spectrum (at higher engine orders, particular half-engine order multiples) between rigid and flexible engine models provide the justification for their inclusion in the model. These frequencies are found to be well below the modal response of flexible parts for the investigated engine. This may not be the case for more modern engines using lighter constructions. Adverse effects would have been observed if the lower natural frequencies of flexible components would be closer to engine excitation frequencies, which can be the case in some modern engines.

The thesis has achieved its primary aims and objectives with good correlation between its analytical predictions and experimental measurements, for the case of engine dynamics. Clearly, it is important to include details of the system up to a certain level that can represent prevailing conditions quite accurately. However, this can lead to a very complex, as well as

---

computationally inefficient numerical model that would tend to become impractical with regard to analysis times from an industrial perspective. Thus, the inclusion of component flexibility was confined only to the connecting rod, crankshaft and the flywheel. This can be regarded as a simplifying assumption.

## **8.2 Contributions to Knowledge**

The development of multi-physics multi-scale model of a single cylinder, 4-stroke internal combustion engine model, which is verified to a certain extent against experimental findings constitutes the main contribution of this thesis. Development of such an integrative model, which is able to predict structural integrity issues, tribological aspects and vibration concerns in a simultaneous manner would yield to a better platform for design engineers. The traditional approach of detailing one tribological conjunction at a time may not represent better overall reliable results due to lack of proper inclusion of excitation and interplay between various conjunctions, through inertial dynamics. Particularly, piston skirt-to-cylinder wall interaction cannot be considered in isolation from piston primary, as well as secondary motions. Such a conjunction may easily be affected by not only large rigid body kinematics, but also from structural deformation, as well as tribological behaviour of crankshaft main bearings. Therefore, development of such an integrated model can provide the necessary information within a reasonable time limit.

## **8.3 Critical Assessment of the approach**

Construction of an accurate numerical model depends on many aspects, since the model is aimed towards examining system dynamic behaviour. Deformation of elastic members under dynamic loads depends on mode shapes for various modal frequencies. Even though the accuracy of these modal deformations is paramount, its accuracy is progressively increased with an increasing number of elements. However, an increasing computing power is needed to solve such a model and thus, the number of elements used were based on experimentation, which indeed neglects the higher frequency modes. The influence of higher frequency modes during a low frequency excitation should not be under-estimated.

1-D analysis for the crankshaft bearing lubrication resolves the bearing reaction force into a single component force acting at the journal bearing position. Even though the bearing width

---

is considered for this analysis, the lubricant pressure reaction force variation along the bearing axis within the confinement of the bearing width is not considered. This force variation may lead to an in-plane and out-of-plane bending moments. Only a 2-D analysis of the journal bearing can possibly be taken into consideration for these bending moments. Even in such an analysis the accuracy is increased along with increased number of grid points, which would dramatically add to the computation times. Extensive use of 1-D solution for journal bearings in literature, in engine applications shows the general acceptance of the method, even though, bending moments are not taken into consideration.

The piston-to-cylinder wall interaction is approximated to a line contact, even though a conformal contact is prevalent at this conjunction. With the available kinematics and geometry the film thickness varies along the circumferential direction, whereas the current model considers this to be uniform within quarter of the circumference at the major and the minor thrust sides. However, in reality the film thickness varies along the circumferential direction.

In piston ring-cylinder wall interaction it is assumed that the film thickness is uniform throughout the circumferential direction, which is not the actual case. The ring stiffness varies along the circumference presenting less stiffness at ring edges. Such that the in-plane as well as out-plane ring modes will be excited causing different film thickness along the ring circumference and in worst cases collapse of film and blow-by to occur.

## **8.4 Suggestions for Future Work**

As already highlighted above, some of the salient features of piston-connecting rod-crankshaft-flywheel sub-system need further developments. Inclusion of 2-D solution for piston skirt and the crankshaft bearings, but with fast convergence would be required. Other improvements of note that may be undertaken can include:

- The big-end and small-end bearings are not included in the current model. There are only described by holonomic joints. The big-end bearing is subjected to global motion other than the sliding motion inside the contact. Even the small-end bearing undergoes global motion and it is subjected to heavy loads, while experiencing relatively small entraining speed with high frequency reversals in the entraining
-

direction. This makes the contact more complicated. Inclusion of such behaviours can be quite important.

- Piston ring flexibility in terms of its global modal behaviour has not been included in the current numerical model. Quite complicated mode shapes can be seen in piston rings particularly due to geometry and material properties. However inclusion of at least in-plane mode shapes that would directly influence the lubrication problem would be quite important.
- Even though thermal effects in some of the contact conjunctions have been considered, as well as its thermal effects on shear thinning of the lubricant, the global thermal distortions of solids were ignored. Such an addition would be the most important addition, particularly in cylinder liner behaviour.
- The flexibility of the engine block can easily be introduced in to the model using the finite element methods and its noise emission to the environment can be subsequently calculated by employing the Boundary Element Method from the engine block to the external environment.

## 9 REFERENCES

- ADAMS/Solver. "User's Reference Manual,." MDI Inc.
- Anderson, B. S. "Company's Perspective in Vehical Tribology." *Leeds-Lyon Symposium on tribology*, 503-506.
- Aoyama, T., Kawamoto, A., Noda, T., Ozasa, T., Kato, T., Murai, Y., and Ito, T. (2003). "Analysis of Noise Occurrence by Cavitation in the Main Bearing of Diesel Engine." *JSAE Review*, 24(1), 59-64.
- Athavale, M. S., and P.R., S. (1999). "Analytical Studies on Influence of Crankshaft Vibrations on Engine Noise Using Integrated Parametric Finite Element Model; Quick Assessment Tool." *SAE Technical Paper Series*, 108(3), 1861-1866.
- Balakrishnan, S. (2002). "Transient Elastohydrodynamic Analysis of Piston Skirt Lubricated Contact under Combined Axial, Lateral and Tilting Motion." PhD Thesis, Loughborough University, Loughborough, UK.
- Balakrishnan, S., and Rahnejat, H. (2005). "Isothermal Transient Analysis of Piston Skirt-to-Cylinder Wall Contacts under Combined Axial, Lateral and Tilting Motion." *Journal of Physics D: Applied Physics*, 38(5), 787-799.
- Bell, J. R., and Rothberg, S. J. (2000a). "Laser Vibrometers and Contacting Transducers, Target Rotation and Six Degree-of-Freedom Vibration: What Do We Really Measure?" *Journal of Sound and Vibration*, 237(2), 245-261.
- Bell, J. R., and Rothberg, S. J. (2000b). "Rotational Vibration Measurements Using Laser Doppler Vibrometry: Comprehensive Theory and Practical Application." *Journal of Sound and Vibration*, 238(4), 673-690.
- Bishop, G. R., and Leavitt, A. H. (1975). "Performance Simulation of a Diesel Piston and Ring System." *SAE Preprints*(750768).
- Blundell, M. V. (1991). "Full Vehicle Modelling and Simulation Using the Adams Software System." *IMEchE Congress Seminar Papers, Seminar 16-Simulation Vehicle Dynamics*, paper C427/16/170.
- Boysal, A., and Rahnejat, H. (1997). "Torsional Vibration Analysis of a Multi-Body Single Cylinder Internal Combustion Engine Model." *Applied Mathematical Modelling*, 21(8), 481-493.
- Cameron, A. (1966). *The Principles of Lubrication / by A. Cameron.*, Longmans.
- Chevalier, F., Lubrecht, A. A., Cann, P. M. E., Colin, F., and Dalmaz, G. "Film Thickness in Starved Ehl Point Contacts." *Proceedings of the 1996 ASME/STLE Joint Tribology Conference, Oct 13-17 1996, San Francisco, CA, USA*, 8.
- Childs, D., Moes, H., and van Leuwen, H. (1977). "Journal Bearing Impedance Descriptions for Rotordynamic Applications." *Trans. ASME, Journal of Lubrication Technology*(2), 198-214.
- Cho, M.-R., Kim, J.-S., Oh, D.-Y., and Han, D.-C. (2003). "The Effects of Crankshaft Offset on the Engine Friction." *International Journal of Vehicle Design*, 31(2), 187-201.
- Cho, S. H., Ahn, S. T., and Kim, Y. H. (2002). "A Simple Model to Estimate the Impact Force Induced by Piston Slap." *Journal of Sound and Vibration*, 255(2), 229-242.
- Cho, S.-W., Choi, S.-M., and Bae, C.-S. (2000). "Frictional Modes of Barrel Shaped Piston Rings under Flooded Lubrication." *Tribology International*, 33(8), 545-551.
- Choi, J.-K., Lee, J.-H., and Han, D.-C. "Oil Film Thickness in Engine Main Bearings: Comparison between Calculation and Experiment by Total Capacitance Method."
-

- International Fuels and Lubricants Meeting and Exposition, Oct 19-22 1992, San Francisco, CA, USA, 147-160.*
- Cooley, J. W., and Tukey, J. W. (1965). "An Algorithm for the Mechines Calculation of Complex Fourier Series." *Mathematics of Computation*, 19(90), 297-311.
- Craig, R. R. (1981). *Structural Dynamics : An Introduction to Computer Methods*, Wiley, New York.
- Craig, R. R., and Brampton, M. C. C. (1968). "Coupling of Substructures for Dynamics Analysis." *AIAA (American Institute of Aeromautics and Astronautics) Journal*, 6, 1313-1319.
- Cummins, C. L. (2000). *Internal Fire*, Wilsonville, Or. : Carnot Press, 2000.
- D'Agostino, V., Valle, S. D., Ruggiero, A., and Senatore, A. "A Study on the Piston Top Ring Lubrication Using the Open-End Boundry Condition." *Aimeta International Tribology Conference*, Salerno, Italy.
- Dowson, D., Economou, P. N., Ruddy, B. L., Strachan, P. J., and Baker, A. J. S. "Piston Ring Lubrication - Part Ii, Theoretical Analysis of a Single Ring and a Complete Ring Pack." *Energy Conservation Through Fluid Film Lubrication Technology: Frontiers in Research and Design*, New York, 23-52.
- Dowson, D., and Higginson, G. R. (1977). *Elasto-Hydrodynamic Lubrication*, Pergamon Press Ltd., Oxford.
- Dowson, D., Ruddy, B. L., and Economou, P. N. (1983). "Elastohydrodynamic Lubrication of Piston Rings." *Proceedings of The Royal Society of London, Series A: Mathematical and Physical Sciences*, 386(1791), 409-430.
- Draminsky, P. (1965). "Extended Treatment of Secondary Resonance." *Shipbldg and Mar. Engng Int.*, 88, 180-186.
- Du, H. Y. I. (1999). "Simulation of Flexible Rotating Crankshaft with Flexible Engine Block and Hydrodynamic Bearings for a V6 Engine." *SAE Techincal Paper Series (1999-011752)*.
- DuBois, O. B., and Ocvirk, F. W. (1953). "Analytical Derivation and Experimental Evaluation of Short Bearing Approximation for Full Journal Bearings." *NASA Technical Report*.
- Dursunkaya, Z., and Keribar, R. "Simulation of Secondary Dynamics of Articulated and Conventional Piston Assemblies." *International Congress and Exposition, Feb 24-28 1992, Detroit, MI, USA, 21-31.*
- Dursunkaya, Z., Keribar, R., and Ganapathy, V. (1994). "Model of Piston Secondary Motion and Elastohydrodynamic Skirt Lubrication." *Trans. ASME, Journal of Tribology*, 116(4), 777-785.
- Dwyer-Joyce, D. S., Green, D. A., Balakrishnan, S., Harper, P., Lewis, R., Howell-Smith, King, P. D., and Rahnejat, H. (2005). "The Measurement of Liner - Piston Skirt Oil Film Thickness by an Ultrasonic Means." *SAE International (P5-06P-596)*.
- Elrod, H. G. (1980). "Cavitation Algorithm." *Trans. ASME - Journal of Lubrication Technology*(80-C2/Lub-54), 5.
- Eyring, H. (1936). "Viscosity, Plasticity, and Diffusion as Examples of Absolute Reaction Rates." *Journal of Chemical Physics*, 4(4), 283-291.
- Fantino, B., Godet, M., and Frene, J. "Dynamic Behaviour of an Elastic Connecting-Rod Bearing - Theoretical Study." *Studies of Engine Bearings and Lubrication, International Congress & Exposition.*, Detroit, MI, 23-32.
- Farahanchi, F., and Shaw, S. W. (1994). "Chaotic and Periodic Dynamics of a Slider-Crank Mechanism with Slider Clearance." *Journal of Sound and Vibration*, 177(3), 307-324.
-

- Garnier, T., Bonneau, D., and Grente, C. (1999). "Three-Dimensional Ehd Behavior of the Engine Block/Crankshaft Assembly for a Four Cylinder Inline Automotive Engine." *Trans. ASME, Journal of Tribology*, 121(4), 721-730.
- Gear, C. W. (1971). "Simultaneous Numerical Soution of Differential Algebraic Equations." *Circuits and Systems, IEEE Transactions on [legacy, pre - 1988]*, 18(1), 89-95.
- Givens, L. (1990). "Technical History of the Automobile." *Automotive Engineering (Warrendale, Pennsylvania)*, 98(6), 61-67.
- Gohar, R. (1988). *Elastohydrodynamics*, Ellis Horwood Ltd., Chichester.
- Goldsbrough, G. R., and Baker, H. (1926). "The Properties of Torsional Vibrations in Reciprocating Engine Shafts." *Proc. R. Soc.*, 113, 259-281.
- Goudas, I., and Natsiavas, S. (2004). "Non-Linear Dynamics of Engine Mechanisms with a Flexible Connecting Rod." *Proceedings of the Institution of Mechanical Engineers, Part K: Journal of Multi-body Dynamics*, 218(2), 67-80.
- Greenwood, J. A., and Tripp, J. H. (1970). "The Contact of Two Nominally Flat Rough Surfaces." *Proc. Instn. Mech. Engrs.*, 185, 625-633.
- Gupta, S. (2002). "Elasto-Multi-Body Dynamics of Internal Combustion Engines with Thin Shell Elastohydrodynamic Journal Bearings," PhD Thesis, Loughborough, Loughborough, UK.
- Haddad, S. D. (1995). "Theoretical Treatment of Piston Motion in I.C. Piston Engine for the Prediction of Piston Slap Excitation." *Mechanism & Machine Theory*, 30(2), 253-269.
- Haddad, S. D., and Howard, D. A. (1980). "Analysis of Piston Slap-Induced Noise and Assessment of Some Methods of Control in Diesel Engines." *SAE Preprints*, 800517-25.
- Haddad, S. D., and Tjan, K.-t. (1995). "Analytical Study of Offset Piston and Crankshaft Designs and the Effect of Oil Film on Piston Slap Excitation in a Diesel Engine." *Mechanism & Machine Theory*, 30(2), 271-284.
- Halliwell, N. A. (1996). "Laser Torsional Vibrometer: A Step Forward in Rotating Machinery Diagnostics." *Journal of Sound and Vibration*, 190(3), 399-418.
- Hamai, K., Masuda, T., and Goto, T. (1990). "Structural Analysis on Crankshaft Considering Oil Film Pressure Distribution around Sliding Bearings." *Tribology Transactions*, 33(2), 179-184.
- Hamrock, B. J., and Dowson, D. (1976). "Isothermal Elastohydrodynamic Lubrication of Point Contacts Em Dash 2. Ellipticity Parameter Results." *Trans. ASME, Journal of Lubrication Technology*, 98 Ser F(3), 375-383.
- Hamrock, B. J., and Dowson, D. (1977a). "Isothermal Elastohydrodynamic Lubrication of Point Contacts." *Trans. ASME, Journal of Lubrication Technology*, 99 Ser F(1), 15-23.
- Hamrock, B. J., and Dowson, D. (1977b). "Isothermal Elastohydrodynamic Lubrication of Point Contacts." *Trans. ASME, Journal of Lubrication Technology*, 99 Ser F(2), 264-276.
- Hamrock, B. J., and Jacobson, B. O. "Elastohydrodynamic Lubrication of Line Contacts." *ASLE Preprints presented at the ASLE/ASME Lubrication Conference.*, Hartford, CT, USA, 12.
- Hamrock, B. J., Schmid, S. R., and Jacobson, B. O. (2004). Fundamentals of Fluid Film Lubrication, Marcel Dekker, Inc., New York, USA.
- Han, D.-C., and Lee, J.-S. (1998). "Analysis of the Piston Ring Lubrication with a New Boundary Condition." *Tribology International*, 31(12), 753-760.
- Harry, W. (1994). Automotive Engines, Gregg Division, McGraw-Hill, New York ; London .:
-

- Hesterman, D. C., and Stone, B. J. (1992). "The Causes of Torsional Resonance in Reciprocating Engines and Pumps at Other Than Interger Multiples of the Fundamental Excitation Frequency." *IMEchE*.
- Hesterman, D. C., and Stone, B. J. (1995). "Secondary Inertia Effects in the Torsional Vibration of Reciprocating Engines - a Literature Review." *Proceedings of the Institution of Mechanical Engineers, Part C: Journal of Mechanical Engineering Science*, 209(1), 11-15.
- Heywood, J. B. (1988). *Internal Combustion Engine Fundamentals*, McGraw-Hill, New York.
- Hoffman, M. W. D., and Dowling, R. D. (1999). "Modeling Fully-Coupled Rigid Engine Dynamics and Vibrations." *Society of Automotive Engineers*.
- Hu, K., Mourelatos, Z. P., and Vlahopoulos, N. (2003). "Computational Analysis for Dynamic Response of a Rotating Shaft on Flexible Support Structure with Clearances." *Journal of Sound and Vibration*, 267(1), 1-28.
- Ichikawa, S., Mihara, Y., and Someya, T. (1995). "Study on Main Bearing Load and Deformation of Multi-Cylinder Internal Combustion Engine: Relative Inclination between Main Shaft and Bearing." *JSAE Review*, 16(4), 383-386.
- Inman, D. J. (2001). *Engineering Vibration*, Prentice-Hall, Inc., London.
- K.L.Johnson. (1985). *Contact Mechanics*, Cambridge University Press, Cambridge.
- Katano, H., Iwamoto, A., and Saitoh, T. (1991a). "Dynamic Behaviour Analysis of Internal Combustion Engine Crankshafts under Operating Conditions." *International Conference on Computers in Engine Technology, Sep 10-12 1991, Procs. Inst. Mech. Engrs., Part C: Journal of Mechanical Engineering Science*, 205 BN - 0-85298-765-x.
- Katano, H., Iwamoto, A., and Saitoh, T. (1991b). "Dynamic Behaviour Analysis of Internal Combustion Engine Crankshafts under Operating Conditions." *International Conference on Computers in Engine Technology, Sep 10-12 1991, Proceedings of the Institution of Mechanical Engineers*, 205 BN - 0-85298-765-x.
- Kelly, P. (1999). *Multi-Body Dynamic Analysis of Engine Induced Automotive Clutch Pedal Vibration*, "PhD Thesis, University of Bradford.
- Keribar, R., and Dursunkaya, Z. "Modeling of Piston Secondary Dynamics and Tribology." *Proceedings of the Annual Automotive Technology Development Contractors' Coordination Meeting, Oct 28-31 1991, Dearborn, MI, USA*, 657-677.
- Kimura, J., Shiono, K., Okamura, H., and Sogabe, K. (1997). "Experiments and Analysis of Crankshaft Three Dimensional Vibrations and Bending Stresses in a V-Type Ten-Cylinder Engine: Influence of Crankshaft Gyroscopic Motions." *Society of Automotive Engineers*.
- Kineshita, M., Sakamoto, T., and Okamura, H. (1989). "An Experimental Study of a Torsional-Bending Damper Pulley for an Engine Crankshaft." *SAE (Society of Automotive Engineers) Transactions* (891127), 23-33.
- Kirk, R. G., and Gunter, E. J. (1975). "Short Bearing Analysis Applied to Rotor Dynamics." *Journal of Lubrication Technology, Transactions ASME*, 98 Ser F(1), 47-56.
- Kjaer, B. (1982). "Measuring Vibrations." *Bruel & Kjaer Co.*
- Knoll, G., Schoenen, R., and Wilhelm, K. "Full Dynamic Analysis of Crankshaft and Engine Block with Special Respect to Elastohydrodynamic Bearing Coupling." *Proceedings of the 1997 Spring Technical Conference of the ASME Internal Combustion Engine Division, Apr 27-30 1997, Fort Collins, CO, USA*, 1-8.
-

- Knoll, G. D., and Peeken, H. J. (1982). "Hydrodynamic Lubrication of Piston Skirts." *Trans ASME, Journal of Lubrication Technology*, 104(4), 504-509.
- Koizumi, T., Tsujiuchi, N., Okamura, M., Kubomoto, I., and Ishida, E. (2000). "Reduction of Piston Slap Excitation with Small Gasoline Engine." *Proceedings of the International Modal Analysis Conference - IMAC, 2*, 1731-1736.
- Kryniski, K. (1991). "Jumping Phenomenon in Journal Bearings." *Transactions of ASME, Journal of Rotating Machinery and Vehicle Dynamics.*, DE-Vol 35, 169-173.
- Kurbet, S. N., and Kumar, R. K. (2004). "A Finite Element Study of Piston Tilt Effects on Piston Ring Dynamics in Internal Combustion Engines." *Proceedings of the Institution of Mechanical Engineers, Part K: Journal of Multi-body Dynamics*, 218(2), 107-117.
- Kushwaha, M. (2000). "Elasto-Multi-Body Dynamics of Valve Train Systems with Transient Elastohydrodynamic Contact Conditions." PhD Thesis, University of Bradford, Bradford.
- Lagrange. (1788). "Mecanique Analytique." *L' Academie de Sciences, Paris*.
- Liu, K., Xie, Y. B., and Gui, C. L. (1998). "Two-Dimensional Lubrication Study of the Piston Ring Pack." *Proceedings of the Institution of Mechanical Engineers, Part J: Journal of Engineering Tribology*, 212(3), 215-220.
- Ma, Z.-D., and Perkins, N. C. (2003). "An Efficient Multibody Dynamics Model for Internal Combustion Engine Systems." *Multibody System Dynamics*, 10(4), 363-391.
- Messe, S., and Lubrecht, A. A. (2000). "Transient Elastohydrodynamic Analysis of an Overhead Cam/Tappet Contact." *Proceedings of the Institution of Mechanical Engineers, Part J: Journal of Engineering Tribology*, 214(5), 415-425.
- Mihailidis, A., Retzepis, J., Salpistis, C., and Panajiotidis, K. (1999). "Calculation of Friction Coefficient and Temperature Field of Line Contacts Lubricated with a Non-Newtonian Fluid." *Proceedings of the NORDTRIP'98 Conference*, 232(2), 213-220.
- Mihara, Y., Hayashi, T., Nakamura, M., and Someya, T. (1995). "Development of Measuring Method for Oil Film Pressure of Engine Main Bearing by Thin Film Sensor." *JSAE Review*, 16(2), 125-130.
- Mihara, Y., Kajiwara, M., Fukamatsu, T., and Someya, T. (1996). "Study on the Measurement of Oil-Film Pressure of Engine Main Bearing by Thin-Film Sensor - the Influence of Bearing Deformation on Pressure Sensor Output under Engine Operation." *JSAE Review*, 17(3), 281-286.
- Mihara, Y., and Someya, T. (1995). "Study of Main Bearing Load and Deformation in a Multi-Cylinder Internal Combustion Engine." *JSAE Review*, 16(2), 188-189.
- Mihara, Y., and Someya, T. (2002). "Measurement of Oil-Film Pressure in Engine Bearings Using a Thin-Film Sensor." *Lubrication Engineering*, 58(5), 10-19.
- Mizuho Inagaki, A. K., Takayuki Aoyama, Ken-ichi Yamamoto. (2002). "Prediction of Structural and Kinematic Coupled Vibration on Internal Combustion Engine." R&D Review of Toyota CRDL.
- Moreau, H., Maspeyrot, P., Chomat-Delalex, A. M., Bonneau, D., and Frene, J. (2002). "Dynamic Behaviour of Elastic Engine Main Bearings: Theory and Measurements." *Proceedings of the Institution of Mechanical Engineers, Part J: Journal of Engineering Tribology*, 216(4), 179-193.
- Morita, T., and Okamura, H. "Dynamic Stiffness Matrix Approach to the Analysis of Three-Dimensional Vibrations of Automobile Engine Crankshafts. Part 2. Application to Firing Conditions." *Winter Annual Meeting of the American Society of Mechanical Engineers, Nov 25-30 1990, Dallas, TX, USA*, 59-66.
-

- Morita, T., Tsuna, Y., and Okada, A. (2001). "Influence of Dynamic Damper Pulley Design on Engine Front Noise." *SAE transactions (SAE transact.)*, 110(6) (ISSN 0096-736X), 1547-1552.
- Mourelatos, Z. P. (2000). "Efficient Crankshaft Dynamic Analysis Using Substructuring with Ritz Vectors." *Journal of Sound and Vibration*, 238(3), 495-527.
- Mourelatos, Z. P. (2001a). "A Crankshaft System Model for Structural Dynamic Analysis of Internal Combustion Engines." *Computers and Structures*, 79(20-21), 2009-2027.
- Mourelatos, Z. P. (2001b). "An Efficient Journal Bearing Lubrication Analysis for Engine Crankshafts." *Tribology Transactions*, 44(3), 351-358.
- MSC/Nastran. "Encyclopedia."
- Nagamatsu, A., and Nakao, A. (1983). "Analysis of Forced Vibration by Reduced Impedance Method (Part 3 Damped Vibration)." *Bulletin of the JSME*, 26(214), 592-597.
- Nakayama, K., Tamaki, S., Hiroyuki, M., and Takiguchi, M. (2000). "The Effect of Crankshaft Offset on Piston Friction Force in a Gasoline Engine." *SAE transactions (SAE transact.)*, 109(3), 885-892.
- Newkirk, B. L. (1924). "Shaft Whipping." *General Electric Review*, 27, 169.
- Newland, D. E. (1993). *Random Vibration and Spectral Analysis*, Longman, New York.
- Okamoto, M., and Sakai, I. (2001). "Contact Pressure Distribution of Piston Rings - Calculation Based on Piston Ring Contour." *Society of Automotive Engineers*.
- Okamura, H., and Morita, T. (1999). "Efficient Modelling and Analysis for Crankshaft Three-Dimensional Vibrations under Firing Conditions." *Proceeding of the Institution of Mechanical Engineers - K*, 213(1), 33-44.
- Okamura, H., Shinno, A., Yamanaka, T., Suzuki, A., and Sogabe, K. "Dynamic Stiffness Matrix Approach to the Analysis of Three-Dimensional Vibrations of Automobile Engine Crankshafts. Part 1. Background and Application to Free Vibrations." *Winter Annual Meeting of the American Society of Mechanical Engineers, Nov 25-30 1990, Dallas, TX, USA*, 47-58.
- Okamura, H., Shinno, A., Yamanaka, T., Suzuki, A., and Sogabe, K. (1995). "Simple Modeling and Analysis for Crankshaft Three-Dimensional Vibrations, Part 1: Background and Application to Free Vibrations." *Journal of Vibration and Acoustics, Transactions of the ASME*, 117(1), 70-79.
- Okamura, H., and Yamashita, K. "Influence of the Valve and Accessory Gear Train on the Crankshaft Three-Dimensional Vibrations in High Speed Engines." *SAE Conference Proceedings*.
- Orlandea, N., Chace, M. A., and Calahan, D. A. (1976). "Sparsity-Oriented Approach to the Dynamic Analysis and Design of Mechanical Systems Em Dash 1." *American Society of Mechanical Engineers (Paper)*(76-DET-19), 7.
- Otnes, R. K., and Encochson, L. (1972). *Digital Time Serier Analysis*, Wiley, New York.
- Paranjpe, R. S., and Goenka, P. K. (1990). "Analysis of Crankshaft Bearings Using a Mass Conserving Algorithm." *Tribology Transactions*, 33(3), 333-344.
- Petroff, N. P. (1883). "Friction in Machines and the Effect of the Lubricant." *Inzh. Zh. St. Petersburg*, 1, 71-140.
- Pinkus, O., and Sternlicht, B. (1961). *Theory of Hydrodynamic Lubrication*, McGraw-Hill.
- Piraner, I., Pflueger, C., and Bouthier, O. (2002). "Cummins Crankshaft and Bearing Analysis Process." *North American MDI User Conference*.
- Priest, M., Dowson, D., and Taylor, C. M. (2000). "Theoretical Modelling of Cavitation in Piston Ring Lubrication." *proceeding of the Institution of Mechanical Engineers - C*, 214, 435.
-

- Rahnejat, H. (1984). "Influence of Vibration on the Oil Film in Concentrated Contacts," PhD Thesis, University of London, London.
- Rahnejat, H. (1998). Multi-Body Dynamics: Vehicle, Machines, and Mechanisms, Society of Automotive Engineers, Inc., Warrendale, USA.
- Rahnejat, H. (2000). "Multi-Body Dynamics: Historical Evolution and Application." *Proceedings of the Institution of Mechanical Engineers, Part D: Journal of Automobile Engineering*, 214(1), 149.
- Rahnejat, H., and Gohar, R. Icp Press, in Review Process.
- Rao, S. S. (2002). Applied Numerical Methods for Engineers and Scientists, Prentice Hall, New Jersey.
- Reynolds, O. (1886). "On the Theory of Lubrication and Its Application to Mr. Beauchamp Tower's Experiments, Including an Experimental Determination of the Viscosity of Olive Oil." *Phil. Transaction of Royal Society, London*, 177, 157-234.
- S.H, C., S.T, A., and Y.H, K. (2002). "A Simple Model to Estimate the Impact Force Induced by Piston Slap." *Journal of Sound and Vibrations*, 255.
- Seki, T., Nakayama, K., Yamada, T., Yoshida, A., and Takiguchi, M. (2000). "Study on Variation in Oil Film Thickness of a Piston Ring Package: Variation of Oil Film Thickness in Piston Sliding Direction." *JSAE Review*, 21(3), 315-320.
- Shabana, A. A. (1998). Dynamics of Multibody System, University of Cambridge Press.
- Shell. "Shell Bearings Help Desk."
- Shiao, Y.-j., and Moskwa, J. J. "Investigation of Load Force and Dynamic Error Magnitude Using the Lumped Mass Connecting Rod Model." *International Congress and Exposition, Mar 1-5 1993, Detroit, MI, USA*, 1-10.
- Spessert, B., and Ponsa, R. (1990). "Investigation in the Noise from Main Running Gear, Timing Gears and Injection Pump of Di Diesel Engines." *SAE (Society of Automotive Engineers) Transactions*, 99(Sect 3), 14-33.
- Suh, K.-H., Lee, Y.-K., and Yoon, H.-S. (2000). "A Study on the Balancing of the Three-Cylinder Engine with Balance Shaft." *SAE Technical Paper Series*.
- Taraza, D. (2001). "Quantifying Relationship between the Crankshaft's Speed Variation and the Gas Pressure Torque." *SAE Technical paper series*.
- Taylor, R. I. (2002). "Lubrication, Tribology & Motorsport." *SAE Technical Paper Series*(2002-01-3355).
- Teodorescu, M., Taraza, D., Henein, N. A., and Bryzik, W. (2003). "Simplified Elasto Hydrodynamic Friction Model of the Cam-Tappet Contact." *SAE transactions (SAE transact.)*, 112(3), 1271-1282.
- Teraguchi, S., Suzuki, W., and Takiguchi, M. (2001). "Effects of Lubricating Oil Supply on Reductions of Piston Slap Vibration and Piston Friction." *Society of Automotive Engineers*(2001-01-0566).
- Tian, T. (2002a). "Dynamic Behaviours of Piston Rings and Their Practical Impact. Part 1: Ring Flutter and Ring Collapse and Their Effects on Gas Flow and Oil Transport." *Proceedings of the Institution of Mechanical Engineers, Part J: Journal of Engineering Tribology*, 216(4), 209-228.
- Tian, T. (2002b). "Dynamic Behaviours of Piston Rings and Their Practical Impact. Part 2: Oil Transport, Friction and Wear of Ring/Liner Interface and the Effects of Piston and Ring Dynamics." *Proceedings of the Institution of Mechanical Engineers, Part J: Journal of Engineering Tribology*, 216(4), 229-247.
- Tian, T., Noordzij, L. B., Wong, V. W., and Heywood, J. B. "Modeling Piston-Ring Dynamics, Blowby, and Ring-Twist Effects." *Proceedings of the 1996 18th Annual*
-

- Fall Technical Conference of the ASME Internal Combustion Engine Division. Part 2 (of 5), Oct 20-23 1996, Fairborn, OH, USA, 67-80.*
- Tower, B.** (1883). "First Report on Friction Experiments (Friction of Lubricated Bearings)." *Institution of Mechanical Engineers Part J*, 632-659.
- W.Pullrabeck, W.** (2003). Engineering Fundamentals of the Internal Combustion Engine, Prentice Hall Upper Saddle River, NJ, USA.
- Wakabayashi, K., Honda, Y., Kodama, T., and Iwamoto, S.** (1995). "The Characteristics of the Bending Vibration Stress Coupled with Torsional Vibration of Automobile Diesel Engine Shaftings." *SAE Technical Paper Series*.
- Yang, J., Yang, W., Yu, X., and Wang, C.** (2001). "Design of Internal Combustion Engine Piston Based on Skirt Lubrication Analysis." *Society of Automotive Engineers*(2001-01-2486).
- Yang, Q., and Keith, T. G., Jr.** (1996a). "Two-Dimensional Piston Ring Lubrication - Part I: Rigid Ring and Liner Solution." *Tribology Transactions*, 39(4), 757-768.
- Yang, Q., and Keith, T. G., Jr.** (1996b). "Two-Dimensional Piston Ring Lubrication - Part II: Elastic Ring Consideration." *Tribology Transactions*, 39(4), 870-880.

